Integrated Silicon-based Optical Modulators

100 Gb/s and Beyond

Integrated Silicon-based Optical Modulators

100 Gb/s and Beyond

Kensuke Ogawa

SPIE PRESS
Bellingham, Washington USA

Library of Congress Cataloging-in-Publication Data

Names: Ogawa, Kensuke, author.
Title: Integrated silicon-based optical modulators : 100 Gb/s and beyond / Kensuke Ogawa.
Description: Bellingham, Washington, USA : SPIE Press, [2019] | Includes bibliographical references and index.
Identifiers: LCCN 2018048725 (print) | LCCN 2019003000 (ebook) | ISBN 9781510625822 (pdf) | ISBN 9781510625839 (epub) | ISBN 9781510625846 (mobi) | ISBN 9781510625815 | ISBN 9781510625815 (softcover) | ISBN 151062581X (softcover)
Subjects: LCSH: Light modulators. | Silicon–Optical properties. | Integrated optics.
Classification: LCC TK8360.L5 (ebook) | LCC TK8360.L5 O33 2019 (print) | DDC 621.381/045–dc23
LC record available at https://lccn.loc.gov/2018048725

Published by

SPIE
P.O. Box 10
Bellingham, Washington 98227-0010 USA
Phone: +1 360.676.3290
Fax: +1 360.647.1445
Email: books@spie.org
Web: http://spie.org

Printed in the United States of America.
First Printing.
For updates to this book, visit http://spie.org and type “PM302” in the search field.

Table of Contents

Preface

With the advent of semiconductor diode lasers that emit a coherent light beam under current injection and low-loss silica optical fibers that transmit a light beam over long distances, the technology of optical communications became practically available in the late 1960s to the early 1970s. Since then, optical communications have grown ceaselessly over the decades and have nowadays become indispensable for a variety of networks, such as 5G mobile communication, social networking, video streaming, the Internet of Things, artificial intelligence, virtual/augmented reality, and large-scale simulation. The data transmission capacity (measured in bit rate per wavelength channel, which is allocated in a single core of silica optical fiber) was ~10 Mb/s in the 1970s and a few Gb/s in the 1980s. This capacity has reached 100 Gb/s and beyond in modern optical communications—an increase of more than four orders of magnitude, or roughly ten times per decade from the dawn of optical communications.

Such remarkable growth of data traffic in optical communications was enabled by the progress of high-speed photonic devices that are capable of processing and transmitting optical signals at the bit rates cited above. Photonic integration technologies provide design and fabrication platforms that facilitate the high-density integration of various elements of photonic devices with small footprints. These platforms thereby allow the manufacture of small-form-factor photonic assemblies that consist of photonic integrated circuits. Among these platforms, silicon-photonics platforms are most suited to the design and fabrication of photonic integrated circuits with low power consumption and cost because the platforms are based on electronic design tools and fabrication process lines developed for high-volume manufacturing of silicon integrated circuits that consist of ultra-low-voltage complementary metal–oxide–semiconductor devices. Therefore, there is increasing interest in the research and development of photonic integrated circuits on silicon-photonics platforms to accommodate the demand for versatile and affordable small-form-factor optical equipment in high-volume applications such as intra- and inter-datacenter optical communications around the world.

This book focuses on high-speed, integrated silicon-based optical modulators as the cutting-edge, key photonic device at the forefront of

modern optical-communication equipment. A high-speed optical modulator allows electrical-to-optical conversion in an optical transmitter for optical signal generation in advanced modulation formats with complex intensity- and phase- modulation schemes at bit rates of 100 Gb/s and beyond per wavelength channel. Silicon-photonics platforms allow integration of entire elements on chip to miniaturize the high-speed optical modulator within a footprint less than 1 cm^2. The following chapters describe the basic principles to the latest developments of integrated silicon-based optical modulators. It is hoped that this book will inspire readers to further enhancements of modulator performance and sophistication of photonic integration technology, including diode lasers to realize ultra-compact, high-speed integrated optical transmitters in the next generation of optical communications.

Kensuke Ogawa
February 2019

Glossary of Terms

ADC	Analog-to-digital converter
AOC	Active optical cable
APD	Avalanche photodiode
ASE	Amplified spontaneous emission
ASK	Amplitude-shift keying
BER	Bit error rate
BOX	Buried oxide
BPF	Bandpass filter
BPM	Beam propagation method
BPSK	Binary phase-shift keying
CFP	C form-factor pluggable
CMOS	Complementary metal–oxide–semiconductor
CPW	Coplanar waveguide
CVD	Chemical vapor deposition
CW	Continuous wave
DAC	Digital-to-analog converter
DC	Direct current
DCF	Dispersion compensation fiber
DCI	Datacenter interconnect
DEMUX	Wavelength demultiplexing
DML	Directly modulated laser
DP-QPSK	Dual-polarization quadrature phase-shift keying
DPSK	Differential phase-shift keying
DQPSK	Differential quadrature phase-shift keying
DSP	Digital signal processor
EDFA	Erbium-doped fiber amplifier
EML	Externally modulated laser
E-O	Electrical-optical
ER	Extinction ratio
FDTD	Finite-difference time domain
FEC	Forward error correction
FEM	Finite-element method

FIR	Finite impulse response
FK	Franz–Keldysh
FOM	Figure of merit
FTTH	Fiber-to-the-home
I	In phase
IC	Integrated circuit
IM-DD	Intensity modulation and direct detection
I/O	Input and output
IP	Internet protocol
IQ	In phase and quadrature phase
LAN	Local-area network
LD	Laser diode
LN	Lithium niobate
LO	Local oscillator
MEMS	Micro-electro-mechanical systems
MFC	Mode-field converter
MMI	Multi-mode interferometer
MOS	Metal–oxide–semiconductor
MUX	Wavelength multiplexing
MZI	Mach-Zehnder interferometer
NRZ	Non-return to zero
OOK	On–off keying
OSNR	Optical signal-to-noise ratio
PAMn	Pulse amplitude modulation in n levels
PBC	Polarization-beam combiner
PCB	Printed circuit board
PD	Photodiode
PDK	Process design kit
PDM	Polarization-division multiplexing
PIC	Photonic integrated circuit
PMF	Polarization-maintaining single-mode fiber
PR	Polarization rotator
PRBS	Pseudo-random bit stream
PPG	Pulse pattern generator
Q	Quadrature
QAM	Quadrature amplitude modulation
QCSE	Quantum-confined Stark effect
QPSK	Quadrature phase-shift keying
QSFP	Quad small-form-factor pluggable
QW	Quantum well
RZ	Return to zero
SCM	Scanning capacitance microscopy
SEM	Scanning electron microscopy

SLD	Super-luminescent diode
SMF	Standard-dispersion single-mode fiber
SNR	Signal-to-noise ratio
SOI	Silicon on insulator
SW	Switch
TE	Transverse-electric
TEC	Thermo-electric cooling
TEM	Transmission electron microscopy
TIA	Trans-impedance amplifier
TM	Transverse-magnetic
TO	Thermo-optic
VIA	Vertical interconnect access
VOA	Variable optical attenuator
WDM	Wavelength-division multiplexing

Chapter 1
Introduction

There has been a rapid and ceaseless increase in communication traffic in global networks for the distribution of digital content, such as video streams, visual content, and big data. A forecast of the growth of communication traffic reports an increase in the global internet protocol (IP) traffic, as plotted in Fig. 1.1: the traffic increases beyond 100 exabyte (EB) per month and beyond 1 zettabyte (ZB) per annum in 2017.[1] Fixed internet traffic occupies the major portion in the meantime; mobile data traffic grows more rapidly and will reach the fixed internet traffic some years after 2020. Such a burst of IP traffic creates demand for greater transmission capacity in optical networks spreading over personal mobile terminals, fiber-to-the-home (FTTH) networks, local-area networks (LANs), datacenters, metro networks, and backbone core networks. Therefore, high-capacity optical networks at 100 gigabytes per second (Gb/s) and beyond are essential for the infrastructure that supports the modern information and intelligence era.

High-speed photonic devices are used in optical communication equipment for high-capacity data transmission in optical networks. Among high-speed photonic devices, optical modulators accommodated in optical transceivers (in which optical transmitters and optical receivers are co-packaged) play crucial roles in high-capacity optical networks because optical modulators permit high-quality optical signal generation in high-transmission capacity. The production of optical modulators with conventional design and fabrication platforms requires the assembly of dielectric crystals for phase shifters, RF electrodes for high-speed electrical signals, and elements for optical beam coupling such as mirrors and focusing/collimating lenses.[2–5] With such conventional production approaches, compact-form-factor optical transceivers—which are now essential to enhance the transmission capacity of modern optical networks—have not been realized because conventional optical modulators have a considerable footprint in optical transceivers.

Photonic integration technology has disrupted design and fabrication platforms with on-chip integration, and thus phase-shifter waveguides, planar RF transmission electrodes, and other photonic components have been

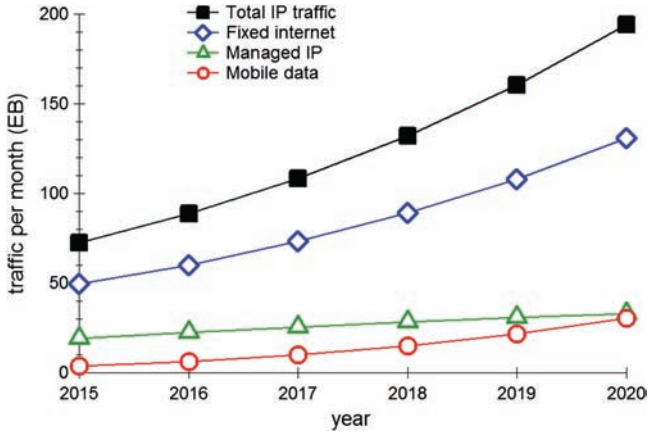

Figure 1.1 Communication traffic per month plotted vs year.[1]

integrated monolithically on small-footprint photonic chips.[6,7] The groundbreaking integration technology has enabled the design and fabrication platforms of compound-semiconductor photonics, silicon photonics, and polymer photonics, and has opened the way to compact-form-factor optical transceivers. Photonic integration platforms now support the technology roadmaps for compact transceivers with high-transmission capacity. A trend in footprint reduction for CFP-series optical transceivers (a series of compact-form-factor pluggable optical transceivers), is illustrated in Fig. 1.2. The footprint, defined as a product of width W and length L, is plotted against

	CFP	CFP2	CFP4
W	82.0 mm	41.5 mm	21.5 mm
L	144.8 mm	107.5 mm	92.0 mm
H	13.6 mm	12.4 mm	9.5 mm

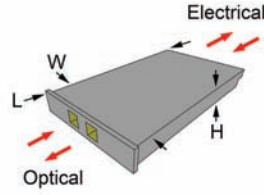

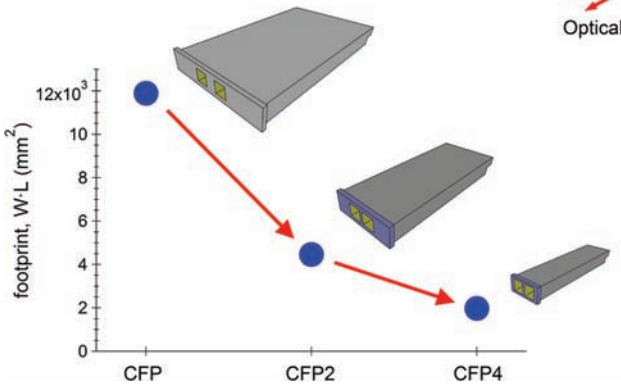

Figure 1.2 Footprint reduction for CFP-series compact-form-factor, pluggable optical transceivers.

CFP-series generation using physical-dimension data in CFP multi-source agreement (CFP-MSA) as an example of compact optical transceivers[8] [the term CFP stands for "C form-factor pluggable," where C is the number 100, or *centum* in Latin]. An almost-one-order reduction in footprint is observed in the refinements from CFP to CFP4. In compact-form-factor, pluggable optical transceivers such as the CFP series, the optical input/output (I/O) ports for optical data are aligned on the front panel of the transceiver housing, whereas the electrical input/output ports for electrical data are on the back edge of the transceiver housing, as indicated in the inset of Fig. 1.2. There are also other MSAs on compact optical tranceievers, such as QSFP and consortiums on small-footprint, onboard optical I/O modules.

Among the platforms for photonic integration, silicon photonics provides most versatile platforms as ecosystems for design and fabrication of small-footprint photonic integrated circuits because it provides the precision, reliability, and mass-production capability established for complementary metal–oxide–semiconductor (CMOS) transistors.[9–16] Active device elements, such as optical modulators and photodetectors, are integrated with passive device elements, such as optical couplers, filters, and multiplexers (including polarization diversity), using high-index-contrast optical waveguides in small footprints. Therefore, small-footprint, integrated, silicon-based optical modulators are extensively interested as keystones in optical signal transmission in high-capacity optical networks. Photonics ecosystems referred to in the next chapter allow design and fabrication of the integrated devices.

Energy efficiency is another critical subject in high-capacity optical networks to assure the sustainable growth of our communities, because high-capacity optical networks consume a considerable portion of the electrical energy supplied to all the infrastructures on the globe.[17–22] More than 50% of the total electrical energy in the networks is spent on optical transceivers and related modules.[19,22] Optical modulators require a significant portion of electrical energy input to the optical transceivers. Therefore, a reduction in electrical energy associated with optical modulators is a popular subject for energy efficiency in high-capacity optical networks, including reducing electrical energy for optical modulation and using thermo-electric cooling with optical modulators to maintain performance during modulation. A silicon-photonics platform based on high-index-contrast optical waveguides with a small footprint and refractive-index modulation in a broad spectral band with an extended temperature range provides feasible technical solutions for efficient optical modulators because it does not require a thermo-electric controller.

This book deals with integrated optical modulators as the key optical components for applications in optical-network domains at 100 Gb/s and beyond with a focus on silicon-photonics platforms. The integrated photonics platform has been developed from a CMOS-based design and microfabrication technologies, and versatile design and fabrication tools are available from

silicon-photonics foundries worldwide. A variety of device libraries that include electronic circuits have been supplied by such foundries. Therefore, readers can easily design, fabricate, and characterize integrated silicon-based optical modulators as key components in optical-network domains at 100 Gb/s and beyond.

Chapter 2 provides background details for integrated silicon-based optical modulators. It opens with a general overview of high-capacity optical networks. High-capacity optical networks at 100 Gb/s and beyond consist of several domains, which are constructed with fiber-optic links. The fiber-optic links are classified into two categories: a wavelength-division multiplexing (WDM) fiber link in the core, and metropolitan-area optical networks and parallel fiber-optic links in datacom applications, such as rack-to-rack optical interconnects in datacenters. The second half of the chapter presents the general aspects and principles of optical modulators in high-capacity optical networks. Semiconductor optical modulators are generally described as small-footprint optical modulators with an emphasis on integrated optical modulators in silicon-photonics platforms as photonic integrated circuits for optical signal generation in the most advanced compact-form-factor optical transceivers.

Generic integrated optical modulators are described in Chapter 3, classified in terms of electronic transition processes for optical modulation, schemes of optical modulation, and types of waveguide geometry. Among these, Mach–Zehnder (MZ) optical modulators using the free-carrier intraband electro-refraction effect are featured because of their superior broadband spectral response and the quality of optical intensity and phase modulation for optical modulators in high-capacity optical networks. Photonic integration in small-footprint optical modulators with a silicon-photonics platform for advanced modulation formats is described.

Chapter 4 covers optical circuits and waveguides in integrated MZ optical modulators. Optical layouts of the integrated MZ optical modulators suiting optical-signal generation in various modulation formats are described to clarify how the optical signals in the respective modulation formats are generated in the respective optical layouts. Simple mathematical models in the transfer-matrix framework are then presented with respect to some cases of the optical layouts to illustrate that fundamental mathematical methods such as matrix algebra are essential to the design and modeling of generic integrated MZ optical modulators. Integrated MZ optical modulators designed and fabricated on various material platforms consist of optical waveguides as the most fundamental building blocks. In particular, high index contrast in optical waveguides on silicon-photonic platforms allows for a very small core cross-section sub-micrometers wide and tall to construct a variety of small-footprint integrated photonic circuits. Optical waveguides and optical modes specifically on silicon-photonics platforms are also addressed.

Chapter 5 deals with electronic and opto-electronic properties of high-speed phase shifters as the most essential building blocks in integrated MZ optical modulators on compound-semiconductor and silicon-photonics platforms. In describing the physics of optical phase modulation, the Pockels effect typically used for modulators based on lithium-niobate electro-optic crystals is also included for comparison with intraband free-carrier plasma refraction and interband optical dipole transition processes, such as the Franz–Keldysh (FK) effect and optical Stark effect (QCSE) in group-IV semiconductors and III-V compound semiconductors under an electric field. Based on spectral and temperature dependences and frequency chirping of the carrier-induced optical phase-shifting processes, free-carrier plasma dispersion is shown to have the advantage of optical phase shifting over a broad spectral band within a wide range of temperature in semiconductor crystals that have inversion symmetry, which makes them useful for energy-efficient, small-footprint MZ optical modulators operating without thermo-electric cooling (TEC) for WDM optical transmission in high-capacity optical networks. Phase shifters based on free-carrier plasma dispersion consist of optical waveguides that contain PN junctions. The carrier concentration in a PN junction in a phase shifter is modulated under a high-frequency electric field; thus, high-speed optical phase modulation is realized via free-carrier plasma dispersion. Phase shifters based on free-carrier plasma dispersion are classified with respect to the profile of the PN junction (lateral or vertical PN junction). The chapter presents the technical procedure and characterization in simulation-based design and modeling of the PN-junction phase shifters to illustrate how to optimize the phase shifter performance.

Optical, electrical, and electro-optical characteristics of integrated silicon-based optical modulators are described in Chapter 6. Current–voltage characteristics and nanometer-scale images produced by scanning capacitance microscopy are presented as DC electrical characteristics. The microscopic capacitance images of the silicon-waveguide phase shifters are shown to be useful for visualizing the profiles of PN junctions in the phase shifters. Optical loss and optical phase shift are dealt with as DC optical characteristics. The integrated silicon-based optical modulators at 100 Gb/s and beyond are high-speed optical modulators with high-frequency radio-frequency (RF) metal electrodes. RF electrical and electro-optical characterizations based on S-parameter measurements provide high-frequency responses of traveling-wave electrodes and the integrated silicon-based optical modulators driven with RF signals fed to the phase shifters through the high-speed electrodes, as described in this chapter. A simple equivalent circuit model consisting of fundamental electrical circuit elements consisting of capacitors, inductors, and resistors is presented to analyze the high-speed characteristics of the modulators. The analysis of transients in optical modulation demonstrates that a simple equivalent circuit model consisting only of a capacitor and a

couple of resistors is sufficient for semi-quantitative analysis of high-speed phase shifters and allows for performance enhancement in high-speed optical modulation. Experimental evidence of temperature-insensitive optical modulation in the integrated silicon-based MZ optical modulators without TEC is also presented.

Optical-network domains, in which the integrated silicon-based MZ optical modulators are deployed, are classified in Chapter 7. The characteristics of the integrated silicon-based MZ optical modulators in transmission through optical-fiber links are then presented for various modulation formats in intensity modulation and phase modulation implemented in the optical-network domains. Subjects specific to the silicon-based optical modulators for the optical-network applications are noted. Subjects specific to the silicon-based optical modulators in the light of transmission characteristics are briefly summarized.

Photonic-electronic integration with silicon-based optical modulators is discussed with respect to two aspects in Chapter 8. Approaches of integration with electronic and photonic devices are discussed in the first part. The integration technologies are classified according to integration methods of devices from monolithic to package levels. Optical waveguides for vertical coupling are also discussed in terms of 3D photonic integration. Performance monitoring using photonic integrated circuits is an emerging subject; the chapter presents a photonic, integrated performance-monitoring circuit monolithically integrated with a silicon-based MZ optical modulator in a small-footprint chip on a silicon-photonics platform.

Supplemental technical items are compiled in an appendix to help readers better understand the contents of this book. These items include the bit rates and modulation formats adopted for optical signal transmission in high-capacity optical networks (Section A.1) and Kramers–Kronig transformation as a basic method for the characterization of the refractive index, and thus optical phase shift (Section A.2).

References

1. "Cisco visual networking index: forecast and methodology, 2015–2020," http://www.cisco.com/c/en/us/solutions/collateral/service-provider/visual-networking-index-vni/complete-white-paper-c11-481360.html.
2. W. W. Rigrod and I. P. Kaminow, "Wide-band microwave light modulation," *Proc. IEEE* **51**(1), 137–140 (1963).
3. C. J. Peters, "Gigacycle-bandwidth coherent-light traveling-wave amplitude modulator," *Proc. IEEE* **53**(5), 455–460 (1965).
4. I. P. Kaminow and E. H. Turner, "Electrooptic light modulators," *Proc. IEEE* **54**(10), 1374–1390 (1966).

5. S. Uehara, "Focusing-type optical modulator," *IEEE J. Quantum Electron.* **QE-9**(10), 984–986 (1977).
6. S. E. Miller, "Integrated optics: an introduction," *Bell System Tech. J.* **48**(7), 2059–2069 (1969).
7. P. K. Tien, "Light waves in thin films and integrated optics," *Appl. Opt.* **10**(11) 2395–2413 (1971).
8. "Next gen PMD CFP MSA baseline specifications," http://www.cfp-msa.org/Documents/CFP_MSA_baseline_specifications_15.pdf.
9. G. T. Reed and A. P. Knights, *Silicon Photonics: An Introduction*, John Wiley and Sons, Chichester, UK (2004).
10. M. Hochberg, "Towards fabless silicon photonics," *Nature Photon*. **4**(8), 492–494 (2010).
11. T. Pinguet, S. Gloeckner, G. Masini, and A. Mekis, "CMOS photonics: a platform for optoelectronics integration," in *Silicon Photonics II: Components and Integration*, D. J. Lockwood and L. Pavesi, Eds, Topics in Applied Physics **119**, Springer-Verlag, Berlin Heidelberg, 187–216 (2011).
12. T. Baehr-Jones, T. Pinguet, G.-Q. Lo, S. Danziger, D. Prather, and M. Hochberg, "Myths and rumours of silicon photonics," *Nature Photon*. **6**(4), 206–208 (2012).
13. M. A. Popović, et al., "Monolithic silicon photonics in a sub-100nm SOI CMOS microprocessor foundry: progress from devices to systems," *Proc. SPIE* **9367**, 93670M-1–93670M-10 (2015).
14. M. Heins, et al., "Design flow automation for silicon photonics: challenges, collaboration, and standardization," in *Silicon Photonics III: Systems and Applications*, D. J. Lockwood and L. Pavesi, Eds, Topics in Applied Physics **122**, Springer-Verlag, Berlin Heidelberg, 99–156 (2016).
15. A. E.-J. Lim, et al., "Path to silicon photonics commercialization: the foundry model discussion," in *Silicon Photonics III: Systems and Applications*, D. J. Lockwood and L. Pavesi, Eds, Topics in Applied Physics **122**, Springer-Verlag, Berlin Heidelberg, 191–216 (2016).
16. T. L. Koch, et al., "The American Institute for Manufacturing Integrated Photonics: advancing the ecosystem," *Proc. SPIE* **9772**, 977202-1–977202-6 (2016).
17. Y. Zhang, P. Chowdhury, M. Tornatore, and B. Mukherjee, "Energy efficiency in telecom optical networks," *IEEE Commun. Survey & Tutorials* **12**(4), 441–458 (2010).
18. O. Tamm, C. Hermsmeyer, and A. M. Rush, "Eco-sustainable system and network architectures for future transport networks," *Bell Labs Tech. J.* **12**(4), 311–328 (2010).
19. K. Ishii, J. Kurumida, S. Namiki, T. Hasama, and H. Ishikawa, "Energy consumption and traffic scaling of dynamic optical path networks," *Proc. SPIE* **8646**, 86460A-1–86460A-10 (2013).

20. P.-H. Ho, G. Shen, S. Subramaniam, H. T. Mouftah, C. Qiao, and L. Wosinska, "Guest editorial energy-efficiency in optical networks," *IEEE J. Sel. Areas Commun.* **32**(8), 1521–1523 (2014).
21. Y. Demir and N. Hardavellas, "Towards energy-efficient photonic interconnects," *Proc. SPIE* **9368**, 93680T-1–93680T-12 (2015).
22. H. Isono, "Recent standardization directions on high-speed client and line side components," *Proc. SPIE* **9775**, 97750C-1–97750C-8 (2016).

Chapter 2
Background

2.1 High-Capacity Optical Networks

2.1.1 Overview

Optical modulators are extensively used in high-capacity optical networks at 100 Gb/s and beyond, which consist of several domains of fiber-optic communication networks, as illustrated schematically in Fig. 2.1. Each domain is connected to each other with fiber-optic links: optical data are transmitted through fiber-optic transmission lines using optical fibers as transmission media.[1–3]

Core domains, which include long-haul optical networks in terrestrial and undersea optical networks extending beyond 1000 km, form worldwide backbone networks and support global data-transmission services, such as the transmission of digital contents over the internet.[1] Metro domains under the core domains cover regional areas such as cities and communities in transmission distance typically 100–1000 km. Plural metro domains are connected to a core domain. As Fig. 2.1 shows, LAN domains, FTTH domains, mobile backhaul domains, high-performance computing domains, and hyper-scale datacenter domains are connected to the metro domains. The optical networks inside the domains are also based on the fiber-optic links, as described in the next subsection. Significant progress has been achieved for massive data-centric architectures of intra- and interdatacenter networks using photonic integrated devices.[4–6] Individual datacenters are connected through datacenter interconnects (DCIs) based on fiber-optic links.[7,8] The datacenters connected through DCI virtually form an aggregation of hyper-scale datacenters to permit massive computing services such as big-data analysis and artificial intelligence.

2.1.2 Basic elements

A fiber-optic link for high-capacity data transmission in metro-area and long-haul domains can be represented with a simple schematic model illustrated in Fig. 2.2. The architecture of WDM link is employed to increase transmission capacity. Optical data are multiplexed in spectral channels of ITU-T grid with

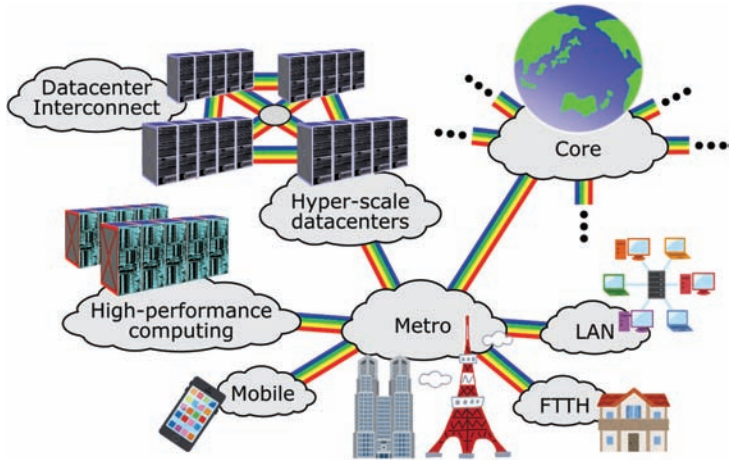

Figure 2.1 Schematic diagram of high-capacity optical networks.

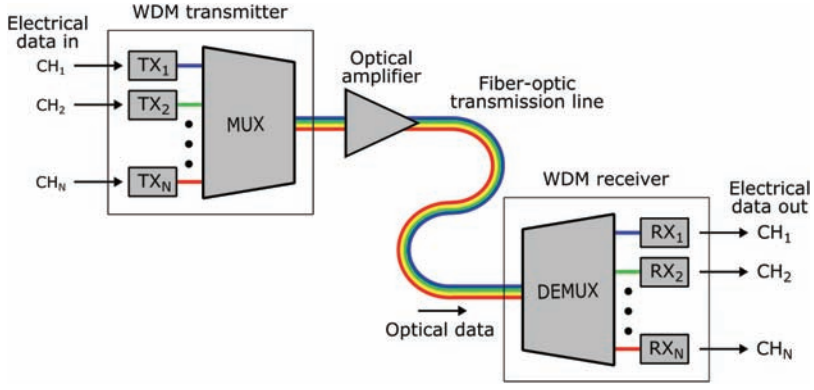

Figure 2.2 Diagram of a fiber-optic link for WDM data transmission.

a channel spacing of 50 GHz or 100 GHz in frequency, for example.[1,9] A channel spacing of 100 GHz in frequency corresponds to 0.8 nm in wavelength in the C-band extending from 1528 nm to 1577 nm by using 2.998×10^8 m/s for the speed of light in vacuum.[10] The basic elements of the link are a WDM transmitter, a fiber-optic transmission line, an optical amplifier and a WDM receiver in one direction of data transmission. The link for high-capacity optical networks allows full-duplex communications, and therefore it also contains another set of a WDM transmitter, fiber-optic transmission line an optical amplifier, and a WDM receiver in the reverse direction of data transmission.

The WDM transmitter consists of individual optical transmitters TX_1–TX_N for N channels, CH_1–CH_N of wavelengths λ_1–λ_N, and a wavelength multiplexer (MUX). Wavelength-selective optical filters—such as lattice filters, arrayed waveguide gratings, and echelle gratings—can be used to construct the optical

circuit of a MUX.[1,9,11–16] Electrical data from the sender are input to the optical transmitters of the WDM channels, respectively. Optical data are generated with the electrical data and output from the optical transmitters. After the MUX, optical data in all of the optical transmitters are multiplexed and input to the fiber-optic transmission line, which consists of a single-mode optical fiber. Optical modulators used in the optical transmitters in the WDM fiber-optic link are required to operate in a spectral range covering all of the WDM channels.

After transmission through the fiber-optic transmission line, the WDM optical data are input to the WDM receiver. The WDM optical data are demultiplexed to the optical data in the wavelength channels with a wavelength demultiplexer (DEMUX) and then received with individual optical receivers (RX_1–RX_N). The optical circuit of DEMUX is equivalent to that of MUX except the reversed propagation direction of the transmission light. Electrical data to recipient are reproduced and output from the individual optical receivers. Optical circuits for optical signal processing including MUX/DEMUX and electronic circuits for electrical signal processing can be integrated on a silicon chip. A single-chip CMOS-integrated WDM transceiver on a silicon-photonics platform is reported.[17]

An erbium-doped fiber amplifier (EDFA) or a semiconductor optical amplifier can be used for an optical amplifier.[1,9,18–23] The number of optical amplifiers is not necessarily limited to one, the number depending on the total span of the fiber-optic link.

Another type of fiber-optic link is illustrated in Fig. 2.3. The link is a parallel fiber-optic link, which is mainly used for short-reach optical networks such as optical interconnects between circuit boards and back planes of servers and computers in datacenters and high-performance computing centers.[24–26] Electrical data in N parallel channels are converted to optical data, which are generated with the individual optical transmitters, and input to parallel fiber-optic transmission lines. Integrated optical transceivers on a silicon-photonics platform have also been proposed.[27–30] Photonic integration for optical transceivers on a silicon-photonics platform is described in

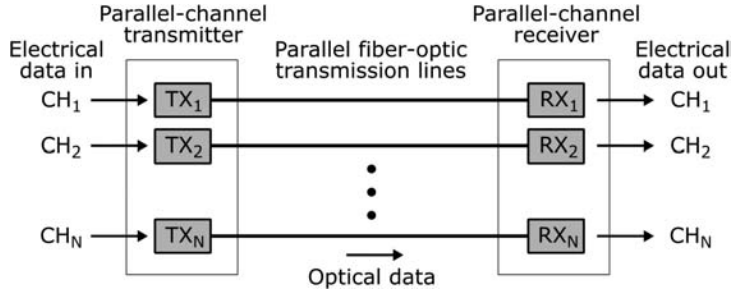

Figure 2.3 Schematic diagram of fiber-optic link for parallel-channel data transmission.

Sections 2.2.3 and 3.3. For full-duplex communications, the entire systems require another set of parallel fiber-optic links in the reverse direction of data transmission. Optical amplifiers are not used in short-reach optical networks.

The parallel fiber-optic transmission lines are made of single-mode or multi-mode optical fibers. In particular, extensive efforts have been made for optical interconnects on a silicon-photonics platform using single-mode optical fibers because transmission capacity in single-mode fiber is not deteriorated by the modal dispersion in multi-mode optical fiber.[1,9,27–30] Silicon-photonic parallel fiber-optic links that use multi-mode optical fibers, however, have been demonstrated recently with specialty multi-mode optical fibers optimized for high-capacity transmission at O-band wavelengths around 1300 nm for higher tolerance of fiber alignment than single-mode optical fiber.[31,32]

2.1.3 Transmission capacity

Transmission capacity is measured as the bit rate, which is the total number of bits contained in the symbols transmitted per second.[33] The number of bits per symbol depends on the modulation format selected for the optical networks in which optical data are transmitted. Modulation formats such as NRZ-OOK, PAM4, BPSK, QPSK, and QAM, which have been incorporated into optical-network data transmission, are listed and described in Section A.1 with a list of bit rates. (Symbol rate is alternatively called the baud rate.)

The bit rate of a fiber-optic link is the total of the bit rates summed over all of the WDM channels, in the case of a WDM fiber-optic link, or over all of the parallel fiber channels, in the case of a parallel fiber-optic link. The maximum achievable bit rate in optical-data generation at an optical transmitter is determined by the response speed or, equivalently, the response frequency of the optical modulators accommodated in the optical transmitter. It is therefore crucial to produce high-speed optical modulators to realize high-capacity optical networks.

According to Shannon's notion, optical data are transmitted under the presence of noise, and the transmission capacity of a fiber-optic link is affected by the noise level in the fiber-optic link.[33] A higher transmission capacity is achieved by lowering the noise level to the maximum transmission capacity in the noise-free limit. The noise level is enhanced relatively if the amplitude of optical data emitted from an optical transmitter is attenuated due to the optical loss of the optical modulators accommodated in the transmitter. As for high-speed optical modulators, a reduction in the optical loss below 15 dB is crucial to realize a high-capacity optical network with a transmission span of 100 km or longer.

2.1.4 Energy efficiency

To avoid power consumption and thus achieve energy efficiency in high-capacity optical networks, it is crucial to reduce the electrical power consumed

in optical transceivers deployed in high-capacity optical networks. The total electrical power to a 400-Gb/s (8×50-Gb/s) CFP2 transceiver is specified as 12 W, for example, and almost 70% of the electrical power must be TX/RX-accommodated in the optical transceiver.[34] Therefore, the power of electrical signals to the optical modulators in the TX must be reduced. A silicon-photonic micro-disk optical modulator, which has the advantage of modulation efficiency enhancement due to optical resonance, was demonstrated to operate in the error-free limit of the bit error rate (BER) with 85 fJ/bit at 10 Gb/s—an extremely small power consumption of 100 μW that sacrifices spectral bandwidth in optical modulation.[35] For more practical optical modulators that operate in a broad spectral range extending over the C-band, power consumption as low as 650 mW, including electrical power for an input laser source, was reported for 4×10-Gb/s integrated optical modulators on a silicon-photonics platform.[36] Integrated optical modulators on a silicon-photonics platform are also capable of athermal operation without TEC, i.e., the electrical power consumption of TEC is eliminated.[37,38] Photonic integration on a silicon-photonics platform is thus suited to the design and fabrication of energy-efficient, high-speed optical modulators. Enhancement of the energy efficiency by a factor of 100 with photonic integration technology on a silicon-photonics platform is predicted in comparison with conventional photonics technology based on the assembly of discrete opto-electronic components.[39] According to the prediction, an energy efficiency as high as 10 Tb/s/W can be achieved, for instance, in optical communications that have very short reach, such as on-chip optical interconnects in photonic integrated circuits (PICs) on a silicon-photonics platform.

2.2 Optical Modulators in High-Capacity Optical Networks

2.2.1 Optical modulator in optical transmitter

An optical modulator is an optoelectronic component for building up an optical transmitter, and plays essential roles in the function of electrical–optical (E-O) conversion in an optical transmitter to generate high-speed optical data in response to input electrical data.[1,30] Figure 2.4 illustrates the components in an optical transmitter (TX_i). Digital electrical data for the i^{th} channel in M bits, for example, are input to parallel electrical ports of the optical transmitter and converted to serial streams of electrical data with front-end electronics, such as a CMOS-based integrated circuit (IC) including a serializer, a memory buffer, electrical power supply to a laser diode (LD), and, if necessary, a digital signal processor (DSP). The serial electrical data are then amplified at a modulator driver with single-ended or differential output according to the configuration of input signal electrodes of an optical modulator to be used. High-speed electronics are required for the front-end electronics and the modulator driver to drive the optical modulator at

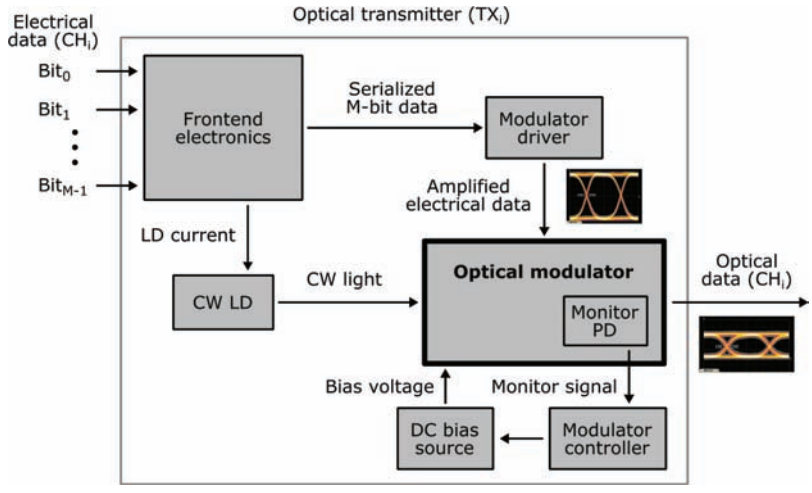

Figure 2.4 Block diagram of components in an optical transmitter.

high-modulation speeds. Continuous-wave (CW) light from a single-mode LD is input to the optical modulator and then modulated in the optical modulator accordingly with the input serial electrical data to generate optical data; thus, the modulated light emitted from the optical modulator carries the optical data after the E-O conversion.

The status of the optical modulator can be monitored and controlled with a feedback circuit consisting of a monitor photodiode (PD), a modulator controller, and a direct-current (DC) bias source. The monitor signal output from the monitor PD is detected and processed with the modulator controller, and the bias voltage from the DC bias source is adjusted to stabilize the condition of the optical modulator. Eye diagrams of amplified electrical data input to the optical modulator and optical data output from the optical modulator in 10-Gb/s non-return-to-zero on–off keying (NRZ-OOK) are presented as the examples of input electrical and output optical waveforms.[40] A discrete monitor PD can be co-packaged with an optical modulator chip based on a conventional design and fabrication platform for an optical modulator. On a silicon-photonics platform, however, the monitor PD can be integrated on-chip. The monolithic integration of a monitor PD on a silicon-photonics optical modulator chip is described in Chapter 8.

In general, directly modulated lasers (DMLs) can also be used to build optical transmitters with a simpler component configuration.[41] External optical modulators and CW LDs are, however, preferred to DMLs for applications in high-capacity optical networks because of the following three advantages:

1. Phase modulation, in combination with digital coherent detection, is more suited to metro-area and long-haul optical networks than

intensity modulation for higher receiver sensitivity and a lower BER in differential detection.[42]

2. An optical modulator can be configured for chirp-free modulation under push–pull drive, whereas a DML produces frequency chirping, which causes inter-symbol interference in the time domain and channel cross-talk in the spectral domain.[43–45] Specific adjustment of the dispersion parameter is thus required for a fiber-optic link to transmit frequency-chirped optical data generated by a DML transmitter at high bit rates.[46] This requirement limits DML-based transceivers when applied to high-capacity optical networks.
3. For data transmission in parallel fiber channels, parallel optical modulators with input light split from a CW LD allow for greater energy efficiency than parallel DMLs. Furthermore, DCI is becoming more important in conjunction with emerging edge-computing and cloud services such as the IoT, big-data manipulation, and artificial intelligence. A transmission capacity of 400 Gb/s in a span up to ~100 km is required for cutting-edge DCI. Coherent-phase modulation formats of DP-QPSK and *n*QAM (described in Section A.1 of the Appendix) meet the transmission capacity per wavelength channel.[7,8] Small-footprint, polarization-multiplexed, coherent optical modulators on a silicon-photonics platform can be used to construct low-cost and compact-form-factor coherent transceivers for 400-G DCI.

2.2.2 Semiconductor optical modulators

Ferroelectric lithium-niobate ($LiNbO_3$, LN) optical modulators, where the linear electro-optic Pockels effect is the physical principle of operation, have been utilized most extensively for high-speed modulation in optical-fiber telecommunication systems.[47–50] Optical modulators on semiconductor photonic integration platforms, however, are more crucial to the evolution of technology roadmaps, e.g., CFP optical transceivers in high-capacity optical networks, as described in Chapter 1. Highly confined optical modes in high-index-contrast semiconductor optical waveguides enable high-efficiency optical modulation in small footprints. Table 2.1 lists semiconductor materials used for optical modulators and their corresponding physical principles. Chapters 3 and 4 describe the classification and basics of semiconductor optical modulators with respect to photonic integration.

Table 2.1 Semiconductor materials and physical principles for optical modulators.

Material	III-V compounds (GaAs, InP)	III-V QWs (InGaAlAs, InGaAs, InAsP)	IV elements & alloys (Si, Ge, SiGe)	IV QWs (Ge, SiGe)
Physical principle	Pockels[51,52]	QCSE[53–56]	Plasma dispersion[57–60] FK[61–64]	QCSE[65–67]

The linear electro-optic effect also appears in III-V compound crystals because they are ionic and lack centrosymmetry in the crystallography, whereas there is no Pockels effect in the group-IV element and alloy crystals because they are covalent and form centrosymmetric crystals.[50] The electro-optic effect is produced by the displacement of crystal ions under an electric field, and thus its response is insensitive to temperature and appears in a broad spectral range extending over visible and near-infrared ranges. Its response frequency is limited by the vibration frequency of optical phonons in the infrared spectra around ~10 THz.[68] The Pockels effect can be applied to ultra-high-speed optical modulation in broad spectral ranges. The relatively low modulation efficiency of the Pockels effect in comparison with other physical processes, on the other hand, leads to relatively high modulation voltage. A Pockels-effect in-phase and quadrature-phase (IQ) optical modulator on a III-V photonics platform operates with a peak-to-peak modulation voltage of 7.5 V_{PP} for a phase-shifter length of 7.5 mm.[52]

Optical modulation based on the QCSE of 2D excitons in semiconductor quantum wells (QWs) in interband optical dipole transition provides high refractive index change, hence efficient optical modulation near the electronic band edge with the expense of limited spectral bandwidth for operation and thermal budget due to temperature dependence of the electronic bandgap.[53,69] A waveguide length of the active part as short as 150 μm and a peak-to-peak modulation voltage as low as 1.2 V_{PP} were reported.[55]

The FK effect occurs due to photon-assisted tunneling in the interband optical dipole transition.[70] The modulation efficiency of the effect is limited by the tunneling rate of photoexcited electrons and holes. The structure of optical waveguides that incorporate the FK effect into optical modulation is simpler than that for QCSE optical modulators because the former effect occurs in bulk 3D semiconductors, and epitaxial growth of 2D QWs is not required in fabrication process.

Plasma dispersion is generated by individual electrons and holes accelerated in alternating electric fields of incident lightwave. The effect is the counterpart of Kramers–Kronig transformation for free-carrier optical absorption in the energy transfer from incident lightwave to the carriers and analyzed theoretically with Drude model in the classical carrier transport theory.[71,72] Some explanation on Kramers–Kronig transformation is given in Section A.2. Plasma dispersion works in a broad spectral range for optical modulators where the materials consisting the optical modulators are transparent because the interband transition does not play any roles. Efficiency in optical modulation depends on distribution profiles of electrons and holes in optical waveguides and can be enhanced if the profiles are designed suitably and produced in fabrication. Therefore, plasma dispersion is essential to energy-efficient small-footprint optical modulators for high-capacity optical networks.

The physical principles of the optical modulators are treated in Chapter 5 to clarify their theoretical bases and their pros and cons with respect to high-speed phase modulation in integrated optical modulators.

2.2.3 Integrated optical modulators on silicon-photonics platforms

Among the semiconductor optical modulators, silicon-based optical modulators are most suitable as PICs for one-chip optical transceivers in small footprints. Figure 2.5 presents a top-view optical-microscope photograph of a one-chip PIC for four-channel parallel optical transceivers on a silicon-photonics platform. The integrated silicon optical modulators with MZ interferometer waveguides for four-channel parallel transmission and four-channel germanium PDs have been fabricated in a silicon-on-insulator (SOI) chip with a 15×15 mm^2 footprint. Front-end electronic circuits are TX and RX ICs, which are mounted on the chip by a back-end integration process of flip-chip bonding.[41,73] Four-channel modulator drivers are included inside the TX IC. An optical-waveguide light source of a CW LD has also been mounted as a CW light source for the parallel channel optical modulators on the chip with flip-chip bonding. Mode-field converters (MFCs) based on silicon optical waveguides were fabricated in the areas encompassed by the circles in Fig. 2.5 for low-profile, compact optical edge coupling to input and output optical fibers. The four parallel MFCs, as shown in a scanning electron microscopy (SEM) photograph in Fig. 2.5, were designed and fabricated on a silicon-photonics platform. The MFCs allow for edge coupling to a four-core optical fiber. The four-core fibers, which have four single-mode cores aligned with a 28-μm pitch in single clads of a 125-μm diameter, were positioned along V-grooves formed on the chip and butt-joint to the facets of the input and output MFC edge couplers. The MFCs, consisting of silicon inverted nano-taper tips in silica inner clads, were suspended in outer air clads.[74] Optical loss in the edge coupling is lower than 2.5 dB for each of the four cores per facet. Vertical-surface optical coupling based on grating couplers was adopted also for one-chip parallel channel optical transceiver PICs on a silicon-photonics platform.[75]

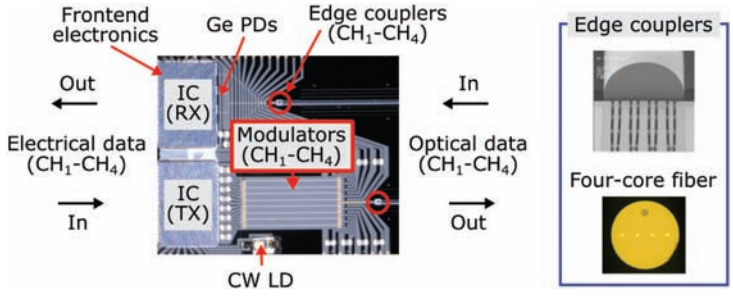

Figure 2.5 Silicon-photonics PIC for parallel four-channel optical transceiver.

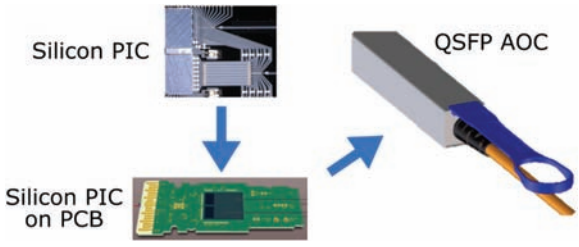

Figure 2.6 An illustrated QSFP AOC module that accommodates a small-footprint silicon PIC mounted on a PCB.

The silicon PIC has been designed for mounting on a print circuit board (PCB) and suitable for compact and low-profile packaging in a module of quad small-form-factor pluggable (QSFP) active optical cable (AOC), as illustrated in Fig. 2.6. A reduction in the number of fibers from four to one leads to a smaller space and a higher packing density of optical-transceiver PICs in rack-to-rack optical interconnects for optical backplanes.[76] A significant portion of the backplane space of the datacenter equipment has been occupied by fiber patch codes, as evidenced in Fig. 2.7.[77] As such, a novel QSFP AOC that accommodates the parallel data transmission channels in a single optical fiber will permit denser aggregation of computers and servers in hyper-scale datacenters. Integrated optical modulators are at the

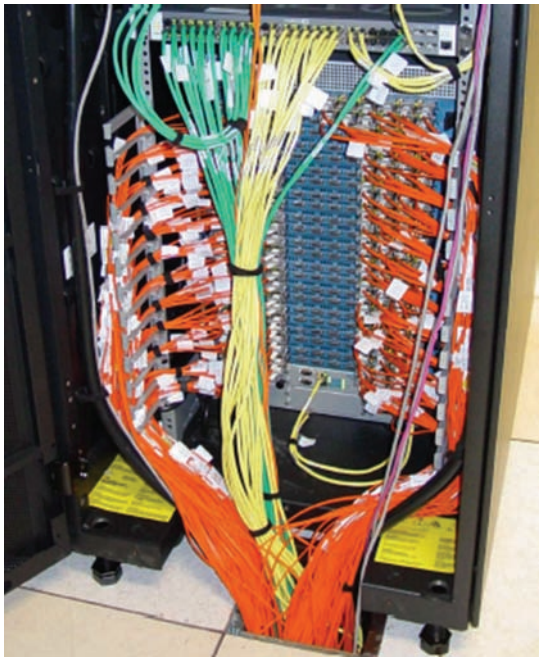

Figure 2.7 Fiber patch codes in the backplane of a switch rack.[77]

core of small-footprint optical transceiver PICs since they produce high-quality optical data for high-capacity optical networks. The science and technology of integrated optical modulators on a silicon-photonics platform are described in the following chapters.

References

1. G. P. Agrawal, *Fiber-Optic Communication Systems*, 4th Ed., John Wiley and Sons, Hoboken, 182–200 (2010).
2. A. Ghatak and K. Thyagarajan, "Optical waveguides and fibers," in *Fundamentals of Photonics*, C. Roychoudhuri, Ed, SPIE Press, Bellingham, Washington, 249–292 (2008).
3. P. Nouchi, P. Sillard, and D. Molin, "Optical fibers," in *Fibre Optic Communication, Key Devices*, H. Venghaus and N. Grote, Eds, Springer-Verlag, Berlin Heidelberg, 55–97 (2012).
4. R. G. Beausoleil, M. McLaren, and N. P. Jouppi, "Photonic architectures for high-performance data centers," *IEEE J. Sel. Top. Quantum Electron.* **19**(2), 3700109–3700109 (2013).
5. L. N. Binh, T. W. Tao, and G. L. Ning, "Exabits/s integrated photonic interconnection technology for flexible data-centric optical networks," *Proc. SPIE* **9753**, 97530V-1–97530V-10 (2016).
6. N. Calabretta, W. Miao, and H. Dorren, "High-performance flat data center network architecture based on scalable and flow-controlled optical switching system," *Proc. SPIE* **9753**, 97530W-1–97530W-10 (2016).
7. S. Elby, "Evolution of networks to meet the explosion of cloud services," *Optical Fiber Communications Conference and Exhibition (OFC)*, Tu2H.5 (2015).
8. A. L. N. Souza, et al., "Optoelectronic specifications of emerging coherent optical solutions for data center interconnect," *Proc. SPIE* **9775**, 97750E-1–97759E-9 (2016).
9. N. Massa, "Fiber-optic telecommunication," in *Fundamentals of Photonics*, C. Roychoudhuri, Ed, SPIE Press, Bellingham, Washington, 293–347 (2008).
10. H. L. Anderson and E. R. Cohen, "General section," in *A Physicist's Desk Reference, The Second Edition of Physics Vade Mecum*, H. L. Anderson, Ed, American Institute of Physics, New York, 2–51 (1989).
11. M. Tur, J. W. Goodman, B. Moslehi, J. E. Bowers, and H. J. Shaw, "Fiber-optic signal processor with applications to matrix-vector multiplication and lattice filtering," *Opt. Lett.* **7**(9), 463–465 (1982).
12. K. Jinguji and M. Kawachi, "Synthesis of coherent two-port lattice-form optical delay-line circuit," *J. Lightwave Technol.* **13**(1) 73–82 (1995).
13. F. Horst, "Silicon integrated waveguide devices for filtering and wavelength demultiplexing," *Optical Fiber Communication Conference and Exposition and the National Fiber Optic Engineers Conference (OFC/NFOEC)*, OWJ3 (2010).

14. H. Takahashi, S. Suzuki, K. Kato, and I. Nishi, "Arrayed-waveguide grating for wavelength division multi/demultiplexer with nanometer resolution," *Electron. Lett.* **26**(2), 87–88 (1990).
15. A. Kaneko, T. Goh, H. Yamada, T. Tanaka, and I. Ogawa, "Design and applications of silica-based planar lightwave circuits," *IEEE J. Quantum Electron.* **5**(5), 1227–1236 (1999).
16. F. Horst, W. M. J. Green, B. J. Offrein, and Y. A. Vlasov, "Silicon-on-insulator echelle grating WDM demultiplexers with two stigmatic points," *IEEE Photonics Technol. Lett.* **21**(23), 1743–1745 (2009).
17. Y. A. Vlasov, "Silicon CMOS-integrated nano-photonics for computer and data communications beyond 100G," *IEEE Commun. Mag.* **50**(2), S67–S72 (2012).
18. R. J. Mears, L. Reekie, I. M. Jauncey, and D. N. Payne, "Low-noise erbium-doped fibre amplifier operating at 1.54 μm," *Electron. Lett.* **23**(19), 1026–1028 (1987).
19. M. Nakazawa, Y. Kimura, and K. Suzuki, "Efficient Er^{3+}-doped optical fiber amplifier pumped by a 1.48 μm InGaAsP laser diode," *Appl. Phys. Lett.* **54**(4), 295–297 (1988).
20. H. Masuda, "Recent progress on optical fiber amplifiers and their applications," *Proc. SPIE* **6389**, 638902-1–638902-10 (2006).
21. G. Eisenstein, et al., "Gain measurements of InGaAsP 1.5 μm optical amplifiers," *Electron. Lett.* **21**(23), 1076–1077 (1985).
22. T. Saitoh and T. Mukai, "1.485 μm GaInAsP traveling-wave semiconductor laser amplifier," *IEEE J. Quantum Electron.* **23**(6), 1010–1020 (1987).
23. S. Cole, et al., "Polarisation-insensitive, near-travelling-wave semiconductor laser amplifiers at 1.5 μm," *Electron. Lett.* **25**(5), 314–315 (1989).
24. W. S. Ishak, K. H. Hahn, B. L. Booth, E. H. Mueller, A. F. J. Levi, and R. R. Craig, "Optical interconnects: the parallel optical link organization (POLO) approach," *Proc. SPIE* **2400**, 214–221 (1995).
25. P. Van Daele, P. Geerinck, G. Van Steenberge, and S. Van Put, "Optical interconnections on PCBs: a killer application for VCSELs," *Proc. SPIE* **4942**, 269–281 (2003).
26. H. Isono, "A global standardization trend for high-speed client and line side transceivers," *Proc. SPIE* **9390**, 939008-1–939008-7 (2015).
27. C. Gunn, "Integration," in *Silicon Photonics: the State of the Art*, G. T. Reed, Ed, John Wiley & Sons, Chichester, England, 269–296 (2008).
28. L. Liao, et al., "High-speed photonic integrated chip on a silicon platform," in *Silicon Photonics II: Components and Integration*, D. J. Lockwood and L. Pavesi, Eds, Springer-Verlag, Berlin Heidelberg, 169–186 (2011).
29. Y. Urino, T. Nakamura, and Y. Arakawa, "Silicon optical interposers for high-density optical interconnects," in *Silicon Photonics III: Systems and Applications*, L. Pavesi and D. J. Lockwood, Eds, Springer-Verlag, Berlin Heidelberg, 169–186 (2016).

30. P. De Dobbelaere, et al., "Silicon-photonics-based optical transceivers for high-speed interconnect applications," *Proc. SPIE* **9775**, 977503-1–977503-5 (2016).
31. X. Chen, S. R. Bickham, H.-F. Liu, O. I. Dosunmu, J. E. Hurley, and M.-J. Li, "25 Gb/s transmission over 820 m of MMF using a multimode launch from an integrated silicon photonics transceiver," *Opt. Express* **22**(2), 2070–2077 (2014).
32. S. R. Bickham, "Multimode and single-mode fibers for data center and high-performance computing applications," *Proc. SPIE* **9735**, 97530R-1–97530R-8 (2016).
33. C. E. Shannon, "A mathematical theory of communication," *Bell System Tech. J.* **27**(3) 379–423 (1948).
34. H. Isono, "Recent standardization directions on high-speed client and line side components," *Proc. SPIE* **9775**, 97750C-1–97750C-8 (2016).
35. M. R. Watts, D. C. Trotter, R. W. Young, A. L. Lentine, and W. A. Zortman, "Limits to silicon modulator bandwidth and power consumption," *Proc. SPIE* **7221**, 72210M-1–72210M-8 (2009).
36. A. Narasimha, et al., "An ultra low power CMOS photonics technology platform for H/S optoelectronic transceivers at less than $1 per Gbps," *Optical Fiber Communication Conference and Exposition and the National Fiber Optic Engineers Conference (OFC/NFOEC)*, OMV4 (2010).
37. H. X. Yi, T. T. Li, J. L. Zhang, X. J. Wang, and Z. Zhou, "Temperature-independent broadband silicon modulator," *Opt. Commun.* **340**, 107–109 (2015).
38. K. Goi, et al., "Low-voltage silicon Mach-Zehnder modulator operating at high temperatures without thermo-electric cooling," *Optical Fiber Communications Conference and Exhibition (OFC)*, W2A.23 (2016).
39. K. Yamada, et al., "High-performance silicon photonics technology for telecommunications applications," *Sci. Technol. Adv. Mater.* **15**, 024603 (2014).
40. K. Ogawa, et al., "Silicon Mach-Zehnder modulator of extinction ratio beyond 10 dB at 10.0-12.5 Gbps," *Opt. Express* **19**(26), B26–B31 (2011).
41. B. Huebner, "Optical transceivers for short and medium reach optical networks," *Proc. SPIE* **7621**, 762103-1–762103-13 (2010).
42. K. Kikuchi, "Fundamentals of coherent Optical fiber communications," *J. Lightwave Technol.* **34**(1), 157–179 (2016).
43. F. Koyama and K. Iga, "Frequency chirping in external modulators," *J. Lightwave Technol.* **6**(1), 87–93 (1988).
44. K. Kishino, S. Aoki, and Y. Suematsu, "Wavelength variation of 1.6 μm wavelength buried heterostructure GaInAsP/InP lasers due to direct modulation," *IEEE J. Quantum Electron*. **QE-18**(3) 343–351 (1982).
45. P. R. Horche, C. del rio Campos, and A. M. Minguez, "Interaction of semiconductor laser chirp with fiber dispersion: impact on WDM directly

modulated system performance," *The Fourth International Conference on Advances in Circuits, Electronics and Micro-electronics (CENICS)*, 17–22 (2011).
46. H. S. Chung and Y. C. Chung, "Directly modulated CWDM/DWDM system using negative dispersion fiber for metro network application," *Opt. Commun.* **245**, 171–176 (2005).
47. M. Izutsu, T. Itoh, and T. Sueta, "10 GHz bandwidth traveling-wave LiNbO3 optical waveguide modulator," *IEEE J. Quantum Electron*. **QE-14**(6), 394–395 (1978).
48. R. C. Alferness, "Waveguide electrooptic modulators," *IEEE Trans. Microwave Theory Tech.* **MTT-30**(8) 1121–1137 (1982).
49. E. L. Wooten, et al., "A review of lithium niobate modulators for fiber-optic communications systems," *IEEE J. Sel. Top. Quantum Electron.* **6**(1), 69–82 (2000).
50. A. Yariv and P. Yeh, *Optical Waves in Crystals: Propagation and Control of Laser Radiation*, John Wiley and Sons, Hoboken, New Jersey, 220–317 (2003).
51. R. A. Griffin, et al., "10 Gb/s Optical differential quadrature phase shift key (DQPSK) transmission using GaAs/AlGaAs integration," *Optical Fiber Communication Conference and Exposition and the National Fiber Optic Engineers Conference (OFC/NFOEC)*, FD6-1 (2002).
52. Y. Ogiso, et al., "Athermal InP(110) twin-IQ modulator with planar single-RF electrode structure," *Optoelectronics and Communications Conference/Australian Conference on Optical Fibre Technology (OECC/ACOFT)* Tu3C-4 (2014).
53. D. A. B. Miller, et al., "Electric field dependence of optical absorption near the band gap of quantum-well structures," *Phys. Rev.* **B32**(2), 1043–1060 (1985).
54. K. Wakita, I. Kotaka, H. Asai, S. Nojima, and O. Mikami, "High-efficiency electroabsorption in quaternary AlGaInAs quantum-well optical modulators," *Electron. Lett.* **24**(21), 1324–1325 (1988).
55. T. Ido, H. Sano, D. J. Moss, S. Tanaka, and A. Takai, "Strained InGaAs/InAlAs MQW electroabsorption modulators with large bandwidth and low driving voltage," *IEEE Photon. Technol. Lett.* **6**(10), 1207–1209 (1994).
56. K. K. Loi, et al., "Low-loss 1.3-μm MQW electroabsorption modulators for high-linearity analog optical links," *IEEE Photon. Technol. Lett.* **10**(11), 1572–1574 (1998).
57. R. A. Soref and B. A. Bennett, "Electrooptical effects in silicon," *IEEE J. Quantum Electron.* **23**(1), 123–129 (1987).
58. G. T. Reed, G. Mashanovich, F. Y. Gardes, and D. J. Thomson, "Silicon optical modulators," *Nature Photon*. **4**, 518–526 (2010).
59. B. Schiippert, J. Schmidtchen, A. Splett, U. Fischer, T. Zinke, R. Moosburger, and K. Petermann, "Integrated optics in silicon and SiGe-heterostructures," *J. Lightwave Technol.* **14**(10), 2311 (1996).

60. Y. Kim, J Fujikata, S. Takahashi, M. Takenaka, and S. Takagi, "First demonstration of SiGe-based carrier-injection Mach-Zehnder modulator with enhanced plasma dispersion effect," *Opt. Express* **24**(3), 1979–1985 (2016).
61. M. S. Dresselhaus, *Solid State Physics Part II Optical Prpoerties of Solids*, MIT course, 6.732 Solid State Physics, 48–50 (2001); http://web.mit.edu/course/6/6.732/www/6.732-pt2.pdf.
62. J. Liu, et al., "Waveguide-integrated, ultralow-energy GeSi electro-absorption modulators," *Nature Photon*. **2**, 433–437 (2008).
63. S. Gupta, et al., "50GHz Ge waveguide electro-absorption modulator integrated in a 220nm SOI photonics platform," *Optical Fiber Communications Conference and Exhibition (OFC)*, Tu2A.4 (2015).
64. H. D. Thacker, et al., "An all-solid-state, WDM silicon photonic digital link for chip-to-chip communications," *Opt. Express* **23**(10), 12808–12822 (2015).
65. L. Lever, Z. Ikonic, A. Valavanis, and R. W. Kelsall, "Design of Ge/SiGe quantum-confined Stark effect modulators for CMOS compatible photonics," *Proc. SPIE* **7606**, 76060Q-1–76060Q-9 (2010).
66. P. Chaisakul, et al., "23 GHz Ge/SiGe multiple quantum well electroabsorption modulator," *Opt. Express* **20**(3), 3219–3224 (2012).
67. S. Ren, et al., "Ge/SiGe quantum well waveguide modulator monolithically integrated with SOI waveguides," *IEEE Photon. Technol. Lett.* **24**(6), 461–463 (2012).
68. K. Seeger, *Semiconductor Physics—an Introduction*, 3rd Ed., Springer-Verlag, Berlin Heidelberg, 181–185 (1985).
69. S. Schmitt-Rink, D. S. Chemla, and D. A. B. Miller, "Linear and nonlinear optical properties of semiconductor quantum wells," *Adv. Physics* **38**(2), 89–188 (1989).
70. L. M. Roth, "Dynamics of electrons in semiconductors in electric and magnetic fields," in *Handbook on Semiconductors*, T. S. Moss, Ed., North-Holland, Amsterdam, New York, Oxford, 451–485 (1982).
71. P. Drude, "Zur iontheorie der metalle," *Physik. Z.* **14**, 161–165 (1900).
72. J. N. Hodgson, *Optical Absorption and Dispersion in Solids*, Chapman and Hall, 62–83 (1970).
73. Y. Urino, et al., "High-density optical interconnects by using silicon photonics," *Proc. SPIE* **9010**, 901006-1–901006-9 (2014).
74. Q. Fang, et al., "Suspended optical fiber-to-waveguide mode size converter for silicon photonics," *Opt. Express* **18**(8), 7763–7769 (2010).
75. T. Pinguet, et al., *IEEE Photon. Soc. Summer Top. Meeting*, WC4.1 (2012).
76. N. Chujo, et al., "Optical interconnect technologies for high-bandwidth ICT systems," *Proc. SPIE* **9775**, 97750D-1–97750D-6 (2016).
77. J. A. Kash, et al., "Communication technologies for exascale systems," *Proc. SPIE* **7221**, 72210F-1–72210F-12 (2009).

Chapter 3
Introduction to Integrated Optical Modulators

Integrated optical modulators consist of active and passive planar optical waveguides designed and fabricated on semiconductor-based integrated photonics platforms. This chapter provides a general overview of integrated optical modulators. In the first part, optical modulators are classified into three types with respect to optical-waveguide layout. The optical waveguides are treated schematically as building blocks. Their structures and theoretical characteristics are described in detail in Chapter 4. This chapter focuses on the MZ optical modulator because of its versatility in the high-quality generation of optical data in intensity modulation and phase modulation in principle. Integrated MZ optical modulators on a silicon-photonics platform are highlighted in the last part of this chapter as the theme of this book.

3.1 Classification of Optical Modulators

3.1.1 Electro-absorption optical modulators

Electro-absorption optical modulators can be used for optical transmitters in WDM and parallel-channel data-transmission systems based on intensity modulation and direct detection (IM-DD). In IM-DD, transmitted signals are detected directly by power detector in receiver equipment. Electro-absorption optical waveguides are incorporated into the optical modulators as active optical waveguides. An electro-absorption optical modulator consists of an input passive optical waveguide, an electro-absorption optical waveguide, and an output passive waveguide, which are aligned contiguously in a line, as Fig. 3.1 illustrates with an optical-waveguide layout diagram. Channel CH_i stands for the WDM slot of wavelength, λ_i or parallel-channel lane of the i^{th} optical fiber. Multiple electro-absorption optical modulators can be integrated up to the total number of WDM slots or parallel fiber lanes on III-V compound-semiconductor photonics and silicon-photonics platforms. On the III-V photonics platforms, electro-absorption optical modulators can be

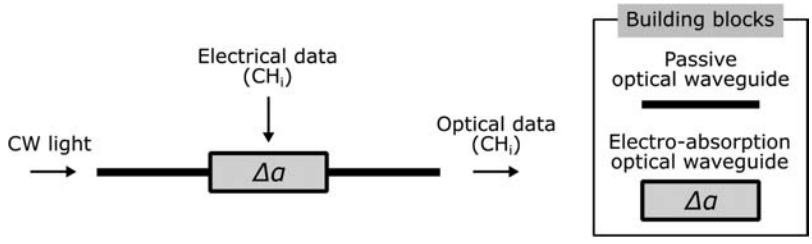

Figure 3.1 Optical-waveguide layout diagram of an electro-absorption optical modulator.

monolithically integrated with LDs, forming externally modulated lasers (EMLs).

Free-carrier absorption is one of the physical principles of electro-absorption optical modulators.[1–3] Carriers, which are electrons in conduction bands and holes in valence bands, are accelerated in their own bands under the electric field of incident CW light. The velocity of individual carriers increases under the electric field, and thus the kinetic energy of individual carrier increases.[4,5] Any loss of incident light power, i.e., optical absorption, occurs in the process of energy transfer from the incident CW light to the carriers. The physics of free-carrier absorption and its optical characteristics are discussed in Chapter 5. The accumulation and depletion of electrons and holes in a PN junction formed in an electro-absorption optical waveguide allows intensity modulation of the incident CW light in response to the input electrical data.[6–9]

The interband dipole transition of electron–hole pairs is the other physical principle of electro-absorption optical modulators. Two-dimensional excitons, which exist as hydrogenic bound states of 2D electron–hole pairs photoexcited in semiconductor QWs via interband optical dipole transition, exhibit strong optical absorption peaks.[10] Under a bias electric field applied to the QWs, electrons and holes are confined in biased QWs, and the optical absorption peaks of the QW excitons shift to lower photon energies in their optical absorption spectra, thus exhibiting QCSE.[11] Electro-absorption optical modulators based on QCSE in QWs on III-V photonics and silicon-photonics platforms have been demonstrated.[12–17] The optical absorption spectra of the interband optical dipole transition associated with the FK effect in bulk semiconductor crystals exhibit band tailing due to photon-assisted tunneling in the spectral region below their band-edge photon energies.[18,19] Band tailing depends on the tunneling rate under a bias electric field applied to the semiconductor materials, thereby controlling the optical absorption with an external bias voltage. Electro-absorption optical modulators based on the FK effect in SiGe optical waveguides have been demonstrated for high-speed optical data generation.[20–22] Chapter 5 also deals with the physics and optical characteristics of QCSE and the FK effect.

The electro-absorption optical modulators are essentially intensity modulators with a simple layout that consists only of a single straight optical

waveguide; thus, they have a very small footprint suitable for high-density integration. However, a high voltage of electrical signals must be applied to generate high-contrast optical signals, and the spectral range of optical modulation is limited near the electronic band-edge of the electro-absorption material.

3.1.2 Ring–resonator optical modulator using electro-refraction effects

Energy-efficient intensity modulation has been realized by using ring-resonator optical modulators as shown in an optical-waveguide layout diagram in Fig. 3.2.[23–26] A straight passive optical waveguide is coupled with a ring optical waveguide via a 2×2 optical coupler with a coupling ratio of 50:50. A 3-dB directional coupler consisting of two straight optical waveguides aligned parallel with a subwavelength spacing between each waveguide can be used as the 2×2 optical coupler. An electro-refraction optical waveguide with length ℓ is inserted in line with the ring optical waveguide. A refractive index change of Δn is produced in the electro-refraction optical waveguide with an applied electric voltage of V, and thus leads to an optical phase shift of $\Delta\phi(V) = \Delta n(V) \cdot \ell$. The optical power emitted from the output end of the straight optical waveguide is minimum if $\Delta\phi(V)$ equals an even integer multiple of π (on resonance). Conversely, maximum optical power is emitted from the output end if $\Delta\phi(V)$ equals an odd integer multiple of π (off resonance). Therefore, the ring–resonator optical modulators also operate as tunable optical notch filters.[26] The inset of Fig. 3.2 illustrates the optical spectrum of a notch filter. The ring resonance enables energy-efficient optical modulation with a low drive voltage.[24]

Optical simulation illustrates the function of a ring–resonator optical modulator in terms of an optical mode field and optical field distribution along the optical waveguides. Figure 3.3 displays the finite-element-method

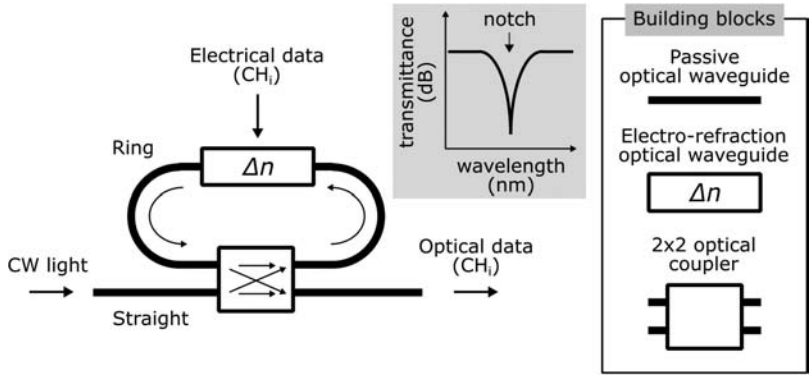

Figure 3.2 Optical-waveguide layout diagram of a ring–resonator optical modulator.

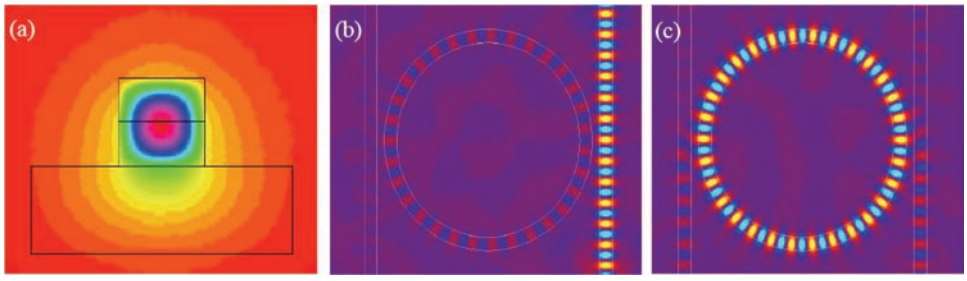

Figure 3.3 Simulated optical mode profile and propagation field distribution.[25]

electro-magnetic simulation characteristics of the optical mode profile and optical propagation field distribution from Fig. 2 in Kekatpure and Brongersma.[25] The optical field is strongly confined in the ring optical waveguide on the ring resonance (Fig. 3.3(c)), and thus there is no output from the straight waveguide. The optical field barely penetrates into the ring on the anti-resonance (Fig. 3.3(b)), on the other hand, thereby providing full transmission through the straight waveguide.

The refractive-index change associated with any of the electro-absorption processes of the electro-absorption materials, free-carrier absorption, QCSE, and FK effect, as in Section 3.1.1, can be used as the physical principle for an electro-refraction optical waveguide. Computational analysis that uses the Kramers–Kronig transform described in Section A.2 allows us to derive the electro-refraction characteristics after the electro-absorption characteristics are obtained by optical absorption spectrum measurements at different electric bias voltages for the electro-absorption optical waveguides.

The sharp notch spectrum as presented in Fig. 3.2 enables high-efficiency intensity modulation with a very low voltage, e.g., 1 V_{PP} or lower for silicon-based ring–resonator optical waveguides. However, thermo-electric stabilization of the sharp notch spectrum is necessary to deploy a ring–resonator optical modulator in optical network applications.

3.1.3 Mach–Zehnder optical modulator using electro-refraction effects

In various modulation formats of intensity modulation and phase modulation, MZ optical modulators have been extensively used because of their potential for high-quality optical modulation.[27–32] A diagram of optical-waveguide layout of a MZ optical modulator is depicted in Fig. 3.4. CW light is input to the input passive optical waveguide, which is connected to the input port of a 1×2 optical splitter. The two output ports of a 1×2 optical splitter are connected to passive optical waveguides of two arms of a MZ interferometer (MZI), respectively. Electro-refraction optical waveguides with an identical length of ℓ are inserted as phase shifters into both arms of the MZI.

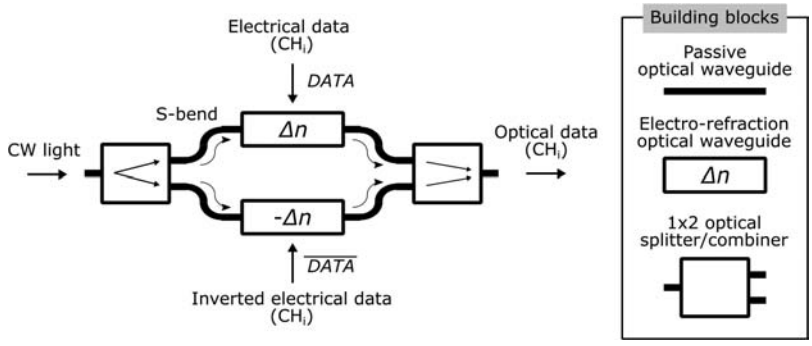

Figure 3.4 Optical-waveguide layout diagram of a MZ optical modulator.

The MZI is symmetric in terms of optical path, and an optical modulator based on the MZI layout is a symmetric MZ optical modulator.

The phase shifters in Fig. 3.4 are driven in push–pull operation, where mutually reversed electrical data $DATA$ and $\overline{DATA}$ are applied to both arms, named arms 1 and 2, respectively, which have the same magnitude. The push–pull operation is crucial for high-quality optical modulation without spectral broadening and frequency chirping.[27,31] A refractive-index change of Δn is produced in the electro-refraction optical waveguide in one MZ arm with an electrical signal voltage of V, thus creating an optical phase shift of $\Delta\phi_+(V) = 2\pi\Delta n(V)\ell/\lambda$ with wavelength λ. On the other hand, the reversed refractive index change of $-\Delta n$ is produced in the electro-refraction optical waveguide in the other MZ arm with the reversed electric signal voltage of $-V$, and thus an optical phase shift of $\Delta\phi_-(V) = -2\pi\Delta n(V)\ell/\lambda$. The total phase shift in the MZI is $\Delta\phi(V) = \Delta\phi_+(V) - \Delta\phi_-(V) = 4\pi\Delta n(V)\ell/\lambda$.

The output ends of the passive optical waveguides in both arms of the MZI are connected to the two input ports of a 2×1 optical combiner. Output light carrying optical data is emitted from the output passive optical waveguide connected to the output port of the 2×1 optical combiner. The 2×1 optical combiner is equivalent to the 1×2 optical splitter with reversed direction of light propagation. The refractive-index change associated with any of the electro-absorption processes, free-carrier absorption, QCSE, and F-K effect is also incorporated to the physical principle for electro-refractive optical waveguides in MZ optical modulators.

During the push–pull operation of intensity modulation, $\Delta\phi_+(V) = -\Delta\phi_-(V) = \Delta\phi(V)/2$, and thus the electric fields E_1 and E_2 of propagated light in arms 1 and 2 are written as

$$E_1 = \frac{|E_{\text{in}}|}{2} e^{-i\{\Delta\phi(V)/2\}} e^{i\omega t}, \tag{3.1}$$

and

$$E_2 = \frac{|E_{\text{in}}|}{2} e^{i\{\Delta\phi(V)/2\}} e^{i\omega t}, \tag{3.2}$$

respectively. Here, E_{in} and ω are the electric field and angular frequency of input CW LD, respectively. Each arm is designed to transmit a single mode, whereby each E_1 and E_2 contains only a single component and provides a high extinction ratio in on/off modulation. The power-splitting ratio of the 1×2 splitter is 50:50. The output electric field E_{out} after the 2×1 combiner with a 50:50 combining ratio is derived from Eqs. (3.1) and (3.2) as

$$E_{\text{out}} = E_1 + E_2 = |E_{\text{in}}| \cos\frac{\Delta\phi(V)}{2} e^{i\omega t}. \tag{3.3}$$

The output power P_{out} is thus given as

$$P_{\text{out}} = E_{\text{out}} \times E_{\text{out}}^* = |E_{\text{in}}|^2 \frac{1 + \cos\Delta\phi(V)}{2}. \tag{3.4}$$

In the derivation of Eqs. (3.1)–(3.4), the modulator is assumed to be lossless. Note that E_{out} is real except for the time-varying oscillating component that is characteristic of the output electric field from a MZ optical modulator during push–pull operation.

Optical intensity distribution of the light propagated through MZI optical waveguides and output intensity profiles of the light immediately after the 2×1 combiner were obtained by the eigenmode-expansion method.[33] The simulation results are shown in Fig. 3.5. In the simulation, a Y-branch splitter and combiner were used as the 1×2 splitter and 2×1 combiner. The branching angle between arms 1 and 2 is 10 degrees. In the ON state, where $\Delta\phi(V) = 0$, constructive interference occurs in the MZI waveguides, and the light is output as the fundamental mode from the output end of the MZI waveguides. For simplicity in the simulation, rib optical waveguides were used throughout the MZI waveguides. The fundamental mode is strongly confined in the silicon core and efficiently coupled to the output optical fiber, and thus a significant portion of the optical power from the MZI modulator can be

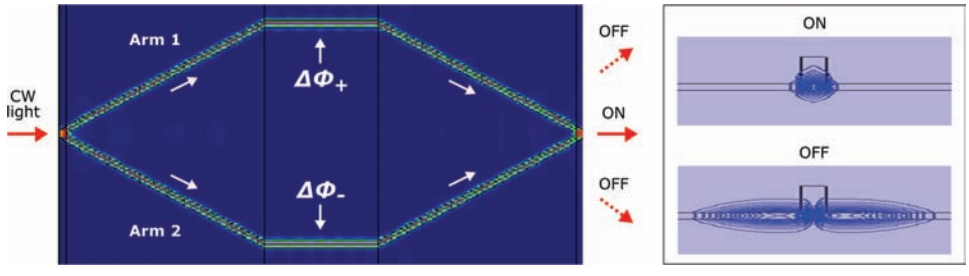

Figure 3.5 Simulated optical intensity distribution and profiles in MZI optical waveguides.

transferred to the output fiber coupled to the output end of the modulator. In contrast, destructive interference occurs in the OFF state, where $\Delta\phi(V) = \pi$, and the fundamental mode is suppressed. The light is emitted from the core as a radiation mode. The radiation mode is not confined and extended toward the surrounding area of the modulator. The optical light cannot be coupled to the output fiber, and there is no light transmission through the output fiber in the OFF state.

A symmetric MZI with two MZ arms of identical optical path length is suited to optical-waveguide layouts for optical modulators in broad spectral bands because the balanced MZI yields an all-band transmission with a phase difference of zero or an even integer multiple of π between the MZ arms. A symmetrically balanced MZI also allows broadband push–pull operation.[34] With respect to PICs for small-footprint WDM optical transceivers, symmetric MZ optical modulators can be integrated with LDs and WDM passive optical waveguide circuits to form integrated WDM EMLs on the III-V photonics platforms or integrated with receiver PDs to form integrated transmitter and receivers.[35,36] Design and fabrication services are available for MZ optical modulators on integrated-photonics platforms because of the versatile modulation functions of the modulators. In particular, services for photonic integration with various optical waveguide elements in a small footprint are available to silicon-based MZ optical modulators in silicon-photonics foundries capable of high-volume production (readers can access these services easily). The following sections and the subsequent chapters deal mainly with integrated silicon-based MZ optical modulators.

3.2 High-Speed Broadband Mach–Zehnder Optical Modulators

3.2.1 Mach–Zehnder interferometer with RF electrodes

Traveling-wave MZ optical modulators are extensively used for high-speed optical modulators in high-capacity optical networks. Figure 3.6 illustrates the optical waveguide system of a traveling-wave MZ optical modulator. The system is based on a silicon-photonics platform and is formed by a thin silicon

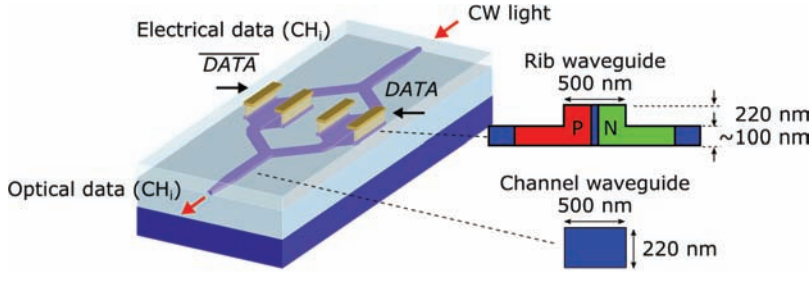

Figure 3.6 Optical-waveguide system of a traveling-wave MZ optical modulator on a silicon-photonics platform.

layer on a SOI wafer. The optical waveguides of a MZI are based on a channeled optical waveguide with a rectangular cross-section typically 500 nm wide and 220 nm tall. Channeled optical waveguides are most commonly used for passive straight or bent optical waveguides to propagate light on integrated photonics platforms, such as silicon-photonics platforms. The height is determined by the thickness of the SOI layer. A rib-waveguide phase shifter for high-speed optical modulation is inserted to each arm of MZI. The rib waveguide has typically 500-nm rib width, 220-nm rib height and ~100-nm slab height, respectively.[37,38] The aspect ratio of the core is about 2:5. Slab wings extended laterally on both sides of the rib are essential for electrical contacts to lateral PN junction for refractive index modulation in the silicon core. The height of 220 nm is often used for optical waveguides on a silicon-photonics platform because SOI wafers with a 220-nm SOI layer thickness are easily available. Therefore, the silicon-photonics waveguides aimed for practical and cost-effective applications, either rib or channel optical waveguides, have low profiles commonly. The height can be further optimized according to requirements on performances and process conditions in foundries.

The input and output ends of the MZI channel waveguides are formed in the shape of a nano-taper MFC, which has a sharp tip with a width of 180 nm or narrower.[39] In optical waveguides with a high-refractive-index contrast between the core and cladding, a cross-section of the core is much smaller than that of the single-mode optical fibers, and hence mode fields of propagated lights in the high-index-contrast waveguides are much smaller than those of the fibers. Therefore, MFCs are introduced for mode-field expansion to mitigate mode–field mismatches and to reduce power loss in optical coupling to input and output single-mode optical fibers.

Electrical connections to phase shifters are achieved by planar metal electrodes and metal vertical interconnect accesses (VIAs), which can be designed and fabricated on integrated photonics platforms. Figure 3.6 shows part of metal electrodes and metal VIAs for an optical modulator on a silicon-photonics platform. Single-longitudinal-mode CW light from a LD in a linear-polarization state is input from a single-mode optical fiber. In optical-fiber communications, the wavelength of the input CW light is 1260–1360 nm in the O band, 1530–1560 nm in the C band, and 1560–1620 nm in L band, respectively. Wavelength channels are defined as an ITU grid in the C and L bands.[40] Electrical data, $DATA$ and $\overline{DATA}$ are applied to the phase shifters in arms 1 and 2, respectively. Optical data are output from the output waveguide.

High-frequency transmission of electrical signals through planar metal electrodes is crucial for high-speed optical modulation, and traveling-wave metal electrodes, such as coplanar waveguides (CPWs) and coplanar striplines, are employed as planar metal electrodes.[34] A high-speed MZ optical modulator fabricated on a SOI wafer is presented with a top-view

microscope photograph in Fig. 3.7. Aluminum CPWs were integrated as traveling-wave electrodes on top of the optical waveguides constituting a single MZI with input and output nano-taper MFCs. The wide metal ground planes of CPWs eliminate cross-talk between center conductor lines.[41] The high-frequency traveling-wave electrodes also yield low microwave dispersion and are appropriate for electrical signal transmission at symbol rates in the microwave frequency range.[42] Figure 3.7 features two center conductors of CPWs that are connected to the phase shifters in both arms of a single MZI through the VIA metals. For push–pull operation, dual electrical drivers generating $DATA$ and $\overline{DATA}$ are connected to the input contact pads of the respective center conductors through bias tees simultaneously with DC bias voltages.[43] A DC reverse-bias voltage is applied to the phase shifter in each MZI arm to facilitate the high-speed transport of carriers with drift velocity in carrier depletion. A bias tee essentially consists of a capacitor connected to one of the electrical drivers and an inductor connected to one of the sources for DC bias voltage. The capacitor blocks the DC bias voltage, and the inductor shuts out the electrical data. Therefore, the electrical driver and the DC bias source are electrically isolated from each other, and stable operation of the optical modulator is ensured.

The optical modulator functions as a traveling-wave optical modulator with a designed characteristic impedance of 50 Ω. Terminators with 50-Ω impedance are connected to the contact pads of the other ends of the center conductors to avoid reflecting the electrical data. The center-conductor (signal) and ground electrodes are wire bonded to external electrodes on the package. To keep input and output optical fibers from interfering with the bonding wires transmitting the electrical signals, input and output MFCs consisting of inverted nano-taper silicon optical waveguides are placed on the

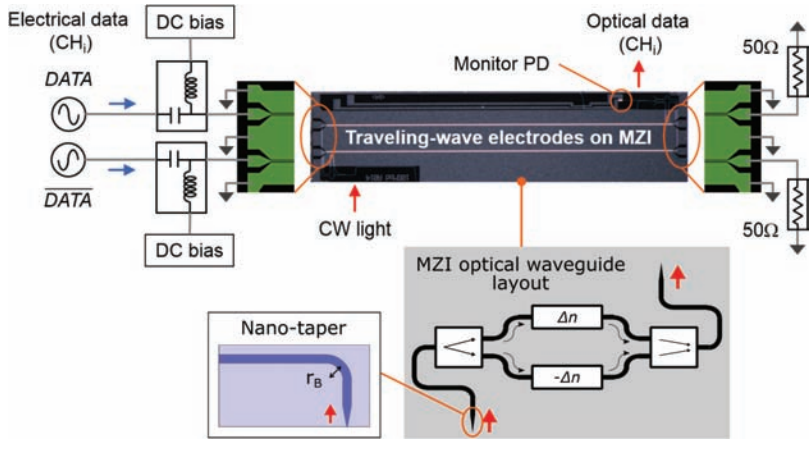

Figure 3.7 Integrated silicon-based traveling-wave MZ optical modulator chip with dual-drive pull–pull operation.

side facets using a bent silicon-channel optical waveguide with a bending radius r_B as small as 25 μm. The modulator chip is copackaged with the aspheric coupling lenses in a ceramic-based metal package. More details are presented as an example of photonic-electronic packaging in Chapter 8. A high-index-contrast optical waveguide on a silicon-photonics platform allows for the placement of bending waveguides in small footprints and for low optical propagation loss. The straight center conductors are directly connected to the contact pads without any extension since RF loss due to intrinsic free carriers distributed in the substrate is significant as well as conductor loss for traveling-wave metal electrodes fabricated on a semiconductor wafer such as a SOI wafer.[44–46] Such RF loss affects the frequency bandwidth of a traveling-wave optical modulator. Therefore, traveling-wave electrodes on a semiconductor substrate are designed to be as short as possible. Velocity mismatch is another factor that affects the frequency bandwidth of traveling-wave optical modulators.[34,47–49] The phase velocity of the electrical data in a microwave frequency range must be equalized with the group velocity of the propagation lights in an optical frequency range. The wavelength of the propagation lights is negligibly shorter than that of the electrical signals, and thus there is no phase relation between the propagation lights and the electrical signals.[47] A group of lightwaves in a symbol period of the optical data must instead be co-propagated with a velocity that equals the phase velocity of the electrical signals.

3.2.2 High-contrast intensity modulation

Equation (3.4) can be used to obtain the optical-power transfer function T_{out} of the symmetric MZ optical modulator shown in Figs. 3.4, 3.6, and 3.7 in the presence of intensity modulation:

$$T_{out} = \frac{1 + \cos \Delta\phi(V)}{2}. \tag{3.5}$$

Its dependence on the electrical signal voltage V is depicted as the schematic curve in a logarithmic scale in Fig. 3.8. The total phase shift $\Delta\phi$ is a function of the electrical signal voltage. In the ON state of binary intensity modulation such as OOK, where $\Delta\phi = 0$ for zero voltage in the MZ optical modulator, the MZ optical modulator yields the maximum transmittance T_{on} due to constructive interference. In the OFF state, where $\Delta\phi = \pi$ for π-shift voltage V_π, the modulator yields the minimum transmittance T_{off} due to destructive interference. In an ideal model of the MZ optical modulator, which yields a 50:50 ratio for optical power splitting and combines in the 1×2 splitter and the 2×1 combiner, T_{out} in Eq. (3.5) is zero in the OFF state. In practical MZ optical modulators obtained after fabrication processes, however, residual optical power transmission is observed because fabrication errors are

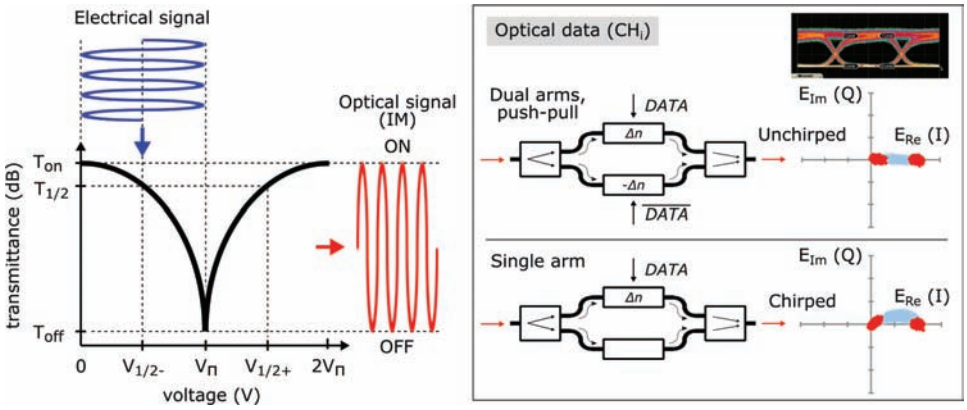

Figure 3.8 Schematic of the (a) optical-power transfer function of a MZ optical modulator in intensity modulation and (b) OOK optical characteristics in dual-arm push–pull and single-arm non-push–pull operation.

unavoidable, and the power-splitting and power-combining ratio deviates from 50:50 in the splitter and the combiner, respectively. Therefore, T_{out} in the OFF state is no longer zero, and the extinction ratio ER, defined using Eq. (3.4) as

$$ER = \frac{P_{\text{out}}(0)}{P_{\text{out}}(V_\pi)}, \tag{3.6}$$

is crucial to performance characterization of the optical modulators. The following equation gives rise to the extinction ratio scaled in the unit of dB:

$$ER_{\text{dB}} = 10 \cdot \log_{10}(ER). \tag{3.7}$$

The optical transfer function in Fig. 3.8 is obtained similarly from Eq. (3.5). In performance characterization of optical modules such as optical transceivers, the optical modulation amplitude OMA (obtained in the following equation using Eq. (3.6)) is also important:

$$OMA = P_{\text{out}}(0) - P_{\text{out}}(V_\pi) = 2P_{1/2} \cdot \frac{ER - 1}{ER + 1}. \tag{3.8}$$

Here, $P_{1/2}$ is the average optical power from the device under test and leads to the average optical power transmittance $T_{1/2}$ in Fig. 3.8.

High-contrast intensity modulation with an ER_{dB} higher than 10 dB is critical for high-quality optical data transmission with a BER of 10^{-9} and lower, as will be discussed in Section 7.6.

Based on the optical power transfer function in Fig. 3.8, E-O conversion in a MZ optical modulator is elaborated using sinusoidal electrical and optical

signals as the simplest example. In the first case of push–pull operation, sinusoidal electrical signals of the same voltage magnitude $V_\pi/2$ but in mutually reversed phases according to Eqs. (3.1) and (3.2) are applied to the phase shifters in both arms. The sum of the two electrical signals provides the single sinusoidal electrical signal of the voltage magnitude V_π, as presented in Fig. 3.8. The phase shifters in the arms are biased to the same level of DC voltage $V_\pi/2$. The sinusoidal optical signal in intensity modulation (IM) is generated from the MZ optical modulator: the ON and OFF states of the optical signal correspond to the maximum and the minimum transmittance states, respectively. In the second case of non-push–pull operation, the single electrical signal of the voltage magnitude V_π is applied to only one of the phase shifters, e.g., the phase shifter in arm 1, with the DC bias voltage $V_\pi/2$. A sinusoidal optical signal that alternates between the ON and OFF states is also generated.

The significant difference in the optical signals between the two cases is clarified if they are displayed in constellation diagrams, wherein optical signals are plotted in coordinates spanned with real (I) and imaginary (Q) electric field components E_{Re} and E_{Im}. Constellation diagrams to measure optical data with electrical data in push–pull and non-push–pull OOKs are presented in Fig. 3.8. An eye diagram of the optical data in a push–pull OOK is inserted to help explain the modulation format. In the push–pull OOK, the electric field of the optical data changes between ON and OFF states along a linear trajectory on the real axis, as expected from Eq. (3.3). In the non-push–pull OOK, on the other hand, the electric field changes along a curved trajectory with real and imaginary electric field components. Highly tolerant optical data transmission has been confirmed by using the MZ optical modulator in push–pull operation.[50] Measurement setups for the constellation and eye diagrams are described in Chapter 7.

The vector sum of electric fields E_1 and E_2 in Eqs. (3.1) and (3.2) prove that the imaginary electric field components in arms 1 and 2 have opposite phase directions and cancel each other during push–pull operation (zero-chirp).[27,31] Such cancellation does not occur in non-push–pull operation (chirped). In this case, the phase shift in arm 1 is $\Delta\phi(V)$ instead of $\Delta\phi(V)/2$, whereas the phase shift in arm 2 is 0 instead of $-\Delta\phi(V)/2/2$. An instantaneous phase shift $\Delta\phi(t)$ causes an instantaneous frequency shift $\Delta\nu(t)$ and hence frequency chirp, as illustrated in Fig. 3.9. Frequency chirp is represented as the time evolution of the instantaneous frequency shift in the following equation:[51,52]

$$\Delta\nu(t) = \frac{1}{2\pi}\frac{d}{dt}\{\Delta\phi(t)\}. \tag{3.9}$$

The phase increases in the clockwise direction in the constellation diagrams in Figs. 3.8 and 3.9. A positive instantaneous phase shift with an increasing electric field magnitude of the optical data leads to upward

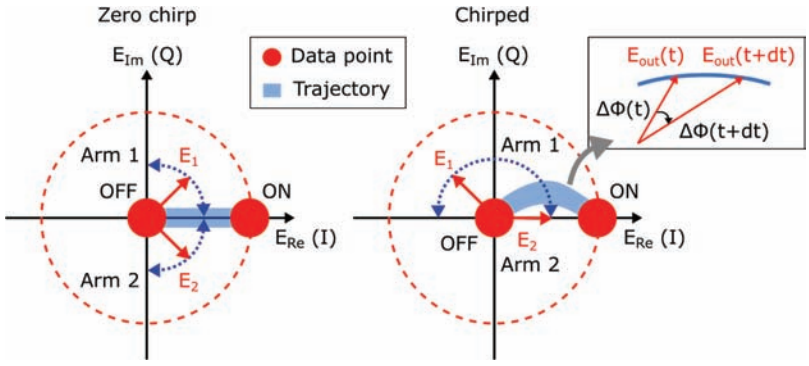

Figure 3.9 Schematic constellation diagrams of unchirped and chirped optical signals from a MZ optical modulator in dual-arm push–pull and single-arm operation cases.

instantaneous frequency shift, and therefore upchirping occurs. Optical modulation is also possible with a DC bias voltage of $3V_{\pi}/2$ to the phase shifter in arm 1. A negative instantaneous phase shift occurs in the latter case, and downchirping is observed.

The frequency chirp of an optical modulator is evaluated in terms of the modulator α-parameter α_{mod}, which is expressed as[27]

$$\alpha_{\mathrm{mod}} = \frac{\frac{d\Delta\phi(t)}{dt}}{\frac{1}{E_{\mathrm{out}}(t)} \cdot \frac{dE_{\mathrm{out}}(t)}{dt}}. \tag{3.10}$$

The mathematical form of the output electric field $E_{\mathrm{out}}(t)$ during the push–pull operation in Eq. (3.3) does not have a complex phase term and is a real function, which implies that $\Delta\phi(t)$ is a constant integer multiple of 2π and thus α_{mod} is zero. The time-oscillating exponent of the central carrier frequency in Eq. (3.3) is taken out of consideration in the analysis of the frequency chirping because the frequency chirping affects the spectral phase of the base-band optical spectrum of the output electric field around the center carrier frequency as elaborated in the analysis of chromatic dispersion of optical electric fields in dielectric optical media.[51]

3.2.3 High-*Q* phase modulation

The symmetric MZ optical modulator can be used also for binary phase modulation such as BPSK except that different conditions are applied to optical phase shifts in arms 1 and 2. In push–pull operation of phase modulation, $\Delta\phi_{+}(V) = \Delta\phi(V)/2 - \pi/2$, and $\Delta\phi_{-}(V) = -\Delta\phi(V)/2 + \pi/2$. The output electric field E_{out} is rewritten as

$$E_{\mathrm{out}} = |E_{\mathrm{in}}| \sin\frac{\Delta\phi(V)}{2} e^{i\omega t}. \tag{3.11}$$

Again, the output electric field is real during push–pull operation. The optical power transfer function in phase modulation includes a phase offset of π relative to the case of intensity modulation,

$$T_{\text{out}} = \frac{1 - \cos \Delta\phi(V)}{2}. \tag{3.12}$$

The optical power transfer function yields the same curve as that of intensity modulation if the aforementioned phase offset is covered with a DC bias voltage adjustment between arms 1 and 2. Figure 3.10 illustrates a phase modulation scheme with measured optical characteristics. The MZ optical modulator is held in the minimum transmittance T_{off} if no electrical signal is applied. The voltage magnitude of $2V_{\pi}$, twice of that of intensity modulation, is required to generate an optical signal in phase modulation (PM) between the 0- and π-phase states. The origin of the PM is the point of minimum transmittance. Zero- and π-phase states are resolved clearly with a linear transition trajectory on the real axis in the chirp-free constellation diagram measured with BPSK electrical data in the dual-arm push–pull operation.[52] Transition dips in the eye diagram indicate a transition across the minimum transmittance point along the linear trajectory. The spectrum of the output optical data is plotted in dB scale. Its symmetry implies a high-quality push–pull operation and is consistent with the symmetric constellation diagram. In the optical spectrum, which was acquired for a silicon-based optical modulator, a 3-dB frequency bandwidth is ~14 GHz, limited by the bandwidth of the 20-Gb/s NRZ-BPSK electrical data. Sharp, comb-like spikes in the spectrum are due to the periodicity of electrical data in a pseudo-random bit stream (PRBS) of a $2^{31} - 1$ frame length.

Chirp-free phase modulation allows long-distance optical data transmission with a low BER in high-capacity optical networks. Frequency chirping in

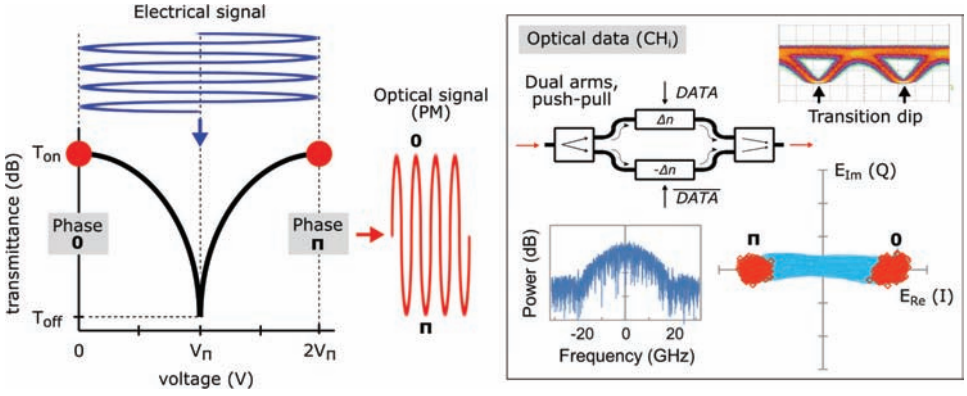

Figure 3.10 (a) Schematic diagram of phase modulation between 0 and π based on the voltage transmittance transfer function of a MZ optical modulator, and (b) BPSK optical characteristics in dual-arm push–pull operation.

phase modulation can be eliminated by using a highly symmetric MZ optical modulator fabricated with high precision and low error. Optical data in the BPSK can be evaluated in terms of the Q-factor, which corresponds to the extinction ratio in an OOK and is defined as[32]

$$Q = \frac{|E_{\mathrm{Re}}^2(0)|^2 + |E_{\mathrm{Re}}^2(\pi)|^2}{\sigma_0^2 + \sigma_\pi^2}. \tag{3.13}$$

Here, σ_0 and σ_π denote signal noise deviations in the 0- and π-phase states, respectively. The constellation diagram in Fig. 3.10 provides a Q-factor as high as 20 dB.[52] Therefore, high-precision low-error fabrication technologies on integrated photonics platforms play a significant role in high-performance optical modulation.

3.3 Integrated Silicon-Based Mach–Zehnder Optical Modulators

3.3.1 Optical-waveguide elements

The basic elements of integrated silicon-based MZ optical modulators are designed and fabricated with high-index-contrast silicon optical waveguides and their derivative structures. Some of the passive optical circuit elements are presented in Fig. 3.11.[39] Straight optical waveguides with rectangular and rib-shaped cross-sections, optical-waveguide bends, directional couplers, and splitters are essential to construct silicon-based MZ optical modulators. Ring resonators, add/drop filters, and arrayed waveguide gratings (AWGs) are useful for small-footprint wavelength-selective devices such as on-chip WDM MUX/DEMUX circuits.[57] Waveguide crossings are essential elements for optical hybrid circuits to coherently detect quadrature optical signals.[58,59] Nano-tapes are inverted taper MFCs for edge optical coupling to input/output

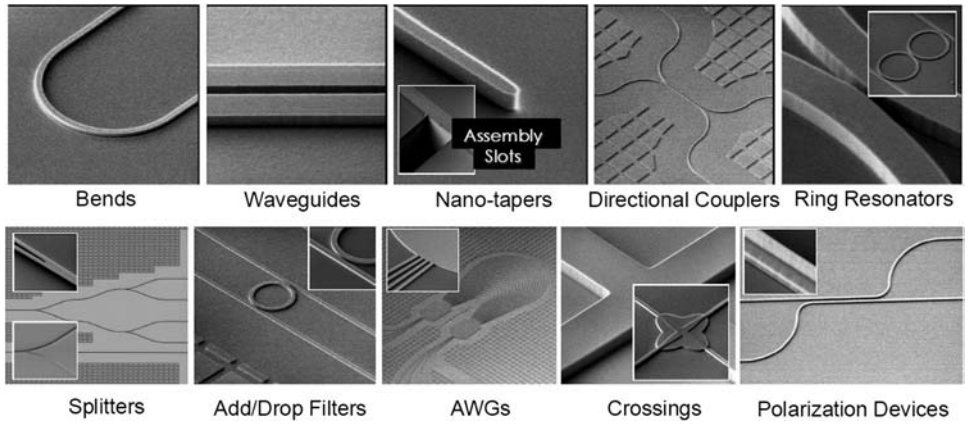

Figure 3.11 Passive optical circuit elements on a silicon-photonic platform.[39]

optical fibers and LDs.[60,61] Polarization devices are indispensable for the PDM function in PDM IQ MZ optical modulators, as will be discussed in this section.[62]

Monolithic integration on a silicon-photonics platform allows small-footprint silicon-based integrated MZ optical modulators for digital coherent communication. In digital coherent communication, optical data are transmitted in IQ modulation formats with PDM in orthogonal linear polarization states.[63,64] Electrical data at a symbol rate of 32 Gbaud are input to an IQ MZ optical modulator in two orthogonal polarization components, and optical data at a bit rate of 128 Gb/s are output from a PDM IQ MZ optical modulator for digital coherent communication. Optical data are detected with a coherent receiver, and optical phase states are identified by a digital phase-retrieval algorithm running on an electronic signal processing circuit.[65]

3.3.2 Monolithic modulator on chip

Figure 3.12 illustrates a monolithic silicon-based PDM IQ MZ optical modulator chip. The monolithic integrated optical modulator consists of the following three substantial units: (1) an input optical waveguide split into two parallel waveguides with a 1×2 multi-mode interferometer (MMI); (2) a couple of silicon-based IQ MZ optical modulators based on nested MZ optical modulators, each of which is connected to a respective output port of the MMI and accommodates I and Q sub-MZ modulator units on both of the parent MZI arms operating in transverse-electric (TE) polarization with an electric field perpendicular to the top interface of planar substrate; and (3) PDM optical circuit consisting of a polarization rotator (PR) to convert TE polarization into transverse-magnetic (TM) polarization with the magnetic field perpendicular to the planar substrate for the light beam propagated through one of the IQ MZ optical modulators and a polarization beam combiner

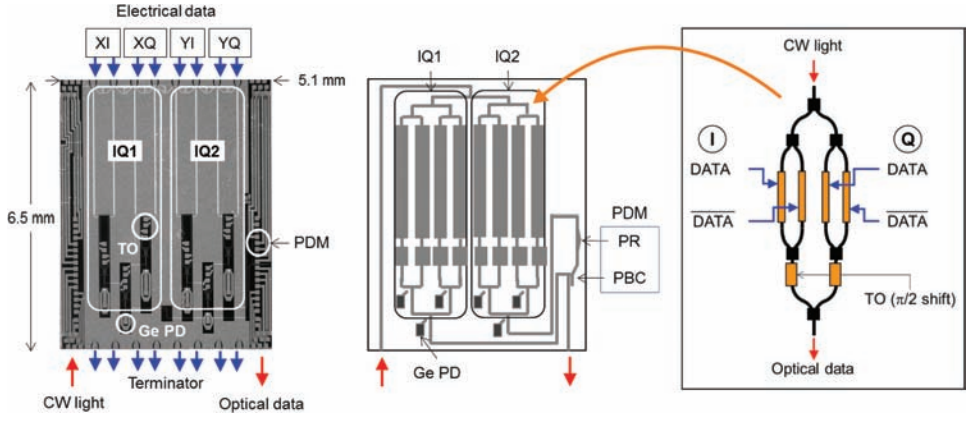

Figure 3.12 Monolithic silicon optical modulator chip for PDM IQ modulation.

(PBC) to multiplex the TE and TM light beams. Rib-waveguide-based PR in the PDM circuit was designed with a common design rule with the rib-waveguide phase shifter, thereby suitable for high-throughput low-cost fabrication.[66] The monolithic integrated optical modulator was fabricated in a footprint as small as 6.5×5 mm^2 with Ge PDs for performance monitoring and silicon rib-waveguide thermo-optic (TO) $\pi/2$ shifters to hold a phase difference of $\pi/2$ between I- and Q-modulated lights emitted from a couple of IQ MZ optical modulators, as shown in Fig. 3.12. Side slab areas of the TO shifters were doped with P-type or N-type dopants to function as electrical resistors. Electric currents are applied to the resistors to generate heat and sustain the $\pi/2$ phase shift between the I and Q arms by stabilizing the MZI temperature against a change in ambient temperature based on the silicon TO effect.[67] The small-footprint PDM IQ optical modulator chip will be well suited to compact-form-factor digital coherent transceivers such as CFP2.

The phase shifters for high-speed E-O conversion on a chip are connected to the straight center conductor lines of the aluminum CPW traveling-wave electrodes disposed on the optical waveguides of the IQ optical modulators. Electrical data for I and Q components in the orthogonal linear polarizations are input to the contact pads on the input ends of the CPWs. The linear polarization sites X and Y correspond, for instance, to the TE and TM modes on the silicon PDM IQ optical modulator chip. The electrical data are supplied to the dual arms of the I and Q sub-MZ optical modulator units for PDM IQ optical data generation during push–pull operation. Optical characteristics such as constellation diagrams of the PDM IQ MZ optical modulator are presented in Chapter 7.

Monolithic integrated optical modulator chips can be obtained by CMOS-based silicon-photonics fabrication processes using a SOI wafer with a 200-mm-diameter starting material. Cross-sections of the building blocks for the integrated optical modulator are shown in Fig. 3.13. The cores of the optical waveguides are formed in the thin silicon layer on the top of the

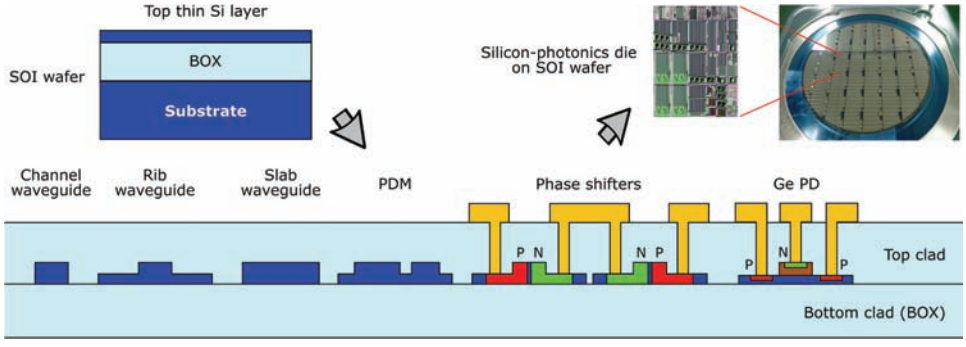

Figure 3.13 Cross-section profiles of building blocks for monolithic integrated optical modulators on a silicon-photonics platform.

unprocessed SOI wafer. The cores of the optical waveguides are embedded in silica top and bottom clads. The buried oxide (BOX) layer of the SOI wafer works as the bottom clad. The top clad is formed by processes of chemical vapor deposition (CVD) and subsequent planarization. The channel optical waveguide is most extensively used as backbones of integrated MZ modulators as straight and bent optical waveguides and base structures for passive optical circuits such as optical couplers and filters. The rib optical waveguide is used as the basis for high-speed PN-junction phase shifters as well as straight and bent optical waveguides for passive optical circuits. The optical waveguide is also used for TO phase shifters using doped silicon cores as resistive heaters.[68] The most well-known application of the slab optical waveguide in terms of integrated MZ optical modulators is MMIs for optical splitters and couplers, such as the 1×2 splitter and the 2×1 coupler described here. Mode conversion between TE and TM polarization modes in coupled asymmetric rib waveguides was used as a PR in PDM optical circuits. A couple of PN-junction phase shifters were inserted into both arms of a MZ optical modulator. The P-doped region of each PN junction was connected to the center conductor of each CPW with a VIA, and the N-doped region of each PN junction was connected to the common-ground plane of the CPWs on the MZI with a VIA. The germanium PD is used for performance monitoring in optical modulation and for optical signal detection in receivers. The active layer of germanium was epitaxially grown on a silicon layer to form an evanescent-coupling PD for high-efficiency optical-electrical conversion in waveguide geometry. In advanced generation of silicon-photonics platforms, a SOI wafer with a 300-mm diameter is used in combination with equipment featuring a higher fabrication precision but more expensive cost. Users can choose the fabrication processes with respect to requirements for precision and costs.

3.3.3 Fabrication processes

The fabrication processes of the monolithic optical modulator are summarized in Fig. 3.14 with a rib-waveguide phase shifter as an example. Optical resist is spin-coated on the top silicon layer, and an optical mask is used to mask specific areas on the resist to develop the optical resist in patterns suitable to fabricate slab patterns after a dry-etching process. Optical-lithography and dry-etching processes are included in (1). Slab patterns, as shown in (2), are fabricated afterward. Rib parts can be formed in the slab patterns during the processes in (3). Shallow etching with precise time control in dry-etching is performed to obtain rib optical waveguides with side slabs, as illustrated in (4) with a slab height deviation within ±5% in an advanced fabrication process optimized for silicon photonics. Passive optical circuits based on the channel, rib, and slab optical waveguides can be fabricated simultaneously. Ion implantation of boron atoms is then performed in (5)

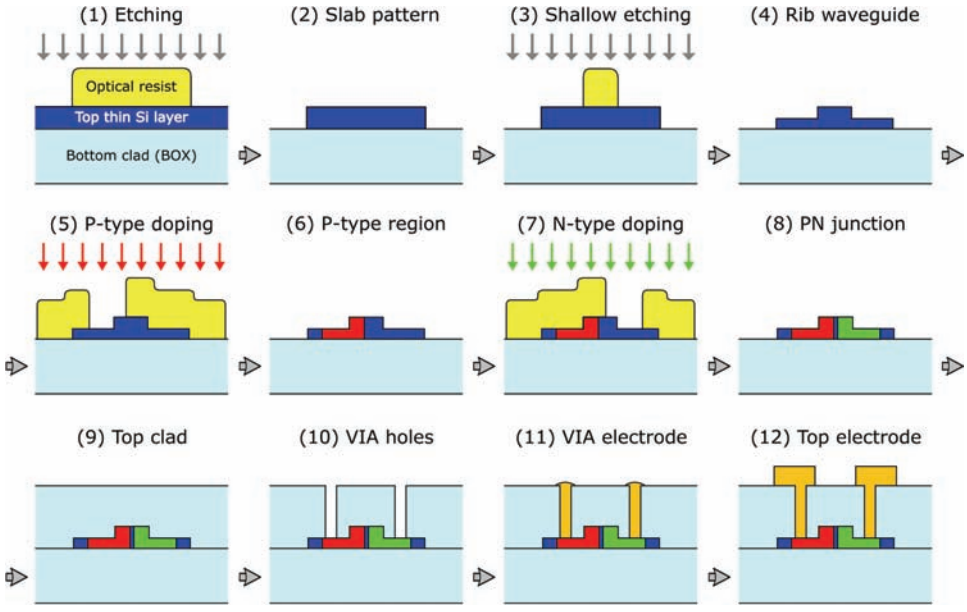

Figure 3.14 Fabrication process flow of a rib-waveguide lateral PN-junction phase shifter.

after optical lithography to dope specified areas in the rib optical waveguides with the P-type dopants. P-type regions of positive conductivity are formed in the rib optical waveguides after dopant activation and defect elimination in thermal annealing in (6). N-type doping processes are performed similarly in (7), and PN-junctions are formed in the rib optical waveguides in (8) after a thermal annealing process. Phosphorus atoms can be used for N-type dopants. The order of the doping processes can be inverted between P-type and N-type dopants. Further doping steps are included to reduce contact and series resistances. The top silica clad is formed in (9) by CVD and planarization processes. To connect electrical contacts to the P-type and N-type regions, VIA holes are opened in the top clad down to the slab parts, as shown in (10). Metallization processes are performed to fabricate VIA electrodes and top CPWs in (11) and (12), respectively, by aluminum deposition with subsequent optical lithography and dry etching. The monolithic integrated optical modulator chips are thus arranged on dies on the SOI wafer. Each chip of the optical modulator is picked up after dicing the wafer.

References

1. G. H. B. Thompson, "A theory for filamentation in semiconductor lasers including the dependence of dielectric constant on injected carrier density," *Opt. Quantum Electron.* **4**(3), 257–310 (1972).
2. R. A. Soref and B. R. Bennett, "Electrooptical effects in silicon," *IEEE J. Quantum Electron.* **QE-23**(1), 123–129 (1987).

3. M. Nedeljkovic, R. Soref, and G. Z. Mashanovich, "Free-carrier electrorefraction and electroabsorption modulation predictions for silicon over the 1–14-μm infrared wavelength range," *IEEE Photonics J*. **3**(6), 1171–1180 (2011).
4. P. Drude, "Zur iontheorie der metalle," *Physik. Z.* **14**, 161–165 (1900).
5. A. H. Kahn, "Theory of the infrared absorption of carriers in germanium and silicon," *Phys. Rev.* **97**(6), 1647–1652 (1955).
6. R. A. Soref and J. P. Lorenzo, "Silicon guided-wave optics," *Solid State Technol*. **31**(11), 95–98, (1988).
7. G. T. Reed, G. Mashanovich, F. Y. Gardes, and D. J. Thomson, "Silicon optical modulators," *Nature Photon.* **4**, 518–526 (2010).
8. B. Schuppert, J. Schmidtchen, A. Splett, U. Fischer, T. Zinke, R. Moosburger, and K. Petermann, "Integrated optics in silicon and SiGe-heterostructures," *J. Lightwave Technol.* **14**(10), 2311–2323 (1996).
9. Y. Kim, J Fujikata, S. Takahashi, M. Takenaka, and S. Takagi, "First demonstration of SiGe-based carrier-injection Mach-Zehnder modulator with enhanced plasma dispersion effect," *Opt. Express* **24**(3), 1979–1985 (2016).
10. R. Dingle, W. Wiegmann, and C. H. Henry, "Quantum states of confined carriers in very thin $Al_xGa_{1-x}As$-GaAs-$Al_xGa_{1-x}As$ heterostructures," *Phys. Rev. Lett.* **33**(14), 827–830 (1974).
11. D. A. B. Miller, D. S. Chemla, T. C. Damen, A. C. Gossard, W. Wiegmann, T. H. Wood, and C. A. Burrus, "Electric field dependence of optical absorption near the band gap of quantum-well structures," *Phys. Rev.* **B32**(2), 1043–1060 (1985).
12. K. Wakita, I. Kotaka, H. Asai, S. Nojima, and O. Mikami, "High-efficiency electroabsorption in quaternary AlGaInAs quantum-well optical modulators," *Electron. Lett.* **24**(21), 1324–1325 (1988).
13. T. Ido, H. Sano, D. J. Moss, S. Tanaka, and A. Takai, "Strained InGaAs/InAlAs MQW electroabsorption modulators with large bandwidth and low driving voltage," *IEEE Photon. Technol. Lett.* **6**(10), 1207–1209 (1994).
14. K. K. Loi, J. H. Hodiak, X. B. Mei, C. W. Tu, W. S. C. Chang, D. T. Nichols, L. J. Lembo, and J. C. Brock, "Low-loss 1.3-μm MQW electroabsorption modulators for high-linearity analog optical links," *IEEE Photon. Technol. Lett.* **10**(11), 1572–1574 (1998).
15. L. Lever, Z. Ikonic, A. Valavanis, and R. W. Kelsall, "Design of Ge/SiGe quantum-confined Stark effect modulators for CMOS compatible photonics," *Proc. SPIE* **7606**, 76060Q-1–76060Q-9 (2010).
16. P. Chaisakul, D. Marris-Morini, M.-S. Rouifed, G. Isella, D. Chrastina, J. Frigerio, X. Le Roux, S. Edmond, J.-R. Coudevylle, and L. Vivien, "23 GHz Ge/SiGe multiple quantum well electroabsorption modulator," *Opt. Express* **20**(3), 3219–3224 (2012).
17. S. Ren, Y. Rong, S. A. Claussen, R. K. Schaevitz, T. I. Kamins, J. S. Harris, and D. A. B. Miller, "Ge/SiGe quantum well waveguide

modulator monolithically integrated with SOI waveguides," *IEEE Photon. Technol. Lett.* **24**(6), 461–463 (2012).
18. M. S. Dresselhaus, *Solid State Physics Part II Optical Prpoerties of Solids*, MIT course, 6.732 Solid State Physics, 48–50 (2001); http://web.mit.edu/course/6/6.732/www/6.732-pt2.pdf.
19. L. M. Roth, "Dynamics of electrons in semiconductors in electric and magnetic fields," in *Handbook on Semiconductors*, T. S. Moss, Ed., North-Holland, Amsterdam, New York, Oxford, 451–485 (1982).
20. J. Liu, M. Beals, A. Pomerene, S. Bernardis, R. Sun, J. Cheng, L. C. Kimerling, and J. Michel, "Waveguide-integrated, ultralow-energy GeSi electro-absorption modulators," *Nature Photon.* **2**, 433–437 (2008).
21. S. Gupta, S. A. Srinivasan, M. Pantouvaki, H. Chen, P. Verheyen, G. Lepage, D. Van Thourhout, G. Roelkens, K. Saraswat, P. Absil, and J. Van Campenhout, "50GHz Ge waveguide electro-absorption modulator integrated in a 220nm SOI photonics platform," *Optical Fiber Communications Conference and Exhibition (OFC)*, Tu2A.4 (2015).
22. H. D. Thacker, X. Zheng, J. Lexau, R. Shafiiha, I. Shubin, S. Lin, S. Djordjevic, P. Amberg, E. Chang, F. Liu, John Simons, J.-H. Lee, A. Abed, H. Liang, Y. Luo, J. Yao, D. Feng, M. Asghari, R. Ho, K. Raj, J. E. Cunningham, and Ashok V. Krishnamoorthy, "An all-solid-state, WDM silicon photonic digital link for chip-to-chip communications," *Opt. Express* **23**(10), 12808–12822 (2015).
23. D. R. Lim, B. E. Little, K. K. Lee, M. Morse, H. H. Fujimoto, H. A. Haus, and L. C. Kimerling, "Micron-sized channel-dropping filters using silicon waveguide devices," *Proc. SPIE* **3847**, 65–71 (1999).
24. Q. Xu, B. Schmidt, S. Pradhan, and M. Lipson, "Micrometre-scale silicon electro-optic modulator," *Nature* **435**, 325–327 (2005).
25. R. D. Kekatpure and M. L. Brongersma, "CMOS compatible high-speed electro-optical modulator," *Proc. SPIE* **5926**, 59260G-1–59260G-10 (2005).
26. D. G. Rabus, *Integrated Ring Resonators The Compendium*, Springer-Verlag, Berlin Heidelberg, 3–40 (2007).
27. F. Koyama and K. Iga, "Frequency chirping in external modulators," *J. Lightwave Technol.* **6**(1), 87–93 (1988).
28. K. Kawano, "High-speed Ti:$LiNbO_3$ and semiconductor optical modulators," *IEICE Trans. Electron.* **E76-C**(2), 183–190 (1993).
29. E. L. Wooten, K. M. Kissa, A. Yi-Yan, E. J. Murphy, D. A. Lafaw, P. F. Hallemeier, D. Maack, D. V. Attanasio, D. J. Fritz, G. J. McBrien, and D. E. Bossi, "A review of lithium niobate modulators for fiber-optic communications systems," *IEEE J. Sel. Top. Quantum Electron.* **6**(1), 69–82 (2000).
30. L. Thylén, U. Westergren, P. Holmstörm, R. Schatz, and P. Jänes, "Recent developments in high-speed optical modulators," *Optical fiber*

telecommunications V A Components and Subsystems, I. Kaminow, T. Li and A. E. Willner, Eds. Academic Press, San Diego, 183–220 (2008).
31. A. H. Gnauck and P. J. Winzer, "Optical phase-shift-keyed transmission," *J. Lightwave Technol.* **23**(1), 115–130 (2005).
32. K.-P. Ho, *Phase-Modulated Optical Communication Systems*, Springer, New York, 301–333 (2005).
33. D. F. G. Gallagher and T. P. Felici, "Eingenmode expansion methods for simulation of optical propagation in photonics: pros and cons," *Proc. SPIE* **4987**, 69–82 (2003).
34. R. G. Walker, "High-speed III-V semiconductor intensity modulators," *IEEE J. Quantum Electron.* **27**(3), 654–667 (1991).
35. M. Ziari, B. Little, M. Kato, P. Evans, S. Chu, Wei Chen, J. Hryniewicz, F. Johnson, W. Chen, D. Gill, O. King, M. Fisher, V. Dominic, A. Nilsson, J. Rahn, S. Corzine, A. Dentai, M. Missey, D. Lambert, R. Muthiah, R. Salvatore, S. Murthy, J. Pleumeekers, R. Schneider, R. Nagarajan, C. Joyner, F. Kish, and D. Welch, "Large scale integration of photonic integrated circuits on indium phosphide and high-index-Contrast Si platforms," *35th European Conference on Optical Communication (ECOC)*, 1.7.2 (2009).
36. C. Doerr, L. Chen, D. Vermeulen, T. Nielsen, S. Azemati, S. Stulz, G. McBrien, X.-M. Xu, B. Mikkelsen, M. Givehchi, C. Rasmussen, and S.-Y. Park, "Single-chip silicon photonics 100-Gb/s coherent transceiver," *Optical Fiber Communications Conference and Exhibition (OFC)*, Th5C.1 (2014).
37. K. Ogawa, K. Goi, Y. T. Tan, T.-Y. Liow, X. Tu, Q. Fang, G.-Q. Lo, and D.-L. Kwong, "Silicon Mach-Zehnder modulator of extinction ratio beyond 10 dB at 10.0-12.5 Gbps," *Opt. Express* **19**(26), B26–B31 (2011).
38. K. Ogawa, "High-speed silicon-based integrated optical modulators for optical-fiber telecommunications," *Proc. SPIE* **8990**, 899010-1–899010-8 (2014).
39. T.-Y. Liow, Q. Fang, A. E.-J. Lim, L. Ding, Q. X. Zhang, J. Zhang, N. Duan, J. Song, F.-F. Ren, H. Cai, S. T. H. Silalahi, M. Yu, G.-Q. Lo, and D.-L. Kwong, "Silicon photonic integrated circuits: from devices to integration," *Proc. SPIE* **7942**, 79420E-1–79420E-10 (2011).
40. G. P. Agrawal, *Fiber-Optic Communication Systems*, 4th Ed., John Wiley and Sons, Hoboken, 223–230 (2010).
41. R. N. Simons, *Coplanar Waveguide Circuits, Components, and Systems*, 1st Ed., John Wiley and Sons, Hoboken, New Jersey, 1–9 (2001).
42. J.-Y. Ke and C. H. Chen, "Dispersion and attenuation characteristics of coplanar waveguides with finite metallization thickness and conductivity," *IEEE Trans. Microwave Theory Tech.* **43**(5), 1128–1135 (1995).
43. M. Aamer, D. J. Thomson, A. M. Gutiérrez, A. Brimont, F. Y. Gardes, G. T. Reed, J. M. Fedeli, A. Hakansson, and P. Sanchis, "10 Gbit/s

error-free DPSK modulation usinga push–pull dual-drive silicon modulator," *Opt. Commun.* **304**(1), 107–110 (2013).
44. D. Lederer and J.-P. Raskin, "Substrate loss mechanisms for microstrip and CPW transmission lines on lossy silicon wafers," *IEEE MTT-S International Microwave Symposium Digest* **2**, 685–688 (2002).
45. C. Schöllhorn, W. Zhao, M. Morschbach, and E. Kasper, "Attenuation mechanisms of aluminum millimeter-wave coplanar waveguides on silicon," *IEEE Trans. Electron Dev.* **50**(3), 740–746 (2003).
46. S. B. Evseev, L. K. Nanver, and S. Milosaviljević, "Surface-charge-layer sheet-resistance measurements for evaluating interface RF losses on high-resistivity-silicon substrates," *IEEE Trans. Microwave Theory Tech.* **60** (11), 3542–3550 (2012).
47. W. W. Rigrod and I. P. Kaminow, "Wide-band microwave light modulation," *Proc. IEEE* **51**(1), 137–140 (1963).
48. M. Izutsu, Y. Yamane, and T. Sueta, "Broad-band. traveling-wave modulator using a $LiNbO_3$ optical waveguide," *IEEE J. Quantum Electron.* **13**(4) 287–290 (1977).
49. R. C. Alferness, "Waveguide electrooptic modulators," *IEEE Trans. Microwave Theory Tech.* **30**(8), 1121–1137 (1982).
50. K. Goi, K. Oda, H. Kusaka, Y. Terada, K. Ogawa, T.-Y. Liow, X. Tu, G.-Q. Lo, and D.-L. Kwong, "11-Gb/s 80-km transmission performance of zero-chirp silicon Mach-Zehnder modulator," *Opt. Express* **20**(26), B350–B356 (2012).
51. J.-C. Diels and W. Rudolph, *Ultrashort Laser Pulse Phenomena: Fundamentals, Techniques, and Applications on a Femtosecond Time Scale*, Academic Press, San Diego, London, 1–21 (1996).
52. K. Goi, H. Kusaka, A. Oka, Y. Terada, K. Ogawa, T.-Y. Liow, X. Tu, G.-Q. Lo, and D.-L. Kwong, "20-Gb/s DPSK transmission with 550-ps/nm dispersion tolerance using silicon Mach-Zehnder modulator," *Optical Fiber Communications Conference and Exhibition (OFC)*, OW4J.5 (2013).
53. M. Hochberg and T. Baehr-Jones, "Towards fabless silicon photonics," *Nature Photon*. **4**(8), 492–494 (2010).
54. F. A. Kish, D. Welch, R. Nagarajan, J. L. Pleumeekers, V. Lal, M. Ziari, A. Nilsson, M. Kato, S. Murthy, P. Evans, S. W. Corzine, M. Mitchell, P. Samra, M. Missey, S. DeMars, R. P. Schneider, M. S. Reffle, T. Butrie, J. T. Rahn, M. Van Leeuwen, J. W. Stewart, D. J. H. Lambert, R. C. Muthiah, H.-S. Tsai, J. S. Bostak, A. Dentai, K.-T. Wu, H. Sun, D. J. Pavinski, J. Zhang, J. Tang, J. McNicol, M. Kuntz, V. Dominic, B. D. Taylor, R. A. Salvatore, M. Fisher, A. Spannagel, E. Strzelecka, P. Studenkov, M. Raburn, W. Williams, D. Christini, K. J. Thomson, S. S. Agashe, R. Malendevich, G. Goldfarb, S. Melle, C. Joyner, M. Kaufman, and S. G. Grubb, "Current status of large-scale InP

photonic integrated circuits," *IEEE J. Sel. Top. Quantum Electron.* **17**(6), 1470–1489 (2011).
55. M. J. R. Heck, "Hybrid and heterogeneous photonic integrated circuits for high-performance applications," *Proc. SPIE* **9365**, 936503-1–936503-8 (2015).
56. J. E. Bowers, T. Komljenovic, M. Davenport, J. Hulme, A. Y. Liu, C. T. Santis, A. Spott, S. Srinivasan, E. J. Stanton, and C. Zhang, "Recent advances in silicon photonic integrated circuits," *Proc. SPIE* **9774**, 977402-1–977402-18 (2016).
57. D. Dai and J. E. Bowers, "Silicon-based on-chip multiplexing technologies and devices for peta-bit optical interconnects," *Nanophotonics* **3**(4–5), 283–311 (2014).
58. W. Bogaerts, P. Dumon, D. Van Thourhout, and R. Baets, "Low-loss, low-cross-talk crossings for silicon-on-insulator nanophotonic waveguides," *Opt. Lett.* **32**(19), 2801–2803 (2007).
59. P. Dong, C. Xie, and L. L. Buhl, "Monolithic polarization diversity coherent receiver based on 120-degree optical hybrids on silicon," *Opt. Express* **22**(2), 2119–2125 (2014).
60. T. Tsuchizawa, K. Yamada, H. Fukuda, T. Watanabe, J. Takahashi, M. Takahashi, T. Shoji, E. Tamechika, S. Itabashi, and H. Morita, "Microphotonics devices based on silicon microfabrication technology," *IEEE J. Sel. Top. Quantum Electron.* **11**(1), 232–240 (2005).
61. K. K. Lee, D. R. Lim, D. Pan, C. Hoepfner, W.-Y. Oh, K. Wada, L. C. Kimerling, K. P. Yap, and M. T. Doan, "Mode transformer for miniaturized optical circuits," *Opt. Lett.* **30**(5), 498–500 (2005).
62. H. Fukuda, T. Tsuchizawa, H. Nishi, R. Kou, T. Hiraki, K. Takeda, K. Wada, Y. Ishikawa, and K. Yamada, "Silicon, silica, and germanium photonic integration for electronic and photonic convergence," *Proc. SPIE* **8628**, 862806-1–862806-8 (2013).
63. K. Kikuchi, "Fundamentals of coherent Optical fiber communications," *J. Lightwave Technol.* **34**(1), 157–179 (2016).
64. Y. Miyamoto and S. Suzuki, "Advanced optical modulation and multiplexing technologies for high-capacity OTN based on 100 Gb/s channel and beyond," *IEEE Comm. Mag.* **48**(3), S65–S72 (2010).
65. K. Roberts, D. Beckett, D. Boertjes, J. Berthold, and C. Laperle, "100G and beyond with digital coherent signal processing," *IEEE Comm. Mag.* **48**(7), 62–69 (2010).
66. K. Ogawa, H. Ishihara, K. Goi, Y. Mashiko, S. T. Lim, M. J. Sun, S. Seah, C. E. Png, T.-Y. Liow, X. Tu, G.-Q. Lo, and D.-L. Kwong, "Fundamental characteristics and high-speed applications of carrier-depletion silicon Mach-Zehnder modulators," *IEICE Electron. Express* **11** (24), 20142010 (2014).

67. K. Ogawa, K. Goi, A. Oka, Y. Mashiko, T.-Y. Liow, X. Tu, G.-Q. Lo, D.-L. Kwong, S. T. Lim, M. J. Sun, and C. E. Png, "Design and characterisation of high-speed monolithic silicon modulators for digital coherent communication," *Proc. SPIE* **9367**, 93670C-1–93670C-8 (2015).
68. N. C. Harris, Y. Ma, J. Mower, T. Baehr-Jones, D. Englund, M. Hochberg, and C. Galland, "Efficient, compact and low loss thermo-optic phase shifter in silicon," *Opt. Express* **22**(9), 10487–10493 (2014).

Chapter 4
Optical Circuits and Waveguides in Integrated Mach–Zehnder Optical Modulators

Integrated MZ optical modulators are constructed with optical waveguide circuits, which are treated simply as building blocks in the previous chapter. In this chapter, the basic theoretical characteristics of the optical waveguide circuits are discussed in depth. Optical layouts of integrated MZ optical modulators exploited to generate optical data in different modulation formats for high-capacity optical networks are summarized first. Then, an integrated MZ optical modulator of a given layout is represented in a transfer matrix framework using 2×2 matrices. Note that the MZ optical modulator is mathematically equivalent to a two-port integrated MZ optical switch; thereby the mathematical framework discussed in this chapter provides a common theoretical platform for the design of integrated photonics devices, such as high-port-count optical switches. The transfer-matrix framework is useful as a tool for design and fabrication in foundries. This chapter then describes optical waveguide systems that comprise small-footprint MZ optical modulators. Simple mathematical analysis based on Snell's law reveals that a high refractive-index contrast between the core and clad leads to a low-profile optical waveguide. Silicon optical waveguide systems are highlighted because the high-index-contrast optical waveguides are extensively used for integrated MZ optical modulators. The characteristics of the optical mode field and wave propagation in optical waveguide systems are described on the basis of computational analysis.

4.1 Optical Circuits

4.1.1 Single Mach–Zehnder optical modulator

Figure 4.1(a) illustrates the optical circuit of a single MZ optical modulator with one-port I/O ends, which is the same as that in Fig. 3.4. The optical waveguide layout of the single MZI is encompassed with a square. In the OFF state of such a one-port MZ optical modulator, the light is emitted out of the core via radiation mode as described by the simulation results in Fig. 3.5. A single MZ optical modulator can be represented with another optical waveguide layout in Fig. 4.1(b), which has two-port I/O ends. In the input and output sides, 2×2 optical couplers as depicted in Fig. 3.2 for the ring-resonator optical waveguide layout are inserted instead of the 1×2 splitter and coupler. In this configuration, there is no input light to port 2, and the radiation mode corresponds to the output light from port 3. Port 1 for the CW light input and port 4 for the optical data output are located in the diagonal positions, respectively. The two-port optical waveguide layout is equivalent with that of a two-port MZI optical switch.[1,2] Therefore, the same process technology can be adopted for these integrated photonic devices on a silicon-photonics platform.

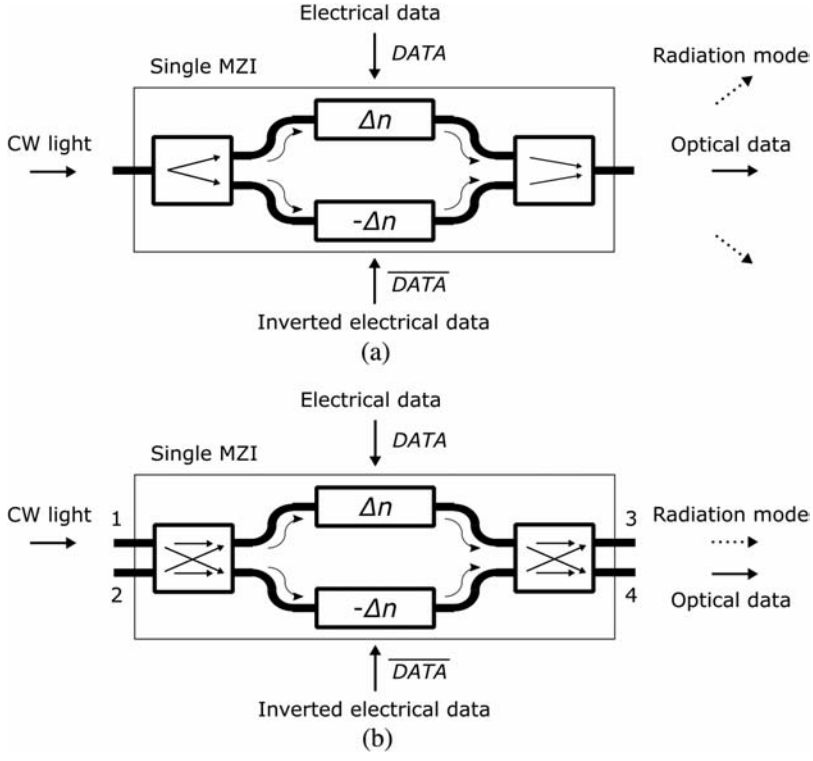

Figure 4.1 (a) Optical-circuit diagram of single MZ optical modulator with one-port I/O configuration. (b) Two-port I/O configuration.

The advantage of the two-port optical waveguide layout is that it can be analyzed mathematically by means of the transfer-matrix method described in the next section.

4.1.2 Quadrature Mach–Zehnder optical modulator

In a quadrature MZ optical modulator, two units of a single MZI are inserted as sub-MZI units for the I and Q components in both arms of the main MZI, respectively. Its optical waveguide layout is depicted in Fig. 4.2 with a one-port I/O configuration. Single MZIs in the configuration shown in Fig. 4.1(a) are used. To sustain a $\pi/2$ phase difference between the I and Q components, DC phase shifters generating $\pi/4$ and $-\pi/4$ phase shifts are also inserted into both arms, respectively. A quadrature MZ optical modulator is utilized for zero-chirp optical data generation in IQ modulation formats.

A quadrature MZ optical modulator can also be configured using two-port single MZIs for I and Q components. The optical waveguide layout for this configuration is illustrated in Fig. 4.3. Single MZIs with the layout shown

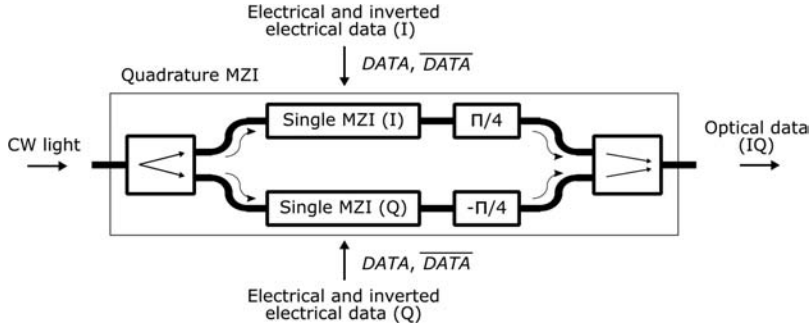

Figure 4.2 Optical-circuit diagram of a quadrature MZ optical modulator with one-port I/O ends.

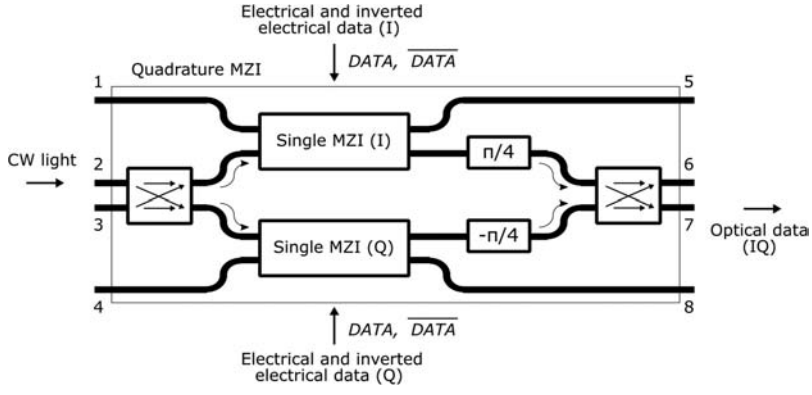

Figure 4.3 Optical circuit diagram of a quadrature MZ optical modulator with two-port I/O ends.

in Fig. 4.1(a) are inserted as sub-MZIs in the I and Q arms in a two-port main MZI. Four I/O ports are set in the optical waveguide layout for mathematical representation using transfer matrices. On the input side, CW light is input to port 2; there are no lights input to ports 1, 3, and 4. Optical data in the IQ components are emitted from port 7 on the output side. For the phase difference between I and Q components, DC phase shifters are also inserted into the I and Q arms.

4.1.3 Polarization-division-multiplexed Mach–Zehnder optical modulator

In digital coherent communications, optical data are transmitted in polarization-division-multiplexed (PDM) IQ formats using a PDM IQ MZ optical modulator with an optical waveguide layout as illustrated in Fig. 4.4 in a one-port I/O configuration. Quadrature MZIs that have the configuration in Fig. 4.2 are inserted. An integrated MZ optical modulator constructed with high-index-contrast optical waveguides such as silicon optical waveguides operates in single linear-polarization mode, such as TE mode with low optical insertion loss in a broad spectral range. Therefore, the two quadrature MZIs in Fig. 4.2 are supposed to operate in the same linear-polarization mode. The linear-polarization mode of light output from a quadrature MZI (in the upper arm in Fig. 4.4) is assigned to x polarization, and the output light from the MZI unit is assigned to the x-polarization component. The linear polarization of output light from the other quadrature MZI is rotated to the orthogonal linear polarization through a PR optical waveguide block, and the output light from the MZI is assigned to the y-polarization component. The output lights in x- and y-polarization components are multiplexed through a PBC optical waveguide block. Designs for PR and PBC optical waveguide blocks are elaborated in Section 4.4. A two-port configuration is also possible for a PDM IQ MZ optical modulator using the two-port quadrature MZ optical modulator shown in Fig. 4.3.

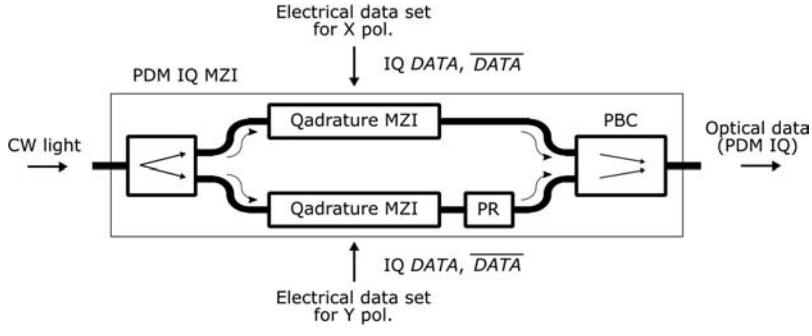

Figure 4.4 Optical circuit diagram of a PDM IQ MZ optical modulator.

4.2 Transfer-Matrix Framework

4.2.1 Representation in transfer matrices

The transfer-matrix method is a versatile tool to construct mathematical models of multi-port photonic integrated circuits by treating building blocks such as passive optical waveguides, 2×2 optical couplers, and phase shifters in the form of mathematical matrices. The method was incorporated into the modeling and analysis of two-port digital ladder circuits consisting of electric capacitors and inductors.[3,4] The method was then applied to signal processing in fiber-optic lattice circuits.[5] Up to the present, extensive efforts have been made to transfer-matrix modeling and the analysis of two-port optical lattice circuit transversal filters in planar lightwave circuits and photonic integrated circuits.[6–9] In the framework of the method, each building block is represented with a square matrix, and the transfer matrix of an integrated circuit as a whole is given as a matrix product of the square matrices of all the constituent building blocks.[6] In the ideal case of no optical loss, the matrices are unitary. Non-unitary matrices, however, are assigned to building blocks in practical cases, where optical loss and other impairments occur due to, e.g., non-negligible optical absorption of waveguide materials, side-wall roughness introduced in fabrication processes, and imperfections in design and fabrication. The transfer-matrix elements of each building block in practical cases can be determined by numerical simulation or by optical measurement.

The transfer matrices of a passive optical waveguide pair (WG), a 2×2 optical coupler (2×2), and a phase shifter (PS) in the ideal case are written in the following forms:

$$\overleftrightarrow{M}_{\mathrm{WG}} = \begin{bmatrix} e^{-i\omega\tau/2} & 0 \\ 0 & e^{i\omega\tau/2} \end{bmatrix}, \tag{4.1}$$

$$\overleftrightarrow{M}_{2\times2} = \begin{bmatrix} \cos\theta & -i\,\sin\theta \\ -i\,\sin\theta & \cos\theta \end{bmatrix}, \tag{4.2}$$

and

$$\overleftrightarrow{M}_{\mathrm{PS}} = \begin{bmatrix} e^{-i^{\Delta\phi}/2} & 0 \\ 0 & e^{i^{\Delta\phi}/2} \end{bmatrix}, \tag{4.3}$$

respectively. For passive optical waveguides in both arms of a symmetric single MZI, there is no propagation time difference between the arms, and thus the delay time τ can be set to zero in Eq. (4.1); its transfer matrix is thereby a unit matrix. Angle θ equals $\pi/4$ for a symmetric 2×2 optical coupler used as an optical splitter or combiner in a MZ optical modulator. Phase $\Delta\phi/2$ denotes an optical phase shift applied to each phase shifter, as in Eqs. (3.1) and (3.2).

In the transfer-matrix framework, a large-scale PIC is decomposed into its constituent building blocks. For the computational modeling and analysis of the PIC, numerical simulation can be done for each building block to determine matrix elements of its transfer matrix, and then the matrix product of all the constituting transfer matrices provides the numerical characteristics of the entire PIC. This procedure is extremely helpful with reducing computational costs such as computational time and storage-memory capacity. Therefore, computational performance optimization is efficient. On the other hand, numerical simulation of the entire optical system of the MZ optical modulator shown in Fig. 3.5, for example, takes a large simulation space and consumes a long simulation time and significant computer memory.

The transfer-matrix framework has also practical importance for scaling up photonic integration. Transfer matrices of the building blocks can be stored as device libraries in process design kits (PDKs) for design and fabrication in foundries. The arbitrary scale of a PIC can be designed and analyzed easily by using the device libraries and transfer-matrix computation. A computational approach based on the transfer-matrix method empowers integrated semiconductor-photonics platforms. Proper performance of this method follows an important design rule: each building block is terminated with the same passive optical waveguide to ensure a common interface for seamless connection to other blocks.

4.2.2 Transfer matrices of Mach–Zehnder optical modulators

The transfer matrix of a single MZ optical modulator with the two-port optical waveguide layout illustrated in Fig. 4.1(b) is obtained from a matrix product defined as

$$\overleftrightarrow{M}_{\mathrm{MZ}} = \overleftrightarrow{M}_{2\times2} \cdot \overleftrightarrow{M}_{\mathrm{WG}} \cdot \overleftrightarrow{M}_{\mathrm{PS}} \cdot \overleftrightarrow{M}_{\mathrm{WG}} \cdot \overleftrightarrow{M}_{2\times2} \tag{4.4}$$

by substituting the transfer matrices in Eqs. (4.1)–(4.3) with $\tau = 0$ for the delay difference between the passive parallel optical waveguides and $\theta = \pi/4$ for a 50:50 power-splitting/combining ratio of the 2×2 optical couplers; therefore, it is expressed as

$$\begin{aligned}\overleftrightarrow{M}_{\mathrm{MZ}} &= \overleftrightarrow{M}_{2\times2}.\overleftrightarrow{M}_{\mathrm{PS}}.\overleftrightarrow{M}_{2\times2} \\ &= \begin{bmatrix} 1/\sqrt{2} & -i/\sqrt{2} \\ -i/\sqrt{2} & 1/\sqrt{2} \end{bmatrix} \cdot \begin{bmatrix} e^{-i^{\Delta\phi}/2} & 0 \\ 0 & e^{i^{\Delta\phi}/2} \end{bmatrix} \cdot \begin{bmatrix} 1/\sqrt{2} & -i/\sqrt{2} \\ -i/\sqrt{2} & 1/\sqrt{2} \end{bmatrix}.\end{aligned} \tag{4.5}$$

Finally, the following equation is derived for input electric field E_{in}, output electric field E_{out}, and electric field in radiation mode E_{rad}:

$$\begin{bmatrix} E_{\mathrm{rad}} \\ E_{\mathrm{out}} \end{bmatrix} = \overleftrightarrow{M}_{\mathrm{MZ}} \cdot \begin{bmatrix} E_{\mathrm{in}} \\ 0 \end{bmatrix} = e^{-i^{\pi}/2} \begin{bmatrix} \sin\frac{\Delta\phi}{2} \\ \cos\frac{\Delta\phi}{2} \end{bmatrix} E_{\mathrm{in}}. \tag{4.6}$$

Because of the diagonal symmetry between I/O ends of the 2×2 MZI, E_{out} is assigned as the second element in the output field vector in Eq. (4.6). The output electric field is essentially the same as in Eq. (3.3), omitting a time-varying oscillating carrier component of $e^{i\omega\tau}$ and a constant phase factor $e^{-i\pi/2}$. The radiation mode is orthogonal to the output field in terms of phase difference. The radiation mode obviously corresponds to the OFF state if the output mode is in the ON state. A deviation of the power-splitting/combining ratio from 50:50 (e.g., $\theta \neq \pi/4$) due to errors and imperfections in design and fabrication leads to a reduction in the ON–OFF extinction ratio in a practical MZ optical modulator.

The transfer matrix of the quadrature MZ optical modulator illustrated in Fig. 4.3 is also obtained in the ideal case. The expression of the symmetric MZI in Eq. (4.5) is substituted for the I and Q sub-MZI units in their respective 2×2 sub-matrices, denoted with suffixes I and Q in the third matrix from the left in the following equation:

$$\begin{bmatrix} E_5 \\ E_6 \\ E_7 \\ E_8 \end{bmatrix} = \begin{bmatrix} 1 & 0 & 0 & 0 \\ 0 & \frac{1}{\sqrt{2}} & \frac{-i}{\sqrt{2}} & 0 \\ 0 & \frac{-i}{\sqrt{2}} & \frac{1}{\sqrt{2}} & 0 \\ 0 & 0 & 0 & 1 \end{bmatrix} \cdot \begin{bmatrix} e^{-i\pi/4} & 0 & & \\ 0 & e^{-i\pi/4} & [0] & \\ & & e^{i\pi/4} & 0 \\ [0] & & 0 & e^{i\pi/4} \end{bmatrix} \cdot \begin{bmatrix} \left[\overleftrightarrow{M}_{\text{MZ}}\right]_{\text{I}} & [0] \\ [0] & \left[\overleftrightarrow{M}_{\text{MZ}}\right]_{\text{Q}} \end{bmatrix} \cdot \begin{bmatrix} 1 & 0 & 0 & 0 \\ 0 & \frac{1}{\sqrt{2}} & \frac{-i}{\sqrt{2}} & 0 \\ 0 & \frac{-i}{\sqrt{2}} & \frac{1}{\sqrt{2}} & 0 \\ 0 & 0 & 0 & 1 \end{bmatrix} \cdot \begin{bmatrix} E_1 \\ E_2 \\ E_3 \\ E_4 \end{bmatrix}. \tag{4.7}$$

Here, [0] denotes a 2×2 zero matrix. The first and fourth matrices from the left represent the input and output sections, including the 2×2 optical couplers connected to the I and Q sub-MZI units. The second matrix from the left is introduced to generate a $\pi/2$ phase difference between the I and Q components. The unitary matrix representing the phase difference is replaced with a non-unitary matrix including the optical loss and phase characteristics of a DC phase shifter in design or fabrication, if necessary. The input and output electric-field vectors for the quadrature optical modulator have their matrix elements presented in the following equations:

$$\begin{bmatrix} E_1 \\ E_2 \\ E_3 \\ E_4 \end{bmatrix} = \begin{bmatrix} 0 \\ E_{\text{in}} \\ 0 \\ 0 \end{bmatrix} \tag{4.8}$$

and

$$\begin{bmatrix} E_5 \\ E_6 \\ E_7 \\ E_8 \end{bmatrix} = \begin{bmatrix} E_{\mathrm{I-rad}} \\ E_{\mathrm{IQ-out}} \\ E_{\mathrm{IQ-rad}} \\ E_{\mathrm{Q-rad}} \end{bmatrix}. \tag{4.9}$$

The I/O electric-field vectors include only one I/O electric field. In the output vector, E_5, E_7, and E_8 are attributed to the electric fields of radiation mode $E_{\mathrm{I\text{-}rad}}$ from the I sub-MZI unit, $E_{\mathrm{IQ\text{-}rad}}$ from the quadrature optical modulator, and $E_{\mathrm{Q\text{-}rad}}$ from the Q sub-MZI unit, respectively.

The transfer matrix of the PDM IQ MZ optical modulator in the ideal case can be obtained with two parallel quadrature MZ optical modulators in Eqs. (4.7)–(4.9), in conjunction with the Muller matrix for a PDM optical circuit.[10]

Once transfer matrices of MZ optical modulators are formulized, the next task is to determine all of the transfer-matrix elements for the computational design and analysis of the modulators on integrated photonics platforms. Numerical simulation of the optical modes in optical waveguides is crucial to perform this task. Optical modes in various waveguide-based building blocks for integrated MZ optical modulators are studied in the following sections in this chapter.

4.3 Optical Waveguide and Optical Mode

4.3.1 Guided wave in ray trace

The basic principle of the confinement of a lightwave in a dielectric optical waveguide is total internal reflection (TIR) at the refractive-index boundary, whereby the lightwave is localized in a core medium with a refractive index higher than that of the surrounding cladding medium.[11–13] Consider a 2D slab optical waveguide with n_{core} and n_{clad} for the refractive indices of the core and cladding, as illustrated with a vertical cross-section in Fig. 4.5. The slab optical waveguide has a symmetric refractive-index profile. The lightwave incident to the slab optical waveguide is TE-polarized. Light refraction at a dielectric interface between core and cladding is illustrated in the inset with

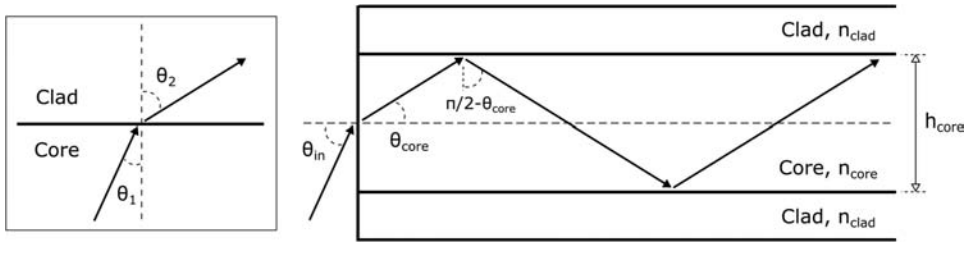

Figure 4.5 Ray traces of a lightwave input to a slab optical waveguide.

incident and refraction angles θ_1 and θ_2. For TIR, the critical angle θ_{crit} is given for the incident angle as

$$\theta_1 = \theta_{crit} = \sin^{-1} \frac{n_{clad}}{n_{core}}, \tag{4.10}$$

where the refraction angle is substituted with $\pi/2$ in the mathematical representation of Snell's law.[14] For a silicon-slab optical waveguide with $n_{core} = 3.48$ and $n_{clad} = 1.45$, the θ_{crit} for the core and cladding refractive indices is 24.6°, whereas it is 83.3° with $n_{core} = 1.46$ and $n_{clad} = 1.45$ for a low-index-contrast optical waveguide such as silica optical fibers. Snell's law also provides an incident angle θ_{in} from air of unity refractive index in the following form:

$$\sin \theta_{in} = n_{core} \sin \theta_{core} = n_{core} \sqrt{1 - \sin^2 \theta_{crit}} = n_{core} \sqrt{\frac{n_{core}^2 - n_{clad}^2}{n_{core}^2}}, \tag{4.11}$$

if TIR occurs at the critical angle, where the following condition holds:

$$\theta_{core} = \frac{\pi}{2} - \theta_{crit}. \tag{4.12}$$

The term in the square root in the right-most term of Eq. (4.11) is the so-called index contrast Δ_{ref}, which is expressed as

$$2\,\Delta_{ref} = \frac{\left(n_{core}^2 - n_{clad}^2\right)}{n_{core}^2} = \frac{2(n_{core} - n_{clad})}{n_{core}}. \tag{4.13}$$

In the limit of low-refractive-index difference, the index contrast is reduced to the mathematical form in the right-most term of Eq. (4.13).

Confined lightwaves lead to standing waves in the direction perpendicular to the refractive-index boundaries (vertical direction) and are guided in the slab optical waveguide along a direction perpendicular to the vertical direction.[13] Such a scheme of guided-lightwave propagation can be expressed in a ray trace for a lightwave, as illustrated in Fig. 4.5. Total internal reflection occurs twice in one round trip of a standing wave in the vertical direction, and the path length in the period is twice the core height, namely, $2h_{core}$. The path length in the round trip for the guided lightwaves in wavelength λ leads to a phase delay of

$$\phi = 2\,h_{core}\, k n_{core} \sin \theta_{core} \tag{4.14}$$

with wavenumber $k = 2\pi/\lambda$. The phase shift δ produced in the TIR at a dielectric interface is known as a phase shift in the Goos–Hänchen effect:[14]

$$\tan\frac{\delta}{2} = -\frac{\sqrt{\cos^2\theta_{\text{core}} - \left(\frac{n_{\text{clad}}}{n_{\text{core}}}\right)^2}}{\sin\theta_{\text{core}}}. \tag{4.15}$$

The total phase shift Φ after the round trip of the standing waves is the sum of the phase delay and twice the Goos–Hänchen phase shift:

$$\Phi = \phi + 2\delta = 2h_{\text{core}}\, k \sin\theta_{\text{core}} - 4\tan^{-1}\left[\frac{\sqrt{\cos^2\theta_{\text{core}} - \left(\frac{n_{\text{clad}}}{n_{\text{core}}}\right)^2}}{\sin\theta_{\text{core}}}\right]. \tag{4.16}$$

The total phase shift is quantized with respect to 2π for positive interference to produce the standing waves, which produces the following relationship:

$$2h_{\text{core}}\, k \sin\theta_{\text{core}} - 4\tan^{-1}\left[\frac{\sqrt{\cos^2\theta_{\text{core}} - \left(\frac{n_{\text{clad}}}{n_{\text{core}}}\right)^2}}{\sin\theta_{\text{core}}}\right] = 2m\pi \tag{4.17}$$

with a zero or positive integer m. Equation (4.17) is modified into the form

$$\tan\left(\frac{2h_{\text{core}}\, kn_{\text{core}} \sin\theta_{\text{core}} - 2m\pi}{2}\right) = \sqrt{\frac{2\Delta_{\text{ref}}}{\sin^2\theta_{\text{core}}} - 1} \tag{4.18}$$

if Eq. (4.13) is satisfied.[12,13] The integer represents the mode index, whereby zero stands for the fundamental mode and positive numbers for higher-order modes.

The single-mode condition for the slab optical waveguide is obtained with the constraint $m < 1$ for the mode index in Eq. (4.18). At the critical angle of TIR, the sinusoidal term and the index contrast are substituted with Eqs (4.11) and (4.13), thus reducing the right side of Eq. (4.18) to zero. The following relationship is then derived:

$$h_{\text{core}} < \frac{\lambda}{2\sqrt{n_{\text{core}}^2 - n_{\text{clad}}^2}}. \tag{4.19}$$

This inequality allows for a slab core height lower than 245 nm for a single-mode silicon slab optical waveguide with $n_{\text{core}} = 3.48$ and $n_{\text{clad}} = 1.45$ at a 1550-nm wavelength. Silicon-on-insulator (SOI) wafers with a layer thickness of 220 nm, which have been used extensively for PICs on a silicon-photonics platform, thus serve as base wafers to fabricate silicon-based

single-mode slab optical waveguides for applications involving optical modules in spectral bands such as C and L bands.

4.3.2 Mode field and wave propagation

Maxwell's equations must be solved to obtain the profiles of mode fields and the characteristics of guided lightwaves in dielectric optical waveguides for integrated MZ optical modulators. Source-free Maxwell's equations for the dielectric optical waveguides are written as

$$\vec{\nabla} \times \vec{E}(x, y, z, t) = -\mu_0 \frac{\partial \vec{H}(x, y, z, t)}{\partial t}, \tag{4.20}$$

$$\vec{\nabla} \times \vec{H}(x, y, z, t) = \varepsilon(x, y, z, \omega)\, \varepsilon_0 \frac{\partial \vec{E}(x, y, z, t)}{\partial t}, \tag{4.21}$$

$$\vec{\nabla} \cdot [\varepsilon(x, y, z, \omega)\, \vec{E}(x, y, z, t)] = 0, \tag{4.22}$$

and

$$\vec{\nabla} \cdot \vec{H}(x, y, z, t) = 0 \tag{4.23}$$

in terms of the electric field $\vec{E}$ and magnetic field $\vec{H}$ of lightwaves in the optical-frequency domain because particle currents due to electrons and holes are negligible, as discussed in Chapter 4.[15,16] Here, x, y, and z represent the coordinate variables of a 3D Cartesian coordinate system, and t stands for time. The propagation direction of guided lightwaves is set parallel to the z axis, and the cross-section of an optical waveguide is defined in the xy plane, where the x and y axes lie along the horizontal and vertical directions, respectively. Optical constants ε_0 and μ_0 denote the dielectric permittivity and magnetic permeability in vacuum, respectively; $\varepsilon(x, y, z, \omega)$ is the angular frequency; and ω denotes the dielectric permittivity coefficient. Nonmagnetic materials are assumed in the dielectric optical waveguides. For single-frequency sinusoidal electro-magnetic waves, $\vec{E}$ and $\vec{H}$ are written as

$$\vec{E}(x, y, z, t) = \vec{E}(x, y, z)\, e^{i\omega t} \tag{4.24}$$

and

$$\vec{H}(x, y, z, t) = \vec{H}(x, y, z)\, e^{i\omega t}. \tag{4.25}$$

Substituting the electro-magnetic fields with the expressions in Eqs. (4.24) and (4.25), Eqs. (4.20) and (4.21) are reduced to the following forms:

$$\vec{\nabla} \times \vec{E}(x, y, z) = -i\omega\mu_0 \vec{H}(x, y, z) \tag{4.26}$$

and

$$\vec{\nabla} \times \vec{H}(x, y, z) = i\omega\varepsilon(x, y, z, \omega)\, \varepsilon_0 \vec{E}(x, y, z). \tag{4.27}$$

Taking the curl of Eq. (4.26) and substituting $\vec{\nabla} \times \vec{H}(x, y, z)$ with Eq. (4.27) produces the following equation:

$$\vec{\nabla} \times \vec{\nabla} \times \vec{E}(x, y, z) = -i\omega\mu_0 \vec{\nabla} \times \vec{H}(x, y, z) = k^2\, \varepsilon(x, y, z, \omega) \vec{E}(x, y, z), \tag{4.28}$$

with $k^2 = \omega^2 \varepsilon_0 \mu_0$ for the wavenumber k. According to vector algebra, the left side of Eq. (4.28) becomes

$$\vec{\nabla} \times \vec{\nabla} \times \vec{E}(x, y, z) = \vec{\nabla}\left[\vec{\nabla} \cdot \vec{E}(x, y, z)\right] - \nabla^2\, \vec{E}(x, y, z), \tag{4.29}$$

and subsequently, Eq. (4.28) leads to

$$\vec{\nabla}\left[\vec{\nabla} \cdot \vec{E}(x, y, z)\right] - \nabla^2 \vec{E}(x, y, z) - k^2 \varepsilon(x, y, z, \omega) \vec{E}(x, y, z) = 0. \tag{4.30}$$

The first term in Eq. (4.30) is modified to

$$\vec{\nabla}[\vec{\nabla} \cdot \vec{E}(x, y, z)] = -\nabla\left[\frac{\vec{E}(x, y, z) \cdot \vec{\nabla}\varepsilon(x, y, z, \omega)}{\varepsilon(x, y, z, \omega)}\right] \tag{4.31}$$

by the following algebra of Eq. (4.22):

$$\begin{aligned} \vec{\nabla} \cdot \left[\varepsilon(x, y, z, \omega)\, \vec{E}(x, y, z, t)\right] &= \vec{E}(x, y, z, t) \vec{\nabla} \cdot \varepsilon(x, y, z, \omega) \\ &\quad + \varepsilon(x, y, z, \omega) \vec{\nabla} \cdot \vec{E}(x, y, z, t) \\ &= 0. \end{aligned} \tag{4.32}$$

Substituting the first term in Eq. (4.30) with Eq. (4.31) produces the following differential equation:

$$\nabla^2\, \vec{E}(x, y, z) + \vec{\nabla}\left[\frac{\vec{E}(x, y, z) \cdot \vec{\nabla}\varepsilon(x, y, z, \omega)}{\varepsilon(x, y, z, \omega)}\right] + k^2 \varepsilon(x, y, z, \omega)\, \vec{E}(x, y, z) = 0. \tag{4.33}$$

The dielectric permittivity coefficient, $\varepsilon(x, y, z, \omega)$ equates to $n^2(x, y, z, \omega)$ by using the complex refractive index $n(x, y, z, \omega)$. For low-index-contrast optical waveguides such as silica optical fibers with standard-refractive-index profiles,

$\vec{\nabla} n^2(x, y, z, \omega)$ in the second term in Eq. (4.33) is negligible, and Eq. (4.33) is reduced to the conventional wave equation in scalar-wave analysis,[17]

$$\nabla^2 \vec{E}(x, y, z) + k^2 n^2(x, y, z, \omega) \vec{E}(x, y, z) = 0. \tag{4.34}$$

For high-index-contrast optical waveguides on a silicon-photonics platform, on the other hand, the second term is not negligible, and Eq. (4.33) must be solved in vector-wave analysis.[16,18–21]

The singularity of a mode field occurs at the corners in the core cross-section of a high-index-contrast 3D optical waveguide, such as a channel or rib optical waveguide on a silicon-photonics platform.[18,19] The mode-matching method has been developed as one of computational methods to solve Eq. (4.33) in vector-wave analysis without suffering from mode-field singularity.[20–27] Rib optical waveguides with vertical and slanted side walls were characterized computationally.[24,26] In this method, the cross-section profiles of channel and rib optical waveguides, for example, are made of dielectric layers stacked along the vertical direction, as shown in Fig. 4.6. The profiles are separated into film guide slices along the horizontal direction. Mode fields in each uniform layer section in each slice are obtained as TE-/TM-mode solutions of Eq. (4.33). The amplitude and its derivative of the mode fields are concatenated at each interface between adjoining slices to construct mode-field profiles across the entire cross-section.[28]

The mode-matching method provides electric-field profiles of fundamental mode field in a rib optical waveguide with a silicon core and silica clads at wavelengths of 1300 nm and 1550 nm as plotted in pseudo-color scale in Fig. 4.7.[28] The rib width, rib height, and slab height are 500 nm, 220 nm and 95 nm, respectively. The more-extended mode field towards the outer clads is confirmed at the longer wavelength.

The finite-element method (FEM), whereby Eq. (4.33) is solved by applying the variational principle, is another computational technique to solve mode fields in high-index-contrast optical waveguides.[20,21,29–40] In FEM, a triangular mesh is applied to discretize the computational area, and solutions in each triangular element are expressed in polynomial expansion. Almost the same mode profile as that produced by the mode-matching method in Fig. 4.7 is

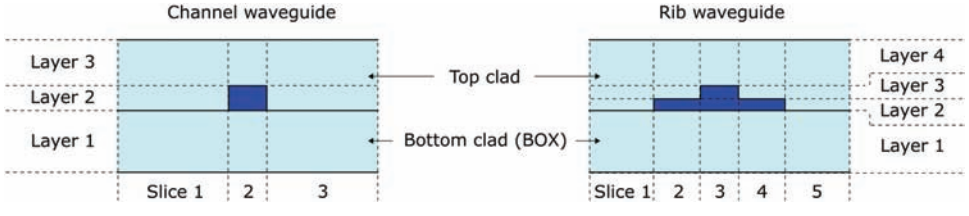

Figure 4.6 Layer and slice arrangements in cross-section profiles of channel and rib optical waveguides in the mode-matching method.

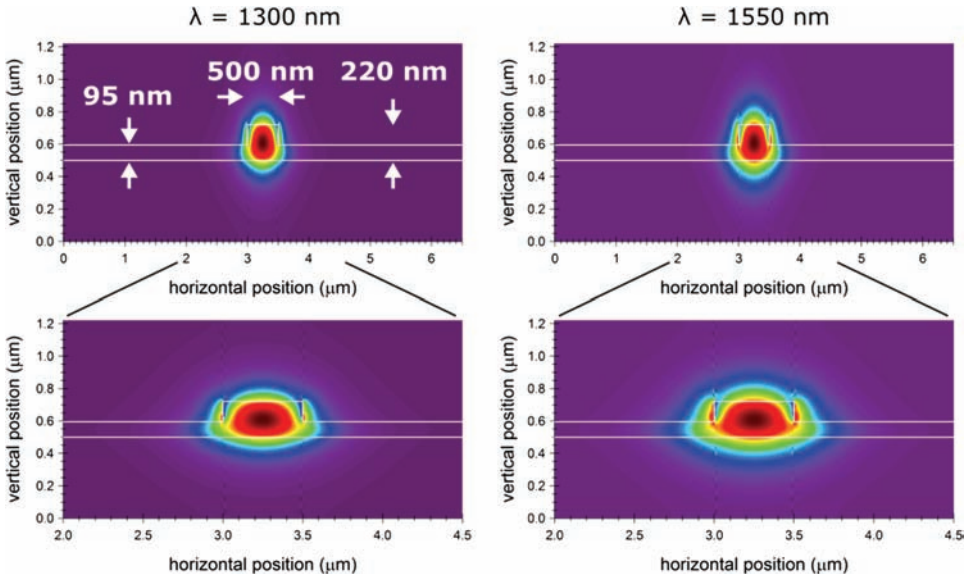

Figure 4.7 Overview and close-up electric-field profiles of the fundamental mode in a silicon rib optical waveguide.

obtained also by FEM. Triangular-mesh discretization for the silicon rib optical waveguide in FEM computation is shown in Fig. 4.8 for the left half of the rib profile under the horizontal symmetry of the core profile.

There are computational methods available for the propagation analysis of guided modes in a high-index-contrast waveguide. One of these is the eigenmode-expansion method, wherein the numerical mode fields of one of

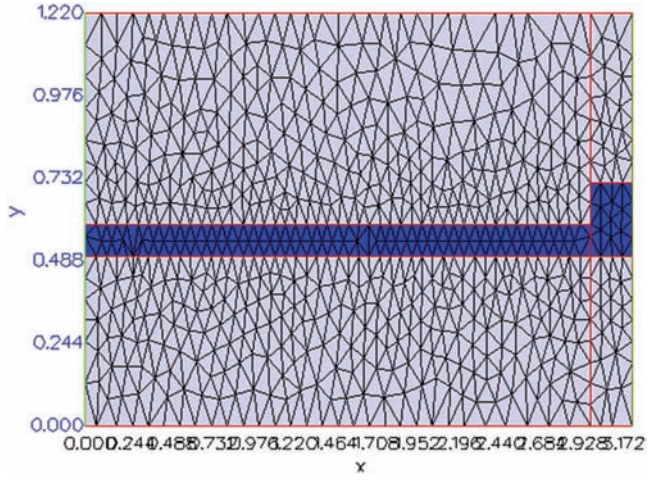

Figure 4.8 Triangular-mesh profile in mode computation by FEM for a silicon rib optical waveguide.

the computational methods described above are utilized as eigenmodes, which form a basis set of orthogonal guided modes.[41–44] A 3D optical waveguide circuit is divided into segments along the propagation direction of the guided modes. The segments are arranged so as not to include any internal refractive-index interfaces along the propagation direction. In each of the segments, solutions to the electric field $\vec{E}$ and magnetic field $\vec{H}$ are written as follows in terms of forward and backward waves based on eigenmodes $\vec{E}_j(x,y)$ and $\vec{H}_j(x,y)$ with a mode index $j=0$ to $M-1$:[43]

$$\vec{E}(x,y,z) = \sum_{j=0}^{M-1} \left[\left(a_j\, e^{-ik_j z} + b_j\, e^{ik_j z} \right) \vec{E}_j(x,y) \right] \tag{4.35}$$

and

$$\vec{H}(x,y,z) = \sum_{j=0}^{M-1} \left[\left(a_j\, e^{-ik_j z} + b_j\, e^{ik_j z} \right) \vec{H}_j(x,y) \right]. \tag{4.36}$$

Axis z goes along the propagation direction. Wavenumber k_j represents the propagation constant of each guided mode with an effective refractive index n_j. The coefficients a_j and b_j are determined to preserve the continuity of the electric and magnetic fields at each interface, respectively.

The other computational methods for propagation analysis are, for instance, the beam propagation method (BPM) and the finite-difference time-domain (FDTD) method. The BPM, which is most computationally efficient, has been applied to the analysis of a variety of optical waveguide circuits and has several variant algorithms, which are suited to the various types of optical waveguide circuits.[20,21,45] The full-vector BPM has been developed and applied to the numerical analysis of high-index-contrast optical waveguide circuits. The BPM algorithm, however, may cause a divergence in the transverse electro-magnetic fields and needs special attention to ensure the accuracy of the numerical results.[46] Rigorous numerical analysis of lightwave propagation is possible with the FDTD method for the time evolution of electro-magnetic fields at the expense of computing resources and computing time.[47]

4.4 Optical Waveguide Features

4.4.1 Channel and rib waveguides

Channel and rib optical waveguides are the most basic building blocks to construct PICs such as integrated optical modulators. In this subsection, the computational characteristics of channel and rib optical waveguides depicted in Fig. 4.9 are obtained by the mode-matching method. The widths of channel

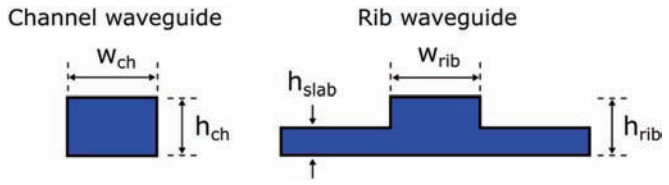

Figure 4.9 Cross-sections of channel and rib optical waveguides.

and rib optical waveguides are denoted as w_{ch} and w_{rib}, and their top heights as h_{ch} and h_{rib}, respectively. The rib optical waveguide has side slab wings of height h_{slab} adjoined to the central rib on the both side. In integrated MZ optical modulators with PN-junction phase shifters, the top heights equal the thickness of the thin SOI layer, as described in Chapter 3.

Electric-field profiles of the fundamental modes in a channel optical waveguide with a 220-nm channel height are presented in pseudo-color scale in Fig. 4.10. These modes have a TE fraction of more than 99%. In a 3D optical waveguide, the TE and TM components are mixed, and the guided mode is called TE-like or TM-like because TE or TM symmetry is broken at corners of the waveguide core. The mode field extends towards the outer cladding at

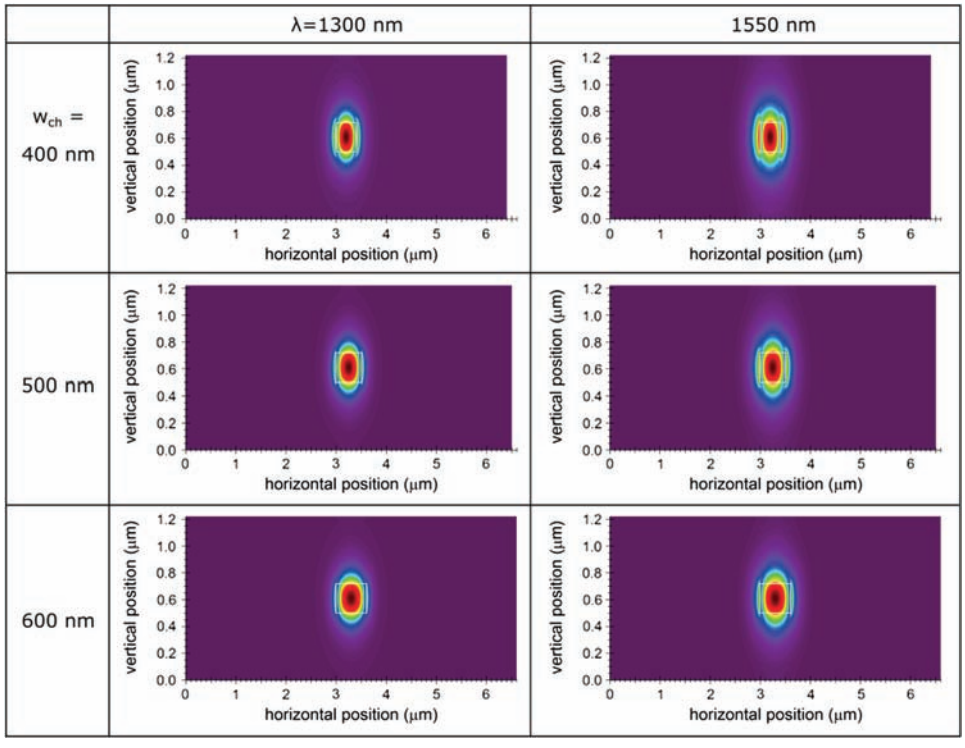

Figure 4.10 Mode-field profiles of the fundamental mode in a channel optical waveguide of different channel widths at wavelengths of 1300 nm and 1550 nm.

the longer wavelengths. At each wavelength, the field is more strongly localized in the core area with increasing channel width w_{ch}. The propagation of a guided lightwave is disturbed by side-wall roughness created during the fabrication processes of optical lithography and subsequent dry etching. A portion of the optical power of the lightwave is thus scattered from the waveguide via light scattering, and the light scattering leads to optical loss in the waveguide. A wider core width is preferred to localize the fundamental mode inside the core more strongly given optical loss reduction caused by suppressing the light scattering. However, higher-order modes are generated more easily with wider core widths, and the performance of optical modulation is deteriorated. Either the extinction ratio [Eq. (3.6)] or the optical modulation amplitude [Eq. (3.8)] in intensity modulation, as well as the Q-factor in Eq. (3.13) in phase modulation, are reduced by the higher-order modes.

A slice cut of the mode field along the horizontal direction in the 500-nm-wide waveguide provides electric-field and optical-power profiles at 1550 nm in wavelength, as plotted in Fig. 4.11. The profiles are taken across the horizontal axis at the half height. Sharp spikes appear in the electric-field profile at both side walls of the core because the continuity of the electric displacement field is required according to Gauss's law, from which Eq. (4.22) originates. The optical power, which is obtained as a component of the Poynting vector in the propagation of a guided wave along the z axis in the

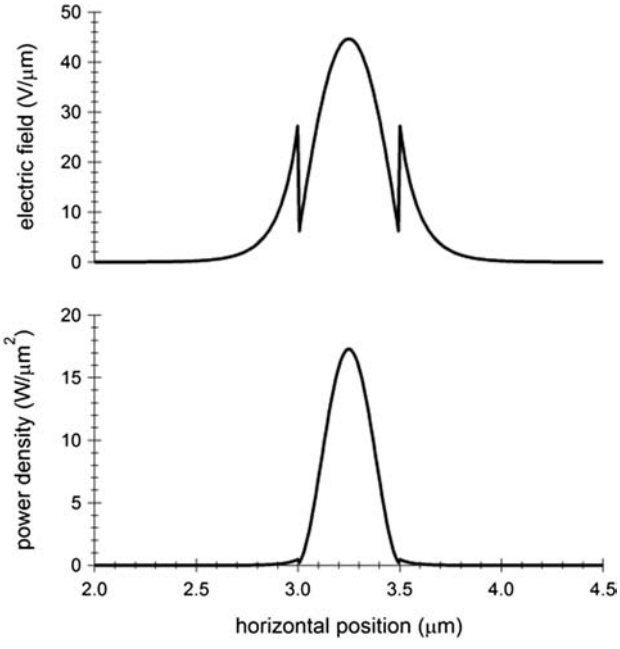

Figure 4.11 Electric-field and optical-power profiles of the fundamental mode in a 500-nm rib optical waveguide along the horizontal direction at a wavelength of 1550 nm.

waveguide, yields a smooth distribution profile as expected from the evanescence of optical power from the core.

Electric-field profiles of the fundamental mode in a rib optical waveguide of a 220-nm rib height and 95-nm slab height appear in pseudo-color scale in Fig. 4.12. These modes are TE-like modes with a TE fraction of more than 98%. The more extended mode field at the longer wavelength and the more strongly localized mode field with the wide rib width are observed as for the channel optical waveguide. The mode fields are utilized for the semi-analytical characterization of PN-junction carrier-depletion rib-waveguide phase shifters in the next chapter.

The effective refractive index n_{eff} is numerically calculated from the following formula:

$$n_{\text{eff}} = \frac{\int_{-\infty}^{+\infty} dx \int_{-\infty}^{+\infty} dy |E_{\text{mode}}(x, y)| n(x, y)}{\int_{-\infty}^{+\infty} dx \int_{-\infty}^{+\infty} dy |E_{\text{mode}}(x, y)|}. \tag{4.37}$$

Here, $E_{\text{mode}}(x, y)$ and $n(x, y)$ represent the electric-field profile of a mode in an optical waveguide of interest and the refractive-index profile across the

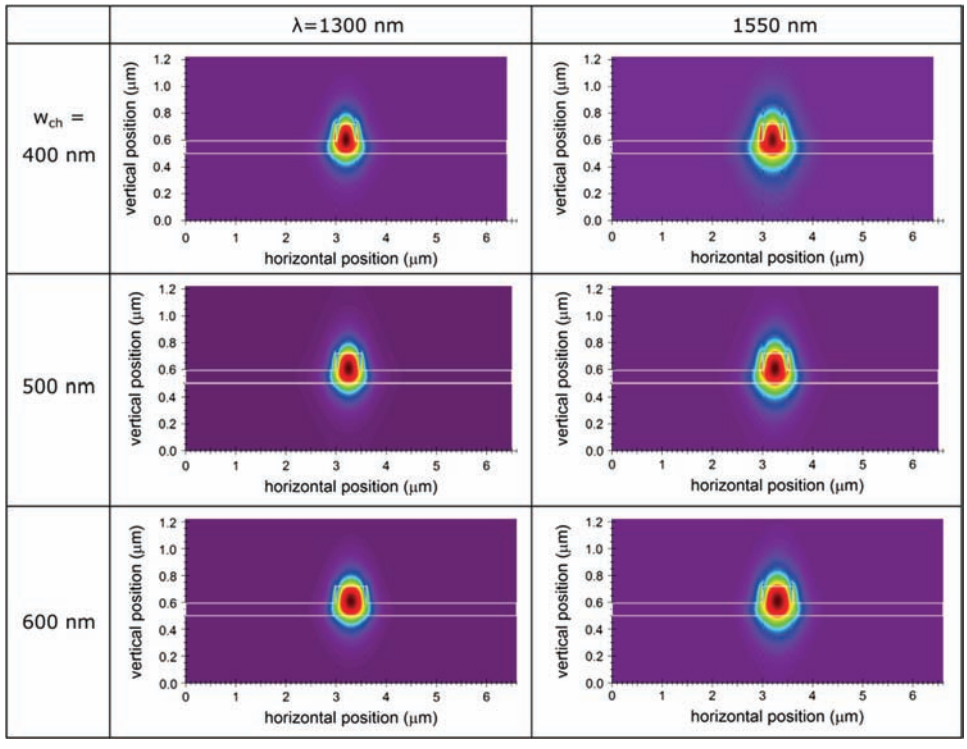

Figure 4.12 Mode-field profiles of the fundamental mode in a rib optical waveguide of different rib widths at wavelengths of 1300 nm and 1550 nm.

cross-section of an optical waveguide. For single-mode optical waveguides for MZ optical modulators, the fundamental mode field with mode index, $m = 0$ is taken as $E_{\text{mode}}(x, y)$. (Refer to the literature on the programming code of multi-dimensional integrals in Eq. (4.37) for the numerical calculation of the effective refractive index of channel and rib optical waveguides, as plotted in Fig. 4.13.[48]) As discussed in terms of the mode fields, the effective refractive indices are higher at shorter wavelengths and with wider channel/rib widths. The effective refractive index of the rib optical waveguide is higher than that of the channel optical waveguide with the same width because the rib core with the side slab wings has a larger core cross-section than the channel core. In integrated carrier-depletion MZ optical modulators on a silicon-photonics platform, a PN-junction rib optical waveguide is connected with a channel optical at each input and output end in each MZI arm. The abrupt connection to a channel optical waveguide causes an index mismatch and hence undesirable reflection. An adiabatic rib–channel transition using slab tapers, as illustrated in Fig. 4.13, permits a reflection-free connection. The term "adiabatic" implies that the fundamental mode is propagated from channel to rib, and vice versa, without optical power leakage to higher-order guided or radiation modes in forward propagation (and the fundamental mode in backward propagation).[49]

In the rib optical waveguide, in particular, optical power transfers to higher-order modes occur more easily than in the channel optical waveguide via side-wall roughness or fluctuation in slab thickness because these process imperfections induce mode coupling with higher-order modes extended in the side slab wings. Special care must be taken to eliminate higher-order mode

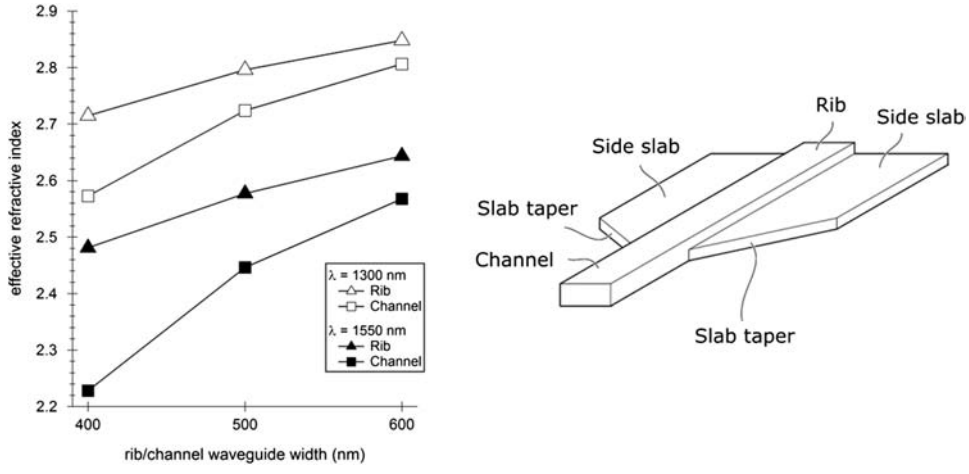

Figure 4.13 Effective refractive index of fundamental modes in channel and rib optical waveguides vs. channel/rib width at wavelengths of 1300 nm and 1550 nm, and illustration of the rib–channel transition section.

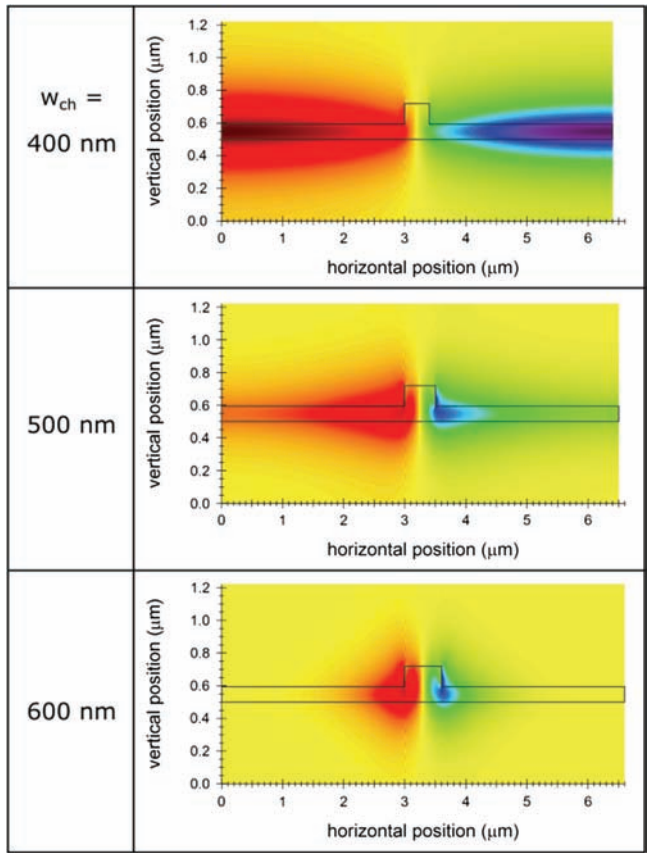

Figure 4.14 Mode-field profiles of the first higher-order modes in a rib optical waveguide with different rib widths at a wavelength of 1550 nm.

propagation in the rib optical waveguide. Electric-field profiles of the first higher-order mode in a rib optical waveguide are presented in Fig. 4.14. The first higher-order mode in a 400-nm rib optical waveguide does not form a guided mode but rather a slab mode and is very weakly overlapped with the fundamental mode field. Therefore, higher-order mode propagation is unlikely in 400-nm rib optical waveguides. Field profiles of the first higher-order mode in 500-nm and 600-nm rib optical waveguides yield the characteristics of guided modes and more overlap with the fundamental mode fields. Therefore, optical power transfer to higher-order modes may occur in these rib optical waveguides, although a wider rib width is preferred with respect to optical loss due to side-wall roughness. This point is discussed in detail and the concept of a quasi-single mode is introduced in the next chapter.

The mode-matching method provides an effective index of 2.5772 for a 500-nm rib optical waveguide at a 1550-nm wavelength, and the FEM produces almost the same result, $n_{\text{eff}} = 2.5780$. The latter method can also be

employed for the computational mode-field analysis of high-index-contrast optical waveguides.

4.4.2 Optical splitter/coupler

In integrated MZ optical modulators, a 1×2 optical splitter and coupler are indispensable to construct MZI circuits. Small-footprint 1×2 optical splitters and couplers are available by utilizing 1×2 MMIs.[50–54] To address the theoretical characteristics of a 1×2 MMI, the optical modes in a 2D MMI, as illustrated in Fig. 4.15, are considered. The optical modes in the main slab section of a 2D 1×2 MMI are obtained in a ray trace model. Wavenumber or propagation constants $k_{x,j}$ and $k_{x,j}$ of the j^{th} slab-guided modes in the 2D slab section are written as[52]

$$k_{x,j} = \frac{(j+1)\pi}{W_{\text{MMI}}} \tag{4.38}$$

and

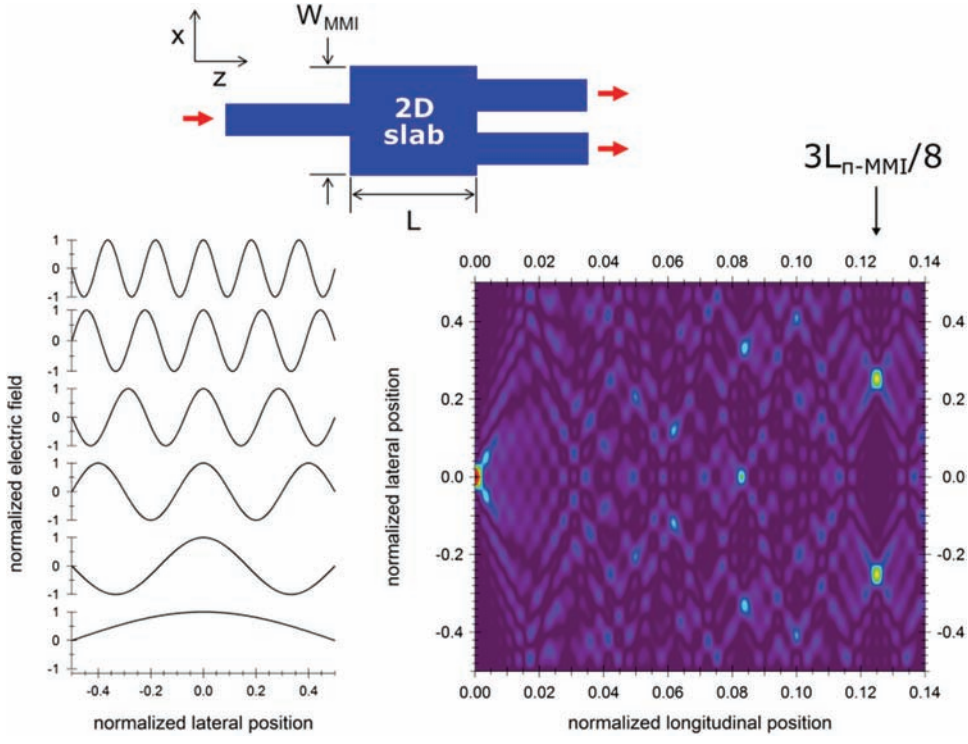

Figure 4.15 Electric-field profiles of the lowest orders and the optical intensity distribution in a 2D slab.

$$k_{z,j} = \frac{2\pi n_{\text{eff}}}{\lambda} - \frac{(j+1)\pi^2}{3L_{\pi\cdot\text{MMI}}}, \tag{4.39}$$

with n_{eff} for the effective refractive indices for the guided modes in the 2D slab section, and W_{MMI} for the 2D slab width along the lateral direction (x) perpendicular to the longitudinal propagation direction (z) of the guided modes. Here, $k_{x,j}$ is assumed to be much smaller than the total propagation constant. Mode index j runs from 0 for the fundamental mode to positive integers 1, 2, ... for higher-order modes. Beat length $L_{\pi\text{-MMI}}$ along the longitudinal direction is taken for the lowest two modes as

$$L_{\pi\cdot\text{MMI}} = \frac{\pi}{k_{z,0} - k_{z,1}} = \frac{4\, n_{\text{eff}}\, W_{\text{MMI}}^2}{3\lambda}. \tag{4.40}$$

The difference in propagation constant $\Delta k_{z,j}$ is then represented as follows by using $L_{\pi\text{-MMI}}$:

$$\Delta\, k_{z,j} = k_{z,j} - k_{z,0} = -\frac{\pi j(j+2)}{3L_{\pi\cdot\text{MMI}}}. \tag{4.41}$$

The optical intensity $I(x, z)$ with J guided modes in the 2D slab section is obtained from linear superposition of the guided modes by substituting their propagation constants along the longitudinal direction with Eq. (4.41):

$$I(x,z) = \left| \sum_{j=0}^{J-1} \cos(\pi(2j+1)\, x) \cos(\pi j(j+2)\, z) \right|. \tag{4.42}$$

Here, the lateral and the longitudinal coordinates are normalized with respect to W_{MMI} and $3L_{\pi\text{-MMI}}$, respectively. The electric fields are zero on both sides of the slab section and do not penetrate the cladding areas outside the slab section under the assumption of strong mode confinement in a high-index-contrast slab optical waveguide, whereby the phase shift due to the Goos–Hänchen effect is ignored. Electric-field profiles of the six lowest even modes and the optical intensity distribution in pseudo-color scale in the 2D slab section are plotted in Fig. 4.15. Ten even modes are taken in the summation in Eq. (4.42). In the 1×2 MMI, the input optical beam is launched at the center of the input edge, and the odd modes are excluded in the summation because the antisymmetric modes have zero amplitudes at the center. Propagated waves in the slab section are focused in two intense optical spots at $L = 0.125$, which corresponds to $3L_{\pi\text{-MMI}}/8$, where L denotes the length of the 2D slab section along the longitudinal direction.[52,54] Two-port optical power splitting with a 3-dB ratio is thus possible with the 2D slab of length $\sim 3L_{\pi\text{-MMI}}/8$.

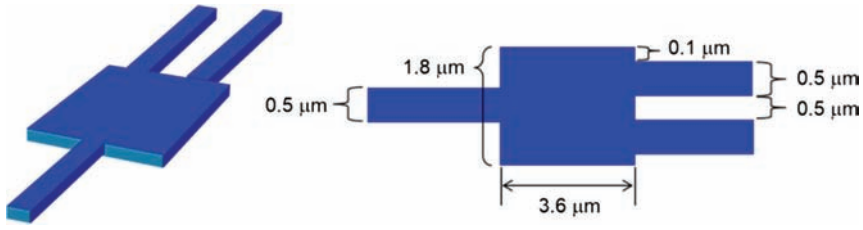

Figure 4.16 Sketch and dimensions of a 1×2 MMI for a 1×2 optical splitter and a 2×1 optical coupler.

An example 3D 1×2 MMI for optical splitters and couplers on a silicon-photonics platform is presented in Fig. 4.16. The main section is a silicon slab optical waveguide of a horizontal area 1.8 μm wide and 3.6 μm long. A single-silicon-channel optical waveguide 500 nm wide is connected to one side of the slab section. A pair of channel optical waveguides of the same width are connected to the opposing side. The input light beam is launched to the single-channel optical waveguide and output from the pair of waveguides in a 1×2 optical splitter. In a 2×1 optical coupler, however, output light beams from both arms of a MZI are launched to the pair waveguides and emitted from the single waveguide. The height is 220 nm across all of the MMI sections for fabrication using an SOI wafer 220 nm thick. The dimensions in the plan view have been optimized computationally by using the eigenmode-expansion method.[55]

An example of the numerical results in computational analysis of the 1×2 MMI is presented in Fig. 4.17. The optical intensity distribution in a

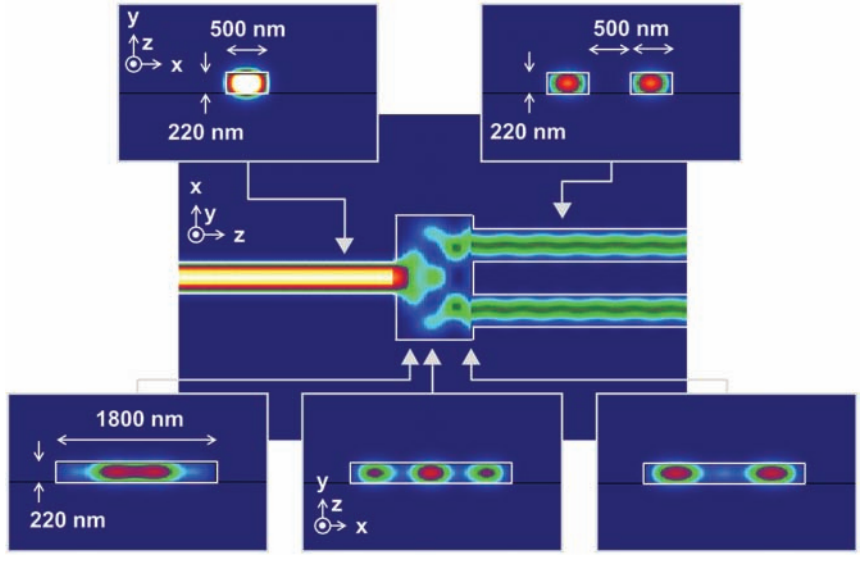

Figure 4.17 Optical intensity distribution in a 1×2 MMI comprising channel and slab optical waveguides.

horizontal (xz) plane at the middle of the channel height and optical power profiles in the vertical (xy) cross-sections are plotted in pseudo-color scale. The distribution characteristics are qualitatively similar to those in the theoretical result for the 2D MMI described above. A light beam launched to a single port in the input side is split into two ports on the output side due to the self-imaging of multiple modes in the slab section.

Rib optical waveguides can be used to construct a 1×2 MMI; 500-nm rib optical waveguides are used for the input and output sections, and a 1.8-μm rib for the slab section. The slab length is also 3.6 μm. The optical power distribution in a horizontal plane at the middle of the rib height and the optical power profiles in vertical cross-sections are plotted in pseudo-color scale in Fig. 4.18. Optical power splitting with a 3-dB ratio is verified in the numerical result.

4.4.3 Polarization-division multiplexer

Optical waveguide circuits for PDM are required to construct integrated MZ optical modulators operating in optical modulation formats, including two orthogonal polarization components. The layout of a PDM optical circuit is shown for a DP-QPSK optical modulator in Fig. 4.19. Optical signals from two QPSK optical modulator units are guided through single-mode optical waveguides, WG1 and WG2. Both QPSK units are identical and generate optical signals in the TE-like polarization because the PN-junction rib-waveguide phase shifters support the TE-like fundamental mode, as shown in

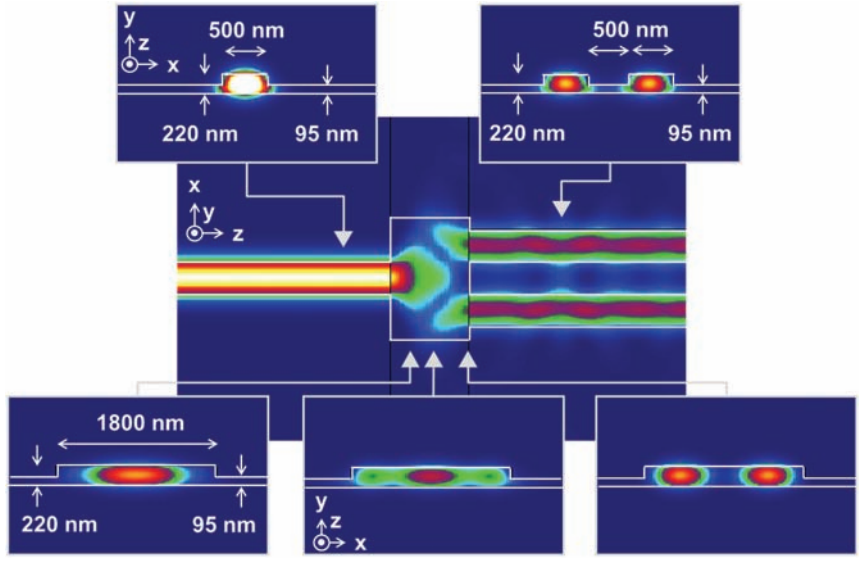

Figure 4.18 Optical intensity distribution in a 1×2 MMI comprising single-mode and multi-mode rib optical waveguides.

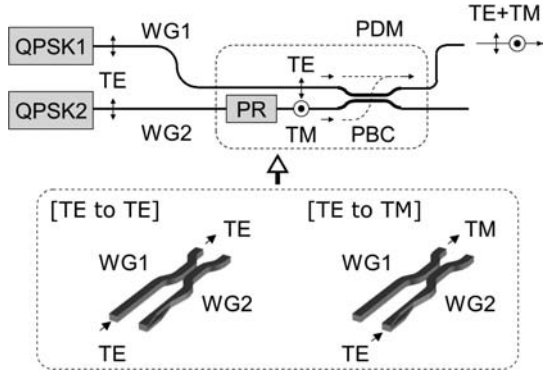

Figure 4.19 Silicon-photonics PDM using a partial-rib optical waveguide polarization rotator.

this chapter.[56] An adiabatic partial-rib PR in WG2 and an asymmetric optical waveguide directional coupler connected with WG1 and WG2 form the PDM optical circuit.[57,58]

A conventional non-adiabatic PR is based on the mode interference between two orthogonal polarization modes as for an optical half-wave plate. An input light beam is propagated in two optical modes of polarization states orthogonal to each other, and polarization rotation occurs with a spatial period of a polarization beat due to the difference in propagation constants between the two modes. Various designs have been proposed, such as slanted-wall waveguides, asymmetrical silicon nanowire waveguides, and asymmetric slab waveguide bends on a silicon-photonics platform.[59–61] There seems to be, however, ellipticity due to an amplitude imbalance between the orthogonal modes generated at the interface with an input channel optical waveguide. The temperature dependence of the beat period leads to thermal instability of the polarization rotation. The wavelength dependence of the period limits the spectral range of the polarization rotation.

Adiabatic polarization rotation based only on the evolution of the polarization of the fundamental mode has been predicted and demonstrated on a silicon-photonics platform.[62–65] The adiabatic partial-rib PR, in which TE-like polarization of the fundamental mode at the input end is rotated along the propagation through the optical waveguide to a TM-like polarization at the output, is also of this type and illustrated in Figs. 4.20(a) and (b), with the computational optical characteristics in Fig. 4.20(c).[57] The PR is designed with the same rule as the rib optical waveguides in terms of rib and slab heights (Fig. 4.19(b)) and can be fabricated simultaneously with the other building blocks using a common optical waveguide system comprising a silicon core and silica top/bottom cladding. Therefore, the partial-rib PR serves as a versatile building block for a small-footprint inline PR on a silicon-photonics platform. The eigenmode-expansion method allows for the computation of the optical

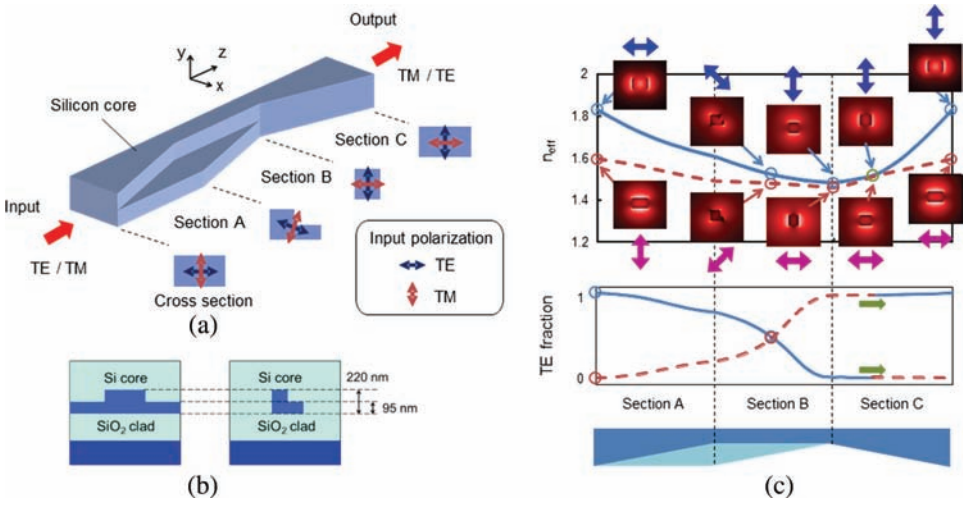

Figure 4.20 Adiabatic partial-rib optical waveguide polarization rotator and its numerical characteristics.

characteristics of mode profiles in cross-section planes (xy) and the polarization evolution along the propagation direction (z) for the two orthogonal modes. Polarization rotation is completed within a total waveguide length of 200–300 μm. There is no ellipticity caused by the mode-amplitude imbalance because the fundamental mode is only involved in the adiabatic polarization rotation. Thermally stable polarization rotation in a broad spectral range beyond the C and L bands is also possible because of the adiabaticity.

In the PDM described above, the spectral band is limited by the asymmetric optical waveguide directional coupler, in which the directional power transfer of the TM-like mode from WG2 to WG1 occurs in a beat period of interference between symmetric and antisymmetric modes in the coupled waveguides. Therefore, the all-adiabatic PDM is desired, in particular, for applications with integrated PDM IQ optical modulators for high-capacity optical networks. All-adiabatic PDMs have also been analyzed, designed, and fabricated on a silicon-photonics platform.[66–69] An all-adiabatic PDM based on silicon rib optical waveguides embedded in silica top/bottom cladding is illustrated in Fig. 4.21(a). The PDM is also designed along with the same design rule as for rib optical waveguides and can be simultaneously fabricated in parallel with the other building blocks on a silicon-photonics platform. Adiabatic mode transfer was established theoretically in coupled tapered optical waveguides.[70] The concept is extended to support the mode transfer from the fundamental TE-like mode TE_0 to the first higher-order TE-like mode TE_1 without optical power leakage to the other modes.[68,71]

Adiabatic mode conversion in the PDM is analyzed computationally by using the full-vectorial BPM, which is predominant in terms of computing speed for a large-scale coupled optical waveguide system.[72] The horizontal

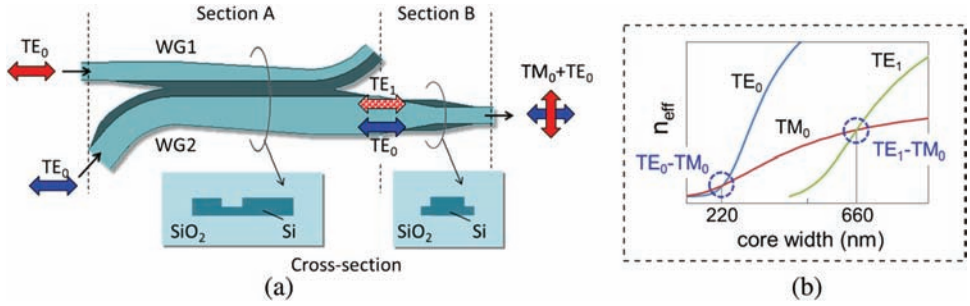

Figure 4.21 All-adiabatic polarization-division multiplexer.

gap between the two parallel ribs is uniformly 300 nm. A light beam in the fundamental TE-like mode is launched to an optical waveguide WG1 of the coupled asymmetric rib optical waveguides in Section A. The mode is transferred to the other optical waveguide WG2 and converted adiabatically in TE_1 mode in WG2 via mode hybridization. The higher-order mode is further converted to the fundamental TM-like mode TM_0 via mode hybridization in a tapered-slab optical waveguide in Section B adiabatically without any optical power transfer to the other modes. High fabrication tolerance is achieved by exploiting TE_1-TM_0 conversion instead of conventional TE_0-TM_0 conversion because the TE_1 mode yields a lower tangential slope and the waveguide is much wider (~660 nm) than for the case of TE_0-TM_0 conversion, as evident in the mode characteristic curves in Fig. 4.21(b). The computational characteristics associated with the sequential mode conversion are presented in Fig. 4.22(a). Another light beam launched

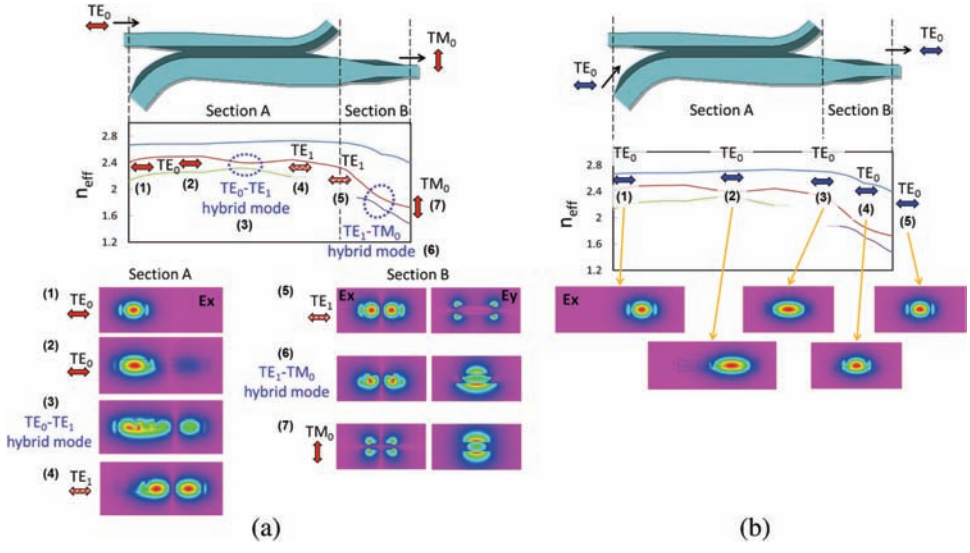

Figure 4.22 Characteristics of the all-adiabatic PDM.

to WG2 in the fundamental TE-like mode is propagated as it is through WG2 Sections A and B, as evident in the characteristics in Fig. 4.22(b). The all-adiabatic PDM is shorter than 400 μm in length. The multiplexed TE-like and TM-like light beams are emitted from the output end of WG2. Electric fields E_x and E_y stand for horizontal and vertical electric-field components in cross-sectional planes.

4.4.4 Other building blocks based on optical waveguides

Inverted nano-taper MFCs such as the suspended coupler described in Chapter 3 are the building blocks essential to low-profile edge coupling to input/output single-mode optical fibers with low coupling loss in broad spectral bands with weak polarization dependence.[73–75] The length of a nano-taper is a few hundred micrometers or longer for the adiabatic expansion of a fundamental-mode beam for high-efficiency fiber coupling. The optical characteristics of the suspended nano-taper MFC, as shown in Fig. 3.22, can be obtained by a computational method such as the full-vectorial BPM or the eigenmode-expansion method.

Optical waveguide bends are crucial to the connection of various building blocks in PICs. In integrated MZ optical modulators, in particular, various types of MZIs cannot be constructed in small footprints without high-index-contrast optical waveguide bends. Significant footprint reduction is realized by using silicon nanowire waveguide bends with a bending radius as short as 5 μm.[76] An equivalent index profile is used to analyze the waveguide bends in intuitive analogy with straight optical waveguides.[53,77] Various theoretical studies have been devoted to reducing optical loss in waveguide bends. Positional offset by the lateral translation of a waveguide bend was proposed and analyzed to reduce optical loss due to mode mismatch at the transition interface between straight and bent optical waveguides.[78] Interference with the cladding mode has been taken into account, and the core location of the waveguide bend has been optimized computationally in a vertical plane perpendicular to the propagation direction of the guided mode in the waveguide bend.[79] Mode mismatches can be eliminated if a mathematical curve called a clothoid curve is accommodated in the design of a waveguide bend because the curvature of the clothoid curve changes linearly from infinity to a smaller radius along the propagation direction. A clothoid-curve waveguide bend was applied to silica planer lightwave circuits, and optical loss reduction was verified.[80] Clothoid-curve waveguide bends have also been designed and fabricated on a silicon-photonics platform.[81]

Computational analysis by the full-vectorial BPM for TE-like fundamental modes generate optical-loss characteristics plotted in Fig. 4.23 for circular and clothoid bends on a silicon-photonics platform.[72] The losses are plotted against the radius of the circle and the minimum radius of the clothoid curve, respectively. Half-circle bends are taken in the analysis for the ease of

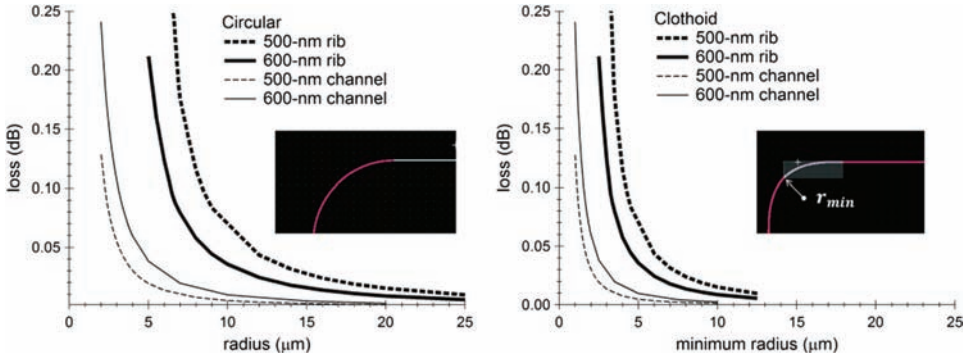

Figure 4.23 Computational optical losses of (a) circular bends and (b) clothoid bends.

comparison with measurement results in the next chapter. For each clothoid bend, a pair of 90-deg bends are aligned and connected in mirror symmetry to form a 180-deg bend free from mode mismatching at the input and output ends. The total losses include mode mismatching and radiation losses. Silicon rib bends yield higher loss than silicon channel bends. Lower optical loss is achieved with the clothoid bends than with the circular bends.

References

1. B. G. Lee, A. V. Rylyakov, W. M. J. Green, S. Assefa, C. W. Baks, R. Rimolo-Donadio, D. M. Kuchta, M. H. Khater, T. Barwicz, C. Reinholm, E. Kiewra, S. M. Shank, C. L. Schow, and Y. A. Vlasov, "Monolithic silicon integration of scaled photonic switch fabrics, CMOS logic, and device driver circuits," *J. Lightwave Technol.* **32**(4), 743–751 (2014).
2. K. Suzuki, G. Cong, K. Tanizawa, S.-H. Kim, K. Ikeda, S. Namiki, and H. Kawashima, "Multiport optical switches integrated on Si photonics platform," *IEICE Electron. Express* **11**(24), 20142011 (2014).
3. S. Mitra and R. J. Sherwood, "Digital ladder networks," *IEEE Trans. Audio and Electroacoustics* **21**(1), 30–36 (1973).
4. A.G. Constantinides, "Design of digital filters from LC ladder networks," *Proc. IEE* **123**(12), 1307–1312 (1976).
5. B. Moslehi, J. W. Goodman, M. Tur, and H. J. Shaw, "Fiber-optic lattice Signal Processing," *Proc. IEEE*. **72**(7), 909–930 (1984).
6. K. Jinguji and M. Kawachi, "Synthesis of coherent two-port lattice-form optical delay-line circuit," *J. Lightwave Technol.* **13**(1), 73–82 (1995).
7. Y. P. Li, C. H. Henry, E. J. Laskowski, C. Y. Mak, and H. H. Yaffe, "Waveguide EDFA gain equalisation filter," *Electron. Lett.* **31**(23), 2005–2006 (1995).
8. G. Lenz and C.K. Madsen, "General optical all-pass filter structures for dispersion control in WDM systems," *J. Lightwave Technol.* **17**(7), 1248–1254 (1999).

9. Z. Lu, Y. Wang, F. Zhang, N. A. F. Jaeger, and L. Chrostowski, "Wideband silicon photonic polarization beamsplitter based on point-symmetric cascaded broadband couplers," *Opt. Express* **23**(23) 29413–29422 (2015).
10. E. Collett, "Field Guide to Polarization," *SPIE Field Guides Vol. FG05*, Ed. J. E. Greivenkamp, SPIE Press, Bellingham, Washington, 12–27 and 75–81 (2005).
11. E. A. J. Marcatili, "Dielectric rectangular waveguide and directional coupler for integrated optics," *Bell System Tech. J.* **48**(7), 2071–2102 (1969).
12. K. Okamoto, *Fundamentals of Optical Waveguides*, 2nd Ed., Academic Press, Burlington, San Diego, 1–12 (2006).
13. G. T. Reed and A. P. Knights, *Silicon Photonics: An Introduction*, John Wiley and Sons, Chichester, UK, 11–36 (2004).
14. M. Born and E. Wolf, *Principles of Optics*, 7th Ed., Cambridge University Press, Cambridge, New York, 38–53 (1999).
15. J. D. Jackson, *Classical Electrodynamics*, 3rd Ed., John Wiley and Sons, Hoboken, NJ, 1–4 (1999).
16. J. Yamauchi, *Propagation Beam Analysis of Optical Waveguides*, 1st Ed., Research Studies Press, Baldock, England, 1–8 (2003).
17. C. H. Henry and B. H. Verbeek, "Solution of the scalar wave equation for arbitrarily shaped dielectric waveguides by two-dimensional Fourier analysis," *J. Lightwave Technol.* **7**(2) 308–313 (1989).
18. J. B. Andersen and V. V. Solodukhov, "Field behavior near a dielectric wedge," *IEEE Trans. Antennas Propagat.* **26**(4), 598–602 (1978).
19. A. S. Sudbø, "Why are accurate computations of mode fields in rectangular dielectric waveguides difficult?," *J. Lightwave Technol.* **10**(4) 418–419 (1992).
20. K. S. Chang, "Review of numerical and approximate methods for the modal analysis of general optical dielectric waveguides," *Opt. Quantum Electron*, **26**(3), S113–S134 (1994).
21. R. Scarmozzino, "Numerical techniques for modeling guided-wave photonic devices," *IEEE J. Sel. Top. Quantum Electron.* **6**(1), 150–162 (2000).
22. R. Mittra, Y.-L. Hou, and V. Jamnejad, "Analysis of open dielectric waveguides using mode-matching technique and variational methods," *IEEE Trans. Microwave Theory Tech.* **28**(1), 36–43 (1980).
23. M. Koshiba and M. Suzuki, "Microwave network analysis of dielectric waveguides for millimeter waves made of dilectric strip and planar dielectric layer," *Trans. IECE Japan* **E63**(5), 344–350 (1980).
24. M. Koshiba and M. Suzuki, "Equivalent network analysis of dielectric thin-film waveguides with trapezoidal cross-section," *Electron. Lett.* **17**(8), 283–285 (1981).

25. S.-T. Peng and A. A. Oliner, "Guidance and leakage properties of a class of open dielectric waveguides: Part I—mathematical formulations," *IEEE Trans. Microwave Theory Tech.* **29**(9), 843–855 (1981).
26. N. Dagli, "Equivalent circuit representation of open guided-wave structures," *IEEE J. Quantum Electron.* **26**(1), 98–108 (1990).
27. A. S. Sudbø, "Film mode matching: a versatile numerical method for vector mode field calculations in dielectric waveguides," *Pure Appl. Opt.* **2**(3), 211–233 (1993).
28. https://www.photond.com/products/fimmwave.htm.
29. Z. J. Csendes and P. Silvester, "Numerical solution of dielectric loaded waveguides: I—finite element analysis," *IEEE Trans. Microwave Theory Techn.* **18**(12), 1124–1131 (1970).
30. M. Ohtaka, M. Matsuhara, and N. Kumagai, "Analysis of the guided modes in slab-coupled waveguides using a variational method," *IEEE J. Quantum Electron.* **12**(7), 378–382 (1976); M Ohtaka, "Correction to "Analysis of the guided modes in slab-coupled waveguides using a variational method"," *IEEE J. Quantum Electron*. **13**(9), 795–795 (1977).
31. C. Yeh, K. Ha, S. B. Dong, and W. P. Brown, "Single-mode optical waveguides," *Appl. Opt.* **18**(10), 1490–1504 (1979).
32. T. Angkaew, M. Matsuhara, and N. Kumagai, "Finite-element analysis of waveguide modes: A novel approach that eliminates spurious modes," *IEEE Trans. Microwave Theory Tech.* **35**(2), 117–855 (1987).
33. S.-J. Chung and C. H. Chen, "Partial variational principle for electromagnetic field problems: Theory and applications," *IEEE Trans. Microwave Theory Tech.* **36**(3), 473–479 (1988).
34. G. Lamouche and S. I. Najafi, "Finite- element analysis of ion-exchanged channel waveguides," *Proc. SPIE* **1128**, 124–131 (1989).
35. M. Koshiba and K. Inoue, "Simple and efficient finite-element analysis of microwave and optical waveguides," *IEEE Trans. Microwave Theory Tech.* **40**(2), 371–377 (1992).
36. T. Young, "Finite element modeling of a polarization independent optical amplifier," *J. Lightwave Technol.* **10**(5) 626–633 (1992).
37. Y. Tsuji and M. Koshiba, "Finite element method using port truncation by perfectly matched layer boundary conditions for optical waveguide discontinuity problems," *J. Lightwave Technol.* **20**(3) 463–468 (2002).
38. S. S. A. Obayya, N. Somasiri, B. M. A. Rahman, and K. T. V. Grattan, "Full vectorial finite element modeling of novel polarization rotators," *Opt. Quantum Electron*, **35**(4), 297–312 (2003).
39. K. Okamoto, *Fundamentals of Optical Waveguides*, 2nd Ed., Academic Press, Burlington, San Diego, 261–328 (2006).
40. G. Sztefka and H. P. Nolting, "Bidirectional eigenmode propagation for large refractive index steps," *IEEE Photon. Technol. Lett.* **5**(5), 554–557 (1993).

41. J. Čtyroký, S. Helfert, and R. Pregla, "Analysis of a deep waveguide Bragg grating," *Opt. Quantum Electron*, **30**(5), 343–358 (1998).
42. D.M.H. Leung, X.B. Kan, B.M.A. Rahman, N. Kejalakshmy, and K.T. V. Grattan, "Optimizing the power confinement in silicon slot waveguides by use of finite element method," *Proc. SPIE* **8307**, 83071A-1–83071A-6 (2011).
43. D. F. G. Gallagher and T. P. Felici, "Eingenmode expansion methods for simulation of optical propagation in photonics: pros and cons," *Proc. SPIE* **4987**, 69–82 (2003).
44. O. V. Ivanova, M. Hammer, R. Stoffer, and E. van Groesen, "A variational mode expansion mode solver," *Opt. Quantum Electron*, **39**(10), 849–864 (2007).
45. J. Yamauchi, *Propagation Beam Analysis of Optical Waveguides*, 1st Ed., Research Studies Press, Baldock, England, 9–202 (2003).
46. H. Xie, W. Lu, and Y. Y. Lu, "Complex modes and instability of full-vectorial beam propagation methods," *Opt. Lett.* **36**(13), 2474–2476 (2011).
47. A. Taflove and S. C. Hagness, *Computational Electrodynamics: The Finite-Difference Time-Domain Method*, 3rd. Ed., Artech House, Boston, London, 3–79 (2005).
48. W. H. Press, S. A. Teukolsky, W. T. Vetterling, and B. P. Flannery, *Numerical Recipes, The Art of Scientific Computing*, 3rd Ed., Cambridge University Press, Cambridge, New York, 196–199 (2007).
49. A. F. Milton and W. K. Burns, "Mode coupling in optical waveguide horns," *IEEE J. Quantum Electron.* **13**(10), 828–835 (1977).
50. R. Ulrich and T. Kamiya, "Resolution of self-images in planar optical waveguides," *J. Opt. Soc. Am.* **68**(5), 583–592 (1978).
51. M. Bachmann, P. A. Besse, and H. Melchior, "General self-imaging properties in N x N multimode interference couplers including phase relations," *Appl. Opt.* **33**(18), 3905–3911 (1994).
52. L. B. Soldano and E. C. M. Pennings, "Optical multi-mode interference devices based on self-imaging: Principles and applications," *J. Lightwave Technol.* **13**(4), 615–627 (1995).
53. A. Liu, N. Izhaky, and L. Liao, "Passive silicon photonic devices," in *Silicon Photonics: the State of the Art*, G. T. Reed, Ed, John Wiley & Sons, Chichester, England, 229–267 (2008).
54. K. Utaka, "Multi-mode interference devices," *Encyclopedic Handbook of Integrated Optics*, Eds. K. Iga and Y. Kokubun, CRC Press, Boca Raton, 151–163 (2006).
55. https://www.photond.com/products/fimmprop.htm.
56. K. Ogawa, K. Goi, A. Oka, Y. Mashiko, T.-Y. Liow, X. Tu, G.-Q. Lo, D.-L. Kwong, S. T. Lim, M. J. Sun, and C. E. Png, "Design and characterisation of high-speed monolithic silicon modulators for digital coherent communication," *Proc. SPIE* **9367**, 93670C-1–93670C-8 (2015).

57. K. Goi, A. Oka, H. Kusaka, K. Ogawa, T.-Y. Liow, X. Tu, G.-Q. Lo, and D.-L. Kwong, "Low-loss partial rib polarization rotator consisting only of silicon core and silica cladding," *Opt. Lett.* **40**(7), 1410–1413 (2015).
58. H. Fukuda, K. Yamada, T. Tsuchizawa, T. Watanabe, H. Shinojima, and S. Itabashi, "Ultrasmall polarization splitter based on silicon wire waveguides," *Opt. Express* **14**(25), 12401–12408 (2006).
59. H. Deng, D. O. Yevick, C. Brooks, and P. E. Jessop, "Design Rules for Slanted-Angle Polarization Rotators," *J. Lightwave. Technol.* **23**(1), 432–445 (2005).
60. H. Fukuda, K. Yamada, T. Tsuchizawa, T. Watanabe, H. Shinojima, and S. Itabashi, "Polarization rotator based on silicon wire waveguides," *Opt. Express* **16**(4), 2628–2635 (2008).
61. Z. Wang and D Dai, "Ultrasmall Si-nanowire-based polarization rotator," *J. Opt. Soc. Am. B* **25**(5), 747–753 (2008).
62. M. R. Watts and H. A. Haus, "Integrated mode-evolution-based polarization rotators," *Opt. Lett.* **30**(2), 138–140 (2005).
63. J. Zhang, M. Yu, G.-Q. Lo, and D.-L. Kwong, "Silicon-waveguide-based mode evolution polarization rotator," *IEEE J. Sel. Top. Quantum Electron.* **16**(1), 53–60 (2010).
64. L. Chen, C. R. Doerr, and Y.-K. Chen, "Compact polarization rotator on silicon for polarization-diversified circuits," *Opt. Lett.* **36**(4), 469–471 (2011).
65. H. Zhang, S. Das, Y. Huang, C. Li, and S. Chen, "Efficient and broadband polarization rotator using horizontal slot waveguide for silicon photonics," *Appl. Phys. Lett.* **101**(02), 021105-1–021105-4 (2012).
66. D. Dai and J. E. Bowers, "Novel concept for ultracompact polarization splitter-rotator based on silicon nanowires," *Opt. Express* **19**(11), 10940–10949 (2011).
67. W. D. Sacher, T. Barwicz, B. J. F. Taylor, and J. K. S. Poon, "Polarization rotator-splitters in standard active silicon photonics platforms," *Opt. Express* **22**(4), 3777–3786 (2014).
68. A. Oka, K. Goi, H. Kusaka, K. Ogawa, T.-Y. Liow, X. Tu, G.-Q. Lo, and D.-L. Kwong, "Low-loss all-adiabatic silicon-waveguide polarization-division multiplexer in C and L bands," *2014 OptoElectronics and Communication Conference and Australian Conference on Optical Fibre Technology (OECC/ACOFT)*, 570–572 (2014).
69. K. Tan, Y. Huang, G.-Q. Lo, C. Yu, and C. Lee, "Ultra-broadband fabrication-tolerant polarization splitter and rotator," *Optical Fiber Communications Conference and Exhibition (OFC)*, Th1G.7 (2017).
70. Y. Shani, Ch. H. Henry, R. C. Kistler, R. F. Kazarinov, and K. J. Orlowsky, "Integrated optic adiabatic devices on silicon," *IEEE J. Quantum Electron.* **27**(3), 556–566 (1991).
71. N. Riesen and J. D. Love, "Tapered velocity mode-selective couplers," *J. Lightwave Technol.* **32**(13), 2163–2169 (2013).

72. https://optics.synopsys.com/rsoft/rsoft-passive-device-beamprop.html
73. T. Shoji, T. Tsuchizawa, T. Watanabe, K. Yamada, and H. Morita, "Low loss mode size converter from 0.3 μm square Si wire waveguides to singlemode fibres," *Electron. Lett.* **38**(25), 1669–1670 (2002).
74. Q. Fang, T.-Y. Liow, J. F. Song, C. W. Tan, M. Yu, G.-Q. Lo, and D.-L. Kwong, "Suspended optical fiber-to-waveguide mode size converter for silicon photonics," *Opt. Express* **18**(8), 7763–7769 (2010).
75. B. Ben Bakir, A. Vazquez de Gyves, R. Orobtchouk, P. Lyan, C. Porzier, A. Roman, and J-M. Fedeli, "Low loss (<1dB) and polarization-insensitive edge fiber couplers fabricated on 200 mm silicon-on-insulator wafers," *IEEE Photon. Technol. Lett.* **22**(11), 739–741 (2010).
76. Y. A. Vlasov and S. J. McNab, "Losses in single-mode silicon-on-insulator strip waveguides and bends," *Opt. Express* **12**(8), 1622–1631 (2004).
77. W. W. Lui, C.-L. Xu, T. Hirono, K. Yokoyama, and W.-P. Huang, "Full-vectorial wave propagation in semiconductor optical bending waveguides and equivalent straight waveguide approximations," *J. Lightwave Technol.* **16**(5), 910–914 (1998).
78. E.-G. Neumann, "Curved dielectric optical waveguides with reduced transition losses," *IEE Proc. Pt. H* **129**(5), 278–280 (1982).
79. Y. Nito, B. Yatabe, J. Yamauchi, and H. Nakano, "Reduction in bend losses of a buried waveguide on a silicon substrate by adjusting the core location," *J. Lightwave Technol.* **34**(4), 1344–1349 (2016).
80. T. Kominato, Y. Hida, M. Itoh, H. Takahashi, S. Sohma, T. Kitoh, and Y. Hibino, "Extremely low-loss (0.3 dB/m) and long silica-based waveguides with large width and clothoid curve connection," *30th European Conference on Optical Communication (ECOC)*, TuI.4.3 (2004).
81. M. Cherchi, S. Ylinen, M. Harjanne, M. Kapulainen, and T. Aalto, "Dramatic size reduction of waveguide bends on a micron-scale silicon photonic platform," *Opt. Express* **21**(15), 17814–17823 (2013).

Chapter 5
Electronic and Opto-electronic Properties of High-Speed Phase Shifters

High-speed phase shifters consisting of electro-refraction optical waveguides are the most essential functional blocks of integrated MZ optical modulators used in high-capacity optical networks. This chapter firstly deals with the physics of phase modulation and related matters relevant to high-speed phase shifters. It is stated that free-carrier plasma refraction is most suitable to phase shifters used for quasi-zero-chirp optical modulation in broad spectral ranges without temperature regulation. This chapter focuses on high-speed carrier-depletion phase shifters based on free-carrier plasma refraction. The plasma-refraction phase shifters are classified primarily into two types, lateral and vertical, according to the configuration of the PN junction. The last part of this chapter presents the design and modeling of the carrier-depletion PN-junction phase shifters in two schemes. The first scheme is described as a semi-analytical method comprising the optical simulation of the mode field in a phase-shifter waveguide (described in Chapter 4) and the analytical modeling/calculation of the plasma refraction using the abrupt PN-junction model and mode-field confinement factor. The semi-analytical model serves as a versatile tool for understanding the operational principles of PN-junction phase shifters and proofing new design concepts of phase shifters without time-consuming, massive computing tasks. The other scheme is a computational method performed for the accurate design and modeling of phase shifters on a silicon-photonics platform after the proof of concept is completed.

5.1 Physics in Phase Modulation

5.1.1 Pockels effect

The Pockels effect has been used most extensively in the commercialized optical modulators made of LN. The performance of silicon-based optical

modulators are compared in the following chapters. The electro-optic effect is reviewed first in Table 2.1. The displacement of ionic atoms constituting the unit cells of a non-centrosymmetric crystal under an external electric field causes microscopic changes in its crystallographic structure and thus a change in the refractive index of the crystal. This physical process is known as the Pockels effect, linear electro-optic effect.[1] The linear electro-optic effect is insensitive to temperature and occurs in a broad spectral range extending over the visible and near-infrared bands. A single-mode electro-optic waveguide is used to obtain a unique phase shift in response to an input electrical signal. A phase shift in the linear electro-optic effect is proportional to the input electric field. Therefore, the linear electro-optic coefficient has a dimension that is the inverse of the electric field and is very often scaled to the unit of pm/V. High-speed phase modulation beyond Tbaud is possible in principle because the frequency response of the electro-optic effect is limited by the vibration frequency of optical phonons in the infrared spectra around ~10 THz for most crystalline solid-state materials.[2] Traveling-wave electrodes must be integrated, of course, to avoid the electrical circuit limitation by RC (resistance R times capacitance C) and to realize phase matching between a guided lightwave and a high-frequency electrical signal.[3]

Single-mode optical waveguides made of crystalline LN have been extensively used to fabricate high-speed optical modulators in optical-fiber telecommunications.[4–6] The most fundamental FOM to evaluate optical modulators is the inverse of $V_\pi \cdot \ell_\pi$, where V_π is a voltage at a phase shift of π, and ℓ_π is the phase-shifter length required to generate V_π. A higher figure of $1/(V_\pi \cdot \ell_\pi)$ indicates higher efficiency in optical modulation. For LN optical modulators, the $V_\pi \cdot \ell_\pi$ was reported as 10 V·cm,[7] which implies that V_π is 3.3 or 10 V with a physical phase-shifter length $\ell = 3$ or 1 cm, respectively. With high-index-contrast LN optical waveguides, $V_\pi \cdot \ell_\pi$ was lowered to 4 V · cm: V_π is 4 V with a physical phase-shifter length $\ell = 1$ cm.[8] A high-index-contrast optical waveguide is essential to reduce the footprint of an optical modulator.

Electro-optic polymers have been also used for phase-shifter media in high-speed optical modulators. Polymers with side chains containing polarizable nonlinear optical molecules were developed, and linear electro-optic waveguide modulators using electro-optic polymer phase shifters were fabricated.[9] Electro-optic polymers and cladding layers were deposited on silicon wafers by spin coating, and a poling electric field was applied to the electro-optic polymers to induce a permanent electric dipole aligned along the electric field and break centrosymmetry. A traveling-wave electro-optic polymer MZ intensity modulator operating beyond 40 GHz was demonstrated.[10] A π-shift voltage and the most fundamental FOM as low as 0.8 V and 2.2 V·cm, respectively, were reported with an electro-optic coefficient of 58 pm/V for a guest–host polymer electro-optic waveguide at a datacom

wavelength of 1318 nm.[11] Further enhancement of the electro-optic coefficient up to 170 pm/V, which is six times larger than that of $LiNbO_3$ was achieved at a telecom wavelength of 1550 nm by using a suitable combination of cross-linked polymers and electro-optic chromophores[12] (Ref. 12 cites some of the other references related to the development of electro-optic polymers).

The material system of electro-optic polymers was incorporated into a silicon-photonics waveguide system to form silicon–organic hybrid optical modulators.[13] Fabrication processes, such as spin coating and poling of electro-optic polymers, which are not fully compatible with the current CMOS-based silicon-photonics fabrication processes, require further investigation and study to be accommodated with a silicon-photonics platform, and long-term stability and reliability must be ensured for mass production and commercialization.[14] Electro-optic polymers were deposited and poled in the 120-nm center gaps of silicon slot optical waveguides in IQ MZIs for high-speed, low-voltage modulation in advanced modulation formats. Both the optical mode field of a guided lightwave in TE mode and the electric field of an input RF electrical signal are strongly localized in the center gap of the silicon slot optical waveguide in a traveling-wave silicon MZ optical modulator, as shown in Fig. 5.1, whereby efficient phase modulation is realized.[15] High-speed optical modulation with a V_π and $V_\pi \cdot \ell$ as low as 1.6 V and 1 V·cm, respectively, was reported in 16 QAM at 100 Gbaud.[14]

5.1.2 Intraband free-carrier plasma dispersion and Drude model

The Pockels effect does not appear in centrosymmetric materials such as crystalline silicon and germanium. Instead, intraband free-carrier plasma dispersion has been exploited extensively for high-speed optical modulators on a silicon-photonics platform. Refractive-index changes and thus phase modulation are generated in the interaction of a guided lightwave with individual conduction-band electrons and valence-band holes distributed in a phase-shifter

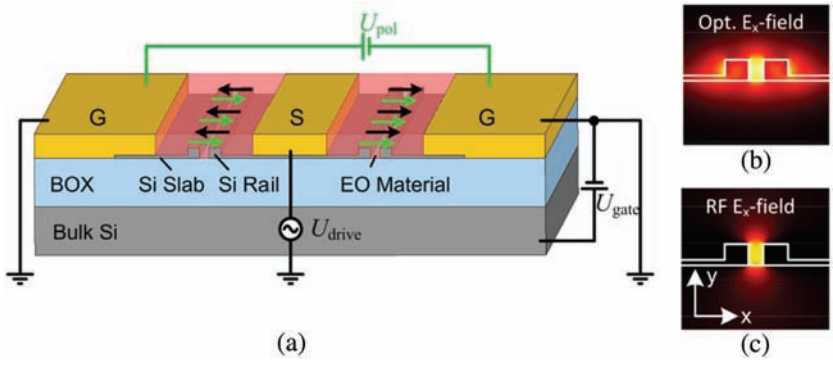

Figure 5.1 Electro-optic waveguide with (a) traveling-wave electrodes, (b) optical mode field, and (c) RF electric field in a silicon–organic-hybrid optical modulator (after Ref. 15).

optical waveguide. A resonant optical dipole transition in electron–hole states is not associated with the free-carrier plasma dispersion, and thus phase modulation in broad spectral bands over a wide temperature range is obtained. However, the phase modulation efficiency is lower than that of interband resonant dipole transition processes. This downside can be overcome with design optimization to maximize the spatial overlap of the optical mode field with an active region where the electron and hole densities change as elaborated in Section 5.2. Here, intraband free-carrier plasma dispersion is reviewed from a microscopic point of view.

Free-carrier plasma dispersion is the real part of the optical response function of charged individual free carriers (electrons or holes) interacting with the electric field of a guided lightwave.[16–24] The imaginary part of the optical response function is free-carrier absorption, which has been extensively studied in crystalline semiconductors.[25–38] The kinetic energy and velocity of the charged individual free carriers are depicted schematically against time t in Fig. 5.2. The velocity increases linearly while the kinetic energy increases quadratically under a constant magnitude of the optical field applied to the free carriers. The free-carrier plasma dispersion is suitable for optical modulation in a broad spectral range such as the C and L bands in optical-fiber communications because the interaction is non-resonant and occurs irrespective of the wavelength of the electric field. Unbound individual carriers are involved in the interaction and decrease the refractive index with respect to an increase in carrier concentration, similar to electrons in metals.[39,40]

In the case of Fig. 5.2(a), where no scattering, or no dephasing in other words, occurs, the free carriers are accelerated coherently without disruption in oscillation according to the optical field, and the energy of the optical field is transferred efficiently to the free carriers. The optical-to-electronic energy transfer is inefficient, on the other hand, in the case of Fig. 5.2(b), where the

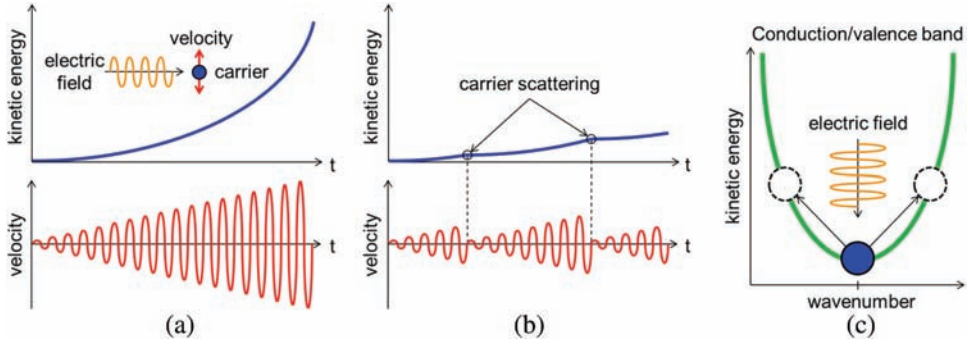

Figure 5.2 Intraband free-carrier interation with an optical field: (a) Time evolution of the kinetic energy and velocity of charged free carriers (electrons or holes) interacting with the electric field in the case of carrier transport with no carrier scattering. (b) The same scenario with carrier scattering. (c) Intraband transition in the electric field.

free carriers are not accelerated coherently due to dephasing caused by carrier scattering. In the electronic-band picture in Fig. 5.2(c), free electrons in a conduction band or free holes in a valence band transfer to higher-wavenumber states within the same band in the electric field of the guided lightwave.[41,42] A large refractive-index change and a high optical absorption are generated if the free carriers yield high mobility according to the classical model of free-carrier transport.[39–42] Electronic band engineering for higher carrier mobility is an essential approach for a lower V_π in silicon-based optical modulators.[43]

The theory of intraband free-carrier plasma dispersion was presented in the framework of the classical Drude model for free carriers.[39,44] A description of the model starts with the following equation of motion defined in Drude's model:

$$\frac{dv}{dt} + \frac{1}{\tau(N)} v = \frac{eE_0}{m^*} e^{-i\omega t} \tag{5.1}$$

in conjunction with the average carrier scattering time τ as a function of carrier density N. In Eq. (5.1), m^* and q denote the carrier effective mass and carrier charge, respectively. Carrier velocity v includes the oscillating term $e^{-i\omega t}$ at frequency ω of the incident lightwave, and the solution of Eq. (5.1) can be expressed as

$$v = v(\omega) e^{-i\omega t}. \tag{5.2}$$

Substituting Eq. (5.2) for v in Eq. (5.1) produces the following solution:

$$v(\omega) = \frac{q\tau(N)}{m^*} \frac{1}{1 - i\omega\tau(N)} E_0 \tag{5.3}$$

for the velocity term $v(\omega)$. The velocity term of Eq. (5.3) leads to the carrier mobility μ as a function of N in the following form:

$$\mu(N) = \frac{v(\omega)}{E_0} = \frac{q\tau(N)}{m^*} \frac{1}{1 - i\omega\tau(N)}. \tag{5.4}$$

After substituting Eq. (5.4) for the carrier mobility, the conductivity $\sigma(\omega)$ is written as

$$\sigma(\omega) = Nq\mu(N) = \frac{Nq^2\tau(N)}{m^*} \frac{1}{1 - i\omega\tau(N)}. \tag{5.5}$$

The contribution of free carriers to the frequency-dependent term $\Delta\varepsilon(\omega)$ of the dielectric permittivity coefficient can be derived from the following equation:

$$\Delta\varepsilon(\omega) = \frac{4\pi i\sigma(\omega)}{\omega}. \tag{5.6}$$

The total dielectric permittivity coefficient $\varepsilon(\omega)$ equals the square of the complex refractive index with the real part $n_r(\omega)$ and imaginary part $n_i(\omega)$, namely,

$$\varepsilon(\omega) = \varepsilon_B + \Delta\varepsilon(\omega) = [n_r(\omega) + in_i(\omega)]^2. \tag{5.7}$$

Here, ε_B is the background dielectric constant, which is assumed to be constant in this model. Substituting Eqs. (5.5) and (5.6) for $\sigma(\omega)$ and $\Delta\varepsilon(\omega)$, respectively, produces simultaneously the real part as

$$n_r(\omega) = \sqrt{\frac{A + \sqrt{A^2 + B^2}}{2}}, \tag{5.8}$$

and the imaginary part, which is converted to the absorption coefficient $\alpha(\omega)$, as

$$\alpha(\omega) = 2\frac{\omega}{c}n_i(\omega) = 2\frac{\omega}{c}\sqrt{\frac{-A + \sqrt{A^2 + B^2}}{2}}, \tag{5.9}$$

where terms A and B have the following forms:

$$A = [n_r(\omega)]^2 - [n_i(\omega)]^2 = \varepsilon_B - \frac{4\pi Nq^2}{m^*}\frac{\tau^2(N)}{1 + \omega^2 r^2(N)} \tag{5.10}$$

and

$$B = 2n_r(\omega)n_i(\omega) = \frac{4\pi Nq^2}{m^*}\frac{\tau(N)}{\omega}\frac{1}{1 + \omega^2 r^2(N)}, \tag{5.11}$$

respectively. In general, the term $\alpha(\omega)$ should denote optical loss or attenuation, which includes not only optical absorption but also optical reflection. Optical reflection, however, is not substantial in Drude's model, and the coefficient $\alpha(\omega)$ can be regarded as the optical absorption coefficient due to free carriers so long as the optical frequency is far beyond the plasma frequency, as mentioned below.

Free-carrier plasma dispersion and free-carrier absorption can be characterized theoretically by computing the electron and hole terms of the optical constants of n_r and α, respectively, in Eqs. (5.8) and (5.9) once mathematical representations of the scattering time are given. Mathematical representations of electron and hole mobilities as functions of the carrier density N are obtained by curve fitting to the experimental electron and hole

mobilities in silicon crystals doped with N-type and P-type impurities in varous doping concentrations.[45] Ionized impurity scattering and carrier–carrier scattering cause dopant-concentration dependence of the carrier mobilities. Free-carrier refraction terms Δn_e and Δn_h for electrons and holes, respectively, exhibit negative change with the electron and hole densities, similar to the characteristics of electrons in metals. The absolute values of the free-carrier refraction terms are plotted in Fig. 5.3. Absorption coefficient terms $\Delta\alpha_e$ and $\Delta\alpha_h$ for electrons and holes, respectively, are plotted in Fig. 5.4. In the computation, the electron- and hole-conductivity effective masses reported in the literature are used.[45] The empirical formulae presented below are also plotted in the graphs.

Experimentally, on the other hand, the optical absorption spectra of doped crystalline semiconductors were reported in early experimental studies. Characterization of free-carrier absorption and free-carrier plasma dispersion using the experimental optical-absorption spectra was performed in spectral analysis in conjunction with Kramers–Kronig transformation.[16,24,46,47] Empirical formulae were thus derived for dopant-concentration dependences of the refractive index and optical-absorption coefficient Δn and $\Delta\alpha$ after spectral analysis. The latest study on silicon provided the following empirical formulae at a wavelength of 1550 nm (an optical frequency of 193.4 THz):[46]

$$\Delta n = -5.40 \times 10^{-22} N_e^{1.011} - 1.53 \times 10^{-18} N_h^{0.838} \tag{5.12}$$

and

$$\Delta\alpha = 8.88 \times 10^{-21} N_e^{1.167} + 5.84 \times 10^{-20} N_h^{1.109}, \tag{5.13}$$

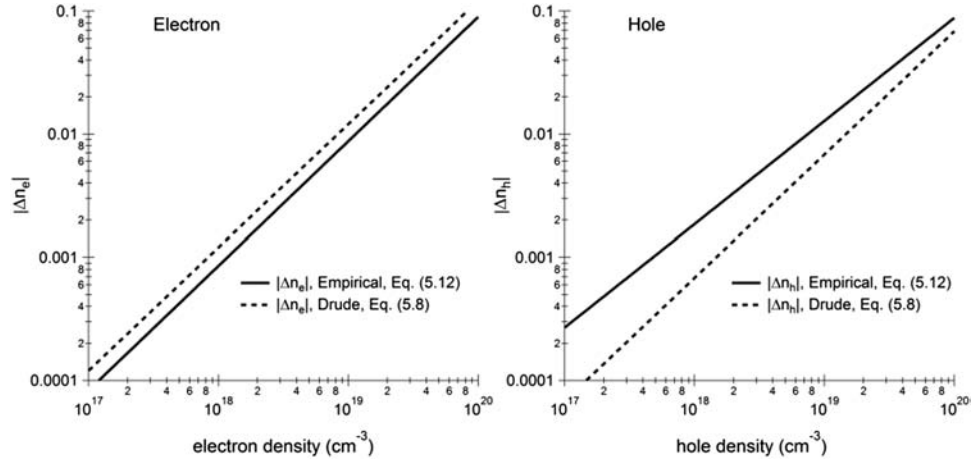

Figure 5.3 Free-carrier refraction terms in absolute value vs. carrier densities.

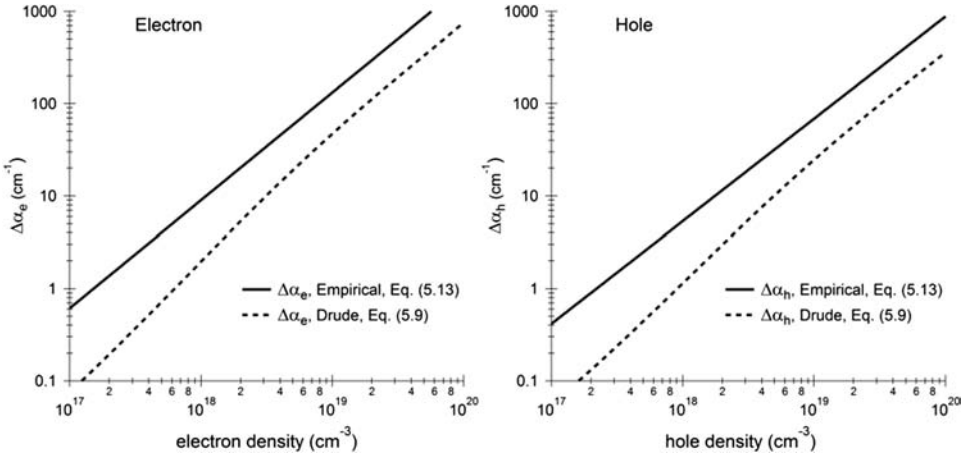

Figure 5.4 Free-carrier absorption coefficients vs. carrier densities.

where N_e and N_h denote the electron and hole densities, respectively. These empirical formulae, which are substantially valid in the entire range of the C band, are also plotted in Figs. 5.3 and 5.4 for comparison with the theoretical curves based on the Drude model.

There are discrepancies between the empirical and theoretical characteristics. The discrepancies are more significant at lower electron and hole densities. The average scattering time in the Drude model implies scattering events occur frequently in carrier transport. Time evolution in the carrier–light interaction shown in Fig. 5.2(b) is more valid than the no-scattering limit in Fig. 5.2(a), whereas the latter scheme is appropriate at lower electron and hole densities of 10^{18} cm^{-3}. Therefore, a more efficient energy transfer from the incident lightwave to electrons and holes will be achieved at the lower electron and hole densities, where $\omega\tau \gg 1$, as mentioned below. In the low-scattering regime, carrier scattering events are not regarded as a continuous flow but as a discrete stochastic process. Theoretical modeling and analysis including ballistic carrier transport will be necessary to achieve better agreement with the experimental characteristics in free-carrier plasma dispersion and absorption.[48,49] High-index-contrast optical waveguides, such as a silicon optical waveguide, has a nanometer-scale core dimension, e.g., 500 nm wide and 220 nm high, as described in Chapter 4. The optical power density in the optical waveguide is 10 MW/cm^2 for an input optical power of 1 mW (0 dBm). The optical power density leads to an electric field of 17 KV/cm. At a wavelength of 1550 nm (an optical frequency of 195.7 THz), for example, individual electrons and holes are accelerated under the high electric field in a time period as short as 5.2 fs, thereby easily reaching a ballistic transport regime.[50] Further discussion of modeling analysis, including ballistic carrier transport, is left for future theoretical study, and the empirical

formulae are used for the modeling and analysis of high-speed phase shifters based on the free-carrier effect throughout this book.

Note that doped semiconductors behave not as metallic materials but rather as dielectric materials and thus can be utilized as base materials for the fabrication of dielectric optical waveguides comprising high-speed phase shifters, even though the carriers exhibit optical properties similar to electrons in metals. For verification, refer to plasma frequency ω_p, including carrier scattering, which is written as[39]

$$\omega_p^2 = \frac{4\pi N q^2}{m^* \varepsilon_B} - \frac{1}{\tau^2}. \tag{5.14}$$

Scattering events of individual carriers cause dephasing of the collective plasma oscillation. Therefore, the effective density of carriers involved in plasma oscillation is reduced. For doped semiconductors, optical frequency ω is still higher than the plasma frequency, and thus optical waveguides made of these materials behave substantially like dielectric waveguides even with a carrier density as high as $\sim 10^{19}$ cm^{-3}. The plasma frequency and $\omega\tau$-product of the optical frequency and carrier scattering time are listed in Table 5.1 for crystalline silicon, which has an electron conductivity effective mass of $0.260m_0$ for m^* and a refractive index of 3.48 for $\sqrt{\varepsilon_0}$ in Eq. (5.14) at a wavelength of 1532 nm (an optical frequency of 195.7 THz).[42,51,52] For an input RF electrical signal, the resonance with plasma oscillation is regarded as the energy dissipation of the input electrical signal due to relaxation oscillation; therefore, the plasma frequency limits the speed of optical modulation based on carrier-density modulation.[53] The frequency limit of the optical modulation will go beyond 1 THz according to the plasma frequency in Table 5.1. Product $\omega\tau \gg 1$ implies a carrier-scattering event occurs after several periods of lightwave oscillation, and carrier scattering should be treated as discrete processes.

5.1.3 Interband dipole transition processes

Resonant interband dipole transition processes allow high-efficiency optical modulation with significant changes in optical constants in electro-refraction and electro-absorption in optical spectra near the resonance wavelengths of

Table 5.1 Plasma frequency ω_p and frequency-time product $\omega\tau$ for carrier density N in crystalline silicon.

N	ω_p	$\omega\tau$
1.0×10^{17} cm^{-3}	3.6 THz	20.8
1.0×10^{18} cm^{-3}	20.3 THz	7.98
1.0×10^{19} cm^{-3}	81.5 THz	3.31
1.0×10^{20} cm^{-3}	304.3 THz	2.11

the dipole transition processes under electric bias modulation. Among these, the quantum-confined Stark effect (QCSE) of a 2D exciton in a semiconductor QW has been exploited extensively in high-speed optical modulators on integrated photonics platforms, as described in Chapter 2. Electrons in the conduction band and holes in the valence band are confined in very thin layers of QWs (e.g., 10 nm thick) in semiconductor hetorostructures and obey 2D translational motion.[54] Ground-state free-electron and free-hole wavefunctions in an exemplary model of QWs with and without electric bias voltage are depicted in Fig. 5.5. The wavefunctions drawn in bold lines are computational solutions of the Schrödinger equation by Numerov's method.[55,56] Potential diagrams of the QW (solid lines) and ground-state energy levels for the electron and hole (dashed lines) are also displayed. In a biased QW, the ground-state energy levels of the electron and hole shift to lower energies than in an unbiased QW, and a lower wavelength shift, i.e., red shift, of the band edge of an optical dipole transition is observed in the optical absorption and refraction spectra of the biased QWs. The oscillator strength of the optical dipole transition is decreased due to spatial separation between the electron and hole wavefunctions.

Two-dimensional electron–hole pairs form QW excitons, which exhibit hydrogen-like bound energy levels below the electronic band edge of 2D free electrons and holes in ground states. Sharp dipole-transition peaks associated with hydrogenic energy levels appear below the band edge due to a ground-state free electron and free hole in the optical absorption spectra.[54,57] Excitons in bulk insulators and semiconductors were studied extensively in theoretical and experimental solid state physics.[58–64] The theoretical framework of the excitons was extended to describe the linear and nonlinear optical properties of 2D excitons in QWs.[65] In a biased QW, the ground-state energy levels of the electron and hole shift to lower energies than in unbiased QW,

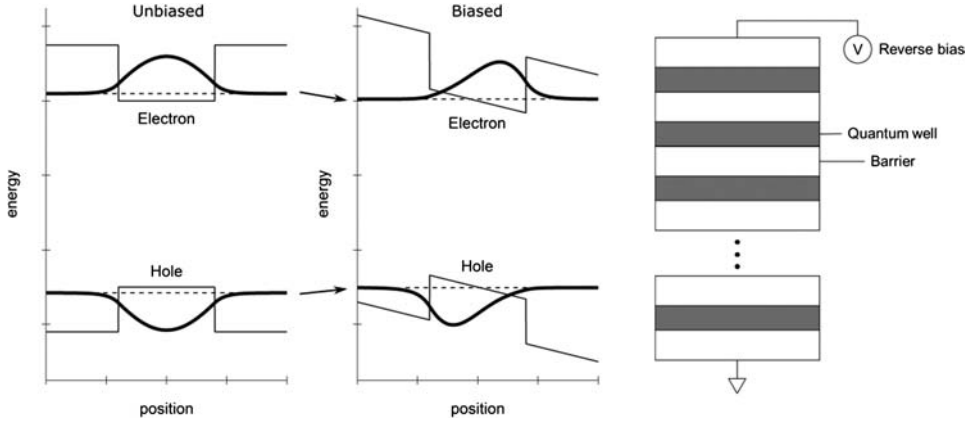

Figure 5.5 Solutions by Numerov's method for electron and hole wavefunctions in a model QW potential without and with electric bias.

and a red shift of the electronic band edge is observed. Therefore, a red shift is induced for the optical absorption peak of the QW exciton with a higher electric bias, reported as the QCSE.[65,66] The intensity of an incident lightwave can be modulated via the QCSE with an electric bias signal at a wavelength below the optical absorption peak of an unbiased QW exciton. Electro-absorption optical intensity modulators based on the QCSE were designed, fabricated, and characterized.[67,68] Refractive index modulation is also produced by the QCSE via the Kramers–Kronig relationship, and an electro-refraction optical phase modulator based on the QCSE was demonstrated.[69–71]

Spectral characteristics of electro-absorption and electro-refraction in the QCSE are described on the basis of optical absorption and refraction spectra shown in Fig. 5.6. Two QW-exciton peaks, which are associated with a heavy-hole exciton (hh-ex) and light-hole exciton (lh-ex), respectively, are observed in the optical absorption spectra.[54] The absorption spectrum in an unbiased QW was obtained by curve fitting with the experimental absorption spectrum of 7-nm $In_{0.53}Ga_{0.47}As/InP$ QWs at room temperature.[72] The other absorption spectrum in a biased QW was then produced by assuming a red shift and line-shape broadening of the QW exciton peaks under electric bias according to the characteristics of the QCSE.[65,66,73] The absorption intensity decreases under electric bias because of a reduction in the oscillator strength, as mentioned above. The linewidth of the exciton absorption is broadened under electric bias due to the field-induced dissociation and resultant lifetime shortening of the QW exciton. At a wavelength of 1570 nm, indicated with a dashed line in the absorption spectra in Fig. 5.6, the loss of an incident lightwave is negligible without electric bias, whereas the loss of the lightwave with $\sim$1000 cm^{-1} is produced with electric bias. Optical intensity modulation is thus possible with the electro-absorption characteristics. Refraction spectra are computed by numerical Kramers–Kronig transformation of the optical

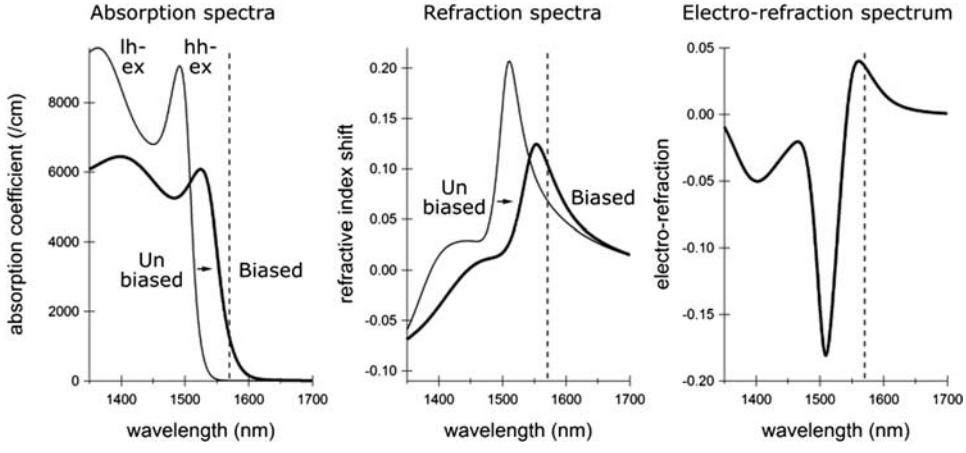

Figure 5.6 Optical absorption, refraction, and electro-refraction spectra of QW excitons.

absorption spectra. The difference between refractive-index shifts in biased and unbiased conditions produces the electro-refraction spectrum in the right graph of Fig. 5.6. Optical phase modulation is realized by the electro-refraction.

Another interband dipole transition process is the FK effect, which occurs in biased bulk semiconductors.[74] Electron and hole wavefunctions in a biased bulk semiconductor were computed by Numerov's method mentioned above and plotted in Fig. 5.7.[55,56] The wavefunctions, which were obtained in a limited space in one dimension, have characteristics typical of the FK effect, although the precise computation of wavefunctions in a bulk semiconductor requires a large computational space. In biased conduction and valence bands, electron and hole wavefunctions extend as plane waves in opposite sides, and the tunneling tails of the wavefunctions overlap in the same area. Electron–hole pairs virtually excited in the forbidden bandgap by the dipole transition are separated into electrons and holes, which tunnel to the biased conduction and valence bands. A red shift of the absorption edge is observed in the optical absorption spectrum because the dipole transition occurs below the bandgap. Therefore, the FK effect also allows electro-absorption and electro-refraction for optical modulation.[65,74]

The efficiency of optical modulation is higher for QCSE optical modulators than for FK optical modulators because ofphoton-assisted tunneling, which is a second-order optical dipole transition process, is involved in FK effect in contrast to a first-order optical dipole transition process in the QCSE.[75] On the other hand, the design and fabrication of optical modulators based on the FK effect are simpler than those based on the

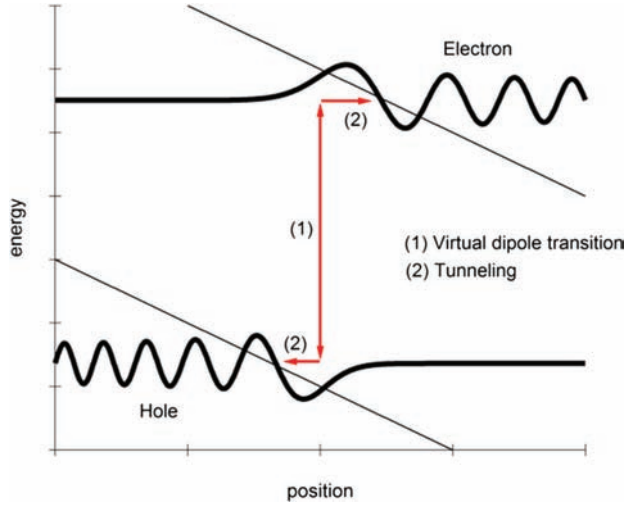

Figure 5.7 Solutions by Numerov's method for electron and hole wavefunctions, and schematic flow of photon-assisted tunneling in the FK effect in a biased bulk semiconductor.

QCSE because the design effort of band engineering for high-performance QWs and the process effort of epitaxial growth for high-quality heterostructures are not required, thereby FK optical modulators are more suitable to silicon-photonics ecosystem for low-cost high-yield production based on CMOS-friendly fabrication processes.[76] In fact, FK optical modulators that use silicon-germanium and germanium bulk systems for the waveguide core have been studied extensively, as described in Chapter 2.[77–79]

5.1.4 Spectral and thermal characteristics

Phase shifters operating in broadband spectral ranges are essential for optical-modulator applications in high-capacity optical networks based on WDM optical data transmission. Athermal phase shifters are important for applications such as integrated optical transceivers for datacenter networks, where energy efficiency is crucial and stabilization using TEC should be avoided. The wavelength and temperature dependences of the physical processes for high-speed phase shifters are reviewed here.

Phase shifters based on the Pockels effect yield weak wavelength and temperature dependences because the Pockels effect is produced by the displacement of ionic atoms in electro-optic crystalline insulators such as LN. The refractive index of LN changes from 2.1410 at a wavelength of 1400 nm to 2.1351 at 1600 nm for an ordinary wave and from 2.2208 at 1400 nm to 2.2139 at 1600 nm for an extraordinary wave at a temperature of 25°C; and it changes from 2.1410 at 25°C to 2.1426 at 80°C for an ordinary wave and from 2.2208 at 25°C to 2.2208 at 80°C for an extraordinary wave at a wavelength of 1400 nm.[80]

Wavelength and temperature dependences of phase shifters based on free-carrier plasma dispersion are basically weak because the plasma dispersion, which is induced by intraband free electrons and holes, is observed in a broad spectral range the bandgap from near-infrared to infrared in doped semiconductors at various temperatures. To explain the wavelength dependence of the plasma dispersion, the empirical formula of the plasma dispersion at a wavelength of 1550 nm in crystalline silicon in Eq. (5.12) is compared with the plasma dispersion at another wavelength (1300 nm) in the O band, which has the following mathematical expression:

$$\Delta n = -2.98 \times 10^{-22} N_{\mathrm{e}}^{1.016} - 1.25 \times 10^{-18} N_{\mathrm{h}}^{0.835}, \tag{5.15}$$

according to the literature.[46] In Eq. (5.15), the electron and hole terms are about 50% and 80% of those at 1550 nm, respectively. Therefore, sufficient optical phase modulation based on plasma dispersion is also obtained in the O band.

The temperature dependence of the plasma dispersion is analyzed next. The background refractive index, carrier scattering time, and carrier effective mass depend on temperature and may affect characteristics of the plasma dispersion against temperature. For crystalline semiconductors such as silicon,

the temperature dependence of the refractive index n has been studied extensively (a part of the literature is listed in the references in this chapter[81–86]); it is characterized with the thermo-optic coefficient $\partial n/\partial T$, which can be written up to the quadratic term in absolute temperature T for silicon at a wavelength of 1523 nm as[85]

$$\frac{\partial n}{\partial T} = 9.48 \times 10^{-5} + 3.47 \times 10^{-7} \times T - 1.49 \times 10^{-10} \times T^2. \tag{5.16}$$

For a temperature rise from 300 K (~25°C) to 400 K (~130°C), the background refractive index increases by 0.02, which will not produce a significant difference in plasma dispersion. At carrier densities of 10^{17} cm^{-3} and higher, carrier scattering is dominated by ionized impurity scattering that remains in the regime of $\omega\tau \gg 1$ in crystalline silicon.[45] The carrier-scattering time due to ionized impurities increases with temperature proportional to $T^{-3/2}$.[87] The temperature dependence of the scattering time is caused by the thermally activated screening length proportional to T^{-1}, based on the Debye–Hückel model of classical nondegenerate electron and hole gases at high temperature.[41] The efficiency of plasma dispersion does not deteriorate at high temperatures. As another factor affecting the plasma dispersion, the temperature dependence of carrier effective masses also leads to temperature dependence of the plasma dispersion.[88,89] An increase in carrier effective masses with a temperature rise from 300 K to 400 K is, however, 10% or less. Therefore, one can conclude that temperature change does not affect the plasma dispersion significantly. The optical modulation performance of phase shifters based on plasma dispersion did not change within a wide temperature range of 25–130°C, and only a 10% increase in free-carrier absorption was predicted theoretically for crystalline compound semiconductors.[90,91] As a result, DC V_π remains 2.6–2.5 V over the temperature range.[90]

High-efficiency high-speed optical modulation is possible with QCSE phase shifters with a 0.77-V drive voltage and 67-GHz modulation bandwidth.[92] In the QCSE, however, efficient electro-refraction is limited in a narrow spectral range below the exciton resonance, as evident from the characteristics in Fig. 5.6. In the literature, V_π changes more than twice over the C band.[93] To maximize optical phase modulation without inducing optical intensity modulation due to electro-absorption, precise adjustment of the electric bias is required according to the wavelength of the lightwave.[93,94]

The electronic band edge in crystalline-compound semiconductors that form a QW yields long-wavelength shift (red shift) with a slope of 0.5–0.6 nm/°C with the temperature rise.[95] Crystalline elemental semiconductors also show a similar temperature dependence of the band edge.[96,97] Therefore, optical modulation based on the QCSE at a fixed input wavelength strongly depends on temperature and requires a thermal budget to stabilize the temperature using TEC or compensation of optical power loss by adding an optical amplifier,

although a resonant optical dipole transition itself is highly efficient with respect to a reduction in power consumption.[98,99] A similar discussion can be applied to the spectral and thermal characteristics of phase shifters based on the FK effect.

5.1.5 Frequency chirping

Frequency chirping causes a deterioration of the quality of optical signals generated in optical modulators, as described in Chapter 3, and zero-chirp operation of an MZ optical modulator driven in push–pull mode is crucial to data transmission in high-capacity optical networks.[100,101] An integrated MZ optical modulator in conjunction with the spectral and thermal characteristics of free-carrier plasma dispersion as clarified above is essential as a small-footprint zero-chirp optical modulator in a broad spectral range over the C and L bands.[102,103] One may argue that the plasma-dispersion phase shifters are not practical for zero-chirp optical phase modulators because simultaneous optical intensity modulation and consequent signal distortion are inevitable due to the carrier-induced optical absorption as the counterpart of the plasma dispersion. This is not true, however, because signal distortion due to the intensity modulation is compensated with the opposing signal distortion induced by the nonlinear bias voltage dependence of the optical phase shift in the trajectories in phase shifting, as illustrated in Fig. 5.8.

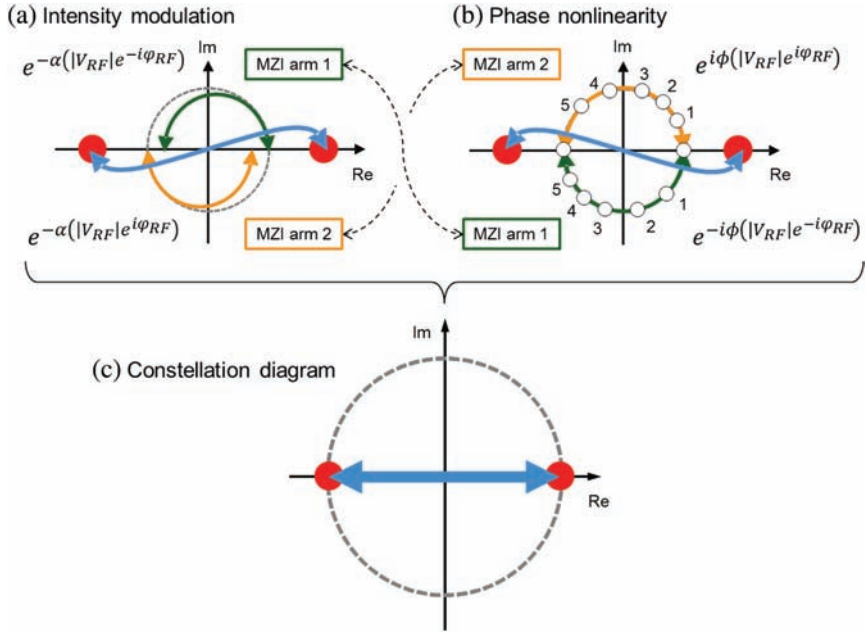

Figure 5.8 Optical signal distortion processes due to (a) simultaneous optical intensity modulation and (b) nonlinear voltage dependence of the optical phase, and (c) quasi-zero-chirp constellation diagram.

In the case of plasma-dispersion optical modulators, as for the single MZ optical modulator with PN-junction phase shifters (shown in Figs. 3.6 and 3.7), RF electrical signals in opposite polarities are applied to MZI arms 1 and 2 in push–pull operation. Electron and hole densities in the phase shifters are controlled with RF electrical signals applied to MZI arms 1 and 2 with DC bias voltages; thus, carrier-induced changes of the refractive index and optical-absorption coefficient Δn and $\Delta\alpha$, respectively, depend on the electrical signals and the DC bias voltages applied to the both arms. The former distortion trajectory in Fig. 5.8(a) is generated by asymmetric intensity modulation between the MZI arms. The latter trajectory in Fig. 5.8(b) is generated by the nonlinear voltage dependence of the optical phase shift and inverted against the former trajectory because of the negative refractive-index change that appears in the carrier-dependent term in Eq. (5.10) of the Drude theory and in Eqs. (5.12) and (5.15) of the empirical formula. The phase nonlinearity originates from the nonlinear voltage dependence of the refractive index change in a PN-junction phase shifter, as elaborated later. As a compound characteristic, quasi-zero-chirp modulation (illustrated in Fig. 5.8(c)) is possible with plasma-dispersion MZ optical modulators. Quasi-zero-chirp modulation in a 20-Gbaud NRZ-BPSK was verified for the integrated silicon-based single MZ optical modulator shown in Fig. 3.10.[104,105] The design effort for lowering the free-carrier loss in PN-junction phase shifters is, nevertheless, essential because the notion of quasi-zero chirp no longer holds with a free-carrier loss too high to be canceled.

Phase shifters based on free-carrier plasma dispersion are the most useful among all phase shifters based on the various physical mechanisms in light of their energy-efficient optical modulation in a broad spectral range. The rest of this chapter focuses on the classification, design, and modeling of plasma-dispersion phase shifters.

5.2 Classification of Phase Shifters using Free-Carrier Plasma Dispersion

5.2.1 Lateral PN-junction phase shifter

Phase shifters consisting of PN-junction rib waveguides on a silicon-photonics platform have the advantage of small-footprint integrated MZ optical modulators produced in low-cost, high-yield manufacturing because of their simple flow of fabrication processes on large-scale wafers. Lateral PN-junction rib-waveguide phase shifters are reviewed first. The lateral PN-junction phase shifters have been used extensively as high-speed integrated optical modulators (described in Chapter 3). A schematic profile of such a lateral PN-junction rib-waveguide phase shifter is illustrated in Fig. 5.9 with a vertical PN-junction rib-waveguide phase shifter and another type of phase shifter for comparison. A lateral PN junction can be formed in a

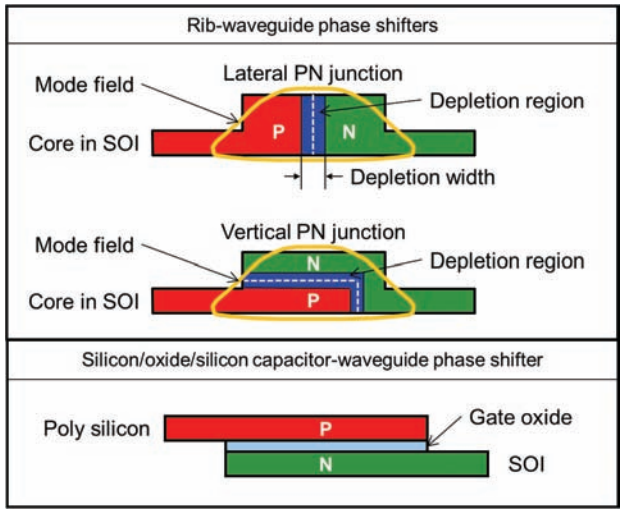

Figure 5.9 Illustrated profiles of lateral PN-junction and vertical PN-junction rib-waveguide phase shifters and silicon/oxide/silicon capacitor-waveguide phase shifter on a silicon-photonics platform.

rib optical waveguide (Fig. 3.6), along with the flow of CMOS-based silicon-photonics fabrication processes, depicted in Fig. 3.14. A reverse-bias voltage is applied to the lateral PN junction to enhance the modulation speed.[53,106] A depletion region is formed around the boundary of the PN junction (a vertical dashed line in Fig. 5.9) in the core of the rib waveguide under reverse bias voltage. Electrons and holes are swept away from the depletion region under the electric field of the reverse bias, and there are no carriers inducing free-carrier plasma dispersion in the depletion region. The depletion region expands wider with a higher reverse bias. The refractive index of the core can be modulated due to the plasma dispersion with an RF electrical signal imposed on the DC reverse-bias voltage, and the optical phase of the lightwave wherein the mode field overlaps with the depletion region is modulated accordingly. This is the basic scheme of optical phase modulation in an optical modulator based on free-carrier plasma refraction.

In the PN junction, carriers travel across the depletion region with drift velocity, which is 1×10^7 cm/s or even higher in the ballistic-transport regime in crystalline silicon.[50] Assuming a few hundred nanometers as the width of the depletion region, denoted as the depletion width in Fig. 5.9, carriers travel ballistically, and the transit time is as short as a few picoseconds or shorter. In such a case, the speed of optical modulation is no longer determined by the transit time but limited by the parasitic resistance-capacitance RC time constant, as described in Chapter 6. High-speed modulation beyond 40 Gbaud was demonstrated with the carrier-depletion phase shifters with various arrangements of a lateral PN junction and traveling-wave electrode.[107–109]

Free-carrier absorption is the most dominant factor of optical loss in PN-junction rib-waveguide phase shifters based on free-carrier plasma dispersion.[110] The design of a lateral PN junction in a rib waveguide can be modified to reduce the carrier-induced optical loss.[111,112] An FOM modified as $\pi/(V_\pi\ \alpha_{PS}\ \ell_\pi)$ is more appropriate than the fundamental FOM of $1/(V_\pi \ell_\pi)$ to evaluate phase-shifter performance when the optical loss of a phase shifter α_{PS} is crucial in terms of system performance. The modified FOM is measured in units of rad/V/dB. The compensation-doping method is efficient in the light of the modified FOM.[112] The doped side areas immediately inside the rib side walls, where carrier densities remained unchanged and do not contribute to refractive index modulation under RF electrical signal, are compensation-doped with counter dopants to eliminate the carriers. Counter-doping processes to form compensated side regions in a rib waveguide and a compensation-doped rib-waveguide phase shifter are illustrated in Fig. 5.10. Width of compensated side region is approximately 100 nm. Counter-doping processes to the P-type and N-type side regions can be inverted in order. Compensation-doped carrier-depletion lateral PN-junction rib-waveguide phase shifters suit small-footprint, low-loss MZ optical modulators on a silicon-photonics platform for high-speed optical signal generation in a broad spectral range of the C and L bands.[113] The fundamental optical characteristics of the lateral PN-junction phase shifters are discussed in the next chapter.

5.2.2 Vertical PN-junction phase shifter

A vertical PN-junction phase shifter is the other type of rib-waveguide phase shifter; Fig. 5.9 depicts the schematic profile. For electrical contacts to the planar traveling-wave electrodes, P-type and N-type contacts are formed in the slab wings on the respective sides of the central rib core, just like lateral PN-junction phase shifters. In Fig. 5.9, the junction boundary is bent like a letter L.[114,115] Boron can be implanted deeper than phosphorus because the

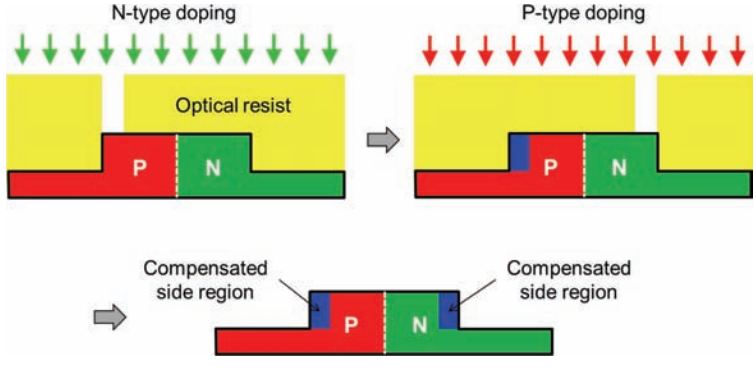

Figure 5.10 Counter-doping processes and compensation-doped lateral PN-junction rib-waveguide phase shifter on a silicon-photonics platform.

former dopant has an atomic mass much lighter than that of the latter dopant. Therefore, a P-type region is placed at the bottom and an N-type region at the top in the central rib section of the core. The order of the P-type and N-type regions, however, can be inverted in the vertical direction according to process limitations, performance requirements, dopant species, and so forth. The top N-type region is supported with a N-type side pillar for electrical connection to the slab wing doped with N-type dopants. In this configuration, most of the PN junction is formed in the vertical direction, and its boundary is substantially along the horizontal direction. The phase shifter is thus classified as a vertical PN-junction phase shifter, which can be produced with CMOS-based silicon-photonics fabrication processes with ion-implantation processes optimized for vertical PN-junction profiles.[115] Doping processes applied to the vertical PN junction are similar to those of the lateral junction in terms of accuracy in optical mask alignment and depth profile control in ion implantation, although multiple N-type doping steps are required. Thus, the fabrication yield will be almost the same as for the lateral junction. One drawback is higher optical loss than that in a lateral-junction phase shifter. The doping level of the N-type region contiguous to the rib side wall was increased up to $\sim 10^{18}$ cm^{-3} to reduce series resistance, and the high density of carriers in the region cause high optical loss due to free-carrier absorption.

The depletion region in the vertical PN junction occupies a much larger area in the rib-waveguide core and overlaps with the mode field more significantly than in the lateral PN-junction phase shifters because the optical waveguides on a silicon-photonics platform for practical applications have low profiles, as mentioned in Chapter 3. Therefore, the drive voltage can be reduced remarkably in vertical PN-junction phase shifters. For a silicon-based MZ optical modulator in which the L-shaped PN-junction phase shifters were disposed in the MZI arms, a $V_\pi \ell_\pi$ as low as 0.81 V·cm with 2.7-V V_π was realized at the expense of a reduction in the modified FOM.[90] The N-type side pillar region was doped with a high concentration of N-type dopants ($>10^{18}$ cm^{-3}) to achieve a low-resistance electrical connection to the vertical PN junction and reduce the parasitic RC time constant for high-speed optical modulation. Phase-shifter optical loss induced by free-carrier absorption increases super-linearly with carrier densities in Eq. (5.13) in contrast to the sub-linear increase in an optical phase shift caused by the free-carrier plasma dispersion in Eq. (5.12). The modified FOM was thus decreased because of high carrier densities even though the vertical PN-junction phase shifter is based on a different design than its lateral counterpart and does not obey the same scaling curve of the FOM. One can select either lateral or vertical PN-junction phase shifters to be disposed in the MZI arms of an integrated MZ optical modulator according to system requirements.

In addition to the vertical PN-junction rib-waveguide phase shifter described above, different designs of vertical PN junction formed in a rib waveguide have been

studied.[115–117] A folded PN junction, which is a mixture of lateral and vertical geometries, was also proposed.[118] Further efforts toward the design refinement of vertical PN-junction profiles in silicon-photonics rib waveguides will improve the modified FOM and MZ optical modulators for high performance.

5.2.3 Other types of phase shifter

Another type of phase shifter is the silicon/insulator/silicon capacitor-waveguide phase shifter (SISCAP in the literature) for small-footprint, advanced-format optical modulators in high-capacity optical networks.[119,120] A cross-section profile of the phase shifter is illustrated in Fig. 5.9. A silica thin layer fabricated with a gate-oxide process was used as the insulator layer. The phase shifter was driven in carrier accumulation mode. High-density electrons and holes were accumulated at a low forward bias voltage. The forward bias voltage was applied across the P-type and N-type silicon layers between the gate oxide, whereby slow-speed carrier diffusion was inhibited and high-efficiency, high-speed optical modulation was ensured: $V_\pi \ell_\pi$ was lower than 0.2 V·cm at a wavelength of 1310 nm with a phase-shifter length of 0.4 mm and an extinction ratio of 9 dB at 28-Gb/s on/off modulation.[119] The fabrication of optical modulators with phase shifters requires more process steps for the gate-oxide layer and the top poly-silicon layer than in rib-waveguide phase shifters. Additional optical loss is induced due to light scattering at grain boundaries in the poly-silicon layer.

Another type of metal–oxide–semiconductor (MOS) phase shifter was designed, fabricated, and characterized at 10-Gb/s on/off modulation.[121,122] Gate oxidization and poly-silicon processes were also included in the fabrication processes. In this phase-shifter type, a vertical MOS capacitor using a poly-silicon gate was built in a silicon-based optical waveguide. Phase modulation of this type is also based on carrier accumulation, and a $V_\pi \ell_\pi$ as low as 0.3 V·cm was reported using a MOS-capacitor phase shifter 0.2 mm long at a wavelength of 1550 nm.[123]

A carrier-depletion vertical PN-junction phase shifter was designed and fabricated using the same poly-silicon process without gate oxide.[124] The bottom P-type region was formed in the SOI layer and the top N-type region in the deposited poly-silicon layer. High-speed on/off intensity modulation at 40 Gb/s with a 3.5-V·cm $V_\pi \ell_\pi$ was demonstrated using a 5-mm carrier-depletion phase shifter under reverse bias.

5.3 Design and Modeling of PN-Junction Phase Shifters

5.3.1 Semi-analytical method

The voltage dependence of an optical phase shift generated in a phase shifter is crucial for the design and modeling of phase shifters based on free-carrier plasma dispersion. Overlap of the mode field with the depletion region dominates the

phase shift of a lightwave propagated through a phase shifter. Therefore, the bias voltage dependence of the depletion width is the first subject to deal with when designing and modeling a PN-junction carrier-depletion phase shifter.

Band diagrams of a PN junction under reverse-, zero-, and forward-bias conditions is illustrated in one dimension in Fig. 5.11.[125] The band diagrams provide energy-band profile of the lateral PN-junction rib-waveguide phase shifter illustrated in Fig. 5.9 along a horizontal coordinate in reverse-, zero- and forward-bias conditions. An illustration of the phase shifter is inserted with the horizontal axis in Fig. 5.11. The depletion region is depicted so as to have abrupt boundaries at the both sides according to the abrupt-junction model.[126] The depletion region still exists at a zero-bias voltage due to the recombination of interdiffused electrons and holes. The junction potential at zero bias voltage corresponds to the built-in potential V_{built}.

A two-sided abrupt PN junction is a good analytical model to begin deriving an approximated expression for the bias voltage dependence of the depletion width. Depletion width W_{dep} in the analytical model is obtained as the following solution of the Poisson equation:[126]

$$W_{\text{dep}} = \sqrt{\frac{4\varepsilon_0}{qN_{\text{D}}}\left(V_{\text{built}} \pm |V_{\text{bias}}| - \frac{2k_{\text{B}}T}{q}\right)}, \tag{5.17}$$

assuming the same dopant concentration N_{D} for P-type and N-type dopants for simplicity. Here, q, ε_0, and k_{B} denote the electron charge, background dielectric constant, and Boltzmann constant, respectively. The plus or minus sign is assigned to the reverse or forward bias voltage V_{bias}. In Eq. (5.17), the built-in potential V_{built} has the following expression:

$$V_{\text{built}} = \frac{2k_{\text{B}}T}{q}\ln\left(\frac{N_{\text{D}}}{N_{\text{I}}}\right), \tag{5.18}$$

where the intrinsic carrier density N_{I} is written as

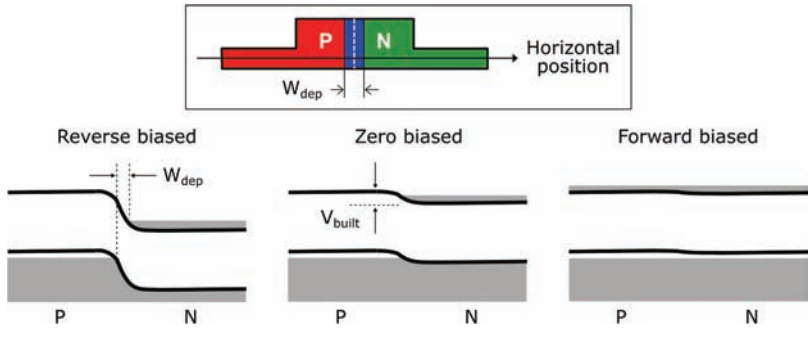

Figure 5.11 Band diagrams of a PN junction along the horizontal position in reverse-, zero- and forward-bias conditions.

$$N_I = 4.9 \times 10^{15} \sqrt{M_C} (\gamma_e \gamma_h)^{\frac{3}{4}} T^{\frac{3}{2}} e^{\frac{-E_G}{k_B T}}, \tag{5.19}$$

with conduction band degeneracy M_C; electron and hole effective density of mass ratios γ_e and γ_h, which are 1.08 and 0.57, respectively; and bandgap E_G of 1.1 eV. Therefore, N_I is $\sim 10^{10}$ cm^{-3} in crystalline silicon at 300 K.[42,126] The depletion width obtained analytically in Eq. (5.17) is plotted in Fig. 5.12 against the reverse-bias voltage with the dopant concentration changed from 2×10^{17} cm^{-3} to 1×10^{18} cm^{-3}.

Electro-refraction due to free-carrier plasma refraction is proportional to the mode-field confinement factor, which is defined as the mode field confined in the depletion region in a phase shifter. Note that field confinement is addressed instead of intensity (square of field) because of a phase shift in a MZ optical modulator, mathematically represented in Eqs. (3.1)–(3.4). In case of a semiconductor waveguide laser, on the other hand, a mode-confinement factor proportional to the optical intensity in the active region is relevant because optical power gain is most crucial in the analysis of laser performance.[127,128] The mode-field confinement factor $\Gamma_{lateral}$ in a lateral PN-junction carrier-depletion phase shifter is written in the following form using the mode field $E_{mode}(x, y)$:

$$\Gamma_{lateral} = \frac{\int_{-\frac{W_{dep}}{2}}^{+\frac{W_{dep}}{2}} dx \int_{-y_{bottom}}^{+y_{top}} dy |E_{mode}(x,y)|}{\int_{-\infty}^{+\infty} dx \int_{-\infty}^{+\infty} dy |E_{mode}(x,y)|}, \tag{5.20}$$

where y_{top} and y_{bottom} denote the vertical top and bottom positions of rib-waveguide core in a phase shifter, respectively. In the abrupt-junction model, the depletion width is given in Eq. (5.17). Numerical calculation of $\Gamma_{lateral}$ is

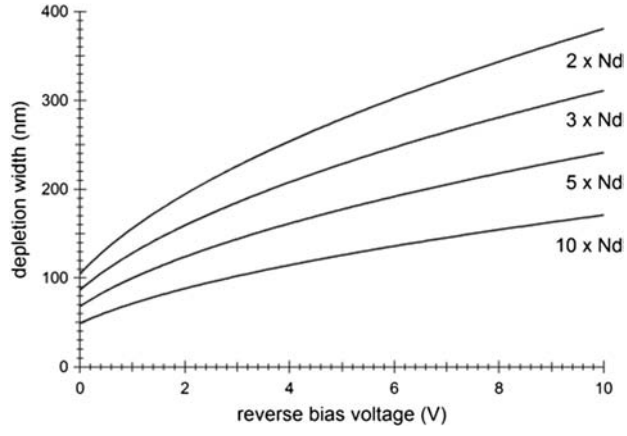

Figure 5.12 Depletion width vs. reverse-bias voltage with a dopant concentration from 2×10^{17} cm^{-3} to 1×10^{18} cm^{-3} ($Nd = 1\times10^{17}$ cm^{-3}).

performed by using $E_{\mathrm{mode}}(x, y)$, presented in Chapter 4, at 1300-nm and 1550-nm wavelengths for a rib-waveguide core 500 nm wide with a 220-nm rib height and a 95-nm slab height. A computational algorithm for multi-dimensional integrals allows for the numerical calculation of Eq. (5.20) as for the effective refractive index in the previous chapter.[129] Reverse-bias voltage dependence of the mode-field confinement factor is shown with respect to dopant concentration, from 2×10^{17} cm^{-3} to 1×10^{18} cm^{-3} at 1300-nm and 1550-nm wavelengths in Fig. 5.13. The mode-field confinement factor at each dopant concentration is higher at the shorter wavelength because the mode field is localized in the depletion region more strongly at the shorter wavelength.

Electro-refraction $\Delta n_{\mathrm{elect}}(V, N_{\mathrm{e}}, N_{\mathrm{h}})$ is then obtained as a function of reverse-bias voltage, and V is obtained from the mode-field confinement factor and the plasma dispersion in Eqs. (5.12) and (5.15) using the following relationship:

$$\Delta n_{\mathrm{elect}}(V, N_{\mathrm{e}}, N_{\mathrm{h}}) = \frac{\Delta n(N_{\mathrm{e}}, N_{\mathrm{h}})}{2}\Gamma_{\mathrm{lateral}}(V), \tag{5.21}$$

assuming horizontal symmetry of the mode fields over the P-type and N-type regions and thus a 50:50 contribution of electron and hole terms in the plasma dispersion. The electron and hole densities are assumed to be the same as N_{D}, namely, $N_{\mathrm{e}} = N_{\mathrm{h}} = N_{\mathrm{D}}$. The relative change in the plasma refraction from zero reverse-bias voltage is taken into account in electro-refraction. In Fig. 5.14, electro-refraction in absolute value is plotted with dopant concentrations from 2×10^{17} cm^{-3} to 1×10^{18} cm^{-3} at wavelengths 1300 nm and 1550 nm, respectively. The wavelength dependence of the plasma dispersion provides almost the same electro-refraction characteristics at both wavelengths in spite of the difference in the mode-field confinement factor.

In the design of electro-refraction phase shifters, the modulator drive voltage V_{mod} supplied to the phase shifter must be decided first because the drive voltage is limited by the modulator drivers in use. High-voltage

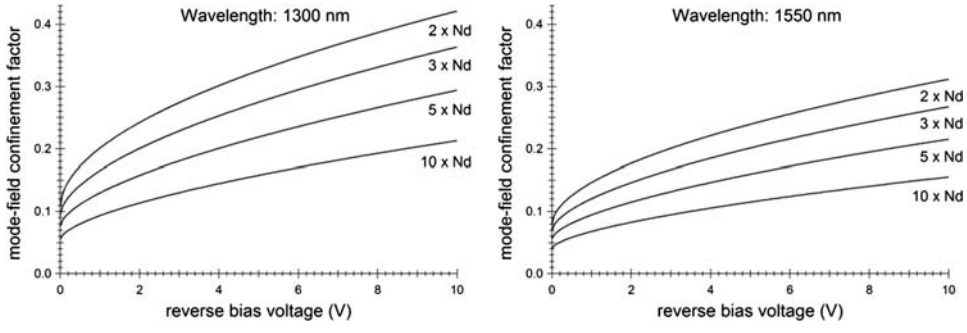

Figure 5.13 Mode-field confinement factor vs. reverse-bias voltage with a dopant concentration from 2×10^{17} cm^{-3} to 1×10^{18} cm^{-3} at 1300-nm and 1550-nm wavelengths.

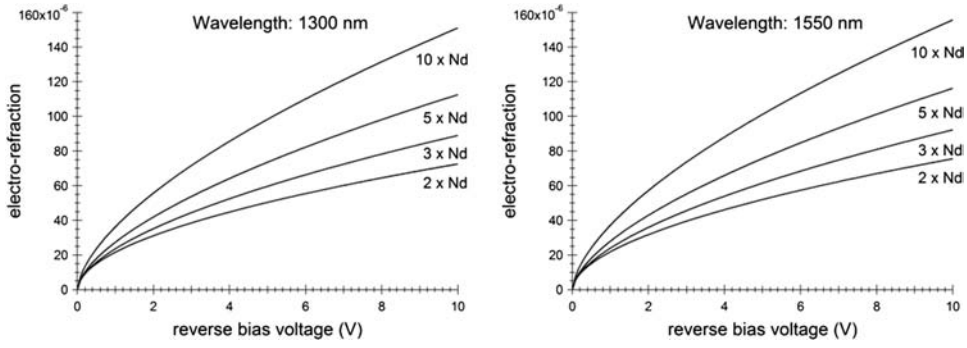

Figure 5.14 Electro-refraction vs. reverse-bias voltage with a dopant concentration from 2×10^{17} cm^{-3} to 1×10^{18} cm^{-3} at 1300-nm and 1550-nm wavelengths.

modulator drivers can be selected for high-end applications such as integrated optical modulators in core optical networks, whereas low-voltage modulator drivers are selected for low-cost, energy-efficient applications such as integrated optical transceivers in datacenter optical networks.

The phase-shifter length for π phase shift ℓ_π is then obtained according to the following equation:

$$\ell_\pi = \frac{\lambda}{4\Delta n_{\text{elect}}(V_{\text{mod}}, N_{\text{D}}, N_{\text{D}})}, \tag{5.22}$$

which is derived by deforming the total phase shift $\Delta\phi(V) = 4\pi\Delta n(V)\ell/\lambda$ in push–pull modulation in Chapter 3 and substituting π for $\Delta\phi(V_{\text{mod}})$ and $\Delta n_{\text{elect}}(V_{\text{mod}}, N_{\text{D}}, N_{\text{D}})$ in Eq. (5.21) for $\Delta n(V_{\text{mod}})$. The phase-shifter length is plotted in Fig. 5.15 as a function of the dopant concentration for V_{mod} in a range from 2 V to 10 V at 1300-nm and 1550-nm wavelengths. The dopant concentration equals the electron and hole densities N_{e} and N_{h}. The longer phase-shifter length is required for the longer wavelength because of the proportionality of the phase-shifter length to the wavelength of the propagated lightwave in Eq. (5.22).

The semi-analytical method based on the abrupt-junction model allows semi-quantitative characterization of carrier-depletion phase shifters with a lateral or vertical PN junction in their rib-waveguide cores. A phase shifter with a longer length and lower dopant concentration is more suitable for an optical modulator of lower optical loss due to free-carrier absorption. For a push–pull modulator drive voltage of 4 V, which corresponds to an 8-V single modulator drive voltage, the phase-shifter length increases by 43% with a decease in electron and hole densities from 7.5×10^{17} cm^{-3} to 2.0×10^{17} cm^{-3}; thus, the optical loss due to free-carrier absorption in Eq. (5.13) is reduced by as much as 69% at a 1550-nm wavelength. A phase shifter with a shorter length is more suitable for an optical modulator of higher frequency response,

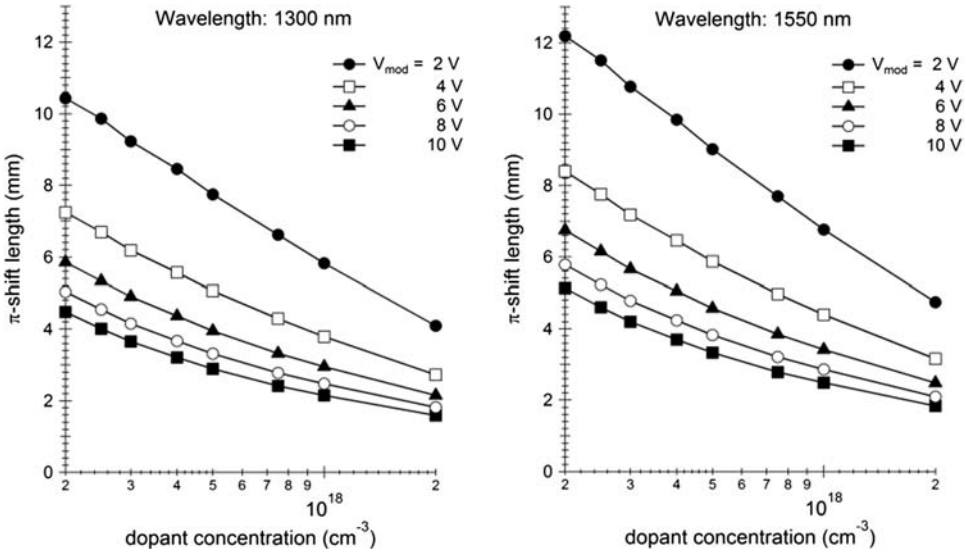

Figure 5.15 Dopant-concentration dependence of phase shifter length for π phase shift, ℓ_π at modulator drive voltages from 2 V to 10 V at wavelengths of 1300 nm and 1550 nm.

as discussed in the next chapter. High dopant concentrations—namely, high electron and hole densities—are required to shorten the phase-shifter length, and a consequent increase in optical loss due to free-carrier absorption is inevitable.

Compensation doping was proven to be an effective design and process module to reduce free-carrier absorption loss in lateral PN-junction rib-waveguide phase shifters, as described in Subsection 5.2.1. The semi-analytical method also allows us to clarify the effect of compensation doping. Optical loss in a lateral PN-junction phase shifter can be calculated numerically by introducing a mode-power confinement factor $\Gamma_{\text{lateral}}^{\text{power}}$, written as

$$\Gamma_{\text{lateral}}^{\text{power}} = \frac{\int_{-\frac{W_{\text{dep}}}{2}}^{+\frac{W_{\text{dep}}}{2}} dx \int_{-y_{\text{bottom}}}^{+y_{\text{top}}} dy |E_{\text{mode}}(x,y)|^2}{\int_{-\infty}^{+\infty} dx \int_{-\infty}^{+\infty} dy |E_{\text{mode}}(x,y)|^2}, \tag{5.23}$$

which is similar to the mode-confinement factor characterizing optical gain in semiconductor waveguide lasers.[127,128] Electro-absorption $\Delta\alpha_{\text{elect}}(V, N_{\text{e}}, N_{\text{h}})$ is defined as

$$\Delta\alpha_{\text{elect}}(V, N_{\text{e}}, N_{\text{h}}) = \frac{\Delta\alpha(N_{\text{e}}, N_{\text{h}})}{2} \Gamma_{\text{lateral}}^{\text{power}}(V), \tag{5.24}$$

assuming horizontal symmetry of the mode fields over the P-type and N-type regions, and $N_{\text{e}} = N_{\text{h}} = N_{\text{D}}$ for the electro-refraction. Electro-absorption in

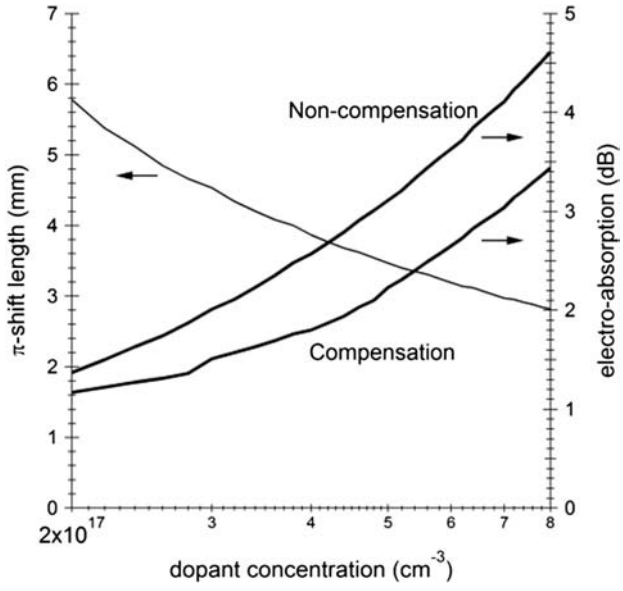

Figure 5.16 Electro-absorption characteristics in lateral PN-junction phase shifters with and without compensation doping at a wavelength of 1550 nm. The phase-shifter length for a π-phase shift is also plotted.

the phase shifters with and without compensation doping is obtained as plotted in Fig. 5.16 as a function of the dopant concentration from 2×10^{17} cm^{-3} to 8×10^{17} cm^{-3} at a wavelength of 1550 nm for a push–pull modulator drive voltage of 8 V.[130] Electro-absorption is scaled in dB-unit, which is converted from that in units of cm^{-1} by a factor of 4.34 dB·cm. Applications in high-speed PSK modulation formats are anticipated for the compensation-doped phase shifters. In contrast to the OOK format, where an electrical modulation signal with a modulation amplitude of V_π produces perfect on/off intensity modulation, as illustrated in Fig. 3.8, twice the V_π is required for the modulation amplitude in PSK applications as in Fig. 3.10.

Electro-absorption is increased with deceasing π-shift length and dopant concentration. For the phase shifter without compensation doping, electro-absorption is higher than 4.5 dB with a length shorter than 3 mm. Electro-absorption must be suppressed for high-quality optical signal generation in PSK formats, although carrier-depletion phase shifters can be driven in quasi-zero chirping as discussed in Subsection 5.1.5. Electro-absorption is suppressed approximately by 0.8 dB at a moderate dopant concentration of 5×10^{17} cm^{-3} and by 1.2 dB at a high dopant concentration of 8×10^{17} cm^{-3}. Phase-shift characteristics are not affected by compensation doping, and a π-shift length is common to both types of doping profile because the compensated side regions are separated from the depletion region and do not interfere with the depletion region in the abrupt-junction model. The concept

of the compensation-doped phase shifter as a low-loss phase shifter to enhance the modified FOM is thus proved in the semi-analytical moethod.

A similar discussion can be applied to a vertical PN-junction rib-waveguide phase shifter based on the concepts of this subsection except for compensation doping. In a vertical PN-junction phase shifter, the mode-field confinement factor is calculated with the depletion region, which expands along the vertical direction under reverse bias applied vertically. Due to the specific profile of the vertical PN junction, the compensation-doping method is not compatible with the fabrication processes of the vertical PN-junction phase shifter. The lateral PN-junction phase shifter may thus be more appropriate for such applications as long-reach optical fiber transmission without an optical amplifier.

5.3.2 Computational method

The accurate design and modeling of carrier-depletion PN-junction phase shifters is realized by means of numerical simulation based on a more realistic model of carrier-depletion phase shifter with an expense of machine time for the numerical simulation. Numerical simulation of silicon-based optical-waveguide phase shifters has been one of the subjects extensively studied in the design and modeling of PICs on a silicon-photonics platform.[131–136] Optical simulation of the mode field and electronic simulation of carrier distribution comprise the numerical simulation of the phase shifters. The optical simulation has been described in Chapter 4, and simulated mode fields are also used to calculate the mode-field confinement factor in the semi-analytical method. The electronic simulation is described in this subsection for carrier-depletion PN-junction rib-waveguide phase shifters. We start with a lateral PN-junction rib-waveguide phase shifter that has a profile like that in Fig. 5.17. The profile represents the lateral PN-junction phase shifter fabricated and characterized in a 32-Gb/s OOK with an extinction ratio higher than 11 dB.[110] The donor concentration N is lower than the acceptor concentration P to reduce free-carrier absorption loss because the loss due to electrons is higher than that due to holes, as shown in Fig. 5.4.

Distribution profiles of electrons and holes in the lateral PN junction are obtained by numerically solving the Poisson equation

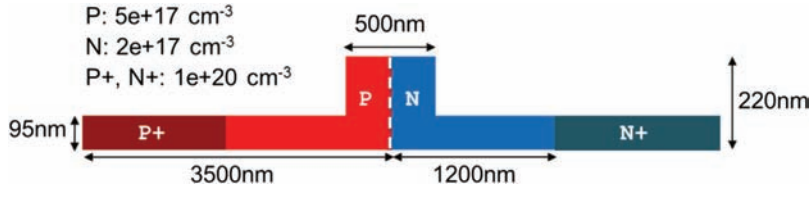

Figure 5.17 Profile of a reverse-bias lateral PN-junction rib-waveguide phase shifter.

$$\nabla \cdot \nabla \Phi = -\frac{q}{\varepsilon}(p - n + N_D - N_A) \tag{5.25}$$

simultaneously with the current-continutity equations for electrons

$$\frac{\partial n}{\partial t} = \frac{1}{q}\nabla \cdot \vec{J}_n - (R_n - G_n) \tag{5.26}$$

and for holes

$$\frac{\partial p}{\partial t} = \frac{1}{q}\nabla \cdot \vec{J}_p - (R_p - G_p), \tag{5.27}$$

respectively.[135] Here, the drift and diffusion terms comprise current terms for electrons

$$\vec{J}_n = qn\mu_n\vec{E} - qD_n\vec{\nabla}p \tag{5.28}$$

and for holes

$$\vec{J}_p = qn\mu_p\vec{E} - qD_p\vec{\nabla}p, \tag{5.29}$$

respectively. In Eqs. (5.25)–(5.29), Φ is the electrostatic potential, p and n are the electron and hole densities, N_A and N_D are the ionized impurity concentrations, J_n and J_p are the electron and hole current densities, R and G are the recombination and generation rates, μ_n and μ_p are the electron and hole mobilities, and D_n and D_p are the electron and hole diffusion constants. These equations are solved numerically by computational methods such as the finite-element method.[137–140] Commercial simulation packages are available for the numerical modeling and analysis of electronic and optoelectronic devices in two and three dimensions.[141–144] These packages can be used without struggling through programming code for computation. Refractive-index changes are much smaller than the refractive index of undoped silicon, so a mode field in a silicon optical waveguide with a PN junction is substantially the same as that in a silicon optical waveguide without the junction as far as the both doped and undoped waveguides have the same cross-section profile. Therefore, the numerical results on the mode fields are applied to the computational analysis in this chapter. Equation (5.14) permits the propagation of lightwaves free from electromagnetic interaction with the electron and hole currents given in Eqs. (5.28) and (5.29), except for the optical loss due to optical absorption by the individual carriers.

The profiles of the electron and hole distribution in the rib-waveguide phase shifter at bias voltages are obtained as numerical solutions of Eqs. (5.25)–(5.29) in steady state, where $\partial n/\partial t = \partial p/\partial t = 0$. Hole-density profiles at zero-bias and 8-V reverse-bias voltages, for example, are presented with mode-field profiles of the fundamental mode in the rib waveguide in

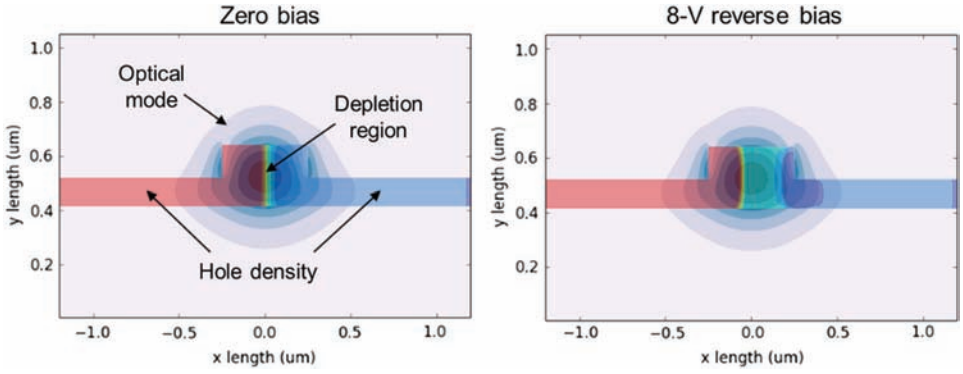

Figure 5.18 Simulated profiles of the hole density and optical mode field in the lateral PN-junction phase shifter at zero-bias and 8-V reverse-bias voltages.

Fig. 5.18.[136] Holes populated in the N-type region are generated by intrinsic thermal excitation over the bandgap of crystalline silicon. The holes behave as minority carriers with a density $<10^6$ cm^{-3}, which is much lower than the intrinsic electron–hole pair density ($\sim 10^{10}$ cm^{-3}) due to recombination with the majority electrons in the N-type region. At the reverse-bias voltage, holes are swept from the junction boundary and the depletion region is expanded toward the P-type and the N-type-regions. In the N-type region, the majority electrons are swept from the junction boundary, and the minority holes are attracted by the majority electrons in the opposite charge and follow them deep into the N-type region. Profiles of electron distribution are also obtained in similar images but inverted around the vertical axis at the junction boundary. Optical mode fields in the rib waveguide are imposed on the hole density profiles in Fig. 5.18. The free-carrier plasma dispersion in the rib waveguide is proportional to a portion of the optical mode field overlapped with electrons and holes at each reverse-bias voltage.

Simulated profiles of the electron and the hole distributions are converted to profiles of free-carrier plasma refraction by using the empirical formulae in Eqs. (5.12) and (5.15) at wavelengths of 1550 nm and 1300 nm, respectively. The profiles at reverse-bias voltages of 4 V and 10 V at a wavelength of 1550 nm are displayed in Fig. 5.19. The depletion region is extended toward the N-type region more significantly than toward the P-type region because the donor concentration is lower than the acceptor concentration. Free-carrier absorption loss profiles are given in a similar manner by using Eq. (5.13).

Based on these profiles, electro-refraction and electro-absorption are obtained at different reverse-bias voltages. The electro-refraction phase shift and electro-absorption loss in the simulation are plotted in Fig. 5.20 in comparison with measurement data. The measured data were acquired for a silicon-based single MZ optical modulator that has 4-mm lateral PN-junction rib-waveguide phase shifters in both MZI arms.[53] Good agreement is

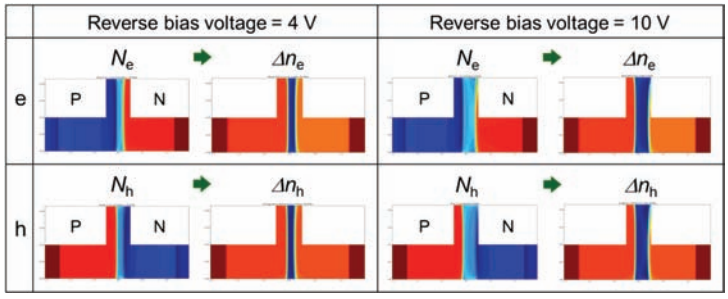

Figure 5.19 Simulated profiles of free-carrier plasma refraction induced by electrons and holes under reverse bias.

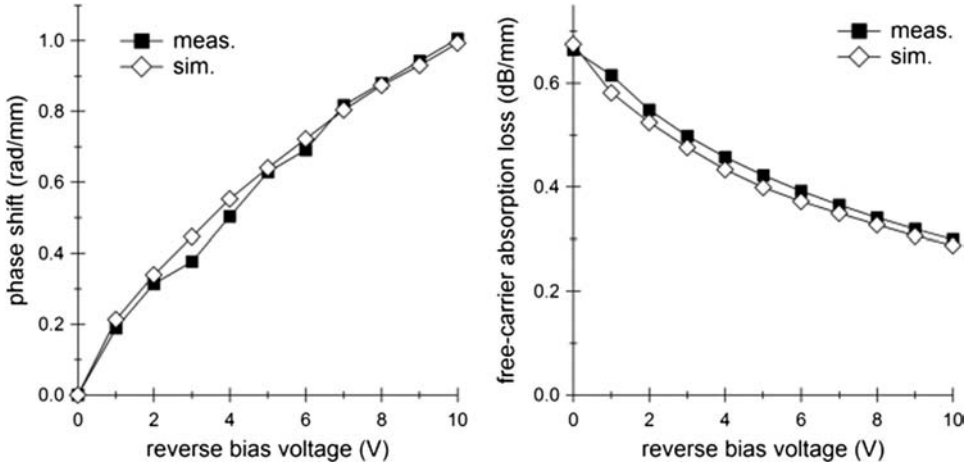

Figure 5.20 Simulated and measured electro-refraction and electro-absorption characteristics of the lateral PN-junction phase shifter under reverse bias.

observed between the simulated and the measured characteristics. Therefore, the computational method described in this subsection allows us to perform accurate design and modeling of the carrier-depletion lateral PN-junction rib-waveguide phase shifters on a silicon-photonics platform.

High-speed performance of the phase shifter is characterized computationally by solving Eqs. (5.25)–(5.29) with the input of an electrical voltage pulse, as presented in Fig. 5.21. The input electrical voltage pulse in Fig. 5.21(a) has linear onset/offset ramps in 1-ps fall and rise times and a 7-V_{pp} amplitude under −1.5-V DC bias voltage.[145] The onset and offset ramps to more and less negative voltages imply carrier depletion and subsequent carrier recovery. The input electrical pulse leads to a dynamic response of the phase shifter in transients of effective refractive index n_{eff} in Fig. 5.21(b). The rise and fall times τ_R and τ_F in n_{eff} are obtained as 3.2 ps and 6.6 ps, respectively, for a 10–90% change in n_{eff}, as indicated in Fig. 5.21(c). The transients of n_{eff} are governed by the dynamics of electrons and holes in the phase shifter.

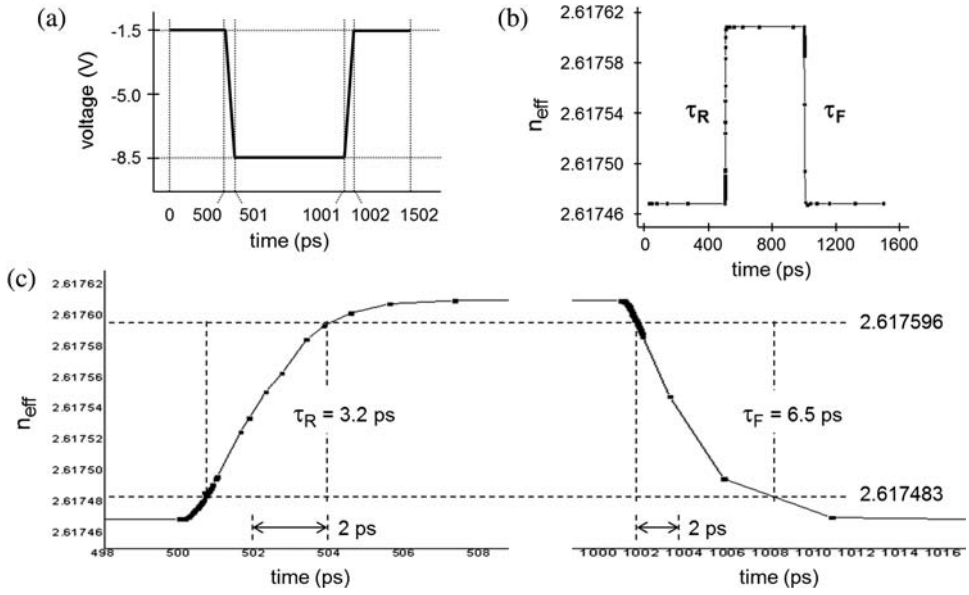

Figure 5.21 (a) Input electrical voltage signal with linear ramps. (b) Simulated transient trace of effective refractive index n_{eff}. (c) Rise and fall edges of the trace in (b).

The rise in n_{eff} is generated by the transport of electrons and holes swept with drift velocities from a region around the junction boundary (carrier-depletion process), whereas the fall in n_{eff} is produced by pumping the carriers toward the junction boundary (carrier-recovery process). In the recovery process, dense carriers are loaded up into the middle of core. A period of time then elapses to relax the loaded carriers into equilibrium distribution via local diffusion. Therefore, τ_F is longer than τ_R. The response time constants are much shorter than 10 ps, so the lateral PN-junction carrier-depletion phase shifter is, in principle, capable of phase modulation beyond a 100-Gbaud symbol rate except for the limitations of RF conductor loss and parasitic electrical resistance.

Optical eye diagrams can be generated computationally with an input electrical bit stream for a mathematical model of a single-drive MZ optical modulator. An optical eye diagram in 10-Gb/s NRZ-OOK is presented in Fig. 5.22. The bit length and frequency bandwidth of the electrical signal are 500 bits and 20 GHz, respectively. White Gaussian noise is added to the electrical signal in an amplitude signal-to-noise ratio (SNR) of 15 dB. High-contrast NRZ-OOK modulation is observed in the simulation with clear eye opening and an extinction ratio $ER \geq 10$ dB.[53] The simulated optical eye diagram can be compared with measured eye diagrams in the light of fundamental optical characteristics in Chapter 6.

The computational approach is also effective for the accurate design and modeling of the vertical PN-junction phase shifter illustrated in Fig. 5.9. The

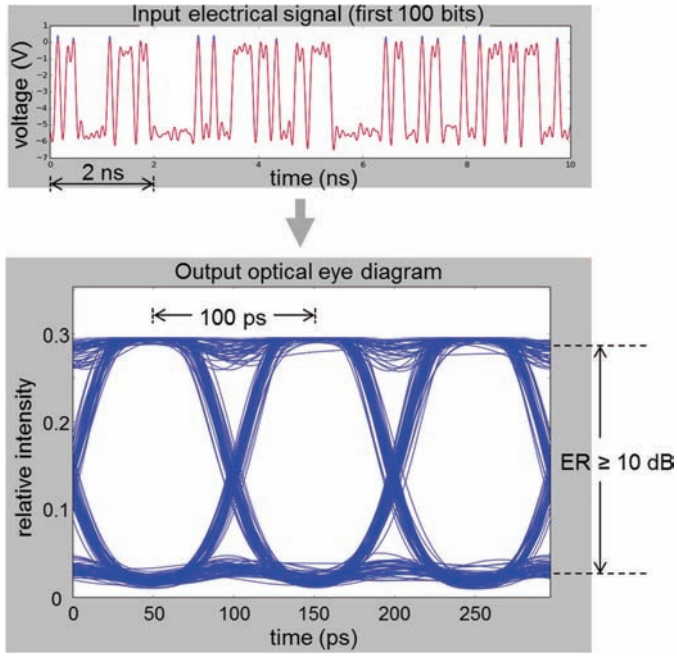

Figure 5.22 Input electrical bit stream (first 100 bits) and simulated optical eye diagram in 10-Gb/s NRZ OOK.

vertical PN-junction phase shifter has a potential of small-footprint phase shifters used for low-voltage MZ optical modulators. The steady-state numerical solution of Eqs. (5.25)–(5.29) provides profiles of electron and hole distributions at reverse bias voltages as well as electron and hole components of free-carrier plasma dispersion obtained from numerical conversion of the carrier distribution profiles as for the lateral PN-junction phase shifter. The profiles at zero-bias and 3-V reverse-bias voltages are presented in Fig. 5.23. The depletion region in the phase shifter is expanded along the vertical direction under revere bias.

Electro-refraction and electro-absorption characteristics of the vertical PN-junction phase shifter are obtained computationally in the same procedure as for the lateral PN-junction phase shifter. Plasma-refraction phase shift and free-carrier absorption loss in the phase shifter are plotted against the reverse-bias voltage in Fig. 5.24. A numerical voltage-transmittance transfer curve of a MZ optical modulator is produced with the simulated phase-shifter characteristics. A simulated output-power curve plotted versus the reverse-bias voltage in Fig. 5.24 is obtained by adjusting optical power levels in the on/off state of the numerical transfer curve between V_π as fitting parameters with respect to a measured optical-power curve at a wavelength of 1544.8 nm. The output power levels are affected by fabrication-related imperfections such as side-wall roughness and pattern distortion, and

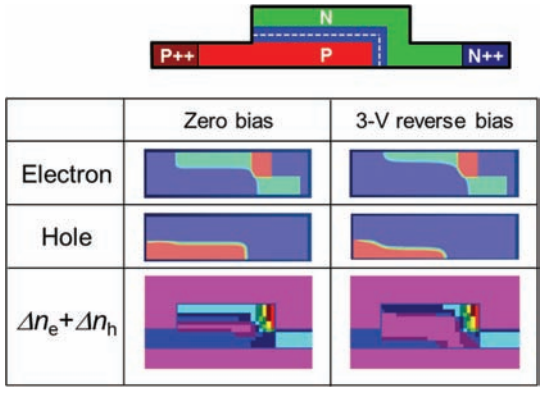

Figure 5.23 Simulated profiles of carrier distributions and spatial variation of plasma refraction.

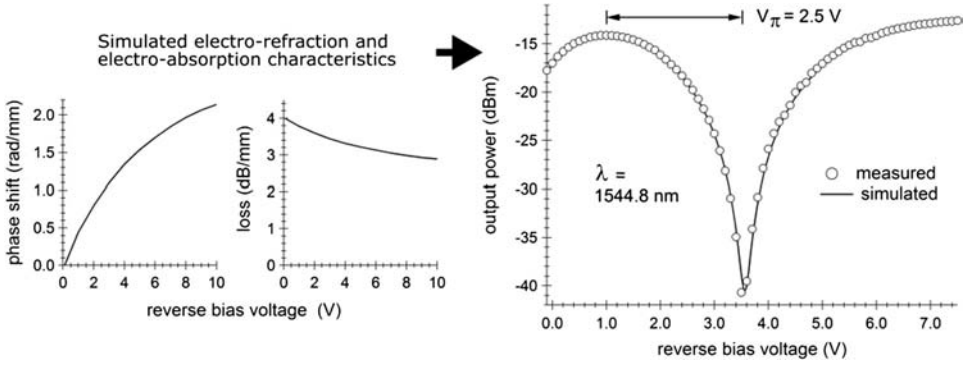

Figure 5.24 Simulated output-power curve generated from computational electro-refractive phase-shift and electro-absorptive loss characteristics of the vertical PN-junction phase shifter in comparison with the measured output-power curve.

thus should be determined empirically. The measured optical-power curve was acquired in a spectral power transmittance experiment with a swept-bias voltage, which is described in the next chapter.

One can see very good agreement between the simulated and the measured characteristics with V_π as low as 2.5 V.[146] This is less than half of the π-shift voltage for the lateral PN-junction phase shifter.[90] In conclusion of this subsection, the computational method proves itself as a tool for accurate design and modeling of carrier-depletion PN-junction phase shifters on a silicon-photonics platform.

5.3.3 Equivalent-circuit model

Theoretical analysis based on the equivalent-circuit model allows for the characterization of the electro-optic response of silicon-based MZ optical modulators integrated with traveling-wave electrodes.[147–150] A lumped-element

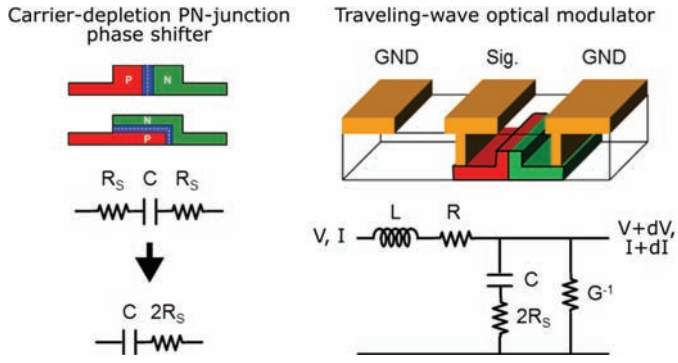

Figure 5.25 Minimal unit of a lumped-element equivalent circuit for a carrier-depletion phase shifter connected with a traveling-wave electrode.

equivalent circuit for carrier-depletion PN-junction phase shifters in traveling-wave electrodes is presented in Fig. 5.25. The reverse-biased PN junction in a carrier-depletion lateral or vertical PN-junction phase shifter can be represented as the electrical capacitance C per unit length. A slab wing adjoining the central rib on each side act as an electrical series resistance R_S per unit length, which is connected to the PN-junction capacitance. These separate series resistances are converted to a combined series resistance of 2 R_S for unit length.[110,148] A lumped-element equivalent circuit of coplanar waveguide that has a center signal (sig.) strip electrode and side ground (GND) planar electrodes includes the electrical resistance R per unit length to represent RF conductor loss.[151–155] The phase-shifter equivalent circuit is embedded between a signal line and a ground plane in an equivalent circuit of a traveling-wave optical modulator. A parallel electrical resistance of G^{-1} per unit length is inserted to deal with the leakage current through the reverse-bias PN junction and RF absorption loss due to carriers in the SOI layer and the silicon substrate. The lumped-element circuit is a minimal unit and iterated along the propagation direction of guided lightwave along the z axis over the phase-shifter optical waveguide. The lumped elements in a microscopic length of dz along the z direction are listed in Table 5.2. The lumped circuit element of combined series resistance is inversely proportional to the length. For simplicity, the parallel electrical resistance is neglected, namely, $G = 0$, in the mathematical analysis below. The lumped-element circuit can be applied for modeling a lumped-element optical modulator.

Table 5.2 Lumped circuit elements of a PN-junction phase shifter with a traveling-wave electrode in a microscopic length of dz.

Inductance of Signal Electrode	Resistance of Signal Electrode	Capacitance of PN Junction	Combined Series Resistance
$L \cdot dz$	$R \cdot dz$	$C \cdot dz$	$2\ R_S/dz$

Kirchhoff's voltage law yields the differential equation for AC voltage V as[156]

$$\frac{\partial V}{\partial z} = -(R + i\omega L)I. \tag{5.30}$$

Here, $\partial/\partial t$ is replaced with $i\omega$ because of AC analysis. Kirchhoff's current law provides the following differential equation:

$$\frac{\partial I}{\partial z} = \frac{-\omega C}{1 - i\omega 2R_S C} \tag{5.31}$$

for a stationary AC current, where I approximates the voltage across the phase shifter as V (dV omitted). The capacitance C of a PN junction is regarded as a constant independent of the AC voltage because of small-signal analysis. Equations (5.30) and (5.31) lead to a telegraphic equation for the AC voltage written as

$$\frac{\partial^2 V}{\partial z^2} = \Gamma^2 V, \tag{5.32}$$

with a forward traveling-wave solution

$$V = V_0 e^{\Gamma z}. \tag{5.33}$$

Here, factor Γ in the exponent is

$$\Gamma = \sqrt{\frac{-\omega C(R + i\omega L)}{1 - i\omega 2R_S C}}. \tag{5.34}$$

Iteration of the minimal circuit unit implies that the definite integral of Eq. (5.32) is the limit of $dz \to 0$. Assuming low electrical resistances, whereby $R \ll \omega L$ and $2R_S C \ll \omega^{-1}$, one can derive the following result:

$$\Gamma = i\Gamma_{\text{prop}} - \Gamma_{\text{atten}}, \tag{5.35}$$

with

$$\Gamma_{\text{prop}} = \omega\sqrt{LC} \tag{5.36}$$

and

$$\Gamma_{\text{atten}} = \omega^2\sqrt{LC}R_S C. \tag{5.37}$$

In the lumped-element circuit, the junction capacitor acts as a high-pass element, and AC electrical signals in the higher frequency flow more through the capacitor and are attenuated due to joule loss in the series resistance,

whereby the electro-optic frequency bandwidth of the silicon-based MZ optical modulator is limited. The transient characteristics of optical modulation in the time domain are also limited by a time constant of $2R_SC$ in capacitance–resistance coupling. For a lateral PN-junction rib-waveguide phase shifter with a 95-nm slab height and a 4-mm length, R_S and C are 5.7 Ω and 1.6 pF, respectively.[148]

Experimental results for the electro-optic and optical-modulation characteristics of silicon-based MZ modulators that have lateral PN-junction phase shifters will be presented in the next chapter. Further, the resistance R of a traveling-wave signal electrode will not be negligible for a long phase shifter, and the attenuation of input electrical signals due to conductor loss will also occur.[157] In such a case, computational analysis is required for accurate characterization. More detailed equivalent-circuit models have been proposed to include parasitic lumped elements in the peripheral area of carrier-depletion PN-junction phase shifters.[149,150]

5.3.4 Remarks on designing traveling-wave electrodes

To design traveling-wave electrodes, the first thing is to lay out the signal and ground electrodes in a cross-sectional plane to adjust the impedance of the traveling-wave electrodes to the specified value such as 50 Ω. Triangular mesh is adopted in modeling traveling-wave electrodes in the FEM.[158] In the case of CPW, its impedance is determined by the widths of the central signal conductor and the gap between the signal conductor and one of the side ground planes. The widths can be optimized in numerical calculation based on the FEM. In the silicon-based traveling-wave modulator, the conductor width and the gap width are 10 μm and 6.4 μm, respectively, for an impedance ∼50 Ω.[53]

To obtain the capacitance of traveling-wave electrodes, numerical calculation can be implemented semi-analytically by conformal mapping and computationally by FEM simulation.[158–160] In conformal mapping, the 2D cross-section of the traveling-wave electrodes is converted to a planar capacitor by coordinate transformation with the electrode thickness neglected. Thereby, the capacitance of the traveling-wave electrodes is obtained analytically as the capacitance of a planar capacitor.[159] The conductor width and gap width are transformed to the width of a planar electrode of the capacitor and the spacing between the planar electrodes, respectively. Two-dimensional mesh is sufficient to compute the capacitance of the electrodes. However, the inductance of traveling-wave electrodes cannot be adjusted independently because it depends only on the conductor width. To resolve this limitation, a silicon-based traveling-wave MZ optical modulator with lumped inductors integrated to traveling-wave electrodes was designed and characterized.[161] Impedance can be controlled precisely with independent adjustment of inductance.

References

1. A. Yariv and P. Yeh, *Optical Waves in Crystals: Propagation and Control of Laser Radiation*, John Wiley and Sons, Hoboken, New Jersey, 220–317 (2003).
2. K. Seeger, *Semiconductor Physics—an Introduction*, 3rd Ed., Springer-Verlag, Berlin, Heidelberg, 181–185 (1985).
3. N. J. Persons, A. C. O'Donnell, and K. K. Wong, "Design of efficient and wideband travelling-wave modulators," *Proc. SPIE* **651**, 148–153 (1986).
4. M. Izutsu, T. Itoh, and T. Sueta, "10 GHz bandwidth traveling-wave $LiNbO_3$ optical waveguide modulator," *IEEE J. Quantum Electron.* **QE-14**(6), 394–395 (1978).
5. R. C. Alferness, "Waveguide electrooptic modulators," *IEEE Trans. Microwave Theory Tech.* **MTT-30**(8) 1121–1137 (1982).
6. E. L. Wooten, K. M. Kissa, A. Yi-Yan, E. J. Murphy, D. A. Lafaw, P. F. Hallemeier, D. Maack, D. V. Attanasio, D. J. Fritz, G. J. McBrien, and D. E. Bossi, "A review of lithium niobate modulators for fiber-optic communications systems," *IEEE J. Sel. Top. Quantum Electron.* **6**(1), 69–82 (2000).
7. K. Noguchi Member, O. Mitomi, and H. Miyazawa, "Millimeter-wave Ti:$LiNbO_3$ optical modulators," *J. Lightwave Technol.* **16**(4), 615–619 (1998).
8. P. Rabiei, J. Ma, J. Chiles, S. Khan, and S. Fathpour, "High-index contrast, low-voltage lithium niobate modulators," *2013 IEEE Avionics, Fiber-Optics and Photonics Technology Conference (AVFOP)*, 43–44 (2013).
9. D. Haas, H. Yoon, H.-T. Man, G. Cross, S. Mann, and N. Parsons, "Polymeric electro-optic waveguide modulator; materials and fabrication," *Proc. SPIE* **1147**, 222–232 (1990).
10. C. C. Teng, "Traveling-wave polymeric optical intensity modulator with more than 40 GHz of 3-dB electrical bandwidth," *Appl. Phys. Lett.* **60** (13), 1538–1540 (1992).
11. Y. Shi, W. Lin, D. J. Olson, J. H. Bechtel, H. Zhang, W. H. Steier, C. Zhang, and L. R. Dalton, "Electro-optic polymer modulators with 0.8 V half-wave voltage," *Appl. Phys. Lett.* **77**(1), 1–3 (2000).
12. Y. Enami, C. T. Derose, D. Mathine, C. Loychik, C. Greenlee, R. A. Norwood, T. D. Kim, J. Luo, Y. Tian, A. K.-Y. Jen, and N. Peyghambarian, "Hybrid polymer/sol-gel waveguide modulators with exceptionally large electro-optic coefficients," *Nature Photon.* **1**, 180–185 (2007).
13. R. Palmer, L. Alloatti, D. Korn, P. C. Schindler, R. Schmogrow, W. Heni, S. Koenig, J. Bolten, T. Wahlbrink, M. Waldow, H. Yu, W. Bogaerts, P. Verheyen, G. Lepage, M. Pantouvaki, J. Van Campenhout, P. Absil, R. Dinu, W. Freude, C. Koos, and J. Leuthold,

"Silicon-organic hybrid MZI modulator generating OOK, BPSK and 8-ASK signals for up to 84 Gbit/s," *IEEE Photon. J.* **5**(2), 6600907 (2013).
14. S. Wolf, H. Zwickel, C. Kieninger, Y. Kutuvantavida, M. Lauermann, J. Lutz, L. Altenhain, R. Schmid, W. Freude, C. Koos, and S. Randel, "Silicon-organic hybrid (SOH) IQ modulator for 100 GBd 16QAM operation," *Optical Fiber Communications Conference and Exhibition (OFC)*, Th5C.1 (2017).
15. M. Lauermann, S. Wolf, R. Palmer, S. Koeber, P. C. Schindler, T. Wahlbrink, J. Bolten, A. L. Giesecke, M. Koenigsmann, M. Kohler, D. Malsam, D. L. Elder, L. R. Dalton, J. Leuthold, W. Freude, and C. Koos, "High-speed and low-power silicon-organic hybrid modulators for advanced modulation formats," *Proc. SPIE* **9516**, 951607-1–951607-5 (2015).
16. R. A. Soref and B. A. Bennett, "Electrooptical effects in silicon," *IEEE J. Quantum Electron.* **QE-23**(1), 123–129 (1987).
17. W. L. Bond, B. G. Cohen, R. C. C. Leite, and A. Yariv, "Observation of the dielectric-waveguide mode of light propagation in p-n junctions," *Appl. Phys. Lett.* **2**(3), 57–59 (1963).
18. A. K. Jonscher and M. H. Boyle, "The flow of carriers and its effect on the spatial distribution of radiation from injection lasers," *Proc. Symp. GaAs*, 12A (1966).
19. G. H. B. Thompson, "A theory for filamentation in semiconductor lasers including the dependence of dielectric constant on injected carrier density," *Opto-electronics* **4**(3), 257–310 (1972).
20. O. Mikami and H. Nakagome, "Waveguide optical switch in InGaAs/InP using free-carrier plasma dispersion," *Electron. Lett.* **20**(6), 228–229 (1984).
21. M. Asada, "Theoretical linewidth enhancement factor α of GaInAs/InP lasers," *IEICE Trans.* **E68**(8), 518–520 (1985).
22. R. A. Soref and J. P. Lorenzo, "All-silicon active and passive guided-wave components for $\lambda = 1.3$ and 1.6 μm," *IEEE J. Quantum Electron.* **22**(6), 873–879 (1986).
23. R. A. Soref and J. P. Lorenzo, "Silicon guided-wave optics," *Solid State Technol.* **31**(11), 95–98, (1988).
24. B. R. Bennett, R. A. Soref, and J. A. Del Alamo, "Carrier-induced change in refractive index of InP, GaAs, and InGaAsP," *IEEE J. Quantum Electron.* **26**(1), 113–122 (1990).
25. M. Becker and H. Y. Fan, "Optical properties of semiconductors. II. Infra-red transmission of germanium," *Phys. Rev.* **76**(10), 1530–1531 (1949).
26. M. Becker and H. Y. Fan, "Optical properties of semiconductors. III. Infra-red transmission of silicon," *Phys. Rev.* **76**(10), 1531–1532 (1949).

27. H. B. Briggs, "Infra-red absorption in silicon," *Phys. Rev.* **77**(5), 727–722 (1950).
28. H. B. Briggs and R. C. Flecher, "Absorption of infrared light by free carriers in germanium," *Phys. Rev.* **91**(6), 1342–1346 (1953).
29. H. Y. Fan, W. Spitzer, and J. R. Collins, "Infrared absorption in n-type germanium," *Phys. Rev.* **101**(2), 566–572 (1956).
30. W. Spitzer and H. Y. Fan, "Infrared absorption in n-type silicon," *Phys. Rev.* **108**(2), 268–271 (1957).
31. R. Rosenberg and M. Lax, "Free-carrier absorption in n-type Ge," *Phys. Rev.* **112**(3), 843–852 (1958).
32. W.G. Spitzer and J. M. Whelan, "Infrared absorption and electron effective mass in n-type gallium arsenide," *Phys. Rev.* **114**(1), 59–63 (1959).
33. H. R. Riedl, "Free-carrier absorption in PbTe," *Phys. Rev.* **127**(1), 162–166 (1962).
34. R. M. Culpepper and J. R. Dixon, "Free-carrier absorption in n-type indium arsenide," *J. Opt. Soc. Am.* **58**(1), 96–102 (1968).
35. J. D. Wiley and M. Didomenico, "Free-carrier absorption in n-type GaP," *Phys. Rev. B* **1**(4), 1655–1659 (1970).
36. A. H. Kahn, "Theory of the infrared absorption of carriers in germanium and silicon," *Phys. Rev.* **97**(6), 1647–1652 (1955).
37. W. P. Dumke, "Quantum theory of free carrier absorption," *Phys. Rev.* **124**(6), 1813–1817 (1961).
38. D.K. Schroder, R.N. Thomas, and J.C. Swartz, "Free carrier absorption in silicon," *IEEE J. Solid-State Circ.* **13**(1), 180–187 (1978).
39. M. S. Dresselhaus, *Solid State Physics Part II Optical Prpoerties of Solids*, MIT course, 6.732 Solid State Physics, 1–14 (2001); http://web.mit.edu/course/6/6.732/www/6.732-pt2.pdf.
40. J. N. Hodgson, *Optical Absorption and Dispersion in Solids*, Chapman and Hall, 62–96 (1970).
41. J. M. Ziman, *Principles of the Theory of Solids*, 2nd Ed., Cambridge University Press, Cambridge, New York, 146–186 (1972).
42. K. Seeger, *Semiconductor Physics—an Introduction*, 3rd Ed., Springer-Verlag, Berlin Heidelberg, 217–221 (1985).
43. M. Takenaka and S. Takagi, "Strain engineering of plasma dispersion effect for SiGe optical modulators," *IEEE J. Quantum Electron.* **48**(1), 8–16 (2012).
44. P. Drude, "Zur Ionentheorie der Metalle," *Physikal. Zeitschr.* **1**(14), 161–165 (1900).
45. G. Masetti, M. Severi, and S. Solmi, "Modeling of carrier mobility against carrier concentration in arsenic-, phosphorus-, and boron-doped silicon," *IEEE Trans. Electron Dev.* **30**(7), 764–769 (1983).

46. M. Nedeljkovic, R. Soref, and G. Z. Mashanovich, "Free-carrier electrorefraction and electroabsorption modulation predictions for silicon over the 1–14-μm infrared wavelength range," *IEEE Photon. J.* **3**(6), 1171–1180 (2011).
47. M. Nedeljkovic, R. Soref, and G. Z. Mashanovich, "Predictions of Free-carrier electroabsorption and electrorefraction in germanium," *IEEE Photon. J.* **7**(3), 2600214 (2015).
48. D. K. Ferry, J. Zimmermann, P. Lugli, and H. Grubin, "Limitations to ballistic transport in semiconductors," *IEEE Electron Dev. Lett.* **2**(9), 228–230 (1981).
49. S.L. Teitel and J.W. Wilkins, "Ballistic transport and velocity overshoot in semiconductors: Part I—Uniform field effects," *IEEE Trans. Electron Dev.* **30**(2), 150–153 (1983).
50. J.G. Ruch, "Electron dynamics in short channel field-effect transistors," *IEEE Trans. Electron Dev.* **19**(5), 652–654 (1972).
51. C. J. Rauch, J. J. Stickler, H. J. Zeiger, and G. S. Heller, "Millimeter cyclotron resonance in silicon," *Phys. Rev. Lett.* **4**(2), 64–66 (1960).
52. D. F. Edwards, "Silicon (Si)," in *Handbook of Optical Constants of Solids*, E. D. Palik, Ed, Academic Press, Orlando, 547–569 (1985).
53. K. Ogawa, H. Ishihara, K. Goi, Y. Mashiko, S. T. Lim, M. J. Sun, S. Seah, C. E. Png, T.-Y. Liow, X. Tu, G.-Q. Lo, and D.-L. Kwong, "Fundamental characteristics and high-speed applications of carrier-depletion silicon Mach-Zehnder modulators," *IEICE Electron. Express* **11** (24), 20142010 (2014).
54. R. Dingle, W. Wiegmann, and C. H. Henry, "Quantum states of confined carriers in very thin $Al_xGa_{1-x}As$-GaAs-$Al_xGa_{1-x}As$ heterostructures," *Phys. Rev. Lett.* **33**(14), pp. 827–830 (1974).
55. J. L. M. Quiroz González and D. Thompson, "Getting started with Numerov's method," *Comp. Phys.* **11**(5), 514–515 (1997).
56. I. Th. Famelis and Ch. Tsitouras, "Symbolic derivation of order conditions for hybrid Numerov-type methods solving $y'' = f(x, y)$," *J. Comput. Appl. Math.* **218**(2), 543–555 (2008).
57. R. C. Miller, D. A. Kleinman, W. T. Tsang, and A. C. Gossard, "Observation of the excited level of the excitons in GaAs quantum wells," *Phys. Rev. B* **24**(2), 1134–1136 (1981).
58. G. H. Wannier, "The structure of electronic excitation levels in insulating crystals," *Phys. Rev.* **52**(3), 191–197 (1937).
59. G. Dresselhaus, "Effective mass approximation for excitons," *J. Phys. Chem. Solids* **1**(1–2) 14–22 (1956).
60. R. J. Elliot, "Intensity of optical absorption by excitons," *Phys. Rev.* **108** (6), 1384–1389 (1957).
61. Y. Toyozawa, "Theory of line-shapes of the exciton absorption bands," *Prog. Theor. Phys.* **20**(1), 53–81 (1958).

62. R. S. Knox, "Theory of Excitons," in *Solid State Physics: Supplement* **5**, F. Seits and D. Turnbull, Eds. Academic Press, New York, London (1963).
63. E. F. Gross, "Optical spectrum of exciton in the crystal lattice," *Il Nuovo Cimento* **3**(S4), 672–701 (1956).
64. M. D. Sturge, "Optical absorption of gallium arsenide between 0.6 and 2.75 eV," *Phys. Rev.* **127**(3), 768–773 (1962); Erratum *Phys. Rev.* **129**(6), 2835–2835 (1963).
65. S. Schmitt-Rink, D.S. Chemla, and D.A.B. Miller, "Linear and nonlinear optical properties of semiconductor quantum wells," *Adv. Physics* **38**(2), 89–188 (1989).
66. D. A. B. Miller, D. S. Chemla, T. C. Damen, A. C. Gossard, W. Wiegmann, T. H. Wood, and C. A. Buruss, "Electric field dependence of optical absorption near the bandgap of quantum well structures," *Phys. Rev. B* **32**(2), 1043–1060 (1985).
67. U. Koren, B. I. Miller, R.S. Tucker, G. Eisenstein, I. Bar-Joseph, D.A.B. Miller, and D.S. Chemla, "High-frequency InGaAs/InP multiple-quantum-well buried-mesa electroabsorption optical modulator," *Electron. Lett.* **23**(12), 621–622 (1987).
68. K. Wakita, S. Nojima, K. Nakashima, and Y. Kawaguchi, "GaInAs/InP waveguide multiple-quantum-well optical modulator with 9 dB on/off ratio," *Electron. Lett.* **23**(20), 1067–1069 (1987).
69. J. S. Weiner, D. A. B. Miller, and D. S. Chemla, "Quadratic electro-optic effect due to the quantum-confined Stark effect in quantum wells," *Appl. Phys. Lett.* **52**(13), 945–947 (1987).
70. Y. Kan, H. Nagai, M. Yamanishi, and I. Suemune, "Field effects on the refractive index and absorption coefficient in AlGaAs quantum well structures and their feasibility for electrooptic device applications," *IEEE J. Quantum Electron.* **23**(12), 2167–2180 (1987).
71. J. E. Zucker and T. L. Hendrickson, "Electro-optic phase modulation in GaAs/AlGaAs quantum well waveguides," *Appl. Phys. Lett.* **50**(12), 842–844 (1988).
72. K. Ogawa and Y. Matsui, "Time-frequency spectroscopy of an InGaAs/InP quantum-well exciton Bragg reflector," *Appl. Phys. Lett.* **74**(18), 2569–2571 (1999).
73. K. Ogawa and K. Nishide, "Is silicon photonics a competitive technology to enable better and highly performing networks?," *Silicon Photonics III, Systems and Applications*, Eds. L. Pavesi and D. J. Lockwood, Topics in Applied Physics **122**, Springer-Verlag, Berlin, Heidelberg, 447–472 (2016).
74. M. S. Dresselhaus, *Solid State Physics Part II Optical Prpoerties of Solids*, MIT course, 6.732 Solid State Physics, 48–50 (2001); http://web.mit.edu/course/6/6.732/www/6.732-pt2.pdf.

75. L. M. Roth, "Dynamics of electrons in semiconductors in electric and magnetic fields," in *Handbook on Semiconductors*, T. S. Moss, Ed., North-Holland, Amsterdam, New York, Oxford, 451–485 (1982).
76. M. Asghari and A. V. Krishnamoorthy, "Silicon photonics: Energy-efficient communication," *Nature Photon*. **5**(5), 268–270 (2011).
77. J. Liu, M. Beals, A. Pomerene, S. Bernardis, R. Sun, J. Cheng, L. C. Kimerling, and J. Michel, "Waveguide-integrated, ultralow-energy GeSi electro-absorption modulators," *Nature Photon.* **2**, 433–437 (2008).
78. S. Gupta, S. A. Srinivasan, M. Pantouvaki, H. Chen, P. Verheyen, G. Lepage, D. Van Thourhout, G. Roelkens, K. Saraswat, P. Absil, and J. Van Campenhout, "50GHz Ge waveguide electro-absorption modulator integrated in a 220nm SOI photonics platform," *Optical Fiber Communications Conference and Exhibition (OFC)*, Tu2A.4 (2015).
79. H. D. Thacker, X. Zheng, J. Lexau, R. Shafiiha, I. Shubin, S. Lin, S. Djordjevic, P. Amberg, E. Chang, F. Liu, John Simons, J.-H. Lee, A. Abed, H. Liang, Y. Luo, J. Yao, D. Feng, M. Asghari, R. Ho, K. Raj, J. E. Cunningham, and Ashok V. Krishnamoorthy, "An all-solid-state, WDM silicon photonic digital link for chip-to-chip communications," *Opt. Express* **23**(10), 12808–12822 (2015).
80. G. D. Boyd, W. L. Bond, and H. L. Carter, "Refractive index as a function of temperature in $LiNbO_3$," *J. Appl. Phys.* **38**(4), 1941–1943 (1967).
81. H. W. Icenogle, B. C. Platt, and W. L. Wolfe, "Refractive indexes and temperature coefficients of germanium and silicon," *Appl. Opt.* **15**(10), 2348–2351 (1976).
82. P. Lautenschlager, M. Garriga, L. Vina, and M. Cardona, "Temperature dependence of the dielectric function and interband critical points in silicon," *Phys. Rev. B* **36**(9), 4821–4830 (1987).
83. G. E. Jellison Jr. and F. A. Modine, "Optical functions of silicon at elevated temperatures," *J. Appl. Phys.* **76**(6), 3758–3761 (1994).
84. G. Ghosh, "Temperature dispersion of refractive indices in semiconductors," *J. Appl. Phys.* **79**(12), 9388–9389 (1996).
85. G. Cocorullo, F. G. Della Corte, and I. Rendina, "Temperature dependence of the thermo-optic coefficient in crystalline silicon between room temperature and 550 K at the wavelength of 1523 nm," *Appl. Phys. Lett.* **74** (22), 3338–3340 (1999).
86. B. J. Frey, D. B. Leviton, and T. J. Madison, "Temperature-dependent refractive index of silicon and germanium," *Proc. SPIE* **6273**, 62732J-1–62732J-10 (2006).
87. E. Conwell and V. F. Weisskopf, "Theory of impurity scattering in semiconductors," *Phys. Rev.* **77**(3), 388–390 (1950).
88. D. M. Riffe, "Temperature dependence of silicon carrier effective masses with application to femtosecond reflectivity measurements," *J. Opt. Soc. Am. B* **19**(5), 1092–1100 (2002).

89. N. Cavassilas and J.-L. Autran, "Energy and temperature dependence of electron effective masses in silicon," *J. Appl. Phys.* **92**(3), 1431–1433 (2002).
90. K. Goi, N. Ishikura, H. Ishihara, S. Sakamoto, K. Ogawa, T.-Y. Liow, X. Tu, G.-Q. Lo, and D.-L. Kwong, "Low-voltage silicon Mach-Zehnder modulator operating at high temperatures without thermo-electric cooling," *Optical Fiber Communications Conference and Exhibition (OFC)*, W2A.23 (2016).
91. S. Krishnamurthy, Z. G. Yu, L. P. Gonzalez, and S. Guha, "Temperature- and wavelength-dependent two-photon and free-carrier absorption in GaAs, InP, GaInAs, and InAsP," *J. Appl. Phys.* **109**, 033102-1–033102-9 (2011).
92. S. Dogru and N. Dagli, "0.77-V drive voltage electro-optic modulator with bandwidth exceeding 67 GHz," *Opt. Lett.* **39**(20), 6074–6076 (2014).
93. P. W. Juodawlkis, F. J. O'Donnell, R. J. Bailey, J. J. Plant, K. G. Ray, D. C. Oakley, A. Napoleone, M. R. Watts, and G. E. Betts, "InGaAsP/InP quantum-well electrorefractive modulators with sub-volt V_{π}," *Proc. SPIE* **5435**, 53–63 (2004).
94. M. U. Sadiq, M. R. Gleeson, N. Ye, J. O'Callaghan, P. Morrissey, H. Y. Zhang, K. Thomas, A. Gocalinska, E. Pelucchi, F. C. G. Gunning, B. Roycroft, F. H. Peters, and B. Corbett, "10 Gb/s InP-based Mach-Zehnder modulator for operation at 2 μm wavelengths," *Opt. Express* **23** (9), 10905–10913 (2015).
95. I. Vurgaftman, J.R. Meyer, and L.R. Ram-Mohan, "Band parameters for III-V compound semiconductors and their alloys," *J. Appl. Phys.* **89** (11), 5815–5875 (2001).
96. H. Y. Fan, "Temperature Dependence of the Energy Gap in Monatomic Semiconductors," *Phys. Rev.* **78**(6), 808–809 (1950).
97. P. Lautenschlager, P. B. Allen, and M. Cardona, "Temperature dependence of band gaps in Si and Ge," *Phys. Rev. B* **31**(4), 2163–2171 (1985).
98. A. Nakanishi, N. Sasada, Y. Sakuma, R. Washino, K. Okamoto, K. Naoe, H. Hayashi, H. Arimoto, and S. Tanaka "Uncooled (0 to 85°C) and full C-band operation of a 10.7 Gbit/s InP Mach-Zehnder modulator monolithically integrated with SOA," *Optical Fiber Communications Conference and Exhibition (OFC)*, OW1G.3 (2013).
99. D. A. B. Miller, "Energy consumption in optical modulators for interconnects," *Opt. Express* **20**(S2), A293–A308 (2012).
100. P. J. Winzer and R.-J. Essiambre, "Advanced optical modulation formats," *Proc. IEEE* **94**(5), 952–985 (2006).
101. K. Kikuchi, "Fundamentals of coherent Optical fiber communications," *J. Lightwave Technol.* **34**(1), 157–179 (2016).
102. F. Koyama and K. Iga, "Frequency chirping in external modulators," *J. Lightwave Technol.* **6**(1), 87–93 (1988).

103. A. H. Gnauck and P. J. Winzer, "Optical phase-shift-keyed transmission," *J. Lightwave Technol.* **23**(1), 115–130 (2005).
104. K. Goi, K. Oda, H. Kusaka, Y. Terada, K. Ogawa, T.-Y. Liow, X. Tu, G.-Q. Lo, and D.-L. Kwong, "11-Gb/s 80-km transmission performance of zero-chirp silicon Mach-Zehnder modulator," *Opt. Express* **20**(26), B350–B356 (2012).
105. K. Goi, H. Kusaka, A. Oka, Y. Terada, K. Ogawa, T.-Y. Liow, X. Tu, G.-Q. Lo, and D.-L. Kwong, "20-Gb/s DPSK transmission with 550-ps/nm dispersion tolerance using silicon Mach-Zehnder modulator," *Optical Fiber Communications Conference and Exhibition (OFC)*, OW4J.5 (2013).
106. G. T. Reed and C.E. Jason Png, "Silicon optical modulators," *Materialstoday* **8**(1), 40–50 (2005).
107. D. J. Thomson, F. Y. Gardes, J.-M. Fedeli, S. Zlatanovic, Y. Hu, B. P. P. Kuo, E. Myslivets, N. Alic, S. Radic, G. Z. Mashanovich, and G. T. Reed, "50-Gb/s silicon optical modulator," *IEEE Photon. Technol. Lett.* **24**(4), 234–236 (2012).
108. M. Ziebell, D. Marris-Morini, G. Rasigade, J.-M. Fédéli, P. Crozat, E. Cassan, D. Bouville, and L. Vivien, "40 Gbit/s low-loss silicon optical modulator based on a pipin diode," *Opt. Express* **20**(10), 10591–10596 (2012).
109. D. Patel, S. Ghosh, M. Chagnon, A. Samani, V. Veerasubramanian, M Osman, and D. V. Plant, "Design, analysis, and transmission system performance of a 41 GHz silicon photonic modulator," *Opt. Express* **23**(10), 14262–14287 (2015).
110. K. Ogawa, K. Goi, H. Kusaka, Y. Terada, T.-Y. Liow, X. Tu, G.-Q. Lo, D.-L. Kwong, V. Dixit, S. T. Lim, and C. E. Png, "Low-loss high-speed silicon Mach-Zehnder modulator for optical-fiber telecommunications," *Proc. SPIE* **8629**, 86290U-1–86290U-8 (2013).
111. X. Tu, T.-Y. Liow, J. Song, M. Yu, and G. Q. Lo, "Fabrication of low loss and high speed silicon optical modulator using doping compensation method," *Opt. Express* **19**(19), 18029–18035 (2011).
112. K. Goi, K. Ogawa, Y. T. Tan, V. Dixit, S. T. Lim, C. E. Png, T.-Y. Liow, X. Tu, G.-Q. Lo, and D.-L. Kwong, "Silicon Mach-Zehnder modulator using low-loss phase shifter with bottom PN junction formed by restricted-depth doping," *IEICE Electron. Express* **10**(17), 20130552 (2013).
113. X. Tu, T.-Y. Liow, J. Song, X. Luo, Q. Fang, M. Yu, and G. Q. Lo, "50-Gb/s silicon optical modulator with traveling-wave electrodes," *Opt. Express* **21**(10), 12776–12782 (2013).
114. J. C. Rosenberg, W. M. J. Green, S. Assefa, D. M. Gill, T. Barwicz, M. Yang, M. Shank, and Y. A. Vlasov, "A 25 Gbps silicon microring modulator based on an interleaved junction," *Opt. Express* **20**(24), 26411–26423 (2012).

115. G. T. Reed, G. Z. Mashanovich, F. Y. Gardes, M. Nedeljkovic, Y. Hu, D. J. Thomson, K. Li, P. R. Wilson, S.-W. Chen, and S. S. Hsu, "Recent breakthroughs in carrier depletion based silicon optical modulators," *Nanophotonics* **3**(4–5), 229–245 (2014).
116. M. R. Watts, W. A. Zortman, D. C. Trotter, R. W. Young, and A. L. Lentine, "Low-voltage, compact, depletion-mode, silicon Mach–Zehnder modulator," *IEEE J. Sel. Top. Quantum Electron.* **16**(1), 159–164 (2010).
117. S. S. Azadeh, F. Merget, S. Romero-García, A. Moscoso-Mártir, N. von den Driesch, J. Müller, S. Mantl, D. Buca, and J. Witzens, "Low V_π silicon photonics modulators with highly linear epitaxially grown phase shifters," *Opt. Express* **23**(18), 23526–23550 (2015).
118. T. Cao, Y. Fei, L. Zhang, Y. Cao, and S. Chen, "Design of a silicon Mach–Zehnder modulator with a U-type PN junction," *Appl. Opt.* **52** (24), 5941–5948 (2013).
119. M. Webster, P. Gothoskar, V. Patel, D. Piede, S. Anderson, R. Tummidi, D. Adams, C. Appel, P. Metz, S. Sunder, B. Dama, and K. Shastri, "An efficient MOS-capacitor based silicon modulator and CMOS drivers for optical transmitters," *IEEE 11th International Conference on Group IV Photonics (GFP)*, WB1 (2014).
120. A. Shastri, C. Muzio, M. Webster, G. Jeans, P. Metz, S. Sunder, B. Chattin, B. Dama, and K. Shastri, "Ultra-low-power single-polarization QAM-16 generation without DAC using a CMOS photonics based segmented modulator, *J. Lightwave Technol.* **33**(6), 1255–1260 (2015).
121. A. Liu, R. Jones, L. Liao, D. Samara-Rubio, D. Rubin, O. Cohen, R. Nicolaescu, and M. Paniccia, "A high-speed silicon optical modulator based on a metal-oxide-semiconductor capacitor," *Nature* **427**, 615–618 (2004).
122. L. Liao, D. Samara-Rubio, M. Morse, A. Liu, D. Hodge, D. Rubin, U. D. Keil, and T. Franck, "High speed silicon Mach-Zehnder modulator," *Opt. Express* **13**(8), 3129–3135 (2005).
123. J. Fujikata, M. Takahashi, S. Takahashi, T. Horikawa, and T. Nakamura, "High-speed and high-efficiency Si optical modulator with MOS junction, using solid-phase crystallization of polycrystalline silicon," *Japanese J. Appl. Phys.* **55**(4), 042202-1–042202-6 (2016).
124. J. Basak, L. Liao, A. Liu, D. Rubin, Y. Chetrit, H. Nguyen, D. Samara-Rubio, R. Cohen, N. Izhaky, and Mario Paniccia, "Developments in gigascale silicon optical modulators using free carrier dispersion mechanisms," *Adv. Opt. Technol.* **2008**, 678948 (2008).
125. W. Shockley, *Electrons and Holes in Semiconductors, with Applications to Transistor Electronics*, 1st Ed., D. van Nostrand, Toronto, New York, London, 86–91 (1950).
126. S. M. Sze, *Physics of Semiconductor Devices*, 2nd. Ed., J. Wiley & Sons, New York, 12–81 (1981).

127. D. Botez, "Analytical approximation of the radiation confinement factor for the TE_0 Mode of a double heterojunction laser," *IEEE J. Quantum Electron.* **14**(4), 230–232 (1978).
128. T. D. Visser, B. Demeulenaere, J. Haes, D. Lenstra, R. Baets, and H. Blok, "Confinement and modal gain in dielectric waveguides," *J. Lightwave Technol.* **14**(5), 885–887 (1996).
129. W. H. Press, S. A. Teukolsky, W. T. Vetterling, and B. P. Flannery, *Numerical Recipes, The Art of Scientific Computing*, 3rd Ed., Cambridge University Press, Cambridge, New York, 196–199 (2007).
130. K. Goi, A. Oka, H. Kusaka, Y. Terada, Kensuke Ogawa, T.-Y. Liow, X. Tu, G.-Q. Lo, and D.-L. Kwong, "Low-loss high-speed silicon IQ modulator for QPSK/DQPSK in C and L bands," *Opt. Express* **22**(9), 10703–10709 (2014).
131. C. K. Tang, G. T. Reed, A. J. Walton, and A. G. Rickman, "Low-loss, single-mode, optical phase modulator in SIMOX material," *J. Lightwave Technol.* **12**(8), 1394–1400 (1994).
132. C. E. Png, G. T. Reed, R. M. Atta, G. J. Ensell, and A. G. R. Evans, "Development of small silicon modulators in silicon-on-insulator (SOI)," *Proc. SPIE* **4997**, 190–197 (2003).
133. F. Gardes, G. Reed, N. Emerson, and C. Png, "A sub-micron depletion-type photonic modulator in silicon on insulator," *Opt. Express* **13**(22), 8845–8854 (2005).
134. L. Chrostowski and M. Hochberg, *Silicon Photonics Design: From Devices to Systems*, Cambridge University Press, Cambridge, New York, 28–46 (2015).
135. C. E. Png, M. J. Sun, S. T. Lim, T. Ang, and K. Ogawa, "Analysis of depletion silicon phase shifter based on computer simulation," *Proc. SPIE* **9752**, 975204-1–975204-6 (2016).
136. C. E. Png, M. J. Sun, S. T. Lim, T. Ang, and K. Ogawa, "Numerical modeling and analysis for high-efficiency carrier-depletion silicon rib-waveguide phase shifters," *IEEE J. Sel. Top. Quantum Electron.* **22**(6), 3300208 (2016).
137. J. J. Barnes and R. J. Lomax, "Finite-element methods in semiconductor simulation," *IEEE Trans. Electron Dev.* **24**(8), 1082–1089 (1977).
138. T. Adachi, A. Yoshii, and T. Sudo, "Two dimensional semiconductor analysis using finite-element method," *IEEE Trans. Electron Dev.* **26**(7), 1026–1031 (1979).
139. R. E. Bank, D. J. Rose, and W. Fichtner, "Numerical methods for semiconductor device simulation," *IEEE Trans. Electron Dev.* **30**(9), 1031–1041 (1983).
140. K. Yamaguchi, S. Sakurai, and K. Tomizawa, "An Accurate and Simplified Modeling of Energy and Momentum Relaxation Rates for

Metal–Oxide–Semiconductor Device Simulation," *Japanese J. Appl. Phys.* **49**(2R), 024303-1–024303-8 (2010).
141. http://www.silvaco.com/products/tcad/device_simulation/device_simulation.html
142. https://www.synopsys.com/silicon/tcad/device-simulation/sentaurus-device.html
143. https://www.lumerical.com/tcad-products/device/
144. https://www.photond.com/products/harold.htm
145. C. E. Png, S. P. Chan, S. T. Lim, and G. T. Reed, "Optical phase modulators for MHz and GHz modulation in silicon-on-insulator (SOI)," *J. Lightwave Technol.* **22**(6), 1573–1582 (2004).
146. N. Ishikura, K. Goi, H. Zhu, M. Illarionov, H. Ishihara, A. Oka, T. Oda, K. Masuko, T. Ori, K. Ogawa, Y. Yoshida, K. Kitayama, T.-Y. Liow, X. Tu, G.-Q. Lo, and D.-L. Kwong, "Transmission characteristics of 32-Gbaud PDM IQ monolithic silicon modulator operating with 2-V_{PPD} drive voltage," 42nd European Conference on Optical Communication (ECOC), W.2.E4 (2016).
147. R. A. Becker, "Broad-band guided-wave electrooptic modulators," *IEEE J. Quantum Electron.* **20**(7), 723–727 (1984).
148. K. Ogawa, K. Goi, Y. T. Tan, T.-Y. Liow, X. Tu, Q. Fang, G.-Q. Lo, and D.-L. Kwong, "Silicon Mach-Zehnder modulator of extinction ratio beyond 10 dB at 10.0-12.5 Gbps," *Opt. Express* **19**(26), B26–B31 (2011).
149. H. Yu and W. Bogaerts, "An equivalent circuit model of the traveling wave electrode for carrier-depletion-based silicon optical modulators," *J. Lightwave Technol.* **30**(11), 1602–1609 (2012).
150. H. Xu, X. Li, X. Xiao, Z. Li, Y. Yu, and J. Yu, "Demonstration and Characterization of High-Speed Silicon Depletion-Mode Mach–Zehnder Modulators, " *IEEE J. Sel. Top. Quantum Electron.* **20**(4), 3400110–3400110 (2014).
151. J. B. Knorr and K.-D. Kuchler, "Analysis of coupled slots and coplanar strips on dielectric substrate," *IEEE Trans. Microwave Theory Tech.* **23** (7), 541–548 (1975).
152. R. W. Jackson, "Considerations in the use of coplanar waveguide for millimeter-wave integrated circuits," *IEEE Trans. Microwave Theory Tech.* **34**(12), 1450–1456 (1986).
153. R. N. Simons, *Coplanar Waveguide Circuits, Components, and Systems*, John Wiley & Sons, New York, Chichester, Brisbane, Tronto, Singapore, 11–62 (2001).
154. C. Schöllhorn, W. Zhao, M. Morschbach, and E. Kasper, "Attenuation mechanisms of aluminum millimeter-wave coplanar waveguides on silicon," *IEEE Trans. Electron Dev.* **50**(3), 740–746 (2003).

155. J. Shin, S. R. Sakamoto, and N. Dagli, "Conductor loss of capacitively loaded slow wave electrodes for high-speed photonic devices," *J. Lightwave Technol.* **29**(1), 48–52 (2011).
156. R. J. Smith and R. C. Dorf, *Circuits, Devices and Systems*, 5th Ed., John Wiley & Sons, New York, Chichester, Brisbane, Tronto, Singapore, 35–47 (1992).
157. C. Schollhorn, Weiwei Zhao, M. Morschbach, and E. Kasper, "Attenuation mechanisms of aluminum millimeter-wave coplanar waveguides on silicon," *IEEE Trans. Electron Dev.* **50**(3), 740–746 (2003).
158. J. C. Yi, S. H. Kim, and S. S. Choi, "Finite-element method for the impedance analysis of traveling-wave modulators," *J. Lightwave Technol.* **8**(6), 817–822 (1990).
159. R. Schinzinger and P. A. A. Laura, *Conformal Mapping: Methods and Applications*, Dover Publications, Mineola, 273–309 (2003).
160. E. Chen and S. Y. Chou, "Characteristics of coplanar transmission lines on multilayer substrates: modeling and experiments," *IEEE Trans. Microwave Theory and Tech.* **45**(6), 939–945 (1997).
161. D. M. Gill, W. M. J. Green, C. Xiong, A. Rylyakov, C. Schow, J. Proesel, J. C. Rosenberg, T. Barwicz, M. Khater, S. Assefa, S. M. Shank, C. Reinholm, E. Kiewra, S. Kamlapurkar, and Y. A. Vlasov, "Distributed electrode Mach-Zehnder modulator with double-pass phase shifters and integrated inductors," *Opt. Express* **23**(13), 16857–16865 (2015).

Chapter 6
Optical, Electrical, and Electro-Optical Characteristics of Integrated Silicon-based Optical Modulators

As discussed in the previous chapter, carrier-depletion PN-junction rib-waveguide phase shifters are suitable for high-speed phase shifters on silicon-photonics platforms for small-footprint integrated MZ optical modulators operating in broad spectral ranges over the C and L bands with high temperature stability. In this chapter, the optical, electrical, and electro-optical characteristics of the integrated MZ optical modulators on a silicon-photonics platform are reviewed on the basis of experimental data. It starts with a review of the optical-loss characteristics of the building blocks in the integrated silicon-based MZ optical modulators. Plasma-refraction phase shift in the carrier-depletion rib-waveguide phase shifters and chromatic dispersion of passive optical waveguides are then discussed. Chromatic dispersion in the spectral phase of passive optical waveguides, which, in general, may deteriorate the dynamic performance of high-speed integrated optical modulators, is proved to be negligible in terms of inter-symbol interference. The electrical characteristics of the phase shifters are described with respect to the electrical and structural characterization of PN junctions in phase shifters on silicon-photonics platforms. Electro-optic responses in the RF frequency domain and optical modulation characteristics in the time domain, which are studied in the last two sections in this chapter, are essential to evaluate the dynamic performance of high-speed silicon-based integrated optical modulators.

6.1 DC Optical Characteristics

6.1.1 Optical loss

Optical losses of passive channel and rib optical waveguides are caused mainly by side-wall roughness in the fabrication processes.[1] The line-edge

roughness of a developed photoresist is transferred to the side walls of optical waveguides during the dry-etching process. Further roughness is also produced during the dry-etching process. The optical transmission spectra acquired for optical waveguides of different lengths provide the optical propagation loss per unit length. A series of optical-transmission measurements in this scheme are often referred to as cut-back measurements (after the optical loss measurements extensively used for optical fibers), although plural optical waveguides of specified lengths are arranged on a chip to measure the length dependence of the optical loss of the waveguide.[2] The measurement apparatus is shown in Fig. 6.1. An optical mask pattern is inserted as an exemplar layout of a test chip. The optical waveguides are folded to occupy the same rectangular footprint in the test sample chip for the ease of design layout as well as to increase the layout density. Channel or rib optical waveguides of different lengths are aligned adjacent to each other in each group of waveguides in a specified channel or rib width.

A single-polarization super-luminescent diode (SLD) is utilized as a low-coherence light source. The low coherence allows ripple-free spectrum measurement by suppressing undesired interference not essential to the characteristics of an optical waveguide under test. Cleaved-facet or lensed-tip fibers made of polarization-maintaining single-mode fiber (PMF) are utilized for polarization-selective input and output optical coupling with the optical waveguide under test. For cleaved-facet fibers, index-matching gel can be inserted in each interface between a PMF and a sample edge facet to avoid Fresnel reflection at the input and output interfaces. Reflection-free optical loss measurement is possible in this case. Lensed-tip fibers are used if a tight-focused light beam is required for optical coupling to the test optical waveguide. Fresnel reflection from the lensed tips and from the sample facets are not negligible. The light source is directly connected to the optical spectrum analyzer for the base optical spectrum to extract the transmission and reflection spectra. An optical

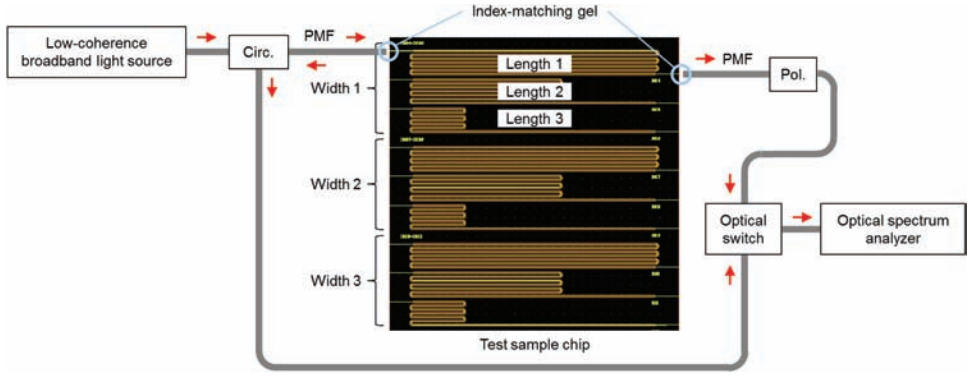

Figure 6.1 Block diagram of the optical-transmission spectrum measurement. Circ.: optical circulator; Pol.: polarizer.

circulator inserted in the input fiber line allows for the acquisition of the reflection spectrum. Transmitted or reflected light can be selected by an optical switch. A scanning optical spectrum analyzer provides the transmission or reflection spectrum of the test optical waveguide.

The optical insertion loss α_{loss} (in dB units) of the test optical waveguide is obtained as a function of wavelength λ from the following equation:

$$\alpha_{loss}(\lambda) = -10 \log_{10}\left[\frac{I_{in}(\lambda) - I_{trans}(\lambda) - I_{refl}(\lambda)}{I_{in}(\lambda)}\right], \tag{6.1}$$

with the input, transmitted, and reflected optical powers I_{in}, I_{trans}, and I_{refl}, respectively. The propagation loss per unit length and the coupling loss for a type of optical waveguide of a specified waveguide width, for instance, are obtained at each wavelength as indicated in Fig. 6.2. The test optical waveguides have a 500-nm channel width. A series of measurements of the test optical waveguides of five different lengths provide the optical loss as a function of length. The polarization of the launched light is in TE polarization. Parameter fitting using a linear fitting function allows for the measurement of the propagation loss from the slope of the line and coupling loss from the crossing point on the loss axis at zero length.[2] The propagation loss coefficient is 0.17 dB/mm, and the coupling loss is 3.3 dB in the graph; thus, a fiber coupling loss of ~1.7 dB per facet is obtained.

The above procedure has allowed for the measurement of the propagation loss for fabricated channel and rib optical waveguides against waveguide widths, plotted as a loss coefficient in Fig. 6.3 and listed in Tables 6.1 and 6.2.[3,4] The channel optical waveguides have a higher propagation loss coefficient than the rib optical waveguides because the vertical side walls

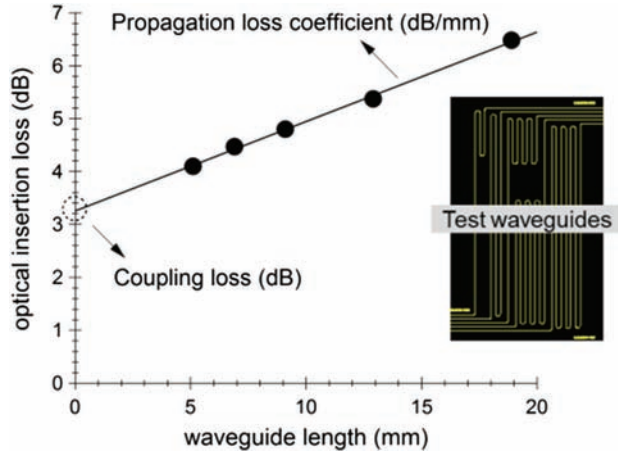

Figure 6.2 Optical insertion loss of a series of test optical waveguides as a function of the optical waveguide length.

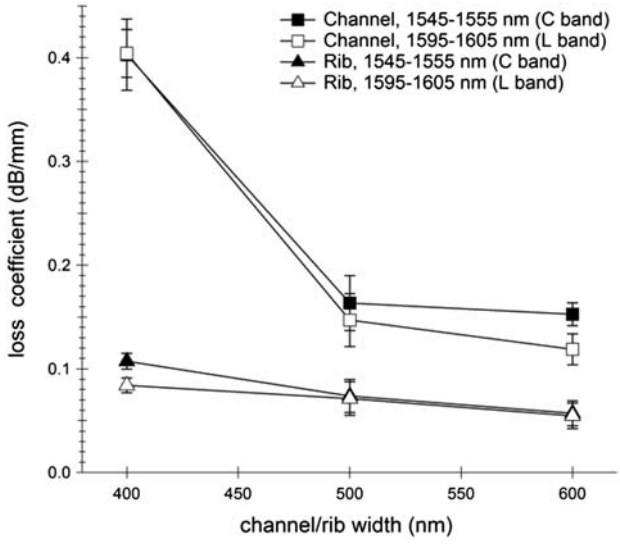

Figure 6.3 Optical propagation loss coefficient as a function of the width of channel or rib waveguides in the C and L bands.

Table 6.1 Optical propagation loss coefficient of channel or rib waveguides in the C band (1545–1555 nm).[3]

Channel Optical Waveguide			Rib Optical Waveguide		
400 nm	500 nm	600 nm	400 nm	500 nm	600 nm
0.403 dB/mm	0.163 dB/mm	0.153 dB/mm	0.107 dB/mm	0.074 dB/mm	0.057 dB/mm

Table 6.2 Optical propagation loss coefficient of channel or rib waveguides in the L band (1595–1605 nm).[3]

Channel Optical Waveguide			Rib Optical Waveguide		
400 nm	500 nm	600 nm	400 nm	500 nm	600 nm
0.404 dB/mm	0.147 dB/mm	0.119 dB/mm	0.084 dB/mm	0.071 dB/mm	0.055 dB/mm

occupy wider areas along the vertical direction. The loss coefficient decreases with an increasing waveguide width because of the weaker mode fields at the side walls with increases in the width, as expected from the computational mode fields presented in Chapter 4. A wider width is better for lower optical loss but with a greater possibility of higher-order mode propagation in the wider optical waveguide. To avoid such propagation, the widths should be set to 500 nm. This will be about the optimal choice because the loss reduction to increase the waveguide width from 500 nm to 600 nm is not substantial. An almost constant loss coefficient is observed over the C and L bands, and the channel and rib optical waveguides are suitable for building blocks of integrated optical modulators over the broad spectral range.

There is another source of optical loss: two-photon absorption under intense optical light. In high-index-contrast optical waveguides on a silicon-photonics platform, optical fields are confined inside nanometer-scale waveguide cores to produce high optical intensity and two-photon absorption. The latter in silicon optical waveguides has been investigated experimentally, and Table 6.3 compares the two-photon absorption coefficient in crystalline silicon with its counterparts in other semiconductor materials.[5–10] The coefficient in crystalline silicon is much smaller than the others and is therefore negligible in comparison with the optical loss due to side-wall roughness at a launched optical power level of ~10 dBm. Carriers generated by two-photon absorption cause free-carrier absorption. The optical loss due to the free-carrier absorption induced by two-photon absorption is still lower than the side-wall roughness loss.

Rib-waveguide phase shifters also yield optical loss due to free-carrier absorption in a PN junction. The optical propagation loss coefficient of a lateral PN-junction rib-waveguide phase shifter that has a 600-nm rib width is plotted as a function of wavelength in Fig. 6.4. The loss coefficient also includes passive optical loss described above. The loss coefficient is higher with a longer wavelength because the free-carrier absorption is higher for longer wavelengths, as we will learn regarding the spectral property of free-carrier absorption, which is expressed mathematically in Eq. (5.11) in Chapter 5 within the framework of Drude's classical theory. A small peak around the 1510-nm wavelength is

Table 6.3 Two-photon absorption (TPA) coefficients in crystalline semiconductors.

Crystalline Material	Si	InP	InGaAs QW
Two-Photon Absorption Coefficient	≤ 0.9 cm/GW[5–8]	10 cm/GW[9]	60 cm/GW[10]

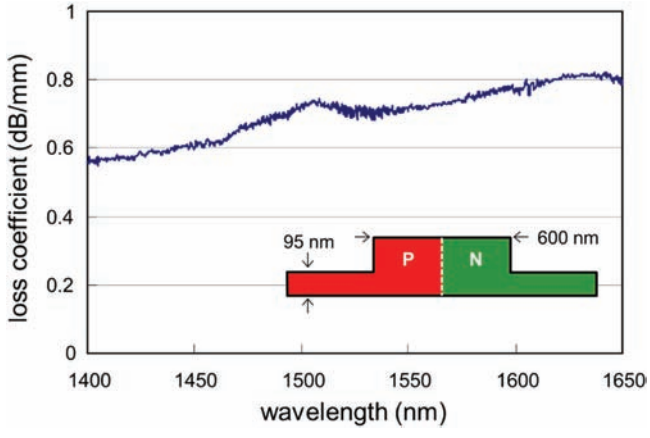

Figure 6.4 Optical propagation loss coefficient of a lateral PN-junction rib-waveguide phase shifter that has a 600-nm rib width.

caused by optical absorption by overtones of the vibration modes associated with hydrogen-related radicals existing in a top silica clad layer fabricated by a CVD process.[11,12] The variation of the loss coefficient is within ±0.05 dB/mm and yields almost the same loss characteristics over the C and L bands. The loss characteristics do not change substantially, and the above discussion is also applied to a phase shifter that has a 500-nm rib width.

For integrated MZ optical modulators, 1×2 MMIs are essential building blocks to construct MZIs. The optical loss of the MMIs affects the total optical loss of the optical modulators. The imbalance in optical loss between two ports deteriorates, in particular, the *ER* in intensity modulation and the *Q*-factor in phase modulation, which are defined in Chapter 3. The total optical loss (i.e., on-chip insertion loss) and loss imbalance measured for a test sample of a 1×2 MMI, which comprises the channel optical waveguides and a slab main section, as shown in Figs. 4.16 and 4.17, are plotted in Fig. 6.5 with a plan-view layout and a SEM photograph, showing that the 1×2 MMI was fabricated as designed.

The on-chip insertion loss $\alpha_{\text{on-chip loss}}$ and the loss imbalance $\Delta\alpha_{\text{loss}}$ for the 1×2 MMI are derived from the following equations:

$$\alpha_{\text{on-chip loss}}(\lambda) = -10\log_{10}\left[\frac{I_{\text{port1}}(\lambda) + I_{\text{port2}}(\lambda)}{I_{\text{in}}(\lambda)}\right] \tag{6.2}$$

and

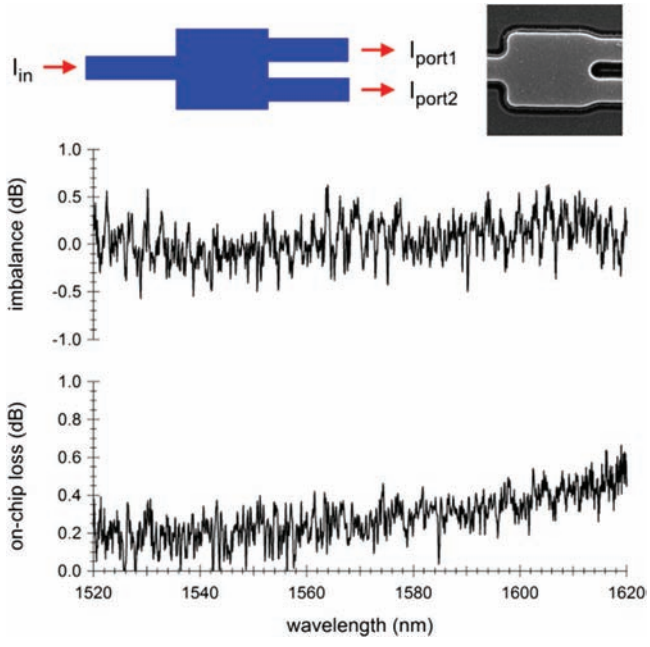

Figure 6.5 On-chip optical insertion loss and loss imbalance of a silicon-based 1×2 MMI with a plan-view layout and SEM photograph.

$$\Delta\alpha_{\text{loss}}(\lambda) = -\left[10\log_{10}\left[\frac{I_{\text{port1}}(\lambda)}{I_{\text{in}}(\lambda)}\right] - 10\log_{10}\left[\frac{I_{\text{port2}}(\lambda)}{I_{\text{in}}(\lambda)}\right]\right], \qquad (6.3)$$

where I_{port1} and I_{port2} denote the respective optical power from output ports 1 and 2, respectively. In a spectral range over the C band, the on-chip insertion loss obtained from spectral measurements is lower than 0.4 dB, and the loss imbalance is within ±0.5 dB with an average on-chip insertion loss of 0.21 dB in a standard deviation of ±0.04 dB and an average imbalance of –0.3 dB in a standard deviation of ±0.095 dB. Low-loss 1×2 MMIs have been reported with different designs on a silicon-photonics platform.[13–17] On-chip optical insertion losses as low as 0.11 dB for TE polarization and 0.18 dB for TM polarization were reported with a similar 1×2 MMI on a silicon-photonics platform.[16] The 1×2 MMI shown in Fig. 6.5 is suitable for small-footprint optical splitters/couplers for low-loss, high-performance integrated MZ optical modulators on a silicon-photonics platform. Low-reflection MMIs were studied for high return loss.[18]

The adiabatic polarization rotation (PR) and polarization division multiplexing (PDM) computationally analyzed in Chapter 4 allow low-loss operation. The polarizer inserted in the output PMF was rotated to resolve the linear polarization of the output light beam. Conversion efficiencies in the partial-rib PR measured in on-chip transmission spectrum measurements are plotted in Fig. 6.6 with launched light beams in TM-like and TE-like

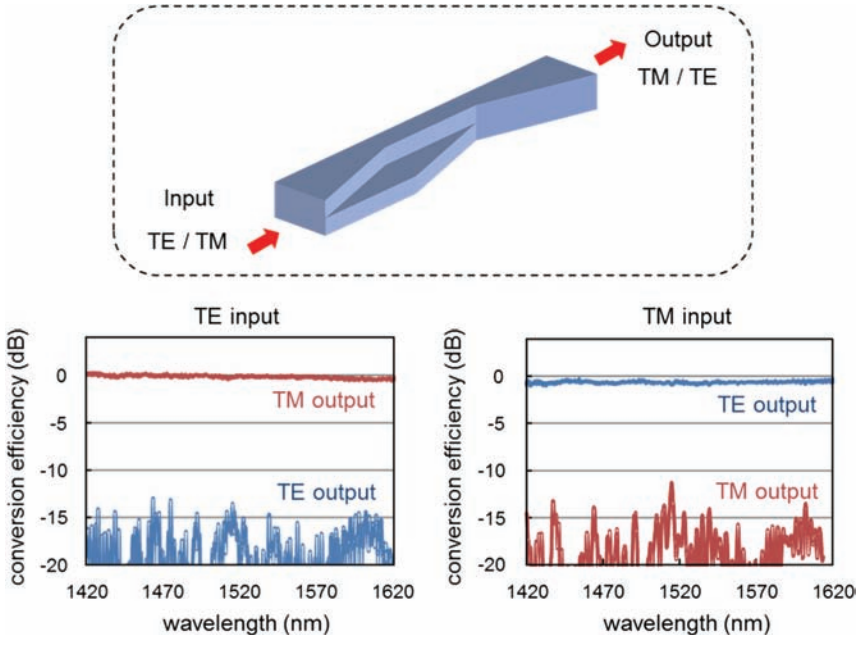

Figure 6.6 Partial-rib PR conversion efficiencies in the transmission spectra.

polarization, respectively.[19] The PR provides on-chip optical insertion losses as low as 0.5 dB and polarization extinction ratios higher than 13 dB for the TM-like and TE-like inputs in broad wavelength over the C and L bands, the lowest on-chip insertion loss and the widest spectral range as ever reported.[20,21] The loss is slightly higher for the TM-like input because of higher side-wall-roughness loss for the converted TE-like polarization. A higher electric field localized at the side walls leads to higher optical loss, as discussed in Chapter 4. The adiabatic PR is suitable to in-line polarization rotation for PICs such as integrated silicon-based MZ optical modulators for digital coherent communication.[22]

The on-chip transmittance spectra measured with the all-adiabatic PDM (450 μm long) are shown in Fig. 6.7.[23] The transmission spectra for the TE_0 guided mode launched to the first waveguide with the input beam to the above waveguide are plotted in the left graph of Fig. 6.7. The on-chip insertion loss in the conversion of the TE_0 mode to the TM_0 mode is less than 0.5 dB in the C and L bands. The polarization extinction ratio is higher than 20 dB in the C and L bands, which is limited by the polarization extinction ratio of the measurement equipment. The transmission spectra for the TE_0 guided mode to the second waveguide with the input beam to the second waveguide in the bottom side are plotted, on the other hand, in the right graph of Fig. 6.7. The on-chip insertion loss for the unconverted TE_0 mode is also lower than 0.5 dB in the C and L bands. Thus, the all-adiabatic PDM is capable of polarization-division

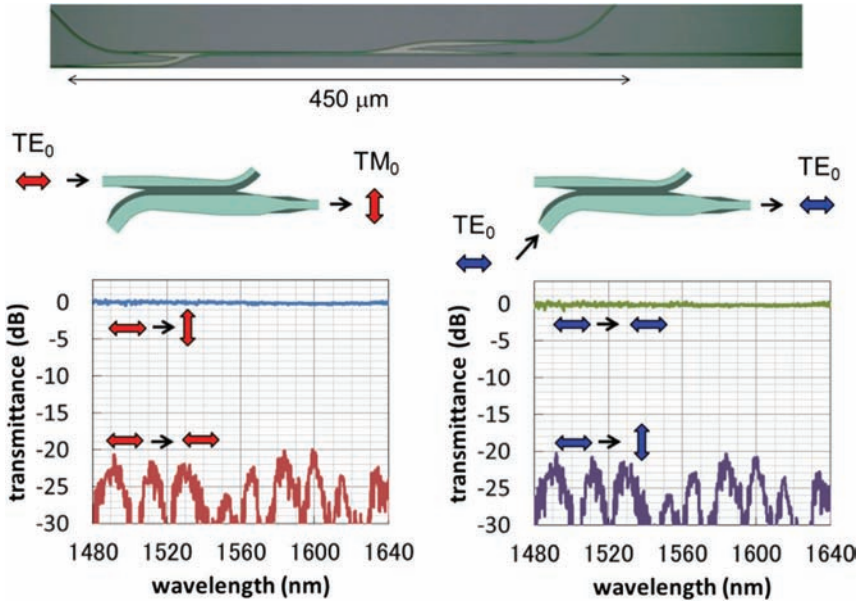

Figure 6.7 On-chip transmission spectra of all-adiabatic PDM and its optical microscope photograph.

multiplexing for the two orthogonal polarizations with on-chip insertion loss less than 0.5 dB with a high polarization extinction ratio beyond 20 dB in the C and L bands. Similar all-adiabatic PDM circuits on a silicon-photonics platform have been proposed theoretically and verified experimentally.[24–26] The PDM is suitable for small-footprint low-loss PDM circuits for integrated PDM IQ MZ optical modulators on a silicon-photonics platform.[27]

Measurement data of on-chip optical insertion losses of 180-deg circular and clothoid optical-waveguide bends are presented in Fig. 6.8 with the computational characteristics described in Chapter 4. Measured on-chip insertion losses agree well with the computational results in ranges of a circle radius and minimum clothoid radius shorter than 20 μm. Measured on-chip insertion losses are significantly higher than the computational results at radii longer than 20 μm. A longer bending radius leads to a longer waveguide length and thus a higher side-wall-roughness loss, which is not accounted for in computational analysis. In the measured loss characteristics, a clothoid bend with a 10-μm minimum radius seems to be optimal as low-loss optical waveguide bends for PICs.

The optical loss of a silicon-based single MZ optical modulator that has a lateral PN-junction rib-waveguide phase shifter can be estimated with the loss data for each building block. For a 4-mm phase shifter, the optical loss is 3 dB or lower in the C band according to the propagation loss coefficient in Fig. 6.4. Two 1×2 MMIs lead to 0.42 dB in the C band according to the average on-chip loss obtained above. The total length of the channel waveguides will be 2 mm for a MZI and the input and output waveguides, which will produce a 0.32-dB loss with a 500-nm channel optical waveguide in the C band from the propagation loss coefficient in Table 6.1. The bending loss using 10-μm minimum-radius clothoid will be lower than 0.1 dB for four 180-deg bends as shown in Fig. 6.8(c). Finally, by assuming a 3.3-dB coupling loss for the input and output fiber coupling in Fig. 6.2, the total insertion loss of a silicon-based integrated single MZ optical modulator is estimated to

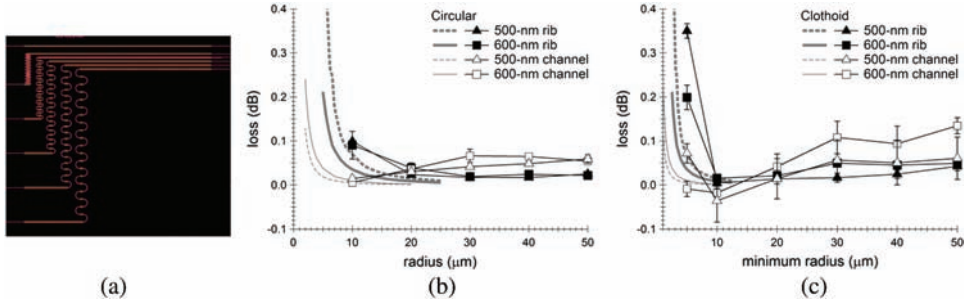

Figure 6.8 (a) Mask layout example of optical waveguides including bends in a sample chip. (b) and (c) Measured optical losses of circular bends and clothoid bends, respectively, in comparison with computational characteristics.

be 7.1 dB. Low-loss integrated MZ optical modulators will be realized on a silicon-photonics platform.

6.1.2 Phase shift and chromatic dispersion

For the measurement and characterization of an electro-refraction phase shift due to free-carrier plasma dispersion, a versatile method is the measurement of the spectral transfer function of MZ optical modulators under a bias voltage. The spectral transfer function under a DC reverse-bias voltage is presented in Fig. 6.9 for an asymmetric MZ optical modulator that has vertical PN-junction rib-waveguide phase shifters in the MZI arms.[28] The MZ optical modulator chip is inserted instead of the passive optical-waveguide chip in the test and measurement apparatus depicted in Fig 6.1. The MZI waveguide system has an excess length of 50 μm in each part of the channel optical waveguide, as indicated with circles in one of the MZI arms, thus the 100-μm asymmetry of the channel optical waveguide in the MZI. Interference fringes, which are characteristics of the asymmetry, are observed in the spectral transfer function. The free spectral range (FSR) $\Delta\lambda_{FSR}$ of the interference fringes in a wavelength is ~10 nm, which agrees very well with the 9.8-nm theoretical FSR obtained from the relationship $\Delta\lambda_{FSR} \sim \lambda^2/(n_{eff}\Delta L)$, where $n_{eff} = 2.45$ at a 1550-nm wavelength in Fig. 4.13 for a 500-nm channel optical waveguide, and $\Delta L = 100$ μm for an asymmetric MZI. An output power of −15 dBm corresponds to an optical power transmittance of −15 dB with an optical power of 0 dBm launched to the MZ optical modulator. The interference fringes are useful measures to visualize the overall characteristics of electro-refraction phase shift at a glance as dark contrast curves in the pseudo-color plot at the bottom of the graph. Interference fringes are also used to analyze the group refractive index and chromatic dispersion.[5,29–34]

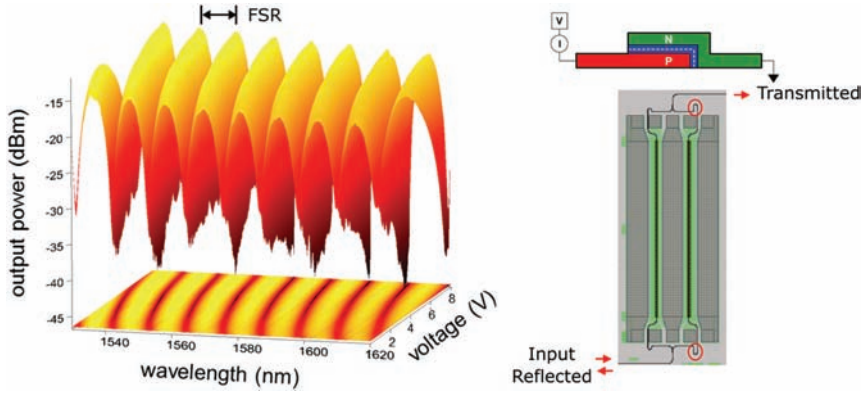

Figure 6.9 Spectral transfer function under a DC reverse-bias voltage for an asymmetric MZ optical modulator that has vertical PN-junction phase shifters, and a mask layout of the asymmetric MZ optical modulator.

Chromatic dispersion is produced by the wavelength dependence of the effective refractive index.[35,36] (Chromatic dispersion in silicon optical waveguides is studied later in this subsection.)

One of the most essential performance factors is the voltage to produce π phase shift, namely, V_π, as discussed in Chapters 3 and 5. The experimental transfer function, which is obtained as a slice of the spectral transfer function at a specified wavelength, provides V_π as a voltage difference between an adjacent peak and bottom transmittance, as illustrated schematically in Fig. 3.8 and indicated in Fig. 5.24. The measured V_π at room temperature is against wavelength across the C and L bands in Fig. 6.10 with the respective transfer functions. Wavelength dependence is not significant over the spectral range: V_π is 2.5–2.6 V in the C band and 2.7 V in the L band.[28] The slight increase in V_π is produced by a extended mode profile of the fundamental mode in the rib-waveguide phase shifter with increasing wavelength, as described in Chapter 4. The wavelength dependence of free-carrier plasma refraction is less effective than that of the mode-field profile. The MZ optical

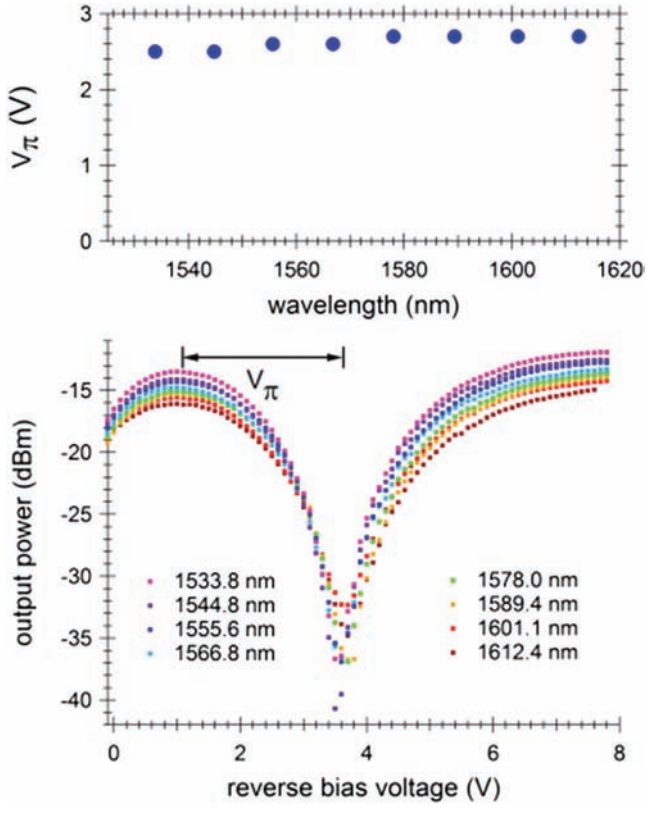

Figure 6.10 Wavelength dependence of V_π and transfer function characteristics in the C and L bands.

modulator is useful for low-voltage optical modulators for high-capacity optical networks in the C and L bands.

Phase shifts via free-carrier plasma refraction are independent of temperature as studied theoretically in Chapter 5, and therefore the V_π of the silicon-based MZ optical modulator will be independent of temperature. This is verified in the characteristics of V_π plotted as a function of temperature in Fig. 6.11.[28] For a temperature increase up to 150°C, V_π is constant or even slightly lower at higher temperatures. The refractive index of crystalline silicon increases with temperature according to the TO coefficient in Eq. (5.16), and thus mode fields are localized more inside silicon cores at higher temperatures, and lead to the higher mode confinement in the depletion region, hence the lower V_π at higher temperatures. This characteristic can be verified theoretically by the semi-analytical and the computational methods in the previous chapter. In summary, operation of a silicon-based MZ optical modulator without TEC is thus permitted, and it serves as an energy-efficient optical modulator for high-capacity optical networks in the broad spectral range.

Chromatic dispersion impairs high-capacity optical networks because it stretches optical signals in the time domain and thus causes inter-symbol interference.[37,38] Therefore, the suppression of chromatic dispersion is crucial to optical components in high-capacity optical networks at 100 Gb/s and beyond. As mentioned above, spectral interference fringes of asymmetric MZ optical modulators reflect spectral characteristics of group refractive index and chromatic dispersion in a channel optical waveguide of excess length. Channel optical waveguides occupy substantial portions of entire MZIs and predominate the group refractive index and chromatic dispersion. The measured transmission spectra of test MZIs with 500-nm and 600-nm channel optical waveguides are plotted in Fig. 6.12(a). The spectral phase is obtained from the interference fringes in each transmission spectrum, as plotted in Fig. 6.12(b).

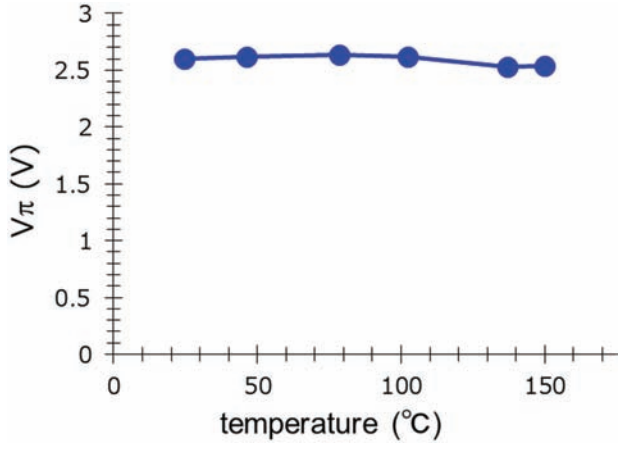

Figure 6.11 Temperature dependence of V_π at a wavelength of ~1550 nm.

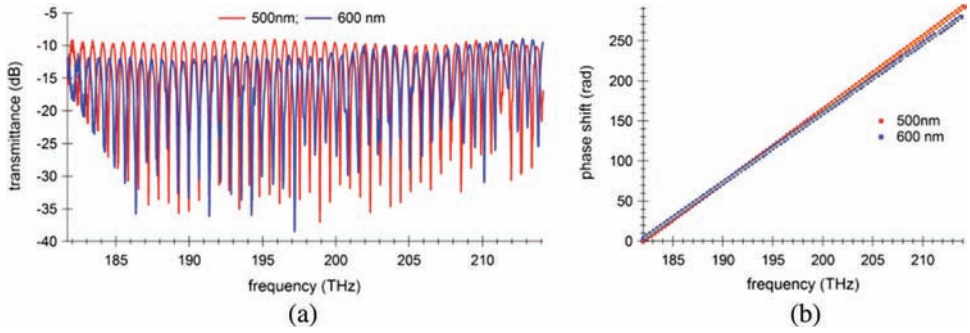

Figure 6.12 (a) Measured transmission spectra of test asymmetric MZIs with 500-nm and 60-nm channel optical waveguides. (b) Spectral phases of the measured transmission spectra and fitting curves.

Group refractive index and chromatic dispersion are defined as coefficients of linear and higher-order polynomial terms of spectral phase expanded in optical frequency.[35] The coefficient of the linear term leads to the group index; the coefficient of the second-order term leads to the most dominant dispersion term, which is referred to as the dispersion parameter in optical fiber communication; and the coefficient of third-order term leads to the dispersion slope, which represents higher-order chromatic dispersion.[35,39] Curve fitting with the experimental spectral phase using the polynomial terms provides group refractive indices of 4.36 and 4.16 for 500-nm and 600-nm widths, respectively, only for channel optical waveguides. The mode-matching method provides computational group refractive indices of 4.18 and 4.05 for 500-nm and 600-nm channel optical waveguides, and 3.88 and 3.86 for 500-nm and 600-nm rib optical waveguides, respectively. The experimental and computational group indices for the channel optical waveguides semi-quantitatively agree with each other with respect to width dependence. A discrepancy in the absolute values may be attributed to core cross-section profile in the fabrication, such as rounded corners and slanted side walls. Chromatic dispersion coefficients, however, cannot be determined accurately in the curve fitting because these terms have minor portions in the spectral phase and are affected significantly by residual errors in the curve fitting.

The chromatic-dispersion characteristics of channel optical waveguides can be characterized by time-domain or spectral-domain interferometry methods.[39–42] These methods allow accurate measurement of chromatic-dispersion coefficients if a sample interferometer arm and a reference interferometer arm are balanced each other in terms of pathlength. With a balanced interferometer, the chromatic-dispersion coefficients can be determined experimentally from spectral phase without resolution limitation by the background of linear frequency term. A test sample chip containing folded straight optical waveguides, as shown in Fig. 6.1, is inserted in the sample arm. In this book, a chromatic dispersion measurement based on auto-stabilized dual-beam

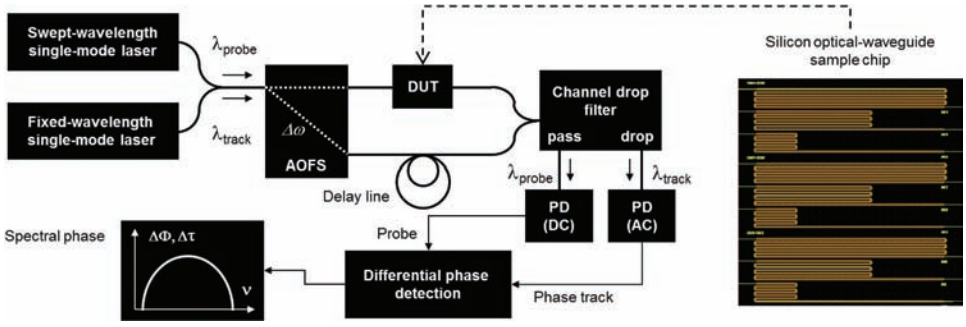

Figure 6.13 Block diagram of a fiber-based apparatus for auto-stabilized dual-beam heterodyne spectral interferometry.

heterodyne spectral interferometry is described for silicon channel optical waveguides of different channel widths. The apparatus of the auto-stabilized heterodyne spectral interferometry is depicted in block diagram in Fig. 6.13.[43] Chromatic dispersion characteristics of a photonic-crystal-based optical waveguide on a silicon-photonics platform as well as optical components such as semiconductor optical amplifiers, fiber Bragg gratings, and Fabry–Pérot etalons have been analyzed experimentally by the auto-stabilized heterodyne spectral interferometry in the C and L bands.[44–46]

A swept-wavelength single-mode laser provides a probe laser beam of which a wavelength is swept in the C and L bands, whereas a fixed-wavelength single-mode laser uses a phase-track laser beam for phase reference. Both of the laser beams are launched to a PMF connected to an acousto-optic frequency shifter (AOFS) that generates a frequency-shifter light beam for a heterodyne beat. Here, the device under test (DUT) is a test sample chip that includes silicon channel optical waveguides as used in the cut-back loss measurements. The probe beam and the phase-track beam after the heterodyne fiber interferometer are separated through a spectral channel drop filter. The probe beam is detected with a DC PD, whereas the phase-track beam is detected with an AC PD. The electrical PD outputs of the former and the latter are input to a signal port and a reference port of a RF lock-in amplifier. Detection of the differential phase between the probe and phase-track beams at the lock-in amplifier allows accurate spectral-phase measurement free from interferometer common-mode noise without active stabilization of the heterodyne interferometer. A variable-delay line allows adjustment of the reference-arm pathlength to balance both interferometer arms at the center wavelength of the spectral phase.

Spectral-phase traces for 500-nm and 600-nm channel optical waveguides of different lengths have been acquired by auto-stabilized heterodyne spectral interferometry and are plotted against optical frequency in Fig. 6.14 with the polynomial fitting curves (dashed lines) for the determination of chromatic-dispersion coefficients. A frequency of 194.00 THz corresponds

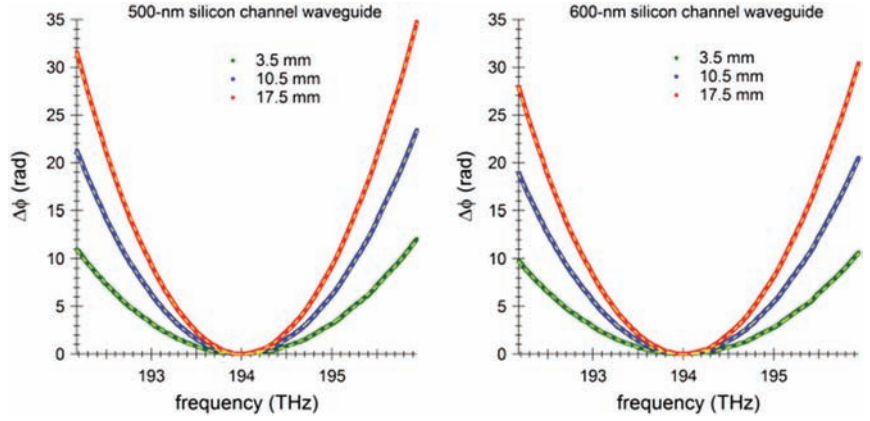

Figure 6.14 Spectral phase plotted against optical frequency for 500-nm and 600-nm silicon channel optical waveguides.

to a wavelength of 1545.3 nm. All of the experimental spectral-phase traces yield a positive parabolic dependence on frequency, indicating that positive second-order chromatic dispersion is dominant in the silicon channel optical waveguides. The second order is the lowest-order chromatic dispersion. Positive second-order chromatic dispersion, which is referred to as upward chirping, implies that the lightwave in the higher optical frequency is propagated slower in terms of group velocity than that in the lower optical frequency.[35] The channel optical waveguide of the narrower width yields the higher chromatic dispersion because the area of the mode field depends more strongly on wavelength and leads to higher dispersion of the effective refractive index against wavelength. Asymmetry in the parabolic shapes is caused by third-order chromatic dispersion. The fitting curves, each of which comprises second- and third-order frequency terms, are fitted very well to the experimental traces.

Second-order and third-order chromatic-dispersion coefficients obtained in the curve fitting are plotted versus waveguide length in Fig. 6.15. The coefficients are proportional to the waveguide length. Offsets at zero waveguide length are attributed to a residual imbalance in the second-order and third-order chromatic-dispersion terms in the optical system of the measurement equipment and in some portion of the input and output nano-taper MFCs. Chromatic-dispersion coefficients per unit waveguide length are obtained as slopes of fitting functions, represented by solid and dashed lines in Fig. 6.15 and listed in Table 6.4. Dispersion parameter D is related to the second-order chromatic-dispersion coefficient in the following formula:

$$D = -\frac{1}{L} \cdot \frac{\omega^2}{2\pi c} \cdot \frac{\partial^2 \phi(\omega)}{\partial \omega^2}, \tag{6.4}$$

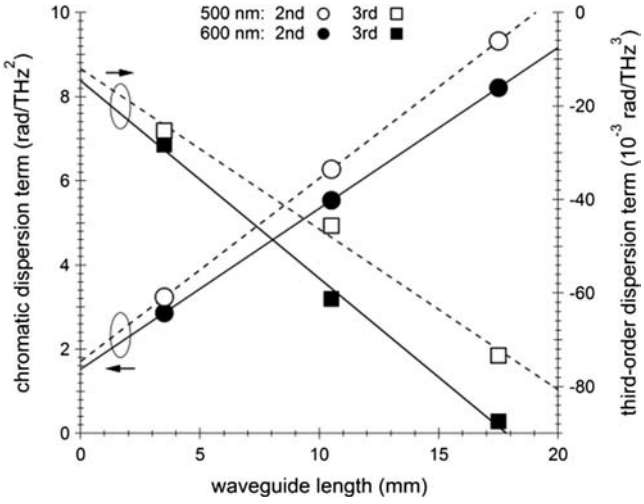

Figure 6.15 Second- and third-order chromatic-dispersion coefficients plotted against waveguide length.

Table 6.4 Second- and third-order chromatic-dispersion coefficients per unit length.

Waveguide Width	Second-Order Coefficient	Third-Order Coefficient
500 nm	0.021 ps/mm	−0.00016 ps^2/mm
600 nm	0.018 ps/mm	−0.00020 ps^2/mm

with waveguide length L. Positive or negative sign in dispersion parameter implies anomalous or normal dispersion, respectively. By substituting the second-order coefficient per unit length in Eq. (6.4) with 0.021 ps/mm for a 500-nm channel optical waveguide, we obtain $D = -0.0086$ ps/nm/mm. Assuming a wavelength bandwidth as broad as 0.8 nm, which is equivalent to a 100-GHz frequency bandwidth in the C band, and a waveguide length as long as 100 mm, the dispersion parameter leads to a group delay time of 0.7 ps in absolute value. The group delay time is much shorter than a symbol interval, which is 10 ps at a symbol rate as high as 100 Gbaud. The group delay is regarded as a measure of optical signal broadening in the time domain. Therefore, inter-symbol interference due to chromatic dispersion is negligible in silicon-based PICs.

The modified FOM, defined as $\pi/(V_\pi \alpha_{PS} \ell_\pi)$ in the previous chapter, has been obtained experimentally for lateral and vertical PN-junction phase shifters from the experimental data of optical loss and V_π. The modified FOM obtained from the measurements is plotted in Fig. 6.16 as a function of the reverse-bias voltage for lateral PN-junction rib-waveguide phase shifters with a 500-nm rib width without and with compensation doping.[47,48] The higher performance of the compensation-doped phase shifter is verified at

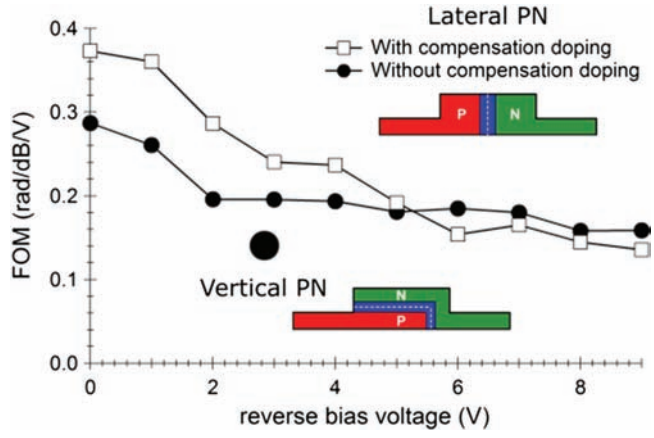

Figure 6.16 Modified FOM plotted against a reverse-bias voltage for lateral PN-junction rib-waveguide phase shifters without and with compensation doping.

reverse-bias voltages lower than 5 V. The junction will be fully depleted in its central area at higher reverse-bias voltages, and there is no advantage to compensation doping. The modified FOM for the vertical PN-junction phase shifter, which is plotted with a larger solid circle, is lower than those of the lateral PN-junction phase shifters. The compensation-doped phase shifter is most suitable to an energy-efficient integrated optical modulator on a silicon-photonics platform.

6.2 DC Electrical Characteristics

6.2.1 Current-voltage characteristics

Under a reverse-bias voltage, the direct current through a carrier-depletion PN-junction phase shifter in the dark is dominated by the leakage current through the PN junction. Current-voltage characteristics of lateral and vertical PN-junction phase shifters in the dark are presented in Fig. 6.17.[28,49] The absolute current through each PN-junction phase shifter under reverse bias is substantially caused by current leakage, namely, dark current through the PN junction. A negative DC voltage applied to the P-type region leads to a reverse-bias voltage and thus carrier depletion. Leakage current in a lateral PN-junction phase shifter 3 mm long is lower than 10^{-9} A under reverse-bias voltages of 9 V or higher. A much higher leakage current is observed in a vertical PN-junction phase shifter in MZ optical modulator, and junction breakdown occurs at about 7 V.

The electric-field profiles under reverse-bias voltage, which are given by the computational method described in Chapter 5, are also presented in Fig. 6.17. The maximum electric field in a lateral PN-junction phase shifter with a dopant concentration of $\sim 5 \times 10^{17}$ cm^{-3} [Fig. 6.17(a)] is lower than

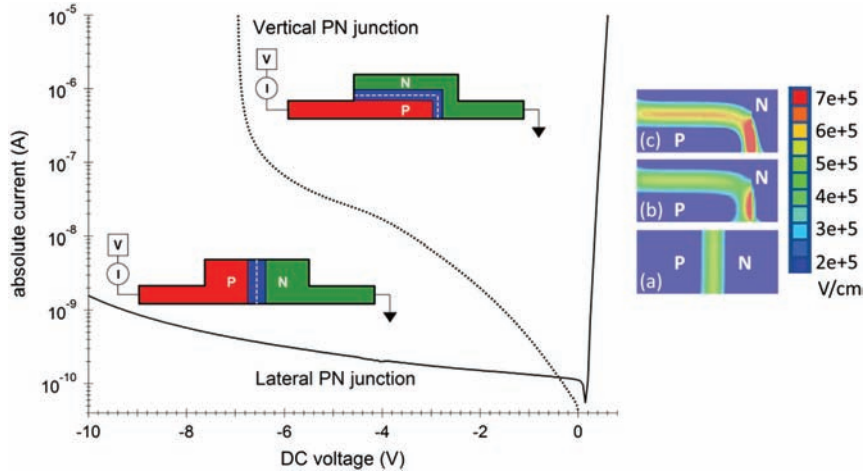

Figure 6.17 Current-voltage characteristics of lateral and vertical PN-junction phase shifters and computed electric-field profiles in (a) lateral and (b) vertical PN-junctions with a concentration of $\sim 5 \times 10^{17}$ cm^{-3}, and (c) a vertical PN-junction with a dopant concentration of $\sim 10^{18}$ cm^{-3}.

6×10^5 V/cm, while the maximum electric field is as high as 7×10^5 V/cm in a lateral PN-junction phase shifter with a dopant concentration the same as for the lateral PN junction [Fig. 6.17(b)] and that with a dopant concentration up to $\sim 10^{18}$ cm^{-3} [Fig. 6.17(c)]. The current-voltage characteristics of the lateral PN-junction phase shifter have been acquired for the phase shifter in case (c). Breakdown in the lateral PN-junction phase shifter occurs in the high-field area of the PN junction.[49] For a more efficient phase shift below the junction breakdown voltage, a more uniform electric-field distribution is required to expand the depletion region in the rib-waveguide core. Further design refinements based on the computational method allow modification of the doping profile generating a uniform electric field-distribution.

The temperature dependence of the absolute current at a reverse-bias voltage of about 1 V is shown with a theoretical fitting curve in Fig. 6.18 for a lateral PN-junction phase shifter in a MZ optical modulator with a dopant concentration [Fig. 6.18(b)].[28] The horizontal axis is scaled to the inverse of temperature T. The dark current increases with temperature due to thermal excitation of intrinsic carriers in crystalline silicon. In semiconductors like crystalline silicon, of which electronic bandgap is relatively wide in energy, the temperature dependence of the leakage current through a reverse-bias PN junction is limited not by thermal diffusion but by thermal excitation of intrinsic carriers.[50] Therefore, the leakage current is proportional to $T^{\frac{3}{2}} e^{-\frac{E_G}{2k_B T}}$ theoretically, where E_G and k_B denote the bandgap energy of crystalline silicon and Boltzmann constant, respectively. The exponential factor in the theoretical expression dominates the temperature dependence of the leakage

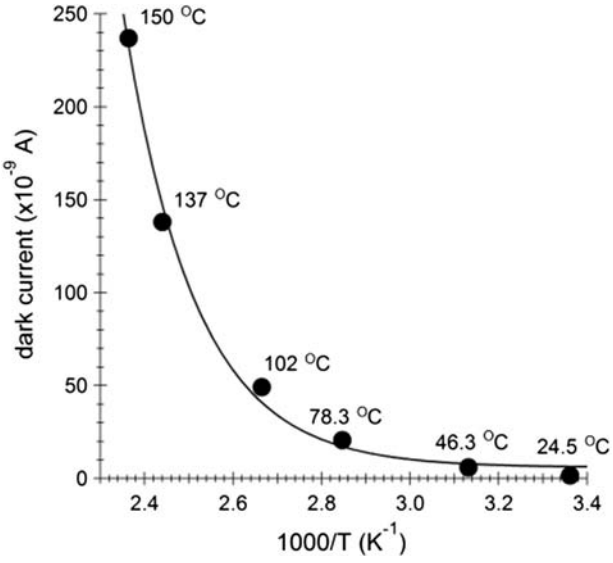

Figure 6.18 Temperature dependence of a dark absolute current through a vertical PN-junction phase shifter in a MZ optical modulator: measurement data (solid circles) and a theoretical fitting curve (solid line) at a reverse-bias voltage of about 1 V.

current, and thus the measured data are fitted by using the exponential term with E_G as a fitting parameter, as shown in Fig. 6.18. The result is 1.07 eV as the E_G in the curve fitting, which agrees very well with the reported bandgap energy of silicon referred to in Chapter 5.[51] The dark current can be a measure of the temperature increase in a PN-junction phase shifter.

Photocurrents through the reverse-bias PN junction phase shifters in the low-dopant concentration of cases [Fig. 6.17(a) and (b)] are clearly observed when guided lights are launched to the phase shifters. Current-voltage characteristics for the vertical PN-junction phase shifter with and without photocurrent are shown in Fig. 6.19. The linear line drawn on the measured data in the right graph has a slope of 1, implying that the photocurrent increases linearly with the launched optical power. The source of the launched light is a single-mode laser at a wavelength of 1550 nm, the photon energy of which is much lower than the bandgap energy of crystalline silicon. Therefore, there is no possibility of one-photon excitation. Two-photon excitation is also excluded because of the linearity in the photocurrent. The absence of two-photon excitation is consistent with the discussion in Subsection 6.1.1.

The photocurrent in reverse-bias silicon PN-junction rib optical waveguides has been observed and studied by several research groups.[52–58] The photocurrent phenomenon has been attributed to the photodissociation of mid-gap defect centers such as divacancy complexes and the resultant excitation of carriers from the defects.[52,57,59,60] These defects reside in crystalline silicon after a doping process that comprises ion implantation and

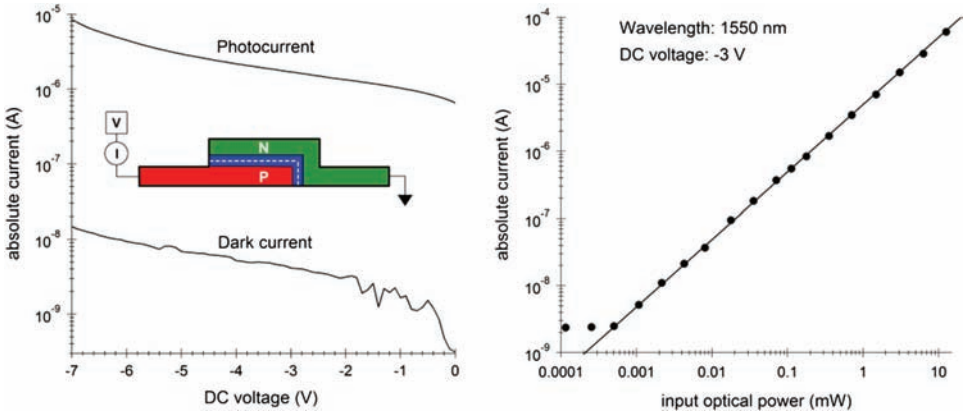

Figure 6.19 (a) Reverse-bias current-voltage characteristics of a vertical PN-junction phase shifter with and without launched guided light. (b) Launched optical-power dependence of the photocurrent current of a vertical PN-junction phase shifter under a reverse-bias voltage of 3 V in a log–log plot.

thermal annealing for dopant activation. The idea of a defect-mediated photocurrent is supported by the fact that the photocurrent increases with dopant concentration from Fig. 6.19(b) to 6.19(c), as reported for other silicon-based carrier-depletion phase shifters.[55] A linear increase in photocurrent with launched laser power has also been confirmed in the literature.[58] The defect-mediated photoresponse in crystalline silicon has been applied to silicon-based PDs in telecom wavelengths such as the C band.[52–58]

6.2.2 Microscopic imaging of the PN junction

During the fabrication of PN-junction phase shifters in integrated silicon-based optical modulators, process simulators are used extensively to optimize the doping conditions to achieve the desired profiles of PN junctions.[61] After fabrication, however, it is rare to implement structural inspection of the fabricated phase shifters to characterize the PN-junction profile, including the distribution of electrical charges. Chemical wet etching optimized for a selective etching rate according to the species of local dopant ions was employed to convert an invisible PN-junction profile into a visible wet-etch profile in a SEM photograph.[62] The chemical technique, however, has technical limitations to reproducing the junction profile because etch chemistry dominates the spatial resolution of the local dopant distribution, and the etch profile is significantly affected by the shape of the host optical waveguide. Recently, an all-electronic imaging method has been applied to image local electronic charges in PN-junction phase shifters in nanometer-scale imaging resolution.[27] The method is based on scanning capacitance microscopy (SCM), which was invented to map micro-capacitances in electronic devices.[63–67] Measurement of the AC conductance through a

nano-probe, such as an atomic-force-microscopy nano-tip capacitively coupled to a surface of the DUT, allows accurate visualization of the local distribution of electrical charges when the nano-tip is scanned over the surface. Positive and negative charges are discriminated directly as positive and negative signs in the conductance, respectively. Junction profiles of the active regions in semiconductor LDs have been characterized by this method.[68,69] Cross-section images of vertical and lateral PN-junctions in silicon rib-waveguide phase shifters have been acquired by SCM and are presented in pseudo-color scale in Fig. 6.20.

The depletion region between P-doped and N-doped areas is clearly displayed in the electronic charge profile. A TEM cross-section photograph of a host rib optical waveguide is presented for reference. Analysis services based on SCM are available commercially.[70–72] One can verify with the SCM images that the vertical and lateral PN junctions have been formed as designed in the phase-shifter waveguides. The imaging method, therefore, serves as an useful tool for the inspection and characterization of PN junctions formed in phase shifters on a silicon-photonics platform. The image resolution in SCM is better than 5 nm because of the nano-probe method. Dopant concentration, however, cannot be measured accurately because the level of AC current is affected by the condition of the sample surface, and so on. There is also some trade-off between the dynamic range of the AC current and the image resolution.

6.3 RF Frequency Characteristics

6.3.1 *S*-parameter characteristics

Electro-optic bandwidth is a major performance factor to evaluate high-speed optical modulators and can be obtained in *S*-parameter measurement. The

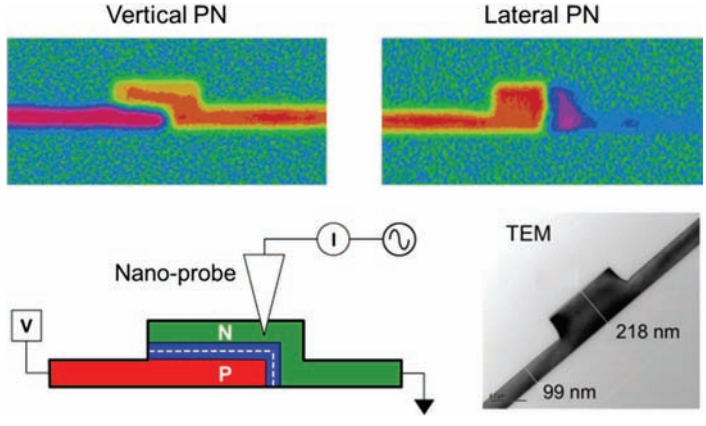

Figure 6.20 Measured profiles of vertical and lateral PN-junctions in rib-waveguide phase shifters by the SCM method based on nano-probe imaging.

electro-optic response of an optical modulator is represented as a 2×2 S-matrix $\overleftrightarrow{S}$, which has the following form:

$$\overleftrightarrow{S} = \begin{bmatrix} S_{11} & S_{12} \\ S_{21} & S_{22} \end{bmatrix}, \tag{6.5}$$

with S-parameters S_{11}, S_{12}, S_{21}, and S_{22}. Forward and backward electromagnetic waves a_1 and b_1 at port 1 and a_2 and b_2 at port 2 are related via S-matrix as[73–77]

$$\begin{bmatrix} a_2 \\ b_2 \end{bmatrix} = \overleftrightarrow{S} \begin{bmatrix} a_1 \\ b_1 \end{bmatrix}. \tag{6.6}$$

A block diagram of the S-parameter measurement apparatus for the characterization of a silicon-based integrated optical modulator is depicted in Fig. 6.21. In the characterization of electro-optic response S_{21}, which provides the optical wave output from the modulator with the RF wave input to a traveling-wave electrode connected to a phase shifter in a MZI, is most essential. The output optical power is detected with a high-speed PD and converted to the electrical voltage output from the PD. The magnitude and phase of the output electrical wave are detected as electro-optic S_{21} with a vector spectrum analyzer. The electrical wave reflected from the traveling-wave electrode is detected as S_{11}.

The optical power is detected with the PD, which is a square detector; thus, the output voltage from the PD must be divided by 2 at the dB scale to obtain the electro-optic S-parameter that equals the electrical S-parameter.[75–77] The magnitude of the electro-optic S-parameter $|S_{21}|$ is plotted in Fig. 6.22 for silicon-based MZ optical modulators that have 3-mm and 5-mm lateral PN-junction phase shifters in different bias conditions. The shorter phase shifter yields the higher electro-optic 3-dB bandwidth, ~33 GHz, under a reverse-bias voltage of 5 V.

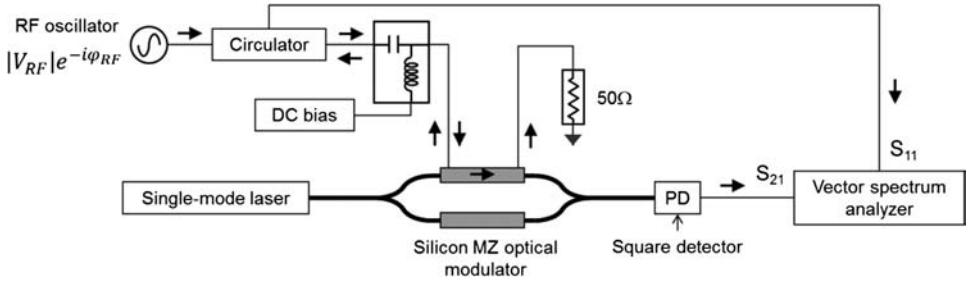

Figure 6.21 Block diagram of the S-parameter measurement apparatus for a silicon-based integrated optical modulator.

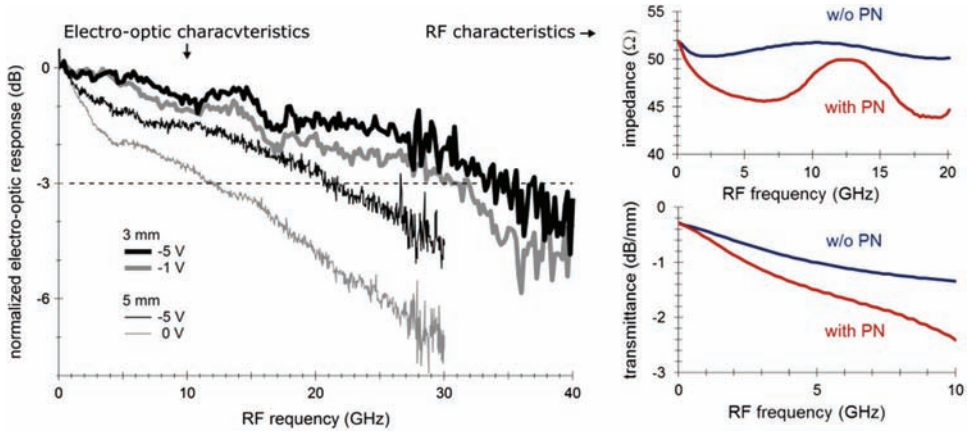

Figure 6.22 Normalized electro-optic $|S_{21}|$ of a silicon-based carrier-depletion MZ optical modulator and the RF characteristics of traveling-wave electrodes.

6.3.2 Effect of parasitics

According to the lumped-element circuit model in the previous chapter, electro-optic bandwidths of the modulators are limited by joule loss of input RF wave in the series resistances in the PN-junction phase shifter. The shorter phase-shifter length leads to the lower joule loss during the propagation of the input electrical waves in the resistance-coupled traveling-wave electrode. Joule loss is evident in the RF transmission characteristics of the traveling-wave electrode connected to the PN-junction phase shifter (with PN) in comparison with the traveling-wave electrode not connected with the PN-junction phase shifter (without PN), as shown in Fig. 6.22. Impedance of the traveling-wave electrode with a PN-junction phase shifter at a reverse-bias voltage of 5 V is lower because of the junction capacitance, whereby the RF wave is pulled into the shunt path. In addition to the joule loss in the phase shifters, RF absorption by carriers due to residual dopants and intrinsic thermal excitation in the SOI layer and the silicon substrate also causes attenuation of the RF wave. A high-resistivity silicon substrate is crucial to reduce loss by eliminating residual dopants.[78–80] Intrinsic thermal excitation is essential and unavoidable. Thinning the substrate thickness by mechanical polishing or chemical etching is effective at reducing RF absorption due to intrinsic thermal carriers in the substrate.

If the reverse-bias voltage increases, the depletion region expands and the junction capacitance decreases. A reduction in the junction capacitance leads to lower AC coupling with the input electrical waves and hence lower joule loss in the series resistance. The electro-optic bandwidth is thus increased by increasing the reverse-bias voltage, although a higher junction capacitance allows more efficient carrier depletion, and hence a lower V_π and higher FOM. Enhancement of the electro-optic bandwidth and modulation speed of silicon-based MZ optical modulators can be achieved by reducing R_S.

Another factor limiting high-speed response is velocity mismatch, namely, refractive index mismatch.[76,82–86] The group refractive index of optical signal waves must equal the phase refractive index of the input electrical signal wave to avoid walk-off between optical and electrical signals in the time domain for efficient optical modulation.[76] An electrical signal wave is applied over an optical wave packet in a symbol slot, and thus the group velocity of the optical waves is involved.[82] The group refractive index of a 500-nm silicon rib optical waveguide, for instance, is 3.88 as the numerical group refractive index quoted in Subsection 6.1.2. The phase refractive index of the traveling electrode, on the other hand, is 3.2 in computational analysis based on FEM electromagnetic simulation. The roll-off frequency at 3-dB attenuation due to velocity mismatch $f_{3\mathrm{dB}}$ is obtained as[85]

$$f_{3\mathrm{dB}} = \frac{c_{\mathrm{light}}}{2|n_{\mathrm{NW}} - n_{\mathrm{G\text{-}Opt}}|\ell}. \tag{6.7}$$

Here, c_{light}, n_{MW}, $n_{\mathrm{G\text{-}Opt}}$, and ℓ denote the light velocity in free space, phase refractive index of the traveling-wave electrode, group refractive indices of the rib optical waveguide, and phase-shifter length, respectively. The phase velocity of the input electrical signal is determined by n_{MW}, and the group velocity of the propagated optical waves is determined by $n_{\mathrm{G\text{-}Opt}}$. After substituting n_{MW} with 3.2 and $n_{\mathrm{G\text{-}Opt}}$ with 3.88 in Eq. (6.7), the roll-off frequency is as high as 150 GHz and 88 GHz with phase-shifter lengths of 3 mm and 5 mm, respectively. The effect of the velocity mismatch is, therefore, less significant than the joule loss and the RF absorption.

6.4 Transient Characteristics

6.4.1 Response limitation by RC time constant

Two approaches are available to reduce series resistance: increase the height of the side slab wings in the rib-waveguide core, or increase the dopant concentration in the slab wings. The latter produces higher optical loss in the phase shifter than the former because optical loss due to free-carrier absorption increases superlinearly with dopant concentration, as shown in Eq. (5.13). The former approach has been taken, and the slab height has been increased from 60 nm to 95 nm, as illustrated in Fig. 6.23. An increase in the slab height leads to more stable propagation of higher-order modes, which are, however, extended toward the heavily doped contact areas (P+ and N+ in Fig. 5.17) and attenuated substantially due to high optical absorption in the contact areas. Therefore, a quasi-single mode is achieved for rib-waveguide phase shifters with a 95-nm slab height. Enhancement of the high-speed response due to a reduction in the $2R_{\mathrm{S}}C$ time constant is evident in time-domain waveforms of optical signals from the carrier-depletion MZ optical modulators with 4-mm

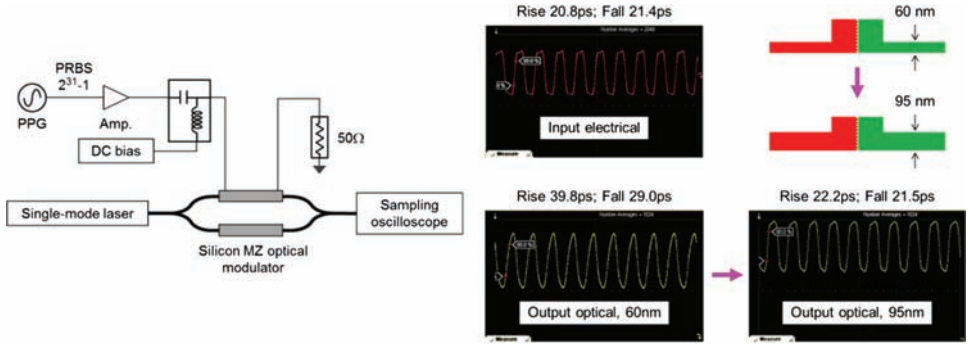

Figure 6.23 Block diagram of a time-domain optical-waveform measurement apparatus and waveforms of an input electrical signal and the output optical signals from carrier-depletion MZ optical modulators that have 600-nm lateral PN-junction rib-waveguide phase shifters.

lateral PN-junction phase shifters that have 60-nm and 95-nm slab heights in Fig. 6.23. The series resistance is reduced from 8.2 Ω with a 60-nm slab height to 5.7 Ω with a 95-nm slab height. The junction capacitance is 1.6 pF at a reverse-bias voltage of 5 V. The $2R_SC$ time constant is thus reduced from 26 ps with a 60-nm slab height to 18 ps with a 95-nm slab height.[87]

Launched electrical signals are periodic square electric pulse trains with a 20.8-ps rise time and 21.4-ps fall time from a pulse pattern generator (PPG). A change in the rise and fall times in the output signal waveforms of modulated light is consistent with the estimation based on the equivalent circuit model comprised of the parasitic elements. The series-resistance reduction is remarkable in terms of the enhancement of the modulation speed of a silicon-based integrated MZ optical modulator.

6.4.2 Intensity modulation characteristics at various modulation speeds

High-contrast on/off intensity modulation in NRZ-OOK format has been verified with 4-mm carrier-depletion lateral PN-junction rib-waveguide phase shifters with a 95-nm slab height at bit rates up to 32 Gb/s in eye diagrams for $2^{31} - 1$ electrical PRBS data from the PPG, as presented in Fig. 6.24.[3,87] The apparatus shown in Fig. 6.23 has been used for eye-diagram measurements. The extinction ratio is as high as 13.9 dB at 10 Gb/s and decreases to 11.3 dB. Defined as ER_{dB} in Eq. (3.7), an extinction ratio as high as 10 dB has been confirmed at 40 Gb/s for a carrier-depletion MZ optical modulators with 3.5-mm self-aligned lateral PN-junction rib-waveguide phase shifters.[88] Lateral PN-junction rib-waveguide phase shifters are, therefore, suitable to low-loss integrated MZ optical modulators on a silicon-photonics platform for high-capacity optical networks.

The high-speed performance of silicon-based MZ optical modulators is verified in the results of eye-diagram mask tests in Fig. 6.25. A Bessel–Thomson

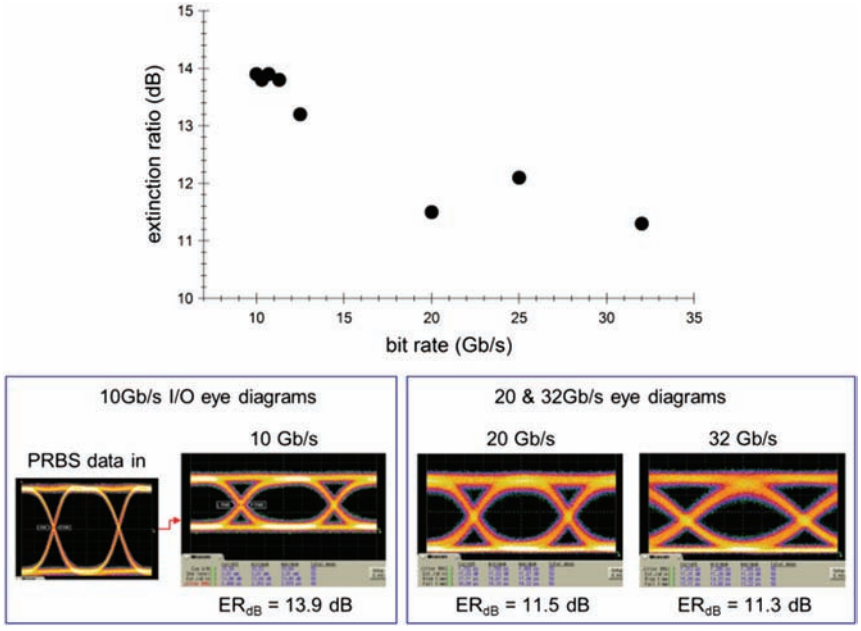

Figure 6.24 Extinction ratio vs. bit rate.

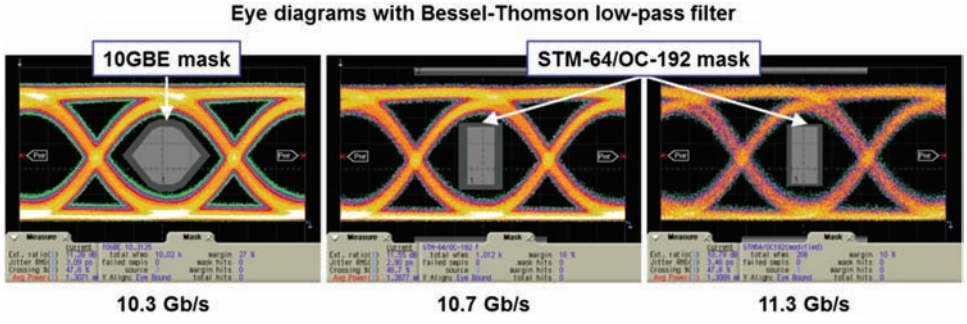

Figure 6.25 Eye diagrams with a Bessel–Thomson low-pass filter for mask test.

low-pass filter has been applied for the mask tests. Two types of mask have been applied: a 10GBE mask commonly used in datacom networks, and a STM-64/OC-192 mask, a standard mask in optical transport systems in telecomm networks. Extinction ratios are slightly lower than the above data because of the low-pass filtering for the mask tests. The mask margin is 10% or larger, as summarized in Table 6.5.

Table 6.5 Extinction ratio and mask margin at 10.3–11.3 Gb/s.

Bit Rate	10.3 Gbps	10.7 Gbps	11.3 Gbps
Extinction Ratio (ER_{dB})	11.3 dB	11.6 dB	10.8 dB
Mask Margin (Mask Type)	27% (10GBE)	16% (STM-64/OC-192)	10% (STM-64/OC-192)

6.4.3 Intensity modulation characteristics at high temperatures

High-speed optical modulation without TEC is essential for low-power optical transceivers in energy-efficient high-capacity optical networks. Electrical power consumption in compact-form-factor optical transceivers is a critical issue. Operation of a silicon optical modulator without TEC allows the electrical power reduction to meet the requirement for further electrical power reduction in transceivers such as CFP2. Currently, III-V QCSE optical modulators have been used in CFP2, in which electrical power is allocated to thermo-electric control of the temperature-sensitive modulators. Modulation characteristics of a silicon-based carrier-depletion MZ optical modulator that has rib-waveguide phase shifters with a 1.5-V·cm $V_\pi L_\pi$ in 10-Gb/s and 25-Gb/s NRZ-OOK were studied at temperatures from 25°C to 55°C.[89] At higher temperatures up to 130°C, TEC-free optical modulation using a silicon-based carrier-depletion MZ optical modulator having 3-mm vertical PN-junction rib-waveguide phase shifters with $V_\pi \ell_\pi$ as low as 0.81-V·cm has been demonstrated in 10-Gb/s NRZ-OOK.[28] The extinction ratio is higher than 10 dB in eye diagrams and clear eye opening is observed over the entire temperature range studied as presented in Fig. 6.26. The apparatus is essentially the same as that in Fig. 6.23 except for the heater setup. A sample chip that includes the silicon-based MZ optical modulator was attached to the top surface of a copper base mount with a thermistor. A heater was set under the back surface of the metal mount. An increase in the dark current through the phase shifter with the monitored temperature of the thermistor in Fig. 6.18 proves an modulator temperature that almost equals the base mount temperature. Peak-to-peak voltage of the input electrical signal is 3.3−3.6 V_{PP}, which is higher than the DC V_π because of RF loss in the conductor electrode and the doped silicon areas. Copper traveling-wave electrodes (instead of aluminum) are effective at reducing the conductor loss and hence the peak-to-peak modulation voltage.[90]

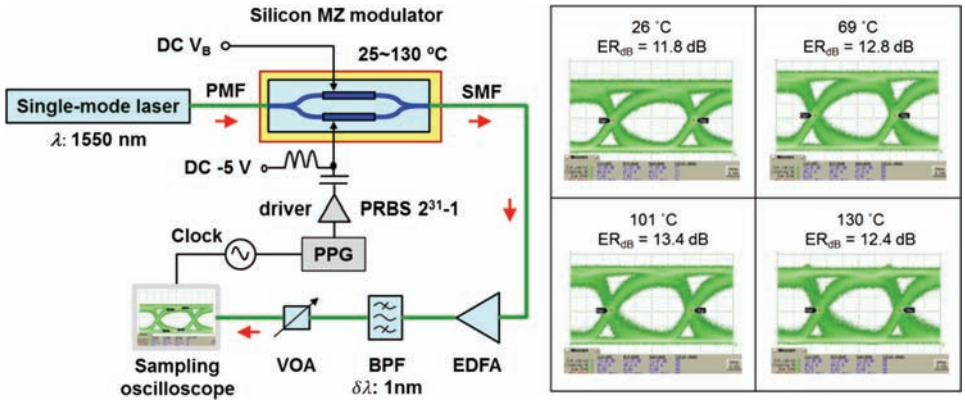

Figure 6.26 Block diagram of an eye-diagram measurement apparatus and eye diagrams at temperatures from 26°C to 130°C.

6.4.4 Phase modulation characteristics and chirp parameter

A silicon-based MZ optical modulator can be used as a chirp-free phase modulator in high-capacity optical networks. For phase modulation in the BPSK format, for instance, phase shifters in both MZI arms are driven in push–pull mode to suppress frequency chirping, as described in Chapter 3.[91–95] A block diagram in Fig. 6.27(a) indicates the setup for NRZ-BPSK modulation using a silicon-based single MZ optical modulator. Complementary electrical data are launched to the traveling-wave electrodes in the MZI arms. Output optical signals from the phase modulator are received by coherent detection with an optical modulation analyzer for constellation diagram measurement. A discrete or accommodated single-mode tunable laser is utilized as a local oscillator (LO) light source for coherent detection.[96,97] A constellation diagram in BPSK format for a carrier-depletion silicon-based single MZ optical modulator that has lateral PN-junction phase shifters is shown in Fig. 6.27(b) with a Q-factor defined in Eq. (3.13) as high as 20 dB.[93] The MZ modulator is driven in parallel push–pull mode.[76] Schemes of push–pull modes will be discussed in the next chapter.

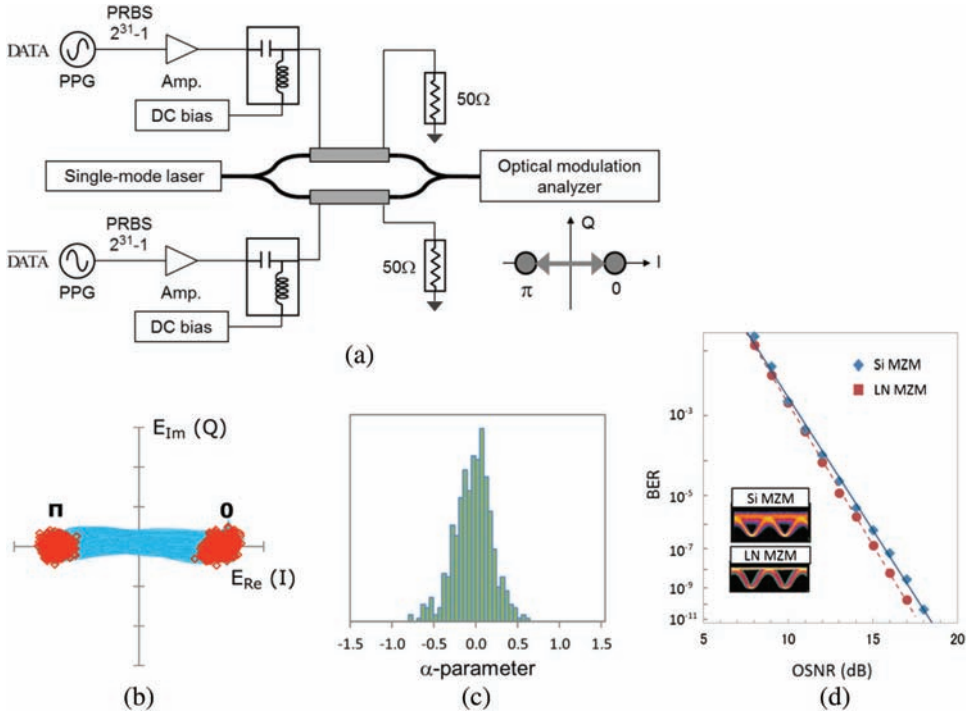

Figure 6.27 (a) Block diagram of a push–pull MZ optical modulator and BPSK constellation measurement. (b) 20-Gb/s NRZ-BPSK constellation diagram. (c) Histogram of the α-parameter in a BPSK. (d) Characteristics of the BER of silicon and LN MZ modulators.

The modulator α-parameter (also known as the modulator chirp parameter) is obtained experimentally by using Eq. (3.10) from the constellation diagram and shown in histogram in Fig. 6.27(c). The average modulator α-parameter is 0.05, and thus the silicon-based MZ modulator is almost zero chirped. In Fig. 6.27(d), the BER for a silicon-based MZ modulator is plotted as a function of the optical signal-to-noise ratio (OSNR) and compared with the BER characteristics of an LN MZ modulator. The penalty in the OSNR for the silicon modulator is lower than 1 dB at a BER of 10^{-11}, and almost the same BER performance is achieved as with the LN modulator. Silicon-based MZ optical modulators are suitable to small-footprint zero-chirped phase modulators in high-capacity optical networks.

References

1. K. K. Lee, D. R. Lim, L. C. Kimerling, J. Shin, and F. Cerrina, "Fabrication of ultralow-loss Si/SiO_2 waveguides by roughness reduction," *Opt. Lett.* **26**(33), 1888–1890 (2001).
2. G. T. Reed and A. P. Knights, *Silicon Photonics: An Introduction*, John Wiley and Sons, Chichester, UK 92–94 (2004).
3. K. Ogawa, K. Goi, H. Kusaka, Y. Terada, T.-Y. Liow, X. Tu, G.-Q. Lo, D.-L. Kwong, V. Dixit, S. T. Lim, and C. E. Png, "Low-loss high-speed silicon Mach-Zehnder modulator for optical-fiber telecommunications," *Proc. SPIE* **8629**, 86290U-1–86290U-8 (2013).
4. K. Ogawa and K. Nishide, "Is silicon photonics a competitive technology to enable better and highly performing networks?," *Silicon Photonics III, Systems and Applications*, Eds. L. Pavesi and D. J. Lockwood, Topics in Applied Physics 122, Springer-Verlag, Berlin, Heidelberg, 447–472 (2016).
5. H. K. Tsang, C. S. Wong, T. K. Liang, I. E. Day, S. W. Roberts, A. Harpin, J. Drake, and M. Asghari, "Optical dispersion, two-photon absorption and self-phase modulation in silicon waveguides at 1.5 μm wavelength," *Appl. Phys. Lett.* **80**(3), 416–418 (2002).
6. M. Dinu, R Quochi, and H. Garcia, "Third-order nonlinearities in silicon at telecom wavelengths," *Appl. Phys. Lett.* **82**(18), 2954–2956 (2003).
7. G. W. Rieger, K. S. Virk, and J. F Young, "Nonlinear propagation of ultrafast l.5 μm pulses in high-index-contrast silicon-on-insulator waveguides" *Appl. Phys. Lett.* **84**(6), 900–902 (2004).
8. H. Yamada, M. Shirane, T. Chu, H. Yokoyama, S. Ishida, and Y. Arakawa, "Nonlinear-optic silicon-nanowire waveguides," *Japanese J. Appl. Phys.* **44** (9A), 6541–6545 (2005).
9. K. Ogawa and M. D. Pelusi, "High-sensitivity pulse spectrogram measurement using two-photon absorption in a semiconductor at 1.5-μm wavelength," *Opt. Express* **7**(3), 135–140 (2000).

10. H. K. Tsang, R. V. Penty, I. H. White, R. S. Grant, W. Sibbett, J. B. D. Soole, H. P. LeBIanc, N. C. Andreadakis, R. Bhat, and M. A. Koza, *J. Appl. Phys*. **70**(7), 3992–3994 (1991).
11. K. Wörhoff, P.V. Lambeck, and A. Driessen, "Design, tolerance analysis, and fabrication of silicon oxynitride based planar optical waveguides for communication devices," *J. Lightwave Technol.* **17**(8), 1401–1407 (1999).
12. O. Cohen, R. Jones, O. Raday, A. Fang, N. Izhaky, D. Rubin, and M. Paniccia, "SOI-based monolithic integration of SiON and Si planar optical circuits," *Proc. SPIE* **6183**, 618313-1–618313-7 (2013).
13. D. J. Thomson, Y. Hu, G. T. Reed, and J.-M. Fedeli, "Low loss MMI couplers for high performance MZI modulators," *IEEE Photon. Technol. Lett.* **22**(20), 1485–1487 (2010).
14. H. Yi, Y. Huang, X. Wang, and Z. Zhou, "Ultra-short silicon MMI demultiplexer," *Proc. SPIE* **8564**, 856410-1–856410-6 (2012).
15. Y. Zhang, S. Yang, A. E.-J. Lim, G.-Q. Lo, C. Galland, T. Baehr-Jones, and M. Hochberg, "A compact and low loss Y-junction for submicron silicon waveguide," *Opt. Express* **21**(1), 1310–1316 (2013).
16. Z. Xiao, X. Luo, P. H. Lim, P. Prabhathan, S. T. H. Silalahi, T.-Y. Liow, J. Zhang, and F. Luan, "Ultra-compact low loss polarization insensitive silicon waveguide splitter," *Opt. Express* **21**(14), 16331–16336 (2013).
17. A. Sakai, T. Fukazawa, and T. Baba, "Low-loss ultra-small branches in a silicon photonic wire waveguide," *IEICE Trans. Electron.* **E85-C**(4), 1033–1038 (2002).
18. R. Hanfoug, L. M. Augustin, Y. Barbarin, J. J. G. M. van der Tol, E. A. J. M Bente, F. Karouta, D. Rogers, Y. S. Oei, X. J. M. Leijtens, and M. K. Smit "A Multimode Interference coupler with low reflections," *Proc. Symposium IEEE/LEOS Benelux Chapter* 97–100 (2005).
19. K. Goi, A. Oka, H. Kusaka, K. Ogawa, T.-Y. Liow, X. Tu, G.-Q. Lo, and D.-L. Kwong, "Low-loss partial rib polarization rotator consisting only of silicon core and silica cladding," *Opt. Lett.* **40**(7), 1410–1413 (2015).
20. D. Vermeulen, S. Selvaraja, P. Verheyen, P. Absil, W. Bogaerts, D. Van Thourhout, and G. Roelkens, "Silicon-on-insulator polarization rotator based on a symmetry breaking silicon overlay," *IEEE Photon. Technol. Lett.* **24**(6), 482–484 (2012).
21. L. Chen, C. R. Doerr, and Y.-K. Chen, "Compact polarization rotator on silicon for polarization-diversified circuits," *Opt. Lett.* **36**(4), 469–471 (2011).
22. K. Ogawa, K. Goi, A. Oka, Y. Mashiko, T.-Y. Liow, X. Tu, G.-Q. Lo, D.-L. Kwong, S. T. Lim, M. J. Sun, and C. E. Png, "Design and characterisation of high-speed monolithic silicon modulators for digital coherent communication," *Proc. SPIE* **9367**, 93670C-1–93670C-8 (2015).
23. A. Oka, K. Goi, H. Kusaka, K. Ogawa, T.-Y. Liow, X. Tu, G.-Q. Lo, and D.-L. Kwong, "Low-loss all-adiabatic silicon-waveguide polarization-division multiplexer in C and L bands," *2014 OptoElectronics and*

Communication Conference and Australian Conference on Optical Fibre Technology (OECC/ACOFT), 570–572 (2014).
24. D. Dai and J. E. Bowers, "Novel concept for ultracompact polarization splitter-rotator based on silicon nanowires," *Opt. Express* **19**(11), 10940–10949 (2011).
25. W. D. Sacher, T. Barwicz, B. J. F. Taylor, and J. K. S. Poon, "Polarization rotator-splitters in standard active silicon photonics platforms," *Opt. Express* **22**(4), 3777–3786 (2014).
26. K. Tan, Y. Huang, G.-Q. Lo, C. Yu, and C. Lee, "Ultra-broadband fabrication-tolerant polarization splitter and rotator," *Optical Fiber Communications Conference and Exhibition (OFC)*, Th1G.7 (2017).
27. N. Ishikura, K. Goi, H. Zhu, M. Illarionov, H. Ishihara, A. Oka, T. Oda, K. Masuko, T. Ori, K. Ogawa, Y. Yoshida, K. Kitayama, T.-Y. Liow, X. Tu, G.-Q. Lo, and D.-L. Kwong, "Transmission characteristics of 32-Gbaud PDM IQ monolithic silicon modulator operating with 2-V_{PPD} drive voltage," *42nd European Conference on Optical Communication (ECOC)*, W.2.E4 (2016).
28. K. Goi, N. Ishikura, H. Ishihara, S. Sakamoto, K. Ogawa, T.-Y. Liow, X. Tu, G.-Q. Lo, and D.-L. Kwong, "Low-voltage silicon Mach-Zehnder modulator operating at high temperatures without thermo-electric cooling," *Optical Fiber Communications Conference and Exhibition (OFC)*, W2A.23 (2016).
29. A. Sakai, G. Hara, and T. Baba, "Propagation characteristics of ulltrahigh-Δ optical waveguide on silicon-on-insulator substrate," *Japanese J. Appl. Phys.* **40**(4B), L383–L385 (2001).
30. E. Dulkeith, F. Xia, L. Schares, W. M. J. Green, and Y. A. Vlasov, "Group index and group velocity dispersion in silicon-on-insulator photonic wires," *Opt. Express* **14**(9), 3853–3763 (2006).
31. D. Duchesne, P. Cheben, R. Morandotti, B. Lamontagne, D.-X. Xu, S. Janz, and D Christodoulides, "Group-index birefringence and loss measurements in silicon-on-insulator photonic wire waveguides," *Opt. Eng.* **46**(10), 104602-1–104602-7 (2007).
32. D. T. H. Tan, K. Ikeda, P. C. Sun, and Y. Fainman, "Group velocity dispersion and self phase modulation in silicon nitride waveguides," *Appl. Phys. Lett.* **90**(6), 061101-1– 061101–3 (2010).
33. S. H. Kim, S. H. Lee, D. W. Kim, K. H. Kim, E.-H. Lee, and J.-M. Lee, "Chromatic dispersion measurement of nano-silicon waveguides using a white-light interferometry method," *Proc. SPIE* **7942**, 79420R-1–79420R-7 (2011).
34. S. Mas, J. Matres, J. Martí, and C. J. Oton, "Accurate chromatic dispersion characterization of nanophotonic waveguides with thermal phase noise cancellation," *IEEE 9th International Conference on Group IV Photonics (GFP)*, WP15 (2012).

35. J.-C. Diels and W. Rudolph, *Ultrashort Laser Pulse Phenomena: Fundamentals, Techniques, and Applications on a Femtosecond Time Scale*, Academic Press, 1st Ed., San Diego, London, 1–22 (1996).
36. A. C. Turner, C. Manolatou, B. S. Schmidt, and M. Lipson, "Tailored anomalous group-velocity dispersion in silicon channel waveguides," *Opt. Express* **14**(10), 4357–4362 (2006).
37. A. E. Willner and B. Hoanca, "Fixed and tunable management of fiber chromatic dispersion," *Optical Fiber Telecommunications IV-B: Systems and Impairments*, Eds. I. P. Kaminow and T. Li, Academic Press, San Diego, London, 642–724 (2002).
38. N. Massa, "Fiber optic telecommunication," in *Fundamentals of Photonics*, C. Roychoudhuri, Ed, SPIE Press, Bellingham, Washington, 293–347 (2008).
39. L. G. Cohen and C. Lin, "Pulse delay measurements in zero material dispersion wavelength region for optical fibers," *Appl. Opt.* **16**(12), 3136–3139 (1977).
40. K. Naganuma and H. Yasaka, "Group delay and α-parameter measurement of 1.3 μm semiconductor traveling-wave optical amplifier using the interferometric method," *IEEE J. Quantum Electron.* **27**(6), 1280–1287 (1991).
41. V. Wong and I. A. Walmsley, "Analysis of ultrashort pulse-shape measurement using linear interferometers," *Opt. Lett.* **19**(4), 287–289 (1994).
42. P. Hlubina, "Spectral interferometry and its applications in classical optics," *Proc. SPIE* **3820**, 120–132 (1999).
43. K. Ogawa, "Characterization of chromatic dispersion of optical filters by high-stability real-time spectral interferometry," *Appl. Opt.* **45**(26), 6718–6722 (2006).
44. K. Ogawa, K. Tomiyama, Y. T. Tan, M. T. Doan, M. B. Yu, D.-L. Kwong, S. Yamada, J. B. Cole, H. Mizuta, and S. Oda, "Broadband variable chromatic dispersion in photonic-band electro-optic waveguide," *Optical Fiber Communication Conference and Exposition and the National Fiber Optic Engineers Conference (OFC/NFOEC)*, OThE4 (2006).
45. K. Ogawa and T. T. Lay, "Chromatic dispersion measurement of SOA in C + L band by self-tracking real-time interferometry," *Optical Fiber Communication Conference and Exposition and the National Fiber Optic Engineers Conference (OFC/NFOEC)*, OThH7 (2005).
46. N.-B. Yim, C. Il Eom, and S.-W. Kim, "Dual mode phase measurement for optical heterodyne interferometry," *Meas. Sci. Technol.* **11**(8), 1131–1137 (2000).
47. K. Ogawa, K. Goi, N. Ishikura, H. Ishihara, S. Sakamoto, T.-Y. Liow, X. Tu, G.-Q. Lo, D.-L. Kwong, S. T. Lim, M. J. Sun, and C. E. Png, "Silicon-based phase shifters for high figure of merit in optical modulation," *Proc. SPIE* **9752**, 975202-1–975202-7 (2016).

48. X. Tu, T.-Y. Liow, J. Song, M. Yu, and G. Q. Lo, "Fabrication of low loss and high speed silicon optical modulator using doping compensation method," *Opt. Express* **19**(19), 18029–18035 (2011).
49. H. Zhu, K. Goi, and K. Ogawa, to be presented in OECC 2017.
50. S. M. Sze, *Physics of Semiconductor Devices*, 2nd. Ed., J. Wiley & Sons, New York, 16–92 (1981).
51. P. Lautenschlager, P. B. Allen, and M. Cardona, "Temperature dependence of band gaps in Si and Ge," *Phys. Rev. B* **31**(4), 2163–2171 (1985).
52. M. W. Geis, S. J. Spector, M. E. Grein, R. T. Schulein, J. U. Yoon, D. M. Lennon, S. Deneault, F. Gan, F. X. Kaertner, and T. M. Lyszczarz, "CMOS-compatible all-Si high-speed waveguide photodiodes with high responsivity in near-infrared communication band," *IEEE Photon. Technol. Lett.* **19**(3) 152–154 (2007).
53. M. W. Geis, S. J. Spector, M. E. Grein, J. U. Yoon, D. M. Lennon, and T. M. Lyszczarz, "Silicon waveguide infrared photodiodes with >35 GHz bandwidth and phototransistors with 50 AW^{-1} response," *Opt. Express* **17** (7), 5193–5204 (2009).
54. D. F. Logan, P. Velha, M. Sorel, R. M. De La Rue, A. P. Knights, and P. E. Jessop, "Defect-Enhanced silicon-on-insulator waveguide resonant photodetector with high sensitivity at 1.55 μm," *IEEE Photon. Technol. Lett.*, **22**(20), 1530–1532 (2010).
55. H. Yu, D. Korn, M. Pantouvaki, J. Van Campenhout, K. Komorowska, P. Verheyen, G. Lepage, P. Absil, D. Hillerkuss, L. Alloatti, J. Leuthold, R. Baets, and W. Bogaerts, "Using carrier-depletion silicon modulators for optical power monitoring," *Opt. Lett.* **37**(22), 4681–4683 (2012).
56. H. Zhu, L. Zhou, X. Sun, Y. Zhou, X. Li, and J. Chen, "On-Chip optical power monitor using periodically interleaved p-n junctions integrated on a silicon waveguide," *IEEE J. Sel. Top. Quantum Electron.* **20**(4), 3800408-1–3800408-8 (2014).
57. B. Souhan, R. R. Grote, J. B. Driscoll, M. Lu, A. Stein, H. Bakhru, and R. M. Osgood, Jr., "Metal-semiconductor-metal ion-implanted Si waveguide photodetectors for C-band operation," *Opt. Express* **22**(8), 9150–9158 (2014).
58. Y. Terada, K. Miyasaka, H. Ito, and T. Baba, "Slow-light effect in a silicon photonic crystal waveguide as a sub-bandgap photodiode," *Opt. Lett.* **41**(2), 289–292 (2016).
59. K. Gill, G. Hall, and B. MacEvoy, "Bulk damage effects in irradiated silicon detectors due to clustered divacancies," *J. Appl. Phys.* **82**(1), 126–136 (1997).
60. S. Libertino, S. Coffa, and J. Benton, "Formation, evolution, and annihilation of interstitial clusters in ion-implanted Si," *Phys. Rev. B* **63** (19), 195206-1–195206-14 (2001).

61. R. W. Dutton, "TCAD—Yesterday, Today and Tomorrow," *IEICE Trans. Electron.* **E82-C**(6), 791–790 (1999).
62. I. Goykhman, B. Desiatov, S. Ben-Ezra, J. Shappir, and U. Levy, "Optimization of efficiency-loss figure of merit in carrier-depletion silicon Mach-Zehnder optical modulator," *Opt. Express* **21**(17), 19518–19529 (2013).
63. J. R. Matey, "Scanning capacitance microscopy," *Proc. SPIE* **897**, 110–117 (1988).
64. Y. Martin, D. W. Abraham, and H. K. Wickramasinghe, "High-resolution capacitance measurement and potentiometry by force microscopy," *Appl. Phys. Lett.* **52**(13), 1103–1105 (1988).
65. C. C. Williams, J. Slinkman, W. P. Hough, and H. K. Wickramasinghe, "Lateral dopant profiling with 200 nm resolution by scanning capacitance microscopy," *Appl. Phys. Lett.* **55**(16), 1662–1664 (1989).
66. V. V. Zavyalov, J. S. McMurray, S. D. Stirling, C. C. Williams, and H. Smith, "Two dimensional dopant and carrier profiles obtained by scanning capacitance microscopy on an actively biased cross-sectioned metal–oxide–semiconductor field-effect transistor," *J. Vac. Sci. Technol. B* **18**(1), 549–554 (2000).
67. D. Ban, E. H. Sargent, St. J. Dixon-Warren, T. Grevatt, G. Knight, G. Pakulski, A. J. SpringThorpe, R. Streater, and J. K. White, "Two-dimensional profiling of carriers in a buried heterostructure multi-quantum-well laser: Calibrated scanning spreading resistance microscopy and scanning capacitance microscopy," *J. Vac. Sci. Technol. B* **20**(5), 2126–2132 (2002).
68. S. Anand, T. Kallstenius, B. Stoltz, U. Smith, and G. Landgren, "Characterization of buried heterostructure lasers by scanning capacitance microscopy," *11th International Conference on Indium Phosphide and Related Materials (IPRM)*, MoB1-7 (1999).
69. E. Bussmann and C. C. Williams, "Sub-10 nm lateral spatial resolution in scanning capacitance microscopy achieved with solid platinum probes," *Rev. Sci. Instrum.* **75**(2), 422–425 (2004).
70. http://www.toray-research.co.jp/en/technicaldata/techniques.html.
71. http://www.parkafm.com/images/spmmodes/electrical/Scanning-Capacitance-Microscopy-(SCM).pdf.
72. https://www.bruker.com/products/surface-and-dimensional-analysis/atomic-force-microscopes/modes/modes/nanoelectrical-modes/scm.html.
73. K. Kurokawa, "Power waves and the scattering matrix," *IEEE Trans. Microwave Theory and Tech.* **13**(2), 194–202 (1965).
74. S. Uehara, "Calibration of optical modulator frequency response with application to signal level control," *Appl. Opt.* **17**(1), 68–71 (1978).
75. R. Becker, "Broad-band guided-wave electrooptic modulators," *IEEE J. Quantum Electron.* **20**(7), 723–727 (1984).

76. R. G. Walker, "High-speed III-V semiconductor intensity modulators," *IEEE J. Quantum Electron.* **27**(3), 654–667 (1991).
77. M. M. Howerton and W. Burns, "Broadband traveling wave modulators in $LiNbO_3$," in *RF Photonics Technology in Optical Fiber Links*, W. S. C. Chang, Ed., Cambridge University Press, Cambridge, New York, 133–164 (2002).
78. A. C. Reyes, S. M. El-Ghazaly, S. J. Dorn, M. Dydyk, D.K. Schroder, and H. Patterson, "Coplanar waveguides and microwave inductors on silicon substrates," *IEEE Trans. Microwave Theory Tech.* **43**(9), 2016–2022 (1995).
79. D. Lederer and J.-P. Raskin, "Substrate loss mechanisms for microstrip and CPW transmission lines on lossy silicon wafers," *IEEE International Microwave Symposium (MTT-S)*, WE1C-7 (2002).
80. T. Makita, I. Tamai, and S. Seki, "Coplanar waveguides on high-resistivity silicon substrates with attenuation constant lower than 1 dB/mm for microwave and millimeter-wave bands," *IEEE Trans. Electron Dev.* **58**(3), 709–715 (2011).
81. T.-Y. Liow, K.-W. Ang, Q. Fang, J.-F. Song, Y.-Z. Xiong, M.-B. Yu, G.-Q. Lo, and D.-L. Kwong, "Silicon modulators and germanium photodetectors on SOI: Monolithic integration, compatibility, and performance optimization," *IEEE J. Sel. Top. Quantum Electron.* **16**(1), 307–315 (2010).
82. W. W. Rigrod and I. P. Kaminow, "Wide-band microwave light modulation," *Proc. IEEE* **51**(1), 137–140 (1963).
83. R. A. Myers and P. S. Pershan, *J. Appl. Phys.* **36**(1), 22–28 (1965).
84. M. Izutsu, Y. Yamane, and T. Sueta, "Broad-band traveling-wave modulator using a $LiNbO_3$ optical waveguide," *IEEE J. Quantum Electron.* **13**(4), 287–290 (1977).
85. R. Alferness, S. Korotky, and E. Marcatili, "Velocity-matching techniques for integrated optic traveling wave switch/modulators," *IEEE J. Quantum Electron.* **20**(3), 301–309 (1984).
86. K. Noguchi, O. Motomi, K. kawano, and M. Yanagibashi, "Highly efficient 40-GHz bandwidth Ti:$LiNbO_3$ optical modulator employing ridge structure," *IEEE Photon. Technol. Lett.* **5**(1), 52–54 (1993).
87. K. Ogawa, K. Goi, Y. T. Tan, T.-Y. Liow, X. Tu, Q. Fang, G.-Q. Lo, and D.-L. Kwong, *Opt. Express* **19**(26), B26–B31 (2011).
88. D. J. Thomson, F. Y. Gardes, Y. Hu, G. Mashanovich, M. Fournier, P. Grosse, J.-M. Fedeli, and G. T. Reed, "High contrast 40Gbit/s optical modulation in silicon," *Opt. Express* **19**(12), 11507–11516 (2011).
89. H.X. Yi, T.T. Li, J.L. Zhang, X.J. Wang, and Z. Zhou, "Temperature-independent broadband silicon modulator," *Optics Commun.* **340**(1), 107–109 (2015).

90. Y. Yang, Q. Fang, M. Yu, X. Tu, R. Rusli, and G.-Q. Lo, "High-efficiency Si optical modulator using Cu traveling-wave electrode," *Opt. Express* **22**(24), 29978–29985 (2014).
91. F. Koyama and K. Iga, "Frequency chirping in external modulators," *J. Lightwave Technol.* **6**(1), 87–93 (1988).
92. A. H. Gnauck and P. J. Winzer, "Optical phase-shift-keyed transmission," *J. Lightwave Technol.* **23**(1), 115–130 (2005).
93. K. Goi, K. Oda, H. Kusaka, Y. Terada, K. Ogawa, T.-Y. Liow, X. Tu, G.-Q. Lo, and D.-L. Kwong, "11-Gb/s 80-km transmission performance of zero-chirp silicon Mach-Zehnder modulator," *Opt. Express* **20**(26), B350–B356 (2012).
94. K. Goi, H. Kusaka, A. Oka, Y. Terada, K. Ogawa, T.-Y. Liow, X. Tu, G.-Q. Lo, and D.-L. Kwong, "20-Gb/s DPSK transmission with 550-ps/nm dispersion tolerance using silicon Mach-Zehnder modulator," *Optical Fiber Communications Conference and Exhibition (OFC)*, OW4J.5 (2013).
95. L. Thylén, U. Westergren, P. Holmström, R. Schatz, and P. Jänes, "Recent developments in high-speed optical modulators," in *Optical Fiber Telecommunications V A: Components and Subsystems*, I. P. Kaminow, T. Li and A. E. Willner, Academic Press, San Diego, 183–220 (2008).
96. K. Kikuchi, T. Okoshi, M. Nagamatsu, and N. Henmi, "Degradation of bit-error rate in coherent optical communications due to spectral spread of the transmitter and the local oscillator," *J. Lightwave Technol.* **2**(6), 1024–1033 (1984).
97. D.-S. Ly-Gagnon, S. Tsukamoto, K. Katoh, and K. Kikuchi, "Coherent detection of optical quadrature phase-shift keying signals with carrier phase estimation," *J. Lightwave Technol.* **24**(1), 12–21 (2006).

Chapter 7
Transmission Characteristics of Integrated Silicon-Based Optical Modulators

Integrated silicon-based MZ optical modulators are used in a variety of optical-network domains. Applications in various modulation formats at 100 Gb/s and beyond are classified with respect to the transmission distance, and the usage of silicon-based optical modulators is discussed in this chapter. Then, the transmission characteristics of silicon-based optical modulators are reviewed in terms of modulation formats such as NRZ-OOK and PAM*n* in intensity modulation; BPSK, QPSK, DP-QPSK, and PDM *n*QAM in phase modulation; and DMT in sub-carrier modulation. Characterization of transmission performances is essential to evaluate optical modulators for a given application. The apparatus for transmission characterization of silicon-based optical modulators and their characteristics is described with respect to the modulation formats. This part can be used as a reference document to conduct transmission measurement of modulators. With the transmission characteristics described there, the reader can verify that integrated silicon-based optical modulators are suitable to a wide range of applications in high-capacity optical networks.

7.1 Applications in Optical Network Domains at 100 Gb/s and Beyond

Applications in optical-network domains are classified with respect to the transmission distance (Fig. 7.1). Different applications in intensity-modulation and phase-modulation formats are listed. Optical modulators are key components for E-O conversion to generate optical signals in a variety of modulation formats. Types of eligible optical modulators are indicated in the applications in Fig. 7.1. Here, Si and III-V indicate integrated MZ optical

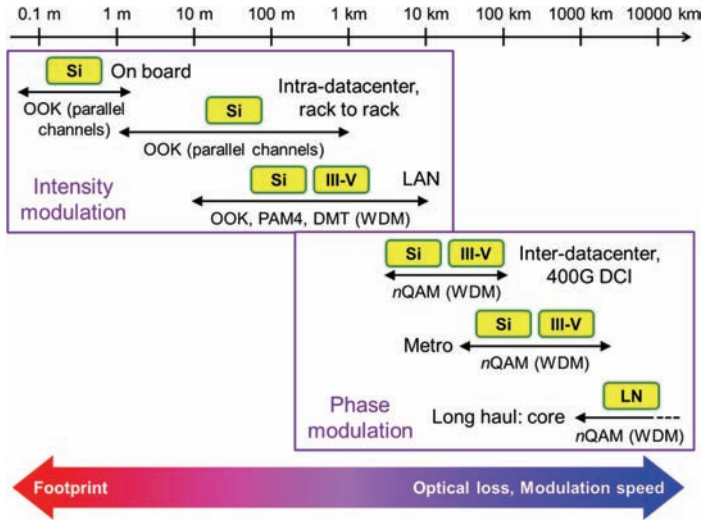

Figure 7.1 Classification of applications with respect to the transmission distance in optical-network domains.

modulators on silicon-photonics and III-V platforms, respectively, and LN indicates a discrete LN MZ optical modulator.

The onboard optical interconnect application has the shortest reach with a maximum distance of ~1 m. A parallel optical interface provides an optical interconnect between processors and memories on PCBs. The small footprint of optical modulators is crucial for compact optical I/Os on PCBs. A intra-datacenter rack-to-rack interconnect extends up to ~1 km in distance. The typical modulation format in these applications is NRZ-OOK in parallel fiber channels. Four fiber channels, or four cores in a single fiber as shown in Fig. 2.5, with 25 Gb/s NRZ-OOK per channel allow multiplication to 100-Gb/s data throughput. In a LAN, optical signals are transmitted with a maximum distance of 10 km in NRZ-OOK, PAM4, or DMT in WDM of an optical fiber. Transmission at 25 Gb/s and 100 Gb/s in each of the four wavelength channels allows 100 Gb/s and 400 Gb/s throughput, respectively. Compact optical transceivers allow high-density optical interconnects of computers and servers in datacenters and LANs.

In applications with a longer reach, where optical signals are transmitted through optical amplifiers to compensate attenuation due to optical loss in a transmission optical fiber, the OSNR of the optical signals is crucial because the optical noise level is increased in optical amplifiers. Therefore, the lower optical loss is required in the longer transmission span. The modulation speed pertaining to the baud rate is also crucial to high-capacity transmission in longer-reach applications because of serial transmission in the limited number of transmission optical fibers installed in underground and undersea pathways.

In longer-reach applications, optical signals are transmitted in phase-modulation formats in spite of the complicated optical-circuit layouts of phase modulators because phase modulation with differential detection has the advantage of a high OSNR, as described in Chapter 3. Photonic-integration platforms enable the design and fabrication of small-footprint phase modulators. In an inter-datacenter network (such as an application of growing importance, DP-QPSK), 4QAM (100 Gb/s) in each of the four-wavelength channels and 16QAM (200 Gb/s) in each of the two-wavelength channels are employed as the major modulation formats, allowing 400-G DCI up to a maximum distance of 120 km.[1–4] In metro applications with a span of 80 km to ~1000 km, DP-QPSK and 16QAM are also used in 100 Gb/s and 400-Gb/s networks, respectively. In a long-haul core network beyond 1000 km, in which LN optical modulators have been used extensively, DP-QPSK is preferred if the OSNR is critical, whereas 16QAM is used if a lower OSNR is allowable.

7.2 On–Off Keying and Pulse Amplitude Modulation

7.2.1 Apparatus and device for OOK transmission

The apparatus for optical data transmission in an optical fiber link with the NRZ-OOK format at a bit rate of 11 Gb/s is depicted in Fig. 7.2. A parallel push–pull carrier-depletion silicon-based single MZ optical modulator chip, described in Chapters 3 and 6, mounted on a metal chip carrier is utilized for optical-data generation with chirp-free transmission. Complementary electrical signals DATA and $\overline{\text{DATA}}$ in $2^{31}-1$ PRBS are applied to the input signal ports of the traveling-wave electrodes on both MZI arms, respectively. The output signal ports are terminated with 50-Ω resistors to eliminate back reflection of the electrical signals. Lateral PN-junction rib-waveguide phase shifters with a 600-nm rib width and 4-mm phase-shifter length are disposed in the arms of the MZI of the MZ optical modulator driven in carrier-depletion mode under DC reverse bias.[5] The wavelength of the input CW light from a

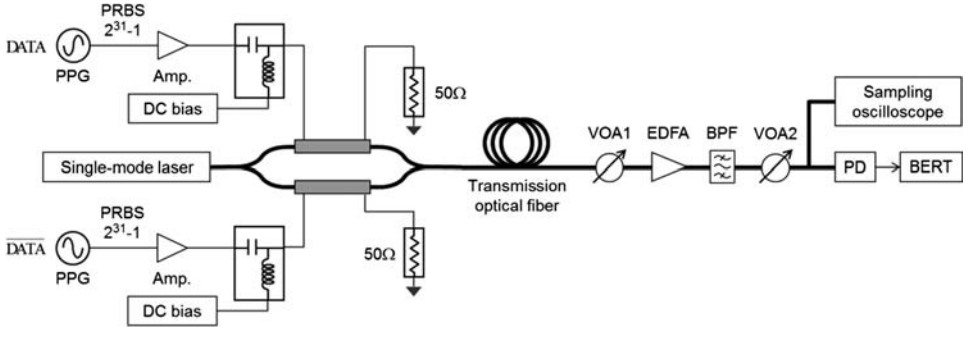

Figure 7.2 Apparatus for OOK transmission measurement with a push–pull silicon MZ optical modulator.

single-mode laser was 1545.7 nm. The CW light was input to the silicon MZ optical modulator chip in TE polarization with a lensed PMF. Modulated light from the modulator was launched to a transmission optical fiber link by optical coupling with a lensed fiber made of a standard-dispersion single-mode fiber (SMF). The insertion loss of the modulator is lower than 10.5 dB in the C band, including fiber coupling on both ends.

The transmission optical fiber link is SMF or dispersion-compensation fiber (DCF) in different spans. The latter fiber, which yields chromatic dispersion with the sign opposite that of the former fiber, has been introduced in commercialized optical fiber transmission links extensively to achieve zero accumulated dispersion and hence eliminate symbol interference in commercial fiber links. By using SMF and DCF in different spans, transmission performance metrics such as BER and optical path power penalty can be characterized accurately. Variable optical attenuator 1 (VOA1) has been inserted to adjust the optical power level of transmitted optical signals with respect to the optical noise level of amplified spontaneous emission (ASE) in EDFA. The spectral bandwidth of the optical noise has been limited within 0.1 nm around the optical signal spectrum through an optical bandpass filter (BPF).[6,7] In the eye-diagram measurement of transmitted optical signals, the output fiber port of the link was connected to a high-speed optical receiver module in a sampling oscilloscope for eye-diagram measurement and to a high-speed PD connected to a BER tester (BERT) for BER measurement, respectively. The optical power level input to the sampling oscilloscope or the PD was adjusted to a specified level with VOA2.

In a parallel push–pull modulator, the phase shifters in the MZI arms are electrically isolated from each other. Electrical signals DATA and $\overline{\text{DATA}}$ in opposite polarities are applied separately to the respective arms.[5,8,9] In this configuration, the dual electrical outputs from a modulator driver are used to generate the complementary electrical-signal pair, and therefore the voltage amplitude from each driver output port is used only to modulate each PN-junction phase shifter. Coplanar waveguides, which comprise traveling-wave electrodes in the parallel push–pull optical modulator, have wide ground planes suitable to RF signal isolation and yield characteristic impedance with weaker dependence of the RF frequency than those of other traveling-wave electrodes, such as coplanar strip lines.[10] In contrast, a single electrical output can drive the phase shifters in the both of MZI arms for series push–pull optical modulators including compound-semiconductor QCSE MZ optical modulators.[11–15] In this configuration, two phase shifters in the MZI arms are connected electrically in series. The voltage amplitude from a single driver output port is required to produce twice that in the parallel push–pull configuration. Coplanar-strip or slotline-type traveling-wave electrodes are utilized instead of coplanar waveguides for electrical-circuit compatibility, although the number of bonding wires for RF signals can be reduced by half.

Silicon-photonics platform with common theoretical and experimental analysis tools can be applied to integrated silicon-based optical modulators in the both configurations. Therefore, the design, fabrication, analysis, and characterization methods discussed in this book can also be applied to series push–pull modulators without loss of generality.

A single-drive push–pull design can be used if the packaging footprint is critical: planar space, such as for contact pads of the traveling electrodes on the modulator chip and transmission RF lines on PCB, is reduced. The cost for a single-end electrical driver may be lower than that for a dual-end electrical driver with a circuit converter to isolate the dual ends. The single-drive modulator, however, will suffer from the parasitic effect of PN-junction capacitance, which limits the modulation speed more seriously than the dual-drive modulator because dual phase shifters are connected in parallel to the signal electrode and the junction capacitance is doubled in the single-drive configuration. A lumped-element silicon-based MZ optical modulator, on the other hand, can be driven directly with the digital outputs of electrical ICs without electrical drivers. The phase shifters are much shorter than 1 mm in length to suppress the traveling-wave effects at symbol rates of 25 Gbaud and higher. Thus, high doping to the PN-junction phase shifters is required to enhance the modulation efficiency with a drive voltage of $\sim$1 V_{PP}, and the optical loss of the phase shifters is significant. The lumped-element modulators can be used mainly in onboard and intra-datacenter domains, where the OSNR is not crucial.

7.2.2 Characteristics of OOK transmission

Measurements based on the apparatus above provide transmission characteristics presented in Fig. 7.3. With increasing span from back (B)-to-back (B), that is 0-km transmission, to 80-km transmission through SMF, the BER increases and a higher OSNR penalty is imposed. Transmission through DCFs provides similar BER characteristics. The optical path power penalty, which is defined as the OSNR penalty at a BER of 10^{-3}, is plotted as a function of the accumulated dispersion and compared with that of a push–pull LN MZ optical modulator.[6] Positive accumulated dispersion is produced in SMFs of different spans, whereas negative accumulated dispersion is produced in DCFs of different spans. Dispersion tolerance is measured at an optical path power penalty of 2 dB and leads to more than ±950 ps/nm for a silicon-based modulator, which is comparable with that of the LN modulator plotted in Fig. 7.3.[16,17] The silicon-based optical modulator can be used for transmission in NRZ-OOK at 11 Gb/s. The dispersion tolerance is limited by residual frequency chirping, which causes distortion of optical signals and hence inter-symbol interference, as shown in Fig. 7.3.

The transmission characteristics in NRZ-OOK can also be measured in non-push–pull modulation with a single-arm drive, as shown with transmission

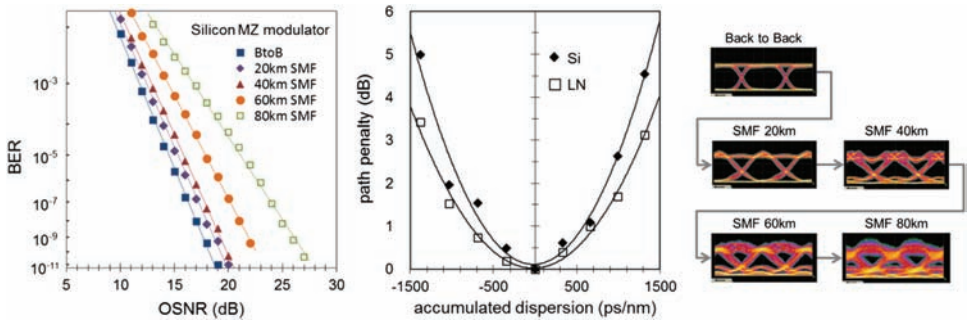

Figure 7.3 Transmission characteristics of a push–pull silicon MZ optical modulator in NRZ-OOK.

eye diagrams in Fig. 7.4. A silicon-based single MZ optical modulator packaged in an $18\times14\times8$-mm^3 ceramic-based metal housing has been utilized in transmission measurements.[18,19] (The package will be described in the next chapter as an example of photonic-electronic packaging.) The thermal expansion coefficient of crystalline silicon is 4.2 ppm/K, compared to the 6.9 ppm of ceramic. This value leads to a deformation of <1 μm with a chip length of 5 mm and a temperature rise from 25°C to 80°C. The ceramic-based metal housing is, therefore, suitable to high-reliability photonic-electronic packaging on a silicon-photonics platform. Passive V-groove alignment to a PIC on a ceramic base has been investigated.[20]

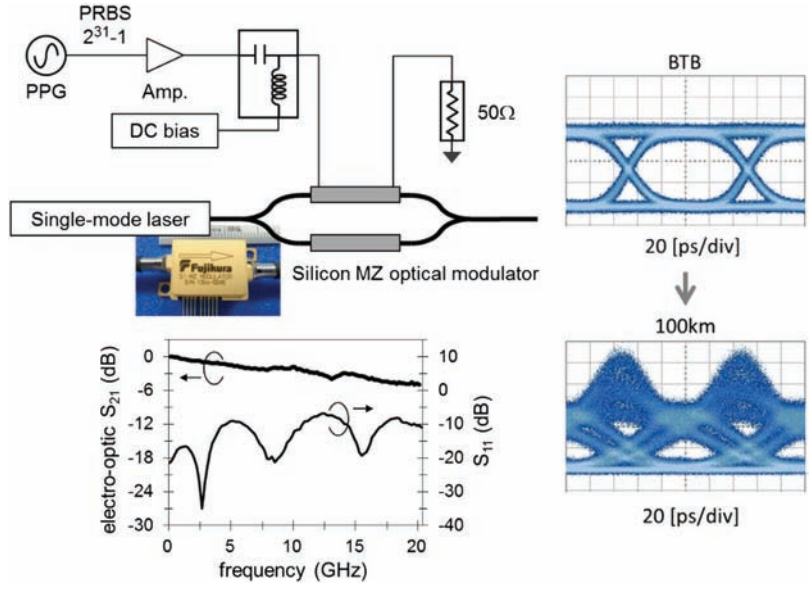

Figure 7.4 Non-push–pull silicon MZ optical modulator in a ceramic-based metal package; *S*-parameter characteristics; and transmission eye diagrams in 11-Gb/s NRZ-OOK.

The extinction ratio of a silicon-based modulator operated under a DC reverse bias of 10 V is as high as 13.7 dB in a back-to-back (BTB) eye diagram of 11-Gb/s NRZ-OOK. Eye opening is still observed in the eye diagram after transmission through a 100-km SMF of ~1600-ps/nm accumulated dispersion. The electro-optic 3-dB bandwidth of the reverse-bias modulator is 12.5 GHz in S_{21} of the *S*-parameter characteristics. The voltage reflectance of the input electrical signal is −9 dB at maximum.

The optical path power penalty of the package modulator is plotted in comparison with that of a LN MZ optical modulator in the Fig. 7.5(a). The optical path power penalty reaches a minimum at a positive accumulated dispersion of about 500 ps/nm, which corresponds to ~30-km transmission through SMF in a dispersion parameter defined in Eq. (6.4) of 16 ps/nm/km. This makes a significant difference qualitatively from the characteristics in the zero-chirped push–pull NRZ-OOK in Fig. 7.3, where the minimum of optical path power penalty occurs at zero accumulated dispersion. To understand the reason why the minimum appears in positive accumulated dispersion, one should note measured transfer characteristics as a function of reverse bias voltage in the right graph of Fig. 7.5 and recall that carrier densities decrease with the reverse-bias voltage in carrier-depletion PN-junction phase shifter, thereby refractive index of the PN-junction phase shifter increases with reverse-bias voltage due to free-carrier plasma refraction as we have studied in Chapter 5. Positive accumulated dispersion in SMF is cancelled with a negative modulator *a*-parameter.

The measured transfer curve yields a transmittance minimum at a reverse-bias voltage of 7 V. The modulator thus operates in a high-voltage regime over the voltage of the transmittance minimum. In this regime, both the refractive index of the phase shifter and the output optical intensity from the modulator increase with an increasing applied voltage, whereas both values decrease with a decreasing applied voltage. Therefore, an increase in the optical intensity leads to phase retardation and thus low-frequency shift,

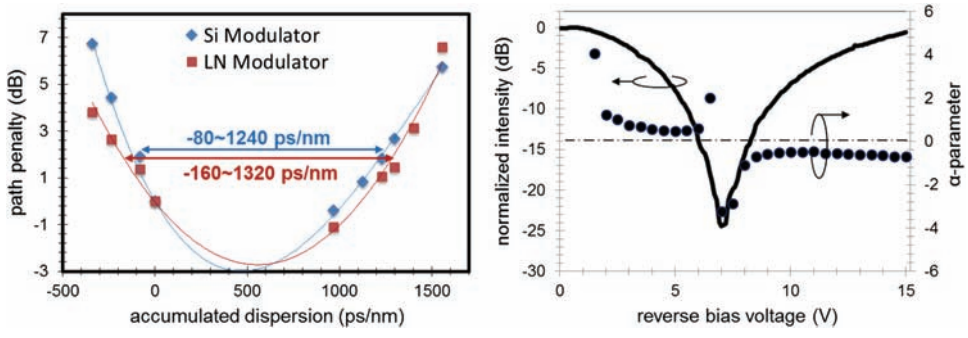

Figure 7.5 Optical path power penalty and bias-dependent α-parameter of a non-push–pull silicon MZ optical modulator in 10-Gb/s NRZ-OOK.

whereas its decrease produces phase acceleration and high-frequency shift.[21] The theoretical modulator *a*-parameter defined in Eq. (3.10) is expected to be negative in this regime but positive in a low-voltage regime within the voltage of the transmittance minimum. Experimentally, a modulator *a*-parameter has been obtained by optical phase-delay measurement in RF sinusoidal modulation that agrees with the theoretical discussion above.[22] The measured a_{mod} is -0.6 at a reverse-bias voltage of 10 V. Characteristics of frequency chirping have been studied extensively for MZ optical modulators, including silicon-based MZ optical modulators.[23–29] In an LN MZ optical modulator, a_{mod} of -0.7 has been reported.[24] Silicon-based modulators yield a transmission performance sufficient for onboard, intra-datacenter, and LAN applications.

The feature described above for the modulator *a*-parameter allows chromatic-dispersion compensation with a prechirped optical signal using a simple configuration of a single-arm driver circuit at a specified transmission span of optical fiber with a preconditioning reverse-bias voltage. Such a method of precompensation has been shown to be useful on the basis of theoretical analysis of optical pulse propagation and the equivalent circuit analysis of semiconductor MZ optical modulators.[29,31] The method can now be exploited for transmission using silicon-based MZ optical intensity modulators that have a dispersion tolerance of -80 ps/nm to 1240 ps/nm, which is almost the same as that obtained for the LN modulator. Therefore, the silicon-based optical modulator in the package is a candidate for prechirped small-footprint MZ optical modulator as well as a zero-chirped MZ optical modulator in NRZ-OOK transmission.

7.2.3 PAM*n* scheme

In PAM*n* fotmat, output optical intensity is modulated at multiple intensity levels. In particular, PAM4 (where $n = 4$) has been extensively interested with respect to high-capacity datacenter and various datacom applications.[31] An apparatus for PAM4 using a high-speed EML is presented, for example, in Fig. 7.6.[32] For generation of electrical signals in multiple levels, digital signal processors are used instead of PPGs in binary modulation, and digital-to-analog converters (DACs) allow electrical signal conditioning for PAM4 in conjunction with linear voltage amplifiers. A back-to-back eye diagram in 56-Gbaud (112-Gb/s) PAM4 using an EML of 31-GHz electro-optic 3-dB bandwidth is presented in Fig. 7.6. Four wavelength channels consisting of equivalent setups are multiplexed to generate 400-Gb/s optical signals. Silicon-based carrier-depletion MZ optical modulators that have lateral PN-junction rib-waveguide phase shifters have been used to generate PAM4 optical signals at 100 Gb/s and beyond.[33–35] Energy-efficiencient PAM4 modulation has been demonstrated at drive voltages from 1.2 V to 2.4 V at 36 Gb/s.[36]

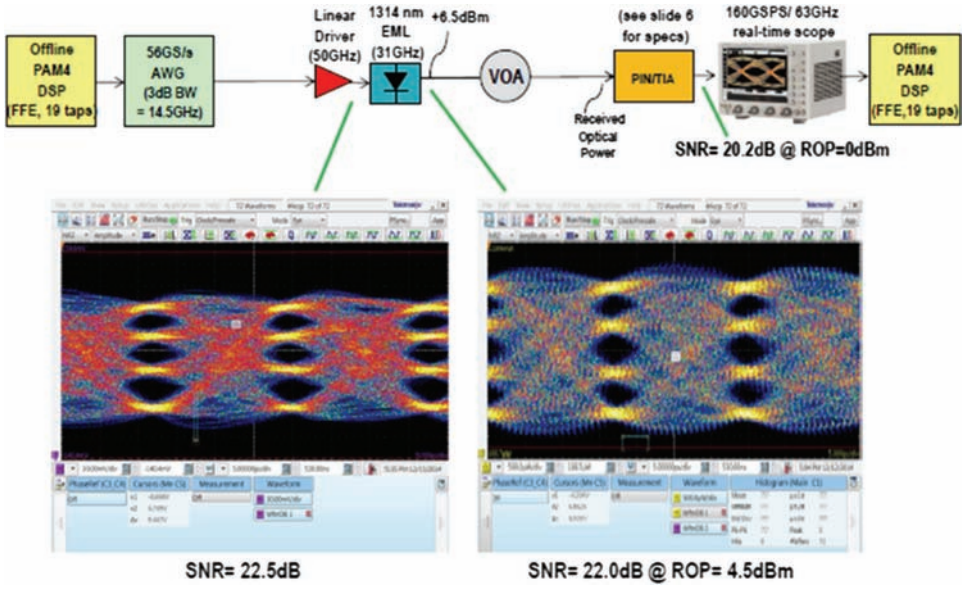

Figure 7.6 Apparatus for 56-Gbaud PAM4 characterization with a 31-GHz EML.[32]

7.3 Phase-Shift Keying

7.3.1 Apparatus and device for PSK transmission

In PSK formats, there are basically two types of optical signal detection: digital coherent detection with a local oscillator (LO) and direct detection using a one-bit delayed interferometer without LO.[16,37–43] The former scheme requires high-speed digital signal processors for ultra-low-latency digital phase retrieval routines and subsequent signal decoding processes.[44–46] In the early stages of PSK transmission, when high-speed digital processors were not yet available commercially, the latter scheme was adopted in conjunction with differential coding, whereby signals are encoded with reference to each previous bit in the transmitter side, and thus a one-bit delayed interferometer is essential for decoding without coherent detection using LO on the receiver side. The detection scheme with differential coding is called direct detection or delayed self-homodyne detection in modulation formats such as differential phase-shift keying (DPSK) and differential quadrature phase-shift keying (DQPSK), which accommodate BPSK and QPSK formats in conjunction with the differential coding, respectively.[38,43] A one-bit delayed interferometer can be constructed by using an asymmetric MZ interferometer with two output ports. An apparatus for BPSK with coherent detection or DPSK with direct detection is depicted in Fig. 7.7. The silicon-based carrier-depletion single MZ optical modulator chip driven in the parallel push–pull configuration is used as a DUT for optical transmission performance in the apparatus.[6] Inline optical modules, VOA1, EDFA, BPF, and VOA2 are

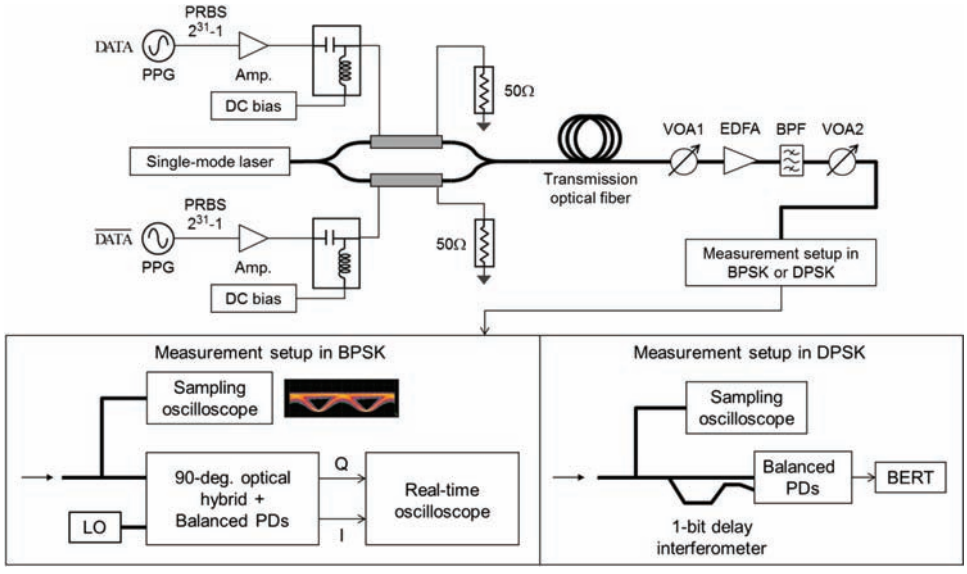

Figure 7.7 Apparatus for BPSK or DPSK transmission measurement with a push–pull silicon MZ optical modulator.

installed for the same purpose as in the transmission measurement apparatus in NRZ-OOK.

An optical hybrid circuit that comprises a passive 2×2 or 1×2 MMI as a building block allows two optical outputs in mutually orthogonal phase states of 90-deg-separated I and Q components.[47–53] In the coherent detection with LO, a 2×2 MMI is used for the 90-deg optical hybrid circuit, whereas an asymmetric 1×2 MMI is used in the direct detection. These MMIs can be designed according to the computational methods presented in Chapter 4.

Multi-level modulation formats such as QPSK and DQPSK in orthogonal phase space have been employed extensively to increase the transmission capacity without increasing the symbol rate. A quadrature optical modulator that comprises I and Q sub-MZIs nested in a main MZI allows zero-chirp generation of multi-level signals in the orthogonal phase components. Multi-level optical signals are generated in 2D phase spaces spanned with I and Q component axes, as shown in Appendix A.1, and each phase state is well isolated from each other. Therefore, it is easier to achieve a low BER with IQ modulation formats than with 1D multi-level intensity modulation. Integrated small-footprint quadrature optical modulators on a silicon-photonics platform have been reported with various designs of phase shfiters.[54–57] A silicon organic quadrature modulator has been also reported.[58] A parallel push–pull integrated silicon-based carrier-depletion quadrature MZ optical modulator in a chip footprint as small as 3.5×2.9 mm^2 is shown in Fig. 7.8 with an optical-waveguide layout and characteristics of integrated TO phase shifters to generate a 90-deg I–Q phase difference and compensation of static

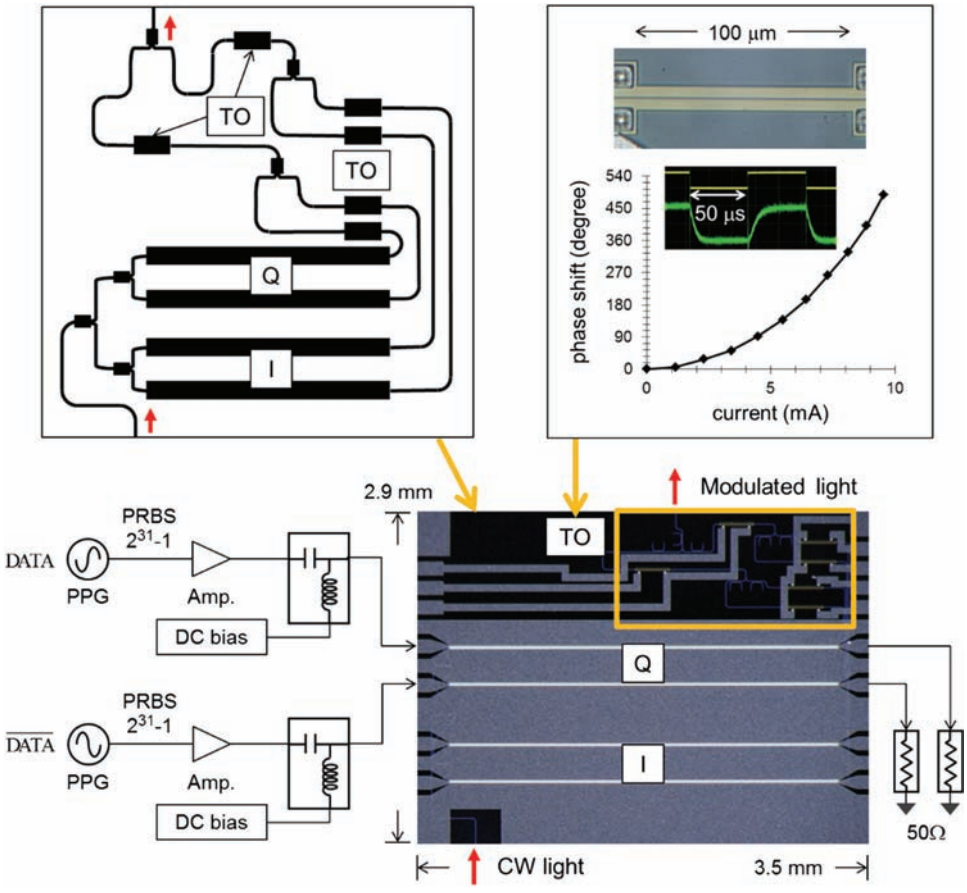

Figure 7.8 Integrated silicon-based quadrature MZ optical modulator with optical-waveguide layout and TO phase-shifter characteristics.

phase errors in each MZI. push–pull electrical driver circuits are shown only to the *Q*-component. Quadrature MZ optical modulators have low-loss compensation-doped lateral PN-junction rib-waveguide phase shifters with a V_π of 8 V under 5-V reverse bias.[56]

Traveling-wave electrodes are of minimal length: Straight coplanar signal electrodes on phase shifters are directly connected with contact pads on the chip edges to avoid RF loss due to intrinsic carriers in the substrate and SOI layer. The input and output optical waveguides are thus bent and laid underneath the RF contact pads. Input and output MFC edge couplers are disposed on the side facets to avoid interference with RF bonding wires. High-index-contrast silicon channel optical waveguides allow strong mode confinement in the channel cores and low optical bending loss and low optical absorption by electrode metals. The optical insertion loss is 9–10 dB over the C band and L band using a lensed PMF for TE-polarized CW input light and a lensed SMF for modulated output light.

Rib-waveguide phase shifters with a resistive heater in the side slab areas have been reported as a small-footprint high-efficiency low-loss TO phase shifter.[59] The rib-waveguide TO phase shifters are integrated in line in the arms of the main MZI to sustain a 90-deg ($\pi/2$) I–Q phase difference and in the sub-MZIs to compensate static phase errors. Static phase errors in a sub-MZI are generated by permanent fluctuations of the effective refractive indices along the optical waveguides that comprise the sub-MZI.[60,61] These permanent fluctuations are caused by imperfections in fabrication processes and in variations in the SOI layer thickness. In silicon-based carrier-depletion MZ optical modulators in push–pull operation, all of the DC bias voltages to the phase shifters are adjusted to optimize the modulation bandwidth and modulation efficiency, and TO phase shifters are essential to cancel the static phase errors independently. A low electrical current of 4.5 mA to the doped resistive side-slab areas, which are electrically connected to each other in series with a metal line in each TO rib optical waveguide, generates a 90-deg phase shift. A dynamic TO response measured in the electrical current switching yields rise and fall times of $\sim$10 μs. The TO phase shifters serve as an efficient adaptive phase controller against ambient temperature fluctuations in conjunction with the monitor PDs (described in Chapter 8). One of the two TO shifters in each MZI is selected for modulator stabilization, although the TO phase shifter is placed in each arm with the aim of achieving optical-path symmetry of the MZI.

A block diagram of an apparatus for QPSK/DP-QPSK transmission measurement is presented in Fig. 7.9. The apparatus for transmission in QSPK is essentially the same as that for BPSK except it has a quadrature MZ modulator instead of the single MZ modulator. A one-bit delayed interferometer and balanced PDs are equipped for the I and Q components for transmission in DQPSK. The other items are the same as for those in NRZ-OOK and BPSK/DQPSK.

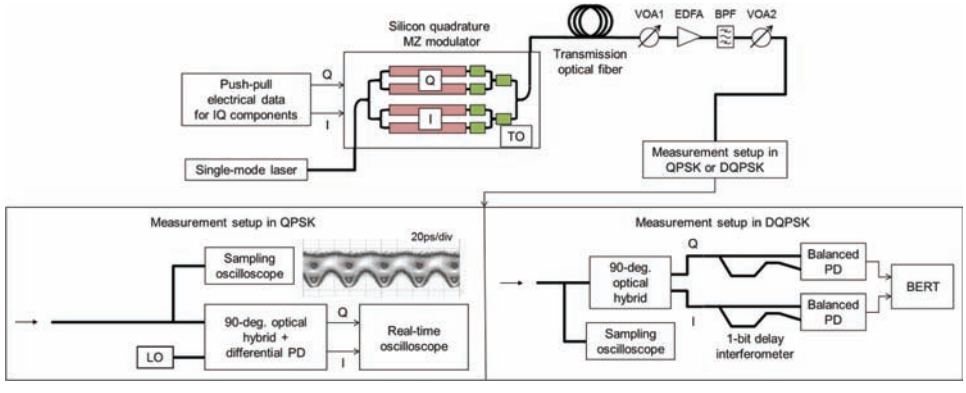

Figure 7.9 Apparatus for QPSK/DQPSK transmission measurement with a push–pull integrated silicon-based quadrature MZ optical modulator.

7.3.2 Characteristics of PSK transmission

The transmission performance of the silicon MZ optical modulator, just like the one utilized in NRZ-OOK, is measured in the apparatus with a BPSK measurement setup with coherent detection. In all of the PSK formats throughout this book, NRZ coding is also selected. First, a back-to-back constellation diagram in 11-Gb/s BPSK is compared with that in 11-Gb/s NRZ-OOK, as presented in Fig. 7.10. The NRZ-OOK constellation diagram has been acquired with the same apparatus and the same silicon-based MZ optical modulator as in the BPSK modulation. Conditions of DC reverse bias voltage and electrical signals in push–pull operation can be determined according to the manner described in Chapter 3 in conjunction with the schematic transfer characteristics in Fig. 3.8 for NRZ-OOK and in Fig. 3.10 for BPSK. The voltage amplitude required for 0-to-π phase modulation in BPSK is twice as high as that required for on–off modulation in OOK. The average optical power levels were adjusted as with VOA2 in constellation diagram measurements in both types of modulation format. Signal voltage amplitude in balanced detection in BPSK is theoretically twice as high as that in single-end unbalanced detection in OOK as indicated in Fig. 7.10. Signal/noise voltage amplitudes are indicated with the arrows and denoted as V_{OOK}/δV_{OOK} in NRZ-OOK and V_{BPSK}/δV_{BPSK} in BPSK, whereby OSNR in BPSK is coarsely estimated to be twice higher than that in NRZ-OOK. Optical data in NRZ-OOK are received and converted to output electrical data by unbalanced single-end detection, whereas those in BPSK are done by balanced detection with two-port balanced PDs. Therefore, the detection sensitivity in BPSK is theoretically predicted to be twice as high as the sensitivity in NRZ-OOK with the expense of input electrical voltage amplitude twice as high as that in NRZ-OOK.[37] The measured constellation diagrams yield experimental OSNR characteristics consistent with theoretical predictions. The silicon-based single MZ optical modulator can be deployed in high-sensitivity BPSK optical networks.

Optical-data transmission in transmission optical fiber using the silicon-based MZ optical modulator chip has been performed in 20-Gb/s BPSK.[62,63] Eye diagrams after transmission in SMFs and DCFs are presented in

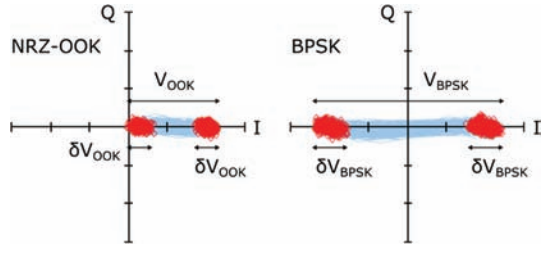

Figure 7.10 Constellation diagrams of NRZ-OOK and BPSK at 11-Gb/s.

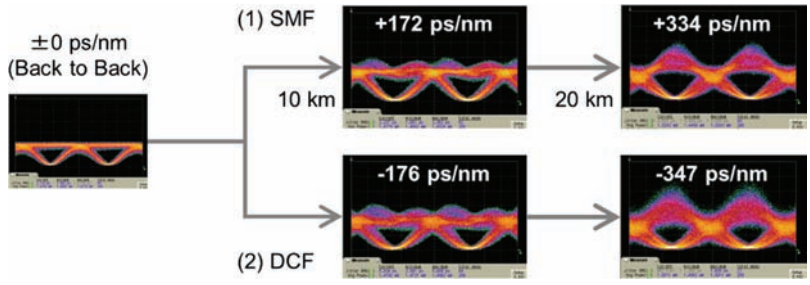

Figure 7.11 Transmission eye diagrams of a push–pull silicon MZ optical modulator in 20-Gb/s BPSK.

Fig. 7.11. Similar shapes of optical signals in SMFs and DCFs imply that optical signals launched to the transmission optical fibers are zero chirped. Clear eye opening is observed in the transmission with accumulated dispersion beyond 330 ps/nm in magnitude.

Computational analysis based on the nonlinear Schrödinger equation for optical pulse propagation under slowly varying envelope approximation provides numerical results for transmission eye diagrams.[64–66] Computational analysis based on the differential equation allows the numerical solution for the transmission of optical signals in an optical fiber transmission link by taking into account the theoretical performance characteristics of photonic and electronic components, such as optical modulators and data-processing electronic circuits. Commercialized simulation packages are available to perform the computational analysis and provide numerical eye diagrams in 20-Gb/s BPSK (see Fig. 7.12).[67] The numerical eye diagrams agree well with the measured eye diagrams. Thus, integrated carrier-depletion MZ optical modulators on a silicon-photonics platform can be added as modules of photonic component library in design and analysis toolkits for high-capacity optical networks.

Transmission characteristics in 20-Gb/s DPSK have been characterized in terms of BER and optical path power penalty as shown in Fig. 7.13. Measurement setup based on one-bit delayed interferometer for direct detection in Fig. 7.7 has been utilized. The optical path power penalty obtained as a OSNR penalty at a BER of 10^{-3} with respect to the back-to-back OSNR yields dispersion tolerance in a range of $-270 \sim +280$ ps/nm, namely, a full span of 550 ps/nm. This is close to a theoretical estimate of $\sim$730 ps/nm for NRZ-DPSK, which is extrapolated from the reported

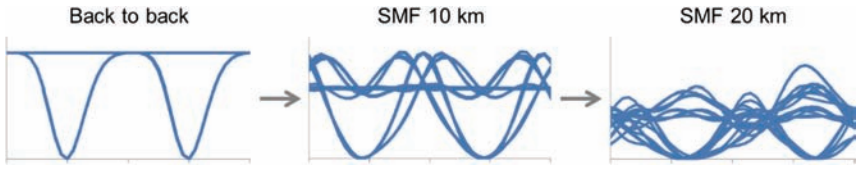

Figure 7.12 Computational eye diagrams in 20-Gb/s BPSK.

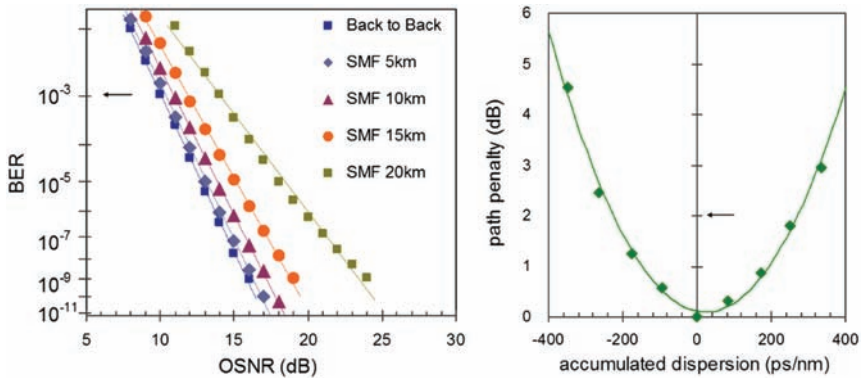

Figure 7.13 Transmission BER and optical path power penalty of a push–pull silicon MZ optical modulator in 20-Gb/s DPSK.

theoretical dispersion tolerance using a theoretically ideal optical modulator at 42.7 Gb/s according to the quadratic dependence on bit rate.[16]

There seems to be a noise floor in the BER in 20-km SMF transmission. In the direct-detection scheme, intensity noise of propagated optical data leads to nonlinear phase noise due to optical nonlinear processes such as self-phase modulation in addition to the linear static phase error, and impairs the BER performance in optical-fiber transmission systems.[39,68–71] The observed noise floor may be caused by these phase noises.

Back-to-back constellation diagrams in 32-Gbaud QPSK in the C band and L band with an electrical signal amplitude of 7 V_{PP} to each phase shifter are presented in Fig. 7.14. The constellation spot in each bit state is not circular-symmetric but distorted due to imbalanced nonlinearity in the

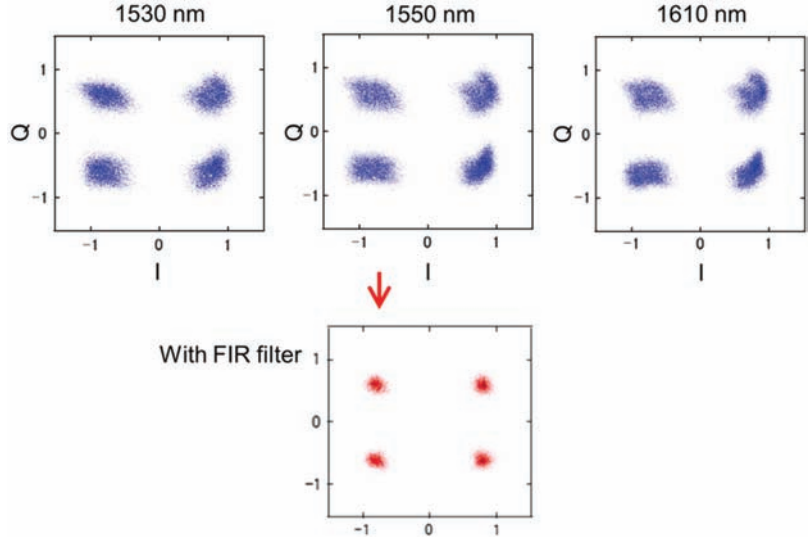

Figure 7.14 32-Gbaud QPSK constellation diagrams in back-to-back configuration.

voltage-power transfer curve in each sub-MZ modulator, as discussed in Chapter 5. This distortion is eliminated by a finite impulse response (FIR) filter in digital signal processing, and clear constellation diagrams are obtained. The integrated silicon-based quadrature MZ optical modulator can be used for optical data transmission in QPSK.

Optical data transmission with the silicon-based quadrature modulator has been characterized in 28-Gbaud DQPSK as back-to-back BER characteristics and optical path power penalty in Fig. 7.15. The optical path power penalty yields a minimum near zero accumulated dispersion, implying that optical signals generated with the quadrature modulator are almost zero chirped.

7.4 Polarization-Division-Multiplexed Quadrature Phase-Shift Keying

7.4.1 Apparatus and device for PDM IQ transmission

In optical data transmission in PDM IQ formats such as *n*QAM including DP-QPSK, a pair of quadrature MZ optical modulators are required to generate optical data in two orthogonal linear polarization states and a PDM optical circuit to multiplex optical data in both polarization components.[37,44,45] Silicon-photonics platforms allow integrated PDM IQ MZ optical modulators in small footprints, as presented in Fig. 3.12 building blocks for MZI and PDM optical circuits based on high-index-contrast optical waveguides as studied in Chapter 4. Two examples of parallel push–pull silicon-based carrier-depletion integrated PDM IQ MZ optical modulators are presented below. One of them has reverse-bias lateral PN-junction rib-waveguide phase shifters with an 8-V V_π in the MZI arms.[19] The adiabatic partial rib polarization rotator and the directional coupler polarization

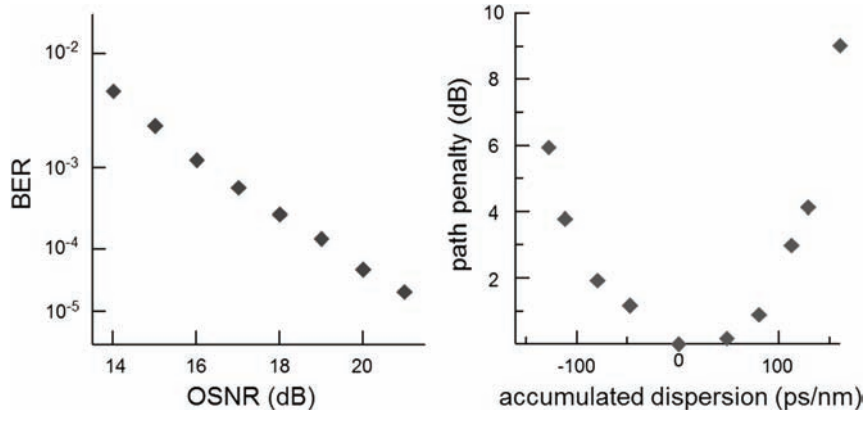

Figure 7.15 Transmission characteristics in 28-Gbaud DQPSK.

combiner are integrated on chip with quadrature MZ modulator units for *x*- and *y*-polarization components. Four high-speed modulator drivers, each of which produces complementary electrical signal outputs DATA and $\overline{\text{DATA}}$, are required to feed amplified electrical signals to eight phase shifters and were copackaged with the modulator chip in a ceramic-based metal housing, as shown in Fig. 7.16. Electrical signals with voltage amplitudes of 3.3 V_{PP} are applied to the phase shifters. With these voltage amplitudes, the PDM IQ modulator allows optical data transmission up to 1000 km, although the modulator is not operated at maximum transmittance.

In transmission up to 1000 km, a 100-km SMF loop circuit is connected to the main transmission line with a 3-dB 2×2 SMF coupler.[19] For example, in 1000-km transmission a burst packet of PRBS optical data is generated by switching on and off an inline optical switch (SW) before the 3-dB coupler, and another SW in the loop is synchronously switched off after the packet travels ten turns through the loop. To recover optical loss in transmission optical fiber, EDFAs are installed in the main transmission line before the first SW and in the loop circuit. An optical modulation analyzer includes optical and electrical instruments for the polarization demultiplexed coherent detection of I and Q components and subsequent offline digital signal processing.

The other modulator has reverse-bias vertical PN-junction rib-waveguide phase shifters with a V_π of 2.5–2.6 V in the MZI arms. The low-voltage modulator can be driven directly with PPGs in DP-QPSK or DACs in other modulation formats, such as PDM 16 or 32QAM.[68] The all-adiabatic PDM

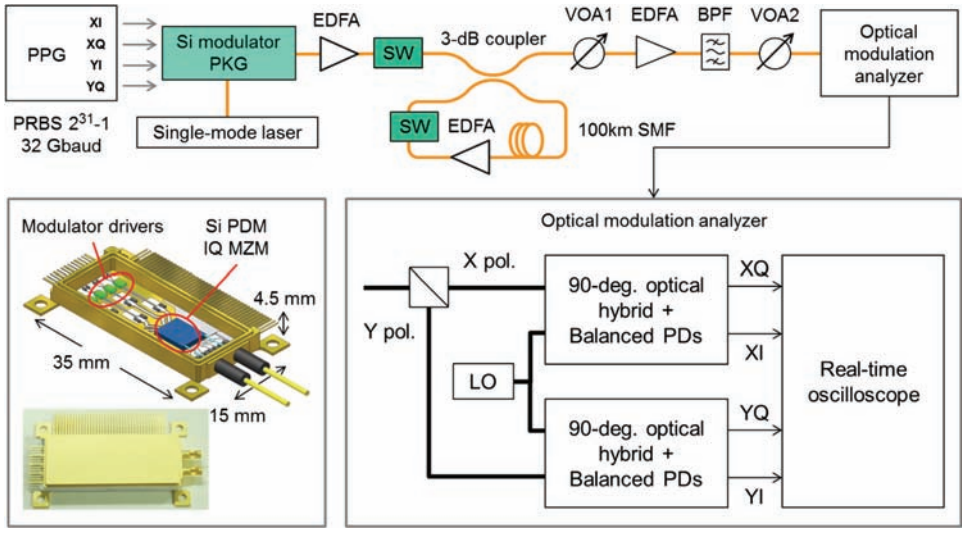

Figure 7.16 Apparatus for DP-QPSK transmission using silicon PDM IQ modulator copackaged with modulator drivers.

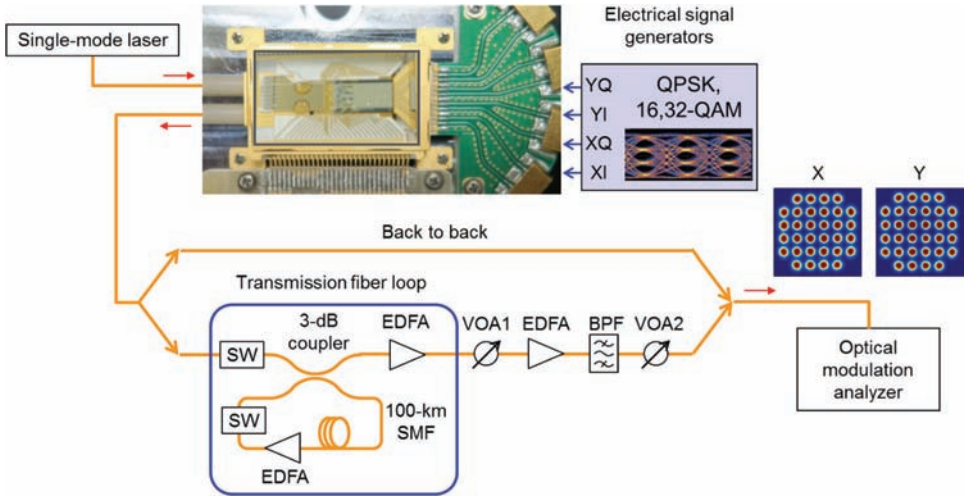

Figure 7.17 Apparatus for PDM IQ transmission using a low-voltage silicon PDM IQ modulator without modulator drivers.

circuit is integrated on chip with the quadrature MZ modulator units. The modulator chip only was packaged in a ceramic-based metal housing, as shown in Fig. 7.17. The voltage amplitudes of electrical signals from PPGs and DACs are 1 V_{PP} and 0.7 V_{PP}, respectively, in each phase shifter. The transmission fiber link with a 100-km SMF loop, as explained above, has been employed in optical data transmission up to 1000 km in 32-Gbaud DP-QPSK.

7.4.2 Characteristics of PDM IQ transmission

Constellation diagrams in optical data transmission with the former carrier-depletion PDM IQ modulator with the lateral PN-junction phase shifters are presented in Fig. 7.18 with BER measured in the real-time oscilloscope. The lowest detectable BER is 10^{-5} due to limited memory capacity for data storage in the oscilloscope. In the constellation diagrams, OSNR is reduced and BER is increased with increasing transmission span. Assuming soft-decision forward error correction (FEC) with a 20% margin of data capacity, errors can be eliminated as far as BER is lower than the threshold of 2.4×10^{-2}.[73] Therefore, error-free transmission is possible at a total SMF span of 2000 km and beyond in DCI and metro networks.

For the latter carrier-depletion PDM IQ modulator with the vertical PN-junction phase shifters, back-to-back constellation diagrams in 16-Gbaud PDM 32QAM, 32-Gbaud PDM 16QAM, 32-Gbaud DP-QPSK and 48-Gbaud DP-QPSK are presented in Fig. 7.19.[72] Clear constellation diagrams are verified in all of the modulation formats investigated. Each constellation diagram is highly symmetric, implying that there is no power imbalance between the I and Q sub-MZI optical modulator units in

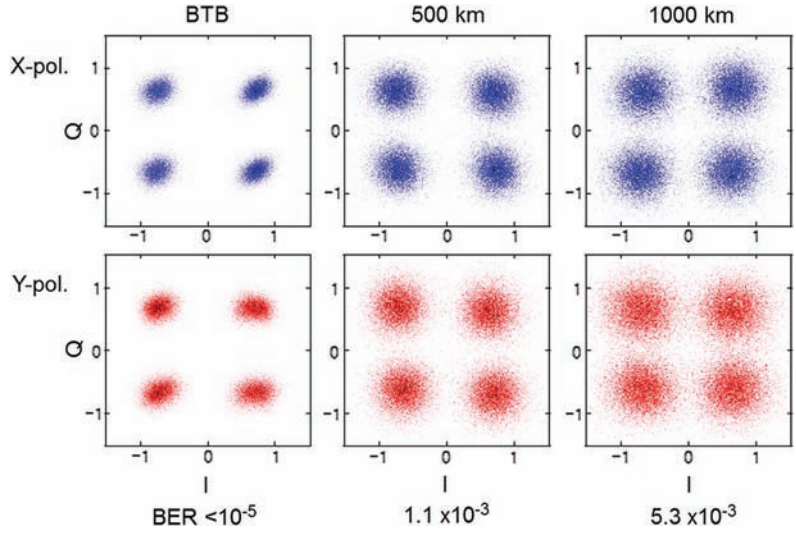

Figure 7.18 Constellation diagrams in 32-Gbuad DP-QPSK transmission.

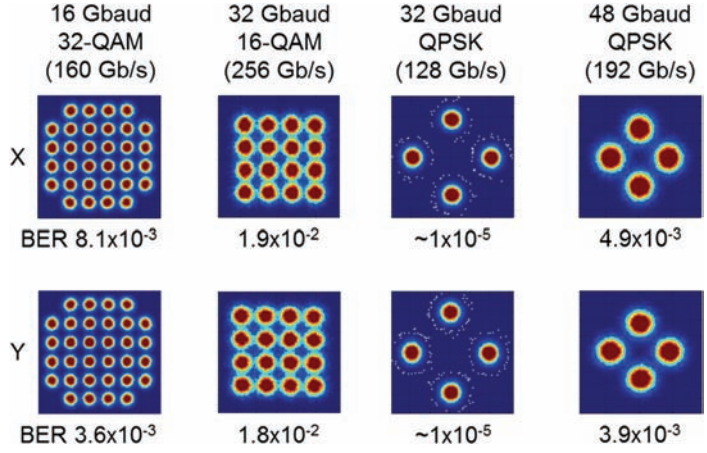

Figure 7.19 Back-to-back constellation diagrams in PDM IQ formats.

x and *y* polarization states. The constellation spots are equally spaced along I and Q axes in both of PDM 16QAM and PDM 32QAM; therefore, the PDM IQ modulator has a high-linearity response to the RF drive voltage in this voltage regime. The BERs are sufficiently below the FEC threshold. High-capacity optical data generation beyond 100 Gb/s is realized with an energy-efficient PDM IQ modulator. The highest symbol rate in DP-QPSK is almost 50 Gbaud. In digital coherent communication, digital-signal-processing algorithms can be used to reduce receiver bit errors due to impairments such as timing jitter and de-synchronization of sampling. To eliminate these impairments, a 1/2 fractionally spaced frequency-domain equalizer and carrier-frequency-offset

estimator have been implemented in digital-signal-processing algorithms.[74,75] In the equalizer, a 512-point FFT has been employed with tap weights based on the minimum mean square error criterion.

The transmission characteristics of the PDM IQ modulator has been characterized in 32-Gbaud DP-QPSK. Figure 7.20 depicts constellation diagrams and BER characteristics of transmission optical fiber with spans up to 2000 km. Clear constellation spots are observed in the diagrams, indicating error-free transmission. The averaged BER over *x*- and *y*-polarization components is plotted as a function of SNR per bit, which is converted from the measured OSNR through the formula given in the literature.[76] The theoretical BER curve for QPSK (plotted as a dashed line) is based on Appendix A.1. The measured BER can be well fitted with the theoretical BER curve with a SNR penalty of 5.5 dB. Note that the modulator is evaluated with a single performance parameter: the SNR penalty can be a FOM to evaluate the dynamic link loss budget of the integrated silicon-based PDM IQ modulator in high-capacity optical data transmission.

Optical transmission characteristics of a lateral PN-junction carrier-depletion PDM IQ modulator monolithically integrated with PDM 90-deg optical hybrids and balanced PDs in a PIC have been reported. Error-free transmission has been verified in DP-QPSK with dual PICs at a combined bit rate of 200-Gb/s in transmission-fiber spans up to 3000 km.[77] Optical modulation in PDM 8QAM and 16QAM have been demonstrated at a symbol rate of 25 Gbaud. A silicon-based photonic–electronic integrated chip, in which a linear BiCMOS modulator driver is integrated on a silicon optical modulator chip by flip-chip bonding, has been reported, and error-free modulation in 321.4 Gb/s (40.175 Gbaud) PDM 16QAM has been demostrated.[78] Capacitor-type carrier-accumulation phase shifters described

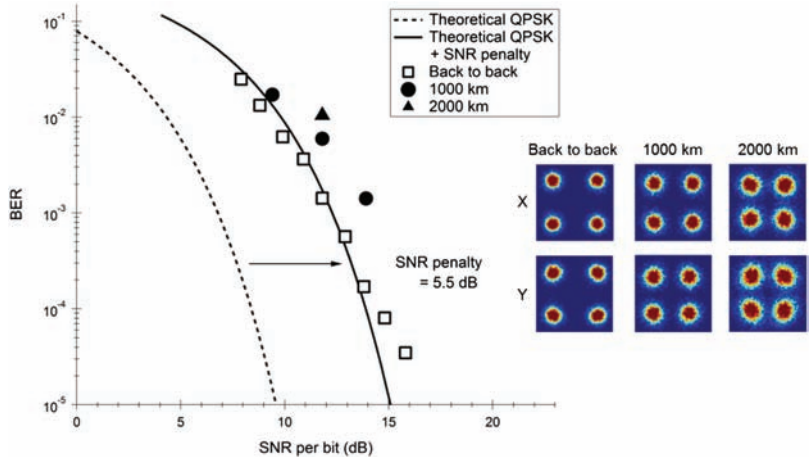

Figure 7.20 Experimental BER characteristics in 32-Gbaud DP-QPSK transmission compared with the theoretical characteristics.

in Subsection 5.2.3 are integrated in PDM IQ optical modulators on the silicon optical modulator chip.

7.5 Discrete Multi-Tone Scheme

7.5.1 Apparatus for DMT transmission

A high transmission capacity is achieved in optical data transmission in DMT format, as described in Appendix A.1 for short-reach applications.[79] A non-push–pull silicon-based carrier-depletion MZ optical modulator in a package, which has an electro-optic bandwidth of 12.5 GHz and utilized in 11-Gb/s NRZ-OOK (as shown in Figs. 7.4 and 7.5), has been exploited for DMT transmission with the apparatus presented in Fig. 7.21.[80] Electrical signals in DMT format are generated digitally in a control PC, converted to analog voltage signals by a 64-GSa/s DAC, and input to the reverse-bias lateral PN-junction rib-waveguide phase shifter in the first MZI arm of the modulator. The bias voltage to the phase shifter in the second MZI arm is adjusted to cancel the static phase errors. Optical data in DMT format is launched to the SMF up to 10 km. The transmitted optical power is directly detected with an unbalanced single-end PD and output from a trans-impedance amplifier (TIA). The output electrical signals are converted to digital data by a 64-GSa/s ADC and demodulated in the control PC. The format is also classified as one of the schemes based on IM-DD, and the transmission apparatus is simple and similar to that for NRZ-OOK except for the high-speed electronics ICs of DAC and ADC to convert between digital and analog data.

7.5.2 Characteristics of DMT transmission

Figure 7.22 presents the SNR and bit-allocation characteristics of the respective sub-carrier components in DMT after 10-km SMF transmission with different α-parameters. The reverse-bias voltage is adjusted to obtain a

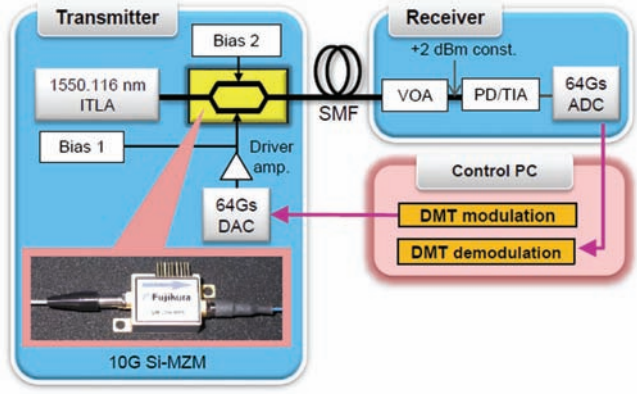

Figure 7.21 Apparatus for DMT transmission.

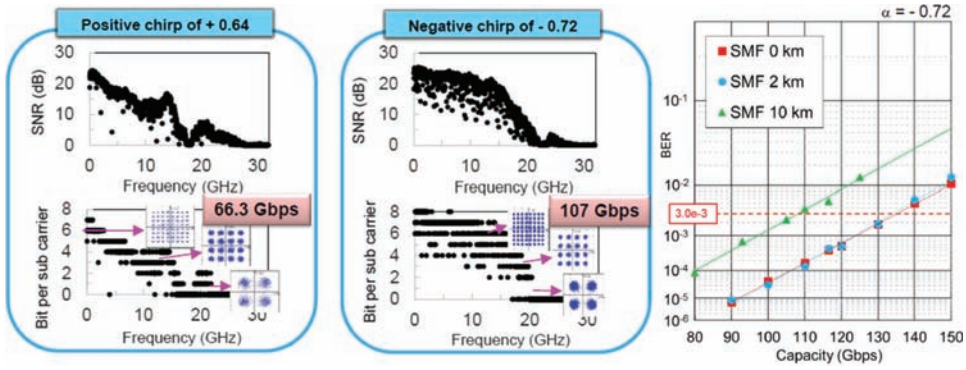

Figure 7.22 Transmission characteristics in DMT.

specific α-parameter according to the characteristics plotted with the transfer curve as a function of reverse bias voltage in Fig. 7.5. In a negative α-parameter of −0.72, a higher SNR and thus a higher bit allocation are achieved than in a positive α-parameter of +0.64 because of the dispersion compensation with pre-chirped optical signals as described for 11-Gb/s NRZ-OOK transmission using the non-push–pull silicon-based optical modulator in Subsection 7.2.2. In contrast to a data capacity of 66.3 Gb/s with a positive α-parameter, a data capacity as high as 107 Gb/s is achieved with a negative α-parameter in 10-km SMF transmission.

In Fig. 7.22, the BER for the silicon-based modulator in SMF transmission with a negative α-parameter is plotted against transmission capacity. Transmission in 2-km SMF yields almost the same BER as that in the back-to-back counterpart. Therefore, a transmission capacity of more than 130 Gb/s is verified in SMF transmission shorter than 2 km at a BER of 3.0×10^{-3}, the FEC threshold in DMT. This result leads to a transmission capacity of 116 Gb/s for 100-GbE payloads with a 12.5% FEC margin in a LAN application. High-capacity optical data transmission at 100 Gb/s and beyond in DMT format in IM-DD is realized by using a silicon-based optical modulator designed and fabricated for 11-Gb/s NRZ-OOK. 100-Gb/s single-side-band DMT transmission in 80-km SMF at a bit rate of 56 Gb/s using a silicon-based MZ modulator and four-channel 100-Gb/s DMT transmission using integrated DWM silicon-based modulators have also been reported.[81,82]

7.6 Note on Transmission Characteristics

The transmission performance of silicon-based MZ optical modulators designed and fabricated for the intensity-modulation and phase-modulation formats has been described with an emphasis on BER characteristics because the BER limits are specified for the operation of optical modulators in the practical optical network domains in Fig. 7.1. Optical, electrical, and

electro-optical characteristics discussed in Chapter 6 are not sufficient to evaluate silicon-based optical modulators in the optical-network applications.

In legacy optical networks, the BER is specified to be lower than 10^{-9}.[83] A BER lower than 10^{-12} is required for the physical layer in optical ethernet.[84] Silicon-based modulators with the BER characteristics in this chapter meet these criteria. In the optical path penalty obtained from the BER characteristics in 11-Gb/s NRZ-OOK, the silicon-based optical modulator retains a power penalty nearly as low as that of the LN MZ optical modulator. Further reductions in the optical loss in the PN-junction rib-waveguide phase shifter, and hence a higher OSNR of the silicon-based optical modulator, by a few decibels will lead to BER characteristics even better than the LN modulator. Adjustments to the doping profile of the PN-junction phase shifter are essential to reduce optical loss.

In the advanced phase-modulation formats of *n*QAM, a BER threshold of 2.4×10^{-2}, more than several magnitudes of order higher than those of NRZ-OOK, are accepted with a boost of digital signal processing such as FEC and electrical signal equalization. 256-Gb/s optical signal generation below the BER threshold has been confirmed in 32-Gbaud 16QAM format. A few-decibels reduction in the phase-shifter loss will allow 512-Gb/s optical signal generation in 32-Gbaud 32QAM, thereby application to 400G DCI. Enhancement of the modulation speed of the phase shifter up to 64 Gbaud allows optical signal generation toward 1 Tb/s in 64-Gbuad *n*QAM formats. A silicon-based phase shifter with length <2 mm will generate 64-Gbaud *n*QAM signals with an electro-optic bandwidth of 40 GHz or higher according to estimations based on the electro-optic characteristics in Fig. 6.22. A higher modulation efficiency than the present efficiency of silicon rib-waveguide phase shifter is, however, essential to realize a phase shifter of such short length. Silicon–germanium-alloy crystal is promising as a core material of high-efficiency phase shifters because of its small effective masses, high mobilities of carriers, and higher plasma-dispersion effect.[85] A reduction in the series resistance R in the phase shifter also allows enhancement of the modulation speed. A couple of solutions have been devised to lower series resistance: design modifications to shorten the lateral slab length, and silicon–germanium phase-shifter design with a low series resistance.

References

1. S. Elby, "Evolution of networks to meet the explosion of cloud services," *Optical Fiber Communications Conference and Exhibition (OFC)*, Tu2H.5 (2015).
2. A. L. N. Souza, V. N. Rozental, A. Chiuchiarelli, T. Pivem, J. D. Reis, and J. R.F. Oliveira, "Optoelectronic specifications of emerging coherent optical solutions for data center interconnect," *Proc. SPIE* **9775**, 97750E-1–97759E-9 (2016).

3. J. D'Ambrosia, "CFI consensus -beyond 10km optical PHYs," http://www.ieee802.org/3/cfi/0717_1/CFI_01_0717.pdf.
4. F. Lipscomb, "What is 400ZR and why is it important?" https://www.neophotonics.com/what-is-400-zr/.
5. K. Ogawa, K. Goi, Y. T. Tan, T.-Y. Liow, X. Tu, Q. Fang, G.-Q. Lo, and D.-L. Kwong, "Silicon Mach-Zehnder modulator of extinction ratio beyond 10 dB at 10.0-12.5 Gbps," *Opt. Express* **19**(26), B26–B31 (2011).
6. K. Goi, K. Oda, H. Kusaka, Y. Terada, K. Ogawa, T.-Y. Liow, X. Tu, G.-Q. Lo, and D.-L. Kwong, "11-Gb/s 80-km transmission performance of zero-chirp silicon Mach-Zehnder modulator," *Opt. Express* **20**(26), B350–B356 (2012).
7. J. Dupre and J. Stimple, "Making OSNR measurements in a modulated DWDM signal environment," http://www.keysight.com/upload/cmc_upload/All/SLDPRE_2_OSNR_Measure.pdf?&cc=JP&lc=jpn.
8. R. G. Walker, "High-speed III-V semiconductor intensity modulators," *IEEE J. Quantum Electron.* **27**(3), 654–667 (1991).
9. A. Shastri, C. Muzio, M. Webster, G. Jeans, P. Metz, S. Sunder, B. Chattin, B. Dama, and K. Shastri, "Ultra-low-power single-polarization QAM-16 generation without DAC using a CMOS photonics based segmented modulator, *J. Lightwave Technol.* **33**(6), 1255–1260 (2015).
10. J. B. Knorr and K.-D. Kuchler, "Analysis of coupled slots and coplanar strips on dielectric substrate," *IEEE Trans. Microwave Theory Tech.* **23**(7), 541–548 (1975).
11. S. Akiyama, H. Itoh, T. Takeuchi, A. Kuramata, and T. Yamamoto, "Low-chirp 10 Gbit/s InP-based Mach-Zehnder modulator driven by 1.2V single electrical signal," *Electron. Lett.* **41**(1), 41–42 (2005).
12. S. J. Spector, M. W. Geis, G.-R. Zhou, M. E. Grein, F. Gan, M.A. Popović, J. U. Yoon, D. M. Lennon, E. P. Ippen, F. X. Kärtner, and T. M. Lyszczarz, "CMOS-compatible dual-output silicon modulator for analog signal processing," *Opt. Express* **16**(15), 11027–11031 (2008).
13. L. Chen, P. Dong, and Y.-K. Chen, "Chirp and Dispersion Tolerance of a Single-Drive Push–Pull Silicon Modulator at 28 Gb/s," *IEEE Photon. Technol. Lett.* **24**(11), 936–938 (2012).
14. M. Streshinsky, A. Ayazi, Z. Xuan, A. E.-J. Lim, G.-Q. Lo, T. Baehr-Jones, and M. Hochberg, "Highly linear silicon traveling wave Mach-Zehnder carrier depletion modulator based on differential drive," *Opt. Express* **21**(3), 3818–3825 (2013).
15. A. Samani, M. Chagnon, D. Patel, V. Veerasubramanian, S. Ghosh, M. Osman, Q. Zhong, and Plant David V., "A low-voltage 35-GHz silicon photonic modulator-enabled 112-Gb/s transmission system," *IEEE Photon. J.* **7**(3), 7901413 (2015).

16. P. J. Winzer and R.-J. Essiambre, "Advanced optical modulation formats for high-capacity optical transport networks," *J. Lightwave Technol.* **24**(12), 4711–4728 (2006).
17. P. Anslow and G. Nicholl, "Optical link budget compatibility," http://www.ieee802.org/3/40GSMF/public/jan10/anslow_02_0110.pdf.
18. H. Ishihara, K. Oda, T. Ori, K. Goi, K. Ogawa, T.-Y. Liow, X. Tu, G.-Q. Lo, and D.-L. Kwong, "High-ON/OFF-contrast 10-Gb/s silicon Mach-Zehnder modulator in high-speed low-loss package," *2014 International Conference on Electronics Packaging (ICEP)*, FE2-1 (2014).
19. K. Ogawa, H. Ishihara, K. Goi, Y. Mashiko, S. T. Lim, M. J. Sun, S. Seah, C. E. Png, T.-Y. Liow, X. Tu, G.-Q. Lo, and D.-L. Kwong, "Fundamental characteristics and high-speed applications of carrier-depletion silicon Mach-Zehnder modulators," *IEICE Electron. Express* **11**(24), 20142010 (2014).
20. Y. Suzaki, S. Sekine, Y. Suzuki, and H. Toba "A 1.3-μm optical transceiver diode module using passive alignment technique on a Si bench with a V-groove," *IEICE Trans. Electron.* **E81-C**(9), 1508–1510 (1998).
21. J.-C. Diels and W. Rudolph, *Ultrashort Laser Pulse Phenomena: Fundamentals, Techniques, and Applications on a Femtosecond Time Scale*, Academic Press, San Diego, London, 1–21 (1996).
22. F. Devaux, Y. Sorel, and J. F. Kerdiles, "Simple measurement of fiber dispersion and of chirp parameter of intensity modulated light emitter," *J. Lightwave Technol.* **11**(12), 1937–1940 (1993).
23. S. Walklin and J. Conradi, "Effect of Mach–Zehnder modulator DC extinction ratio on residual chirp-induced dispersion in 10-Gb/s binary and AM-PSK duobinary lightwave systems," *IEEE Photon. Technol. Lett.* **9**(10), 1400–1402 (1997).
24. E. L. Wooten, K. M. Kissa, A. Yi-Yan, E. J. Murphy, D. A. Lafaw, P. F. Hallemeier, D. Maack, D. V. Attanasio, D. J. Fritz, G. J. McBrien, and D. E. Bossi, "A review of lithium niobate modulators for fiber-optic communications systems," *IEEE J. Sel. Top. Quantum Electron.* **6**(1), 69–82 (2000).
25. T. Kawanishi, K. Kogo, S. Oikawa, and M. Izutsu, "Direct measurement of chirp parameters of high-speed Mach-Zehnder-type optical modulators," *Opt. Commun.* **195**(5–6), 399–404 (2001).
26. P. Bravetti, G. Ghislotti, and S. Balsamo, "Chirp-inducing mechanisms in Mach-Zehnder modulators and their effect on 10 Gb/s NRZ transmission studied using tunable-chirp single drive devices," *J. Lightwave Technol.* **22**(2), 605–611 (2004).
27. Y. Wei, Y. Zhao, J. Yang, M. Wang, and X. Jiang, "Chirp characteristics of silicon Mach-Zehnder modulator under small-signal modulation," *J. Lightwave Technol.* **29**(7), 1011–1017 (2011).

28. S. Liu, D. J. Thomson, F. Y. Gardes, J.-M. Fedeli, P. Petropoulos, and G. T. Reed, "Characterization of the chirp of silicon optical modulators," *38th European Conference on Optical Communication (ECOC)*, Tu.1.E.5 (2012).
29. G. P. Agrawal, *Nonlinear Fiber Optics*, 4th Ed., Academic Press, San Diego, 51–74 (2007).
30. J. C. Cartledge, C. Rolland, S. Lemerle, and A. Solheim, "Theoretical performance of 10 Gb/s lightwave systems using a III-V semiconductor Mach-Zehnder modulator," *IEEE Photon. Technol. Lett.* **6**(2), 282–284 (1994).
31. S. Kipp, B. Smith, C. Cole, and M. Nowell, "The state of Ethernet optics," *Optical Fiber Communications Conference and Exhibition (OFC)*, 23 March, Exhibit Hall Theater II (2016); http://www.ethernetalliance.org/wp-content/uploads/2016/01/The-State-Of-Ethernet-Optics-Final.pdf.
32. W. I. Way, T. K. Chan, and A. Lebedev, "Short-haul transmission links based on 28- and 56-Gbaud PAM4 modulation," *Proc. SPIE* **9775**, 977505-1–977505-4 (2016).
33. M. Poulin, C. Latrasse, J.-F. Gagné, Y. Painchaud, M. Cyr, C. Paquet, M. Morsy-Osman, M. Chagnon, S. Lessard, and D.V. Plant, "107 Gb/s PAM-4 transmission over 1.5 km using a SiP series push-pull modulator at 1310 nm," *40th European Conference on Optical Communication (ECOC)*, Mo.4.5.3 (2014).
34. X. Xu, E. Zhou, G. N. Liu, T. Zuo, Q. Zhong, L. Zhang, Y. Bao, X. Zhang, J. Li, and Z. Li, "Advanced modulation formats for 400-Gbps short-reach optical inter-connection," *Opt. Express* **23**(1), 492–500 (2015).
35. A. Samani, V. Veerasubramanian, E. El-Fiky, D. Patel, and D. V. Plant, "A silicon photonic PAM-4 modulator based on dual-parallel Mach–Zehnder interferometers," *IEEE Photon. J.* **8**(1) 7800610 (2016).
36. S. Zhou, H.-T. Wu, K. Sadeghipour, C. Scarcella, C. Eason, M. Rensing, M. J. Power, C. Antony, P. O'Brien, P. D. Townsend, and P. Ossieur, "Optimization of PAM-4 transmitters based on lumped silicon photonic MZMs for high-speed short-reach optical links," *Opt. Express* **25**(4), 4312–4325 (2017).
37. K. Kikuchi, "Fundamentals of coherent Optical fiber communications," *J. Lightwave Technol.* **34**(1), 157–179 (2016).
38. G. Li, "Recent advances in coherent optical communication," *Adv. Opt. Photon.* **1**(2), 279–307 (2009).
39. J. J. O. Pires and J. R. F. de Rocha, "Performance analysis of DPSK direct detection optical systems in the presence of interferometric intensity noise," *J. Lightwave Technol.* **10**(11), 1722–1730 (1992).
40. R.A. Griffin and A.C. Carter, "Optical differential quadrature phase-shift key (oDQPSK) for high capacity optical transmission," *Optical Fiber*

Communication Conference and Exposition and the National Fiber Optic Engineers Conference (OFC/NFOEC), WX6 (2002).
41. A. Gnauck, "40-Gb/s RZ-differential phase shift keyed transmission," *Optical Fiber Communication Conference and Exposition and the National Fiber Optic Engineers Conference (OFC/NFOEC)*, ThE1 (2003).
42. T. Mizuochi, K. Ishida, T. Kobayashi, J. Abe, K. Kinjo, K. Motoshima, and K. Kasahara, "A comparative study of DPSK and OOK WDM transmission over transoceanic distances and their performance degradations due to nonlinear phase noise," *J. Lightwave Technol.* **21**(9), 1933–1943 (2003).
43. L. G. Kazovsky, G. Kalogerakis, and W.-T. Shaw, "Homodyne phase-shift-keying systems: Past challenges and future opportunities," *J. Lightwave Technol.* **24**(12), 4876–4884 (2006).
44. Y. Miyamoto and S. Suzuki, "Advanced optical modulation and multiplexing technologies for high-capacity OTN based on 100 Gb/s channel and beyond," *IEEE Comm. Mag.* **48**(3), S65–S72 (2010).
45. K. Roberts, D. Beckett, D. Boertjes, J. Berthold, and C. Laperle, "100G and beyond with digital coherent signal processing," *IEEE Comm. Mag.* **48**(7), 62–69 (2010).
46. X. Zhou and L. Nelson, "Advanced DSP for 400 Gb/s and beyond optical networks," *J. Lightwave Technol.* **32**(16), 2716–2752 (2014).
47. R. Ulrich and T. Kamiya, "Resolution of self-images in planar optical waveguides," *J. Opt. Soc. Am.* **68**(5), 583–592 (1978).
48. M. Bachmann, P. A. Besse, and H. Melchior, "General self-imaging properties in N x N multimode interference couplers including phase relations," *Appl. Opt.* **33**(18), 3905–3911 (1994).
49. Y. Painchaud, M. Poulin, J.-F. Gagné, and C. Paquet, "Ultra-compact si-photonic DQPSK demodulator," *Optical Fiber Communication Conference and Exposition and the National Fiber Optic Engineers Conference (OFC/NFOEC)*, OM3J.3 (2012).
50. W. Yang, M. Yin, Y. Li, X. Wang, and Z. Wang, "Ultra-compact optical 90° hybrid based on a wedge-shaped 2×4 MMI coupler and a 2×2 MMI coupler in silicon-on-insulator," *Opt. Express* **21**(23), 28423–28431 (2013).
51. P. Dong, C. Xie, and L. L. Buhl, "Monolithic polarization diversity coherent receiver based on 120-degree optical hybrids on silicon," *Opt. Express* **22**(2), 2119–2125 (2014).
52. J. Klamkin, F. Gambini, S. Faralli, A. Malacarne, G. Meloni, G. Berrettini, G. Contestabile, and L. Potì, "A 100-Gb/s noncoherent silicon receiver for PDM-DBPSK/DQPSK signals," *Opt. Express* **22**(2), 2150–2158 (2014).
53. C. Doerr, L. Chen, D. Vermeulen, T. Nielsen, S. Azemati, S. Stulz, G. McBrien, X.-M. Xu, B. Mikkelsen, M. Givehchi, C. Rasmussen, and S.-Y. Park, "Single-chip silicon photonics 100-Gb/s coherent transceiver,"

Optical Fiber Communications Conference and Exhibition (OFC), TH5C.1 (2014).
54. P. Dong, L. Chen, C. Xie, L. L. Buhl, and Y.-K. Chen, "50-Gb/s silicon quadrature phase-shift keying modulator," *Opt. Express* **20**(19), 21181–21186 (2012).
55. B. Milivojevic, C. Raabe, A. Shastri, M. Webster, P. Metz, S. Sunder, B. Chattin, S. Wiese, B. Dama, and K. Shastri, "112Gb/s DP-QPSK transmission over 2427km SSMF using small-size silicon photonic IQ modulator and low-power CMOS driver," *Optical Fiber Communication Conference and Exposition and the National Fiber Optic Engineers Conference (OFC/NFOEC)*, OTh1D.1 (2013).
56. K. Goi, A. Oka, H. Kusaka, Y. Terada, Kensuke Ogawa, T.-Y. Liow, X. Tu, G.-Q. Lo, and D.-L. Kwong, "Low-loss high-speed silicon IQ modulator for QPSK/DQPSK in C and L bands," *Opt. Express* **22**(9), 10703–10709 (2014).
57. C. Y. Wong, S. Zhang, Y. Fang, L. Liu, T. Wang, Q. Zhang, S. Deng, G. N. Liu, and X. Xu, "Silicon IQ modulator for next-generation metro network," *J. Lightwave Technol.* **34**(2), 730–736 (2016).
58. M. Lauermann, S. Wolf, R. Palmer, S. Koeber, P. C. Schindler, T. Wahlbrink, J. Bolten, A. L. Giesecke, M. Koenigsmann, M. Kohler, D. Malsam, D. L. Elder, L. R. Dalton, J. Leuthold, W. Freude, and C. Koos, "High-speed and low-power silicon-organic hybrid modulators for advanced modulation formats," *Proc. SPIE* **9516**, 951607-1–951607-5 (2015).
59. N. C. Harris, Y. Ma, J. Mower, T. Baehr-Jones, D. Englund, M. Hochberg, and C. Galland, "Efficient, compact and low loss thermo-optic phase shifter in silicon," *Opt. Express* **22**(9), 10487–10493 (2014).
60. T. Goh, S. Suzuki, and A. Sugita, "Estimation of waveguide phase error in silica-based waveguides," *J. Lightwave Technol.* **15**(11), 2107–2113 (1997).
61. K. Okamoto, "Planar waveguide devices for communication and sensing applications," *J. Opt. Soc. Korea* **14**(4), 290–297 (2010).
62. K. Goi, H. Kusaka, A. Oka, Y. Terada, K. Ogawa, T.-Y. Liow, X. Tu, G.-Q. Lo, and D.-L. Kwong, "20-Gb/s DPSK transmission with 550-ps/nm dispersion tolerance using silicon Mach-Zehnder modulator," *Optical Fiber Communications Conference and Exhibition (OFC)*, OW4J.5 (2013).
63. K. Ogawa, K. Goi, H. Kusaka, Y. Terada, T.-Y. Liow, X. Tu, G.-Q. Lo, D.-L. Kwong, V. Dixit, S. T. Lim, and C. E. Png, "Low-loss high-speed silicon Mach-Zehnder modulator for optical-fiber telecommunications," *Proc. SPIE* **8629**, 86290U-1–86290U-8 (2013).
64. P. Balaban, K. Shanmugan, and B. Stuck, "Computer-aided modeling, analysis, and design of communication systems: Introduction and issue overview," *IEEE J. Sel. Areas Commun.* **2**(1), 1–8 (1988).

65. A. J. Lowery and P. C. R. Gurney, "Two simulators for photonic computer-aided design," *Appl. Opt.* **37**(26), 6066–6077 (1998).
66. G. P. Agrawal, *Fiber-Optic Communication Systems*, 4th Ed., John Wiley and Sons, Hoboken, 182–222, 587–588 (2010).
67. https://optiwave.com/resources/applications-resources/optical-communication-system-design/
68. J. J. Bussgang and M. Leiter, "Error rate approximations for differential phase-shift keying," *IEEE Trans. Commun. Syst.* **12**(1), 18–27 (1964).
69. R. W. Boyd, *Nonlinear Optics*, 3rd Ed., Academic Press, San Diego, 375–381 (2008).
70. J. P. Gordon and L. F. Mollenauer, "Phase noise in photonic communications systems using linear amplifiers," *Opt. Lett.* **15**(23), 1351–1353 (1990).
71. Y. Atzmon and M. Nazarathy, "A Gaussian polar model for error rates of differential phase detection impaired by linear, nonlinear, and laser phase noises," *J. Lightwave Technol.* **27**(21), 4650–4659 (2009).
72. N. Ishikura, K. Goi, H. Zhu, M. Illarionov, H. Ishihara, A. Oka, T. Oda, K. Masuko, T. Ori, K. Ogawa, Y. Yoshida, K. Kitayama, T.-Y. Liow, X. Tu, G.-Q. Lo, and D.-L. Kwong, "Transmission characteristics of 32-Gbaud PDM IQ monolithic silicon modulator operating with 2-VPPD drive voltage," *42nd European Conference on Optical Communication (ECOC)*, W.2.E4 (2016).
73. X. Zhou, L. E. Nelson, R. Isaac, P. Magill, B. Zhu, D. W. Peckham, P. Borel, and K. Carlson, "1200km transmission of 50GHz spaced, 5×504-Gb/s PDM-32-64 hybrid QAM using electrical and optical spectral shaping," *Optical Fiber Communication Conference and Exposition and the National Fiber Optic Engineers Conference (OFC/NFOEC)*, OM2A.2 (2010).
74. Y. Yasumura, Y. Yoshida, and K. Kitayama, "Fractionally-spaced frequency domain equalization for optical coherent receivers with interleaved samplers," *Optical Fiber Communication Conference and Exposition and the National Fiber Optic Engineers Conference (OFC/NFOEC)*, JW2A.47 (2013).
75. M. Morelli and U. Mengali, "An improved frequency offset estimator for OFDM applications," *IEEE Commun Lett*. **3**(3), 75–77 (1999).
76. R.-J. Essiambre, G. Kramer, P. J. Winzer, G. J. Foschini, and B. Goebel, "Capacity limits of optical fiber networks," *J. Lightwave Technol.* **28**(4), 662–701 (2010).
77. L. Chen, C. Doerr, R. Aroca, S. Y. Park, J. C. Geyer, T. Nielsen, C. Rasmussen, and B. Mikkelsen, "Silicon photonics for 100G-and-beyond coherent transmissions," *Optical Fiber Communications Conference and Exhibition (OFC)*, Th1B.1 (2016).

78. B. Milivojevic, S. Wiese, S. Anderson, T. Brenner, M. Webster, and B. Dama, "Demonstration of optical transmission at bit rates of up to 321.4Gb/s using compact silicon based modulator and linear BiCMOS MZM driver," *Optical Fiber Communications Conference and Exhibition (OFC)*, Th1F.2 (2016).
79. M. Nishihara, T. Tanaka, T. Takahara, L. Li, Z. Tao, and J. C. Rasmussen, "Impact of modulator chirp in 100 Gbps class optical discrete multi-tone transmission system," *Proc. SPIE* **8646**, 86860N-1–86460N-11 (2013).
80. Y. Kai, M. Nishihara, T. Tanaka, R. Okabe, T. Takahara, J. C. Rasmussen, H. Ishihara, K. Goi, and K. Ogawa, "130-Gbps DMT transmission using silicon Mach-Zehnder modulator with chirp control at 1.55-μm," *Optical Fiber Communications Conference and Exhibition (OFC)*, Th4A.1 (2015).
81. L. Zhang, E. Zhou, Q. Zhang, X. Xu, G. N. Liu, and T. Zuo, "C-band single wavelength 100-Gb/s IM-DD transmission over 80-km SMF without CD compensation using SSB-DMT," *Optical Fiber Communications Conference and Exhibition (OFC)*, Th4A.2 (2015).
82. P. Dong, J. Lee, Y.-K. Chen, L. L. Buhl, S. Chandrasekhar, J. H. Sinsky, and K. Kim, "Four-channel 100-Gb/s per channel discrete multi-tone modulation using silicon photonic integrated circuits," *Optical Fiber Communications Conference and Exhibition (OFC)*, Th5B.4 (2015).
83. N. Massa, "*Fiber optic telecommunication*," in Fundamentals of Photonics, C. Roychoudhuri, Ed, SPIE Press, Bellingham, Washington, 293–347 (2008).
84. P. Dawe, M. Dudek, U. Jonsson, T. Murphy, J. Radcliffe, K. Seto, and V. Bhatt, "Error rates and testability," http://www.ieee802.org/3/efm/public/may03/optics/dawe_optics_1_0503.pdf.
85. M. Takenaka and S. Takagi, "Strain engineering of plasma dispersion effect for SiGe optical modulators," *IEEE J. Quantum Electron.* **48**(1), 8–16 (2012).

Chapter 8
Photonic–Electronic Integration with Silicon-Based Optical Modulators

Photonic–electronic integration is attracting more interest from scientists and engineers in photonics because of its significance in the design and fabrication of small-footprint optical I/Os and compact optical transceivers. In this chapter, photonic–electronic integration is discussed with respect to two aspects. The first aspect covers the technologies for integration with electronic and photonic devices such as modulator drivers, TIAs, PDs, and laser diodes. The integration technologies are classified according to integration methods of devices from monolithic to package levels. Optical waveguides for vertical coupling are also discussed in terms of 3D photonic integration. Emerging photonic–electronic integration for optical performance monitoring is discussed in the second aspect. Such monitoring is significant in fault management for optical data transmission, and therefore, the integration of optical performance monitoring in a small footprint is crucial for compact optical transceivers. In this chapter, the forefront of photonic–electronic integration for optical performance monitoring in optical modulators is discussed.

8.1 Integration with Electronic and Photonic Devices

8.1.1 Monolithic integration

Monolithic integration technologies have been developed on III-V photonics and silicon-photonics platforms. Although the silicon-photonics platform emerged after 2002 (much later than the III-V photonics platform, according to the literature), it has grown much more rapidly by taking advantage of CMOS-based commercialized fabrication technology and has now overwhelmed the III-V photonics platform in terms of the number of integrated components per PIC.[1–3] Monolithic integration technology on a

silicon-photonics platform is more scalable and more suitable to roadmaps for optical transceivers and AOCs of small or compact form factors. For instance, PDM IQ MZ modulators, coherent-detection optical circuits, and high-speed PDs have been integrated monolithically as a sub-assembly on a silicon-photonics platform in applications for 400ZR compact pluggable coherent optical transceivers in DCI and LAN domains at 400 Gb/s.[4] Silicon-photonics platforms have been combined with III-V photonics platform to fabricate large-scale on-chip PICs.[5] On the basis of these technological backgrounds, the rest of this chapter focuses on integrated silicon-based MZ optical modulators and their design and fabrication technologies on silicon-photonics platforms.

Electronic circuits such as modulator drivers and trans-impedance amplifiers for PDs can be monolithically integrated with photonics circuits such as optical modulators and PDs, as illustrated in the front-end integration shown in Fig. 8.1.[6] Active transistor channels in electronic circuits are formed in the thin silicon layer on the same SOI wafer as that of optical modulators. The electron microscope photograph in Fig. 8.2 provides cross-sections of a germanium PD and silicon–germanium transistor co-integrated on a SOI wafer as an example of monolithic photonics and electronics integration.[7,8] Monolithic integration of MZ optical modulators with electronic driver circuits on a SOI wafer was also reported.[9] In monolithic integration, photonic circuits and electronic circuits must be designed under common design rules to co-integrate both types of circuits in the same fabrication

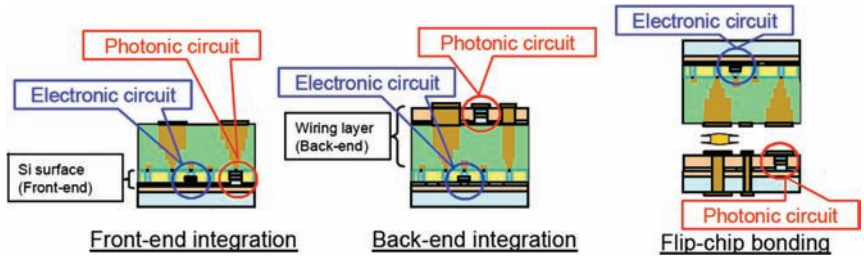

Figure 8.1 Schemes of photonic and electronic integration.[6]

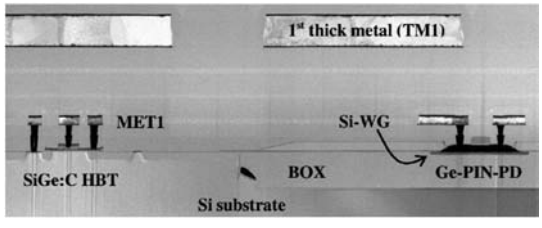

Figure 8.2 Cross-section TEM photograph of photonic and electronic devices in monolithic integration.[7]

process flow. This co-integration is sometimes a technological challenge because the feature sizes and layer structures of photonic circuits and electronic circuits are very different, and the differences cause trade-offs between phonic and electronic circuits with respect to the adjustment of fabrication-process conditions. The other two integration schemes in Fig. 8.1 can be also adopted for photonics and electronics integration if the restrictions on the process adjustment cannot be eliminated or if some other device blocks such as LDs are required. These schemes are described in the next couple of subsections.

8.1.2 Wafer-bonding integration: silicon on silicon

The separate fabrication of photonic circuits and electronic circuits on different wafers is easier than monolithic photonic–electronic integration on a single wafer because different design rules can be adopted for these circuits separately to adjust the fabrication processes of different feature sizes and layer structures. A photonic wafer is obtained by the monolithic integration described above. An electronic wafer is obtained by the most advanced fabrication processes for a cutting-edge CMOS node. After the separate fabrication, both wafers with the same diameter are stacked face to face and then bonded with a thermal treatment to provide an integrated photonic–electronic wafer, as illustrated in Fig. 8.3 with a top-view photograph of the integrated photonic–electronic wafer and an electron microscope cross-section of bonded VIAs through the photonic layer to the electronic layer.[10] Photonic–electronic integration is similar to the back-end integration shown in Fig. 8.1. Drawbacks include increased complexity, reduced yield in back-end processes, and additional parasitic capacitances, inductances and resistances that affect the electrical performance.

8.1.3 Die-bonding integration: III-V on silicon

For a higher degree of integration to realize further reductions in footprint and profile, heterogeneous integration is exploited for photonic integration by using wafers made of different material species. This scheme has been applied to the fabrication of on-chip LDs on a silicon-photonics platform.[5,11] Crystalline III-V compounds based on indium phosphide are most suitable for long-wavelength LDs in spectral ranges such as the O, C, and L bands covered in high-capacity optical networks because of high optical gain due to a direct interband dipole transition in the spectral ranges.[12] Crystalline group-IV elements such as silicon and germanium, on the other hand, have indirect bandgaps and generate electro-luminescence that is too weak to generate optical gain.[13] For on-chip LD integration, a III-V compound wafer is separated into unit dies because the diameter of the III-V wafer is much smaller than that of an SOI wafer and only a small portion of the SOI wafer is used if wafer-to-wafer bonding is employed instead of die-to-wafer bonding.

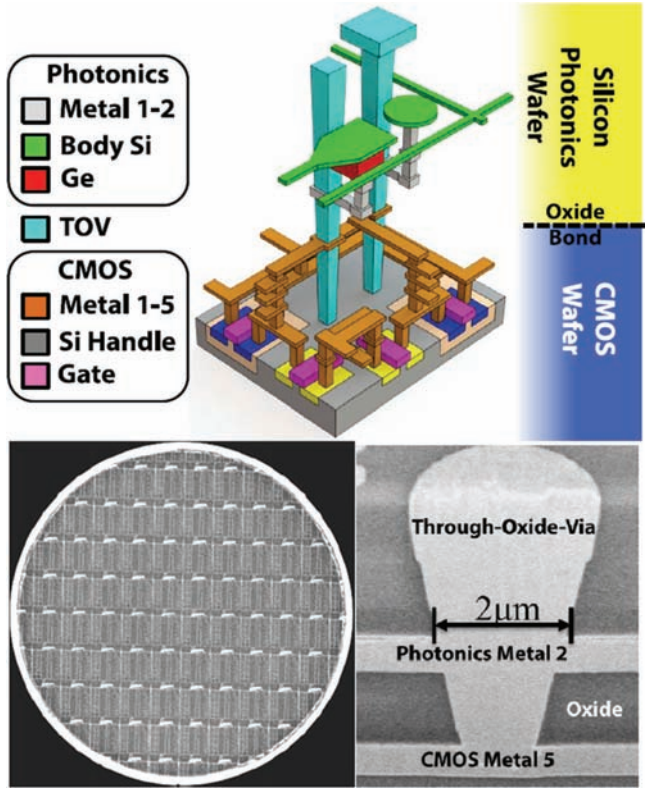

Figure 8.3 Integrated photonic–electronic wafer with face-to-face wafer stacking and bonding.[10]

The III-V compound dies are bonded to form multiple QW gain media and evanescently coupled to laser-resonator cavities made of passive optical waveguides on the SOI wafer, as shown in Fig. 8.4.[5]

Die-bonding integration of novel III-V membrane LDs on silicon wafers was reported, and room-temperature CW operation was confirmed.[14,15] The LDs were integrated on silicon wafers by means of die bonding using spin-coated benzocyclobutene (BCB) as an intermediate adhesive.[14] The structure of a distributed feedback (DFB) membrane LD, in which the active region consists of five GaInAsP QWs in a Bragg grating cavity with lateral current injection, is shown in Fig. 8.5. The fabrication and integration processes of the membrane LD include three-step regrowth to form a laser-cavity optical waveguide with a lateral PIN structure, BCB bonding to the Si host wafer, evaporation of current-injection electrodes, and formation of a surface Bragg grating pattern, as presented in Fig. 8.6.[14]

High contrast of the refractive index in the vertical direction using the silica bottom cladding leads to high optical intensity confined in the laser cavity. Thus, the thin-film LD yields an external differential quantum

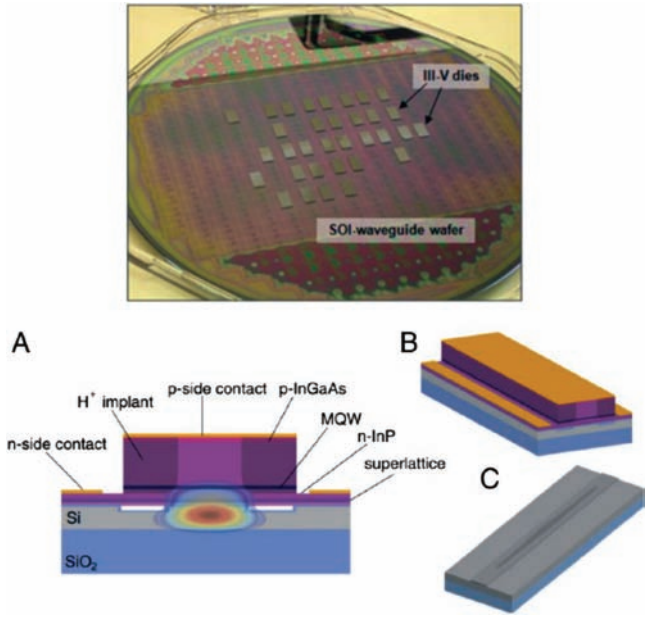

Figure 8.4 Photograph of III-V compound dies bonded on an SOI wafer and schematic illustration of an active optical waveguide in heterogeneous integration.[5]

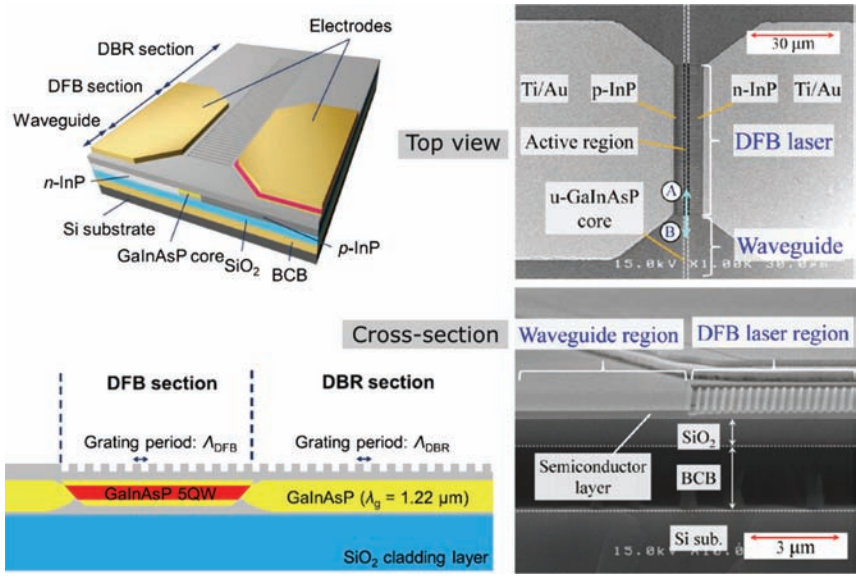

Figure 8.5 Illustrated and SEM images of a DFB membrane LD (image reprinted courtesy of N. Nishiyama, Tokyo Institute of Technology).

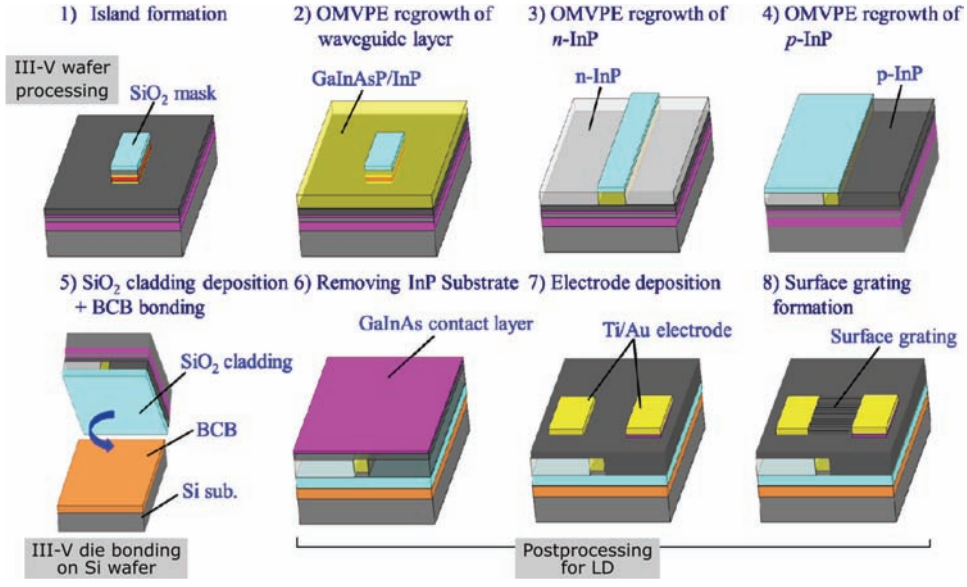

Figure 8.6 Fabrication and integration processes of a DFB membrane LD (image reprinted courtesy of N. Nishiyama, Tokyo Institute of Technology).

efficiency as high as 35% with an injection current as low as 1.7 mA.[16] The current was injected in the lateral PN diode though the electrodes formed on both sides of the cavity. A single longitudinal mode of CW laser light was generated with a side-mode suppression ratio of 40 dB.[16] The membrane LD can be coupled to silicon-photonics circuits such as integrated silicon-based MZ optical modulators via vertical optical interconnect described in Subsection 8.1.5. The membrane LD is eligible for high-efficiency integrated laser sources in optical I/Os and compact optical transceivers with a high packing density. The heterogeneous die-bonding methods serve as versatile design and fabrication platforms to integrate laser diodes for one-chip optical transceivers in small footprints and low profiles.

8.1.4 Hybrid integration

The third approach of photonic–electronic integration shown in Fig. 8.1 is hybrid integration based on flip-chip bonding. The electronic chip and photonic chip, as shown in Fig. 8.7, are fabricated in separate lots based on different design rules and process conditions.[17] The chips are then flip-chip bonded with copper-pillar micro-bumps by die-bonder equipment. An electric connection between the photonic and electronic chips is achieved by flip-chip bonding. In the fabrication of electronic wafers, the most advanced silicon platform for the cutting-edge CMOS node can be applied to create small-footprint, energy-efficient electronics circuits. For monolithic photonic integration, on the other hand, a silicon-photonics platform that uses

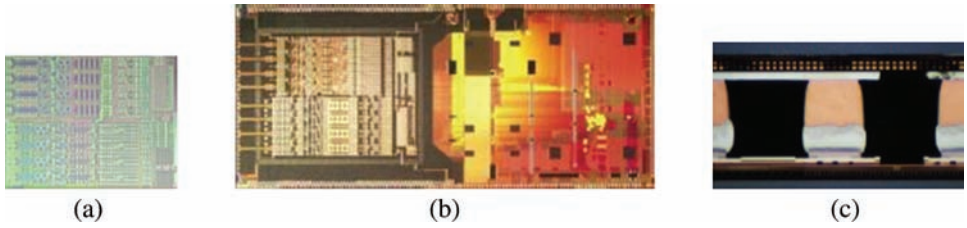

Figure 8.7 (a) Electronic chip and (b) photonic chip are flip-chip bonded face to face with (c) copper-pillar micro-bumps.[17]

fabrication equipment for legacy CMOS nodes can be used for monolithic photonic integration. Flip-chip bonding is more established than monolithic integration and wafer/die-bonding integration. (The silicon PIC presented in Fig. 2.5 was fabricated by flip-chip bonding.)

Photonic-electronic integration by flip-chip bonding has been applied to a variety of applications.[6,17,18] A parallel-channel silicon-photonics interposer designed for on-chip optical interconnects, like that shown in Fig. 8.8, has been fabricated by flip-chip bonding.[6]

8.1.5 Optical coupling and packaging

Coupling to I/O optical fibers is required to modularize the monolithic optical modulators in photonic–electronic packaging with fiber pigtails. There are

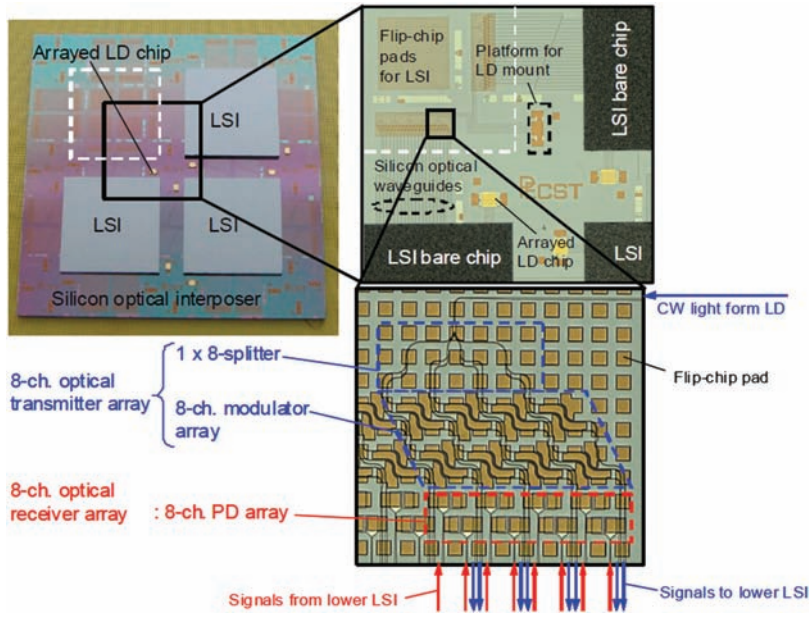

Figure 8.8 Silicon-photonics interposer for on-chip optical interconnects.[6]

three methods for the packaging: (1) spatial lens coupling, (2) butt-joint edge coupling, and (3) direct-contact surface coupling.

1. Spatial lens coupling is the most mature traditional method for the optical coupling of planar optical waveguides and I/O optical fibers. An example of photonic–electronic packaging using spatial lens coupling is presented in Fig. 8.9. The integrated MZ optical modulator chip shown in Fig. 3.7 was mounted on a ceramic-based metal chip carrier and connected to high-frequency feed-through electrodes and 50-Ω terminators on the chip carrier.[19] A pair of aspheric singlet lenses for beam collimation and focusing were set in each side facet of the chip for coupling to the I/O pigtails of a PMF for input and an SMF for output. The chip and the chip carrier were accommodated in a metal housing hermetically sealed in a package 28 mm long, 10 mm wide, and 8 mm high, including two screw-mounting flange pieces. The transmission characteristics of the packaged silicon-based MZ optical modulator in 10G OOK are described in Chapter 7.
2. For butt-joint edge coupling, MFCs that include nano-tapers can be used.[20–22] An example nano-taper MFC is presented in Fig. 8.10. The

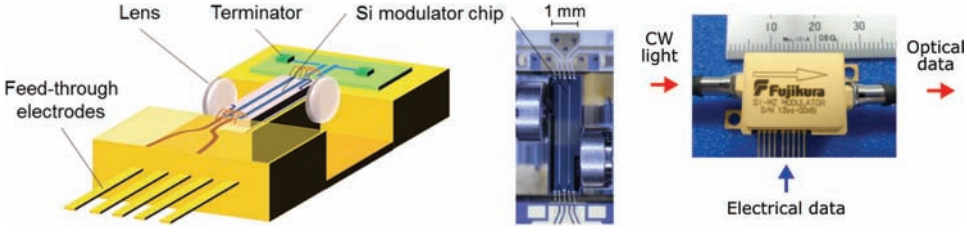

Figure 8.9 Photonic–electronic packaging of an integrated silicon-based MZ optical modulator chip using spatial lens coupling to I/O fiber pigtails.

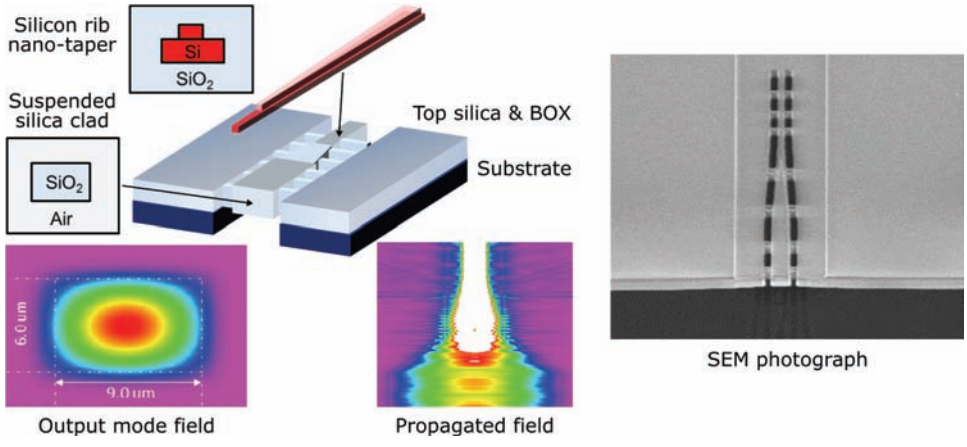

Figure 8.10 Suspended nano-taper MFC for low-loss edge coupling.

MFC is suspended in air with silica side beams supporting silica cladding.[22] The nano-taper was formed using a silicon rib optical waveguide, and thus it has the shape of stepped tandem tapers to prevent radiation escaping from the MFC. Light propagated through a silicon photonic circuit is emitted from the nano-taper, confined inside the suspended silica clad, and propagated through the cladding as the propagated field plotted in pseudo-color scale in Fig. 8.10. Therefore, the suspended silica cladding also serves as an outer silica core. At the edge facet, the output mode field is expanded over the outer silica core in 9-$\times$6-μm^2 cross-section. The suspended MFC shown in the SEM photograph allows coupling efficiencies as high as 80% and 70% for TE- and TM- polarization modes and fiber-alignment tolerances as large as $\pm$2.8 μm and $\pm$2.1 μm at 1-dB excess optical loss in horizontal and vertical directions, respectively.[22] High-efficiency, large-tolerance I/O fiber coupling has been achieved with the suspended MFC.

The butt-joint edge coupling allows low-profile photonic-electronic packaging as presented in Fig. 8.11. The PDM IQ MZ optical modulator chip in Fig. 8.11 was accommodated in a ceramic-based metal housing with modulator drivers, bias tees, and 50-Ω terminators.[19] Differential dual-end electrical drivers commercialized for 32-Gbaud LN MZ optical modulators were utilized as modulator drivers. To convert the differential dual-end outputs from the driver to the isolated single-end inputs to the modulator, a planar converter circuit was copackaged and wire-bonded to the contact pads of the traveling-wave electrodes on the modulator. For the butt-joint edge coupling, fiber-guiding grooves such as V-grooves were formed in front of the I/O suspended MFCs on the chip, as shown in the optical-microscope photographs in Fig. 8.11, by a deep-trench wet etching process after the monolithic integration processes summarized in

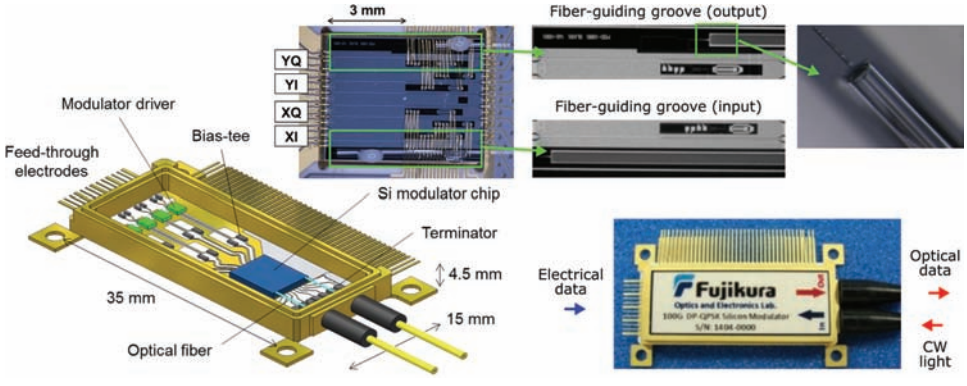

Figure 8.11 Low-profile photonic–electronic packaging of an integrated silicon-based PDM IQ MZ optical modulator chip with butt-joint edge coupling to I/O fiber pigtails.

Fig. 3.14. The I/O pigtails of the input PMF and output SMF were butt-joint coupled to the suspended MFCs with index-matching gel coatings on the cleaved facets of the I/O fibers. The outer dimension of the hermetically sealed metal housing is $35\times15\times4.5$ mm^3. The height of 4.5 mm includes a top metal lid, which is not shown in Fig. 8.11. The low-profile small-footprint photonic-electronic packaging is suitable for compact-form-factor optical transceivers such as the CFP series for high-capacity data transmission in advanced modulation formats in metro-area optical networks and datacenter interconnects at a bit rate of 100 Gb/s or beyond per wavelength channel. The transmission characteristics of integrated silicon-based PDM IQ MZ modulators in photonic–electronic packaging are described in Chapter 7.

Butt-joint edge coupling to I/O MFCs along the fiber-guiding grooves in Fig. 8.11 allows photonic–electronic packaging in a profile as low as 4.5 mm, as described above. The modulator chip and the modulator drivers have been assembled within a housing footprint of 15×35 mm^2. The small-footprint, low-profile photonic–electronic packaging is suitable to pluggable optical transceivers such as the CFP-series modules described in Chapter 1.

3. Grating couplers, as shown in Fig. 8.12, enable direct-contact surface coupling to I/O fibers in photonic–electronic packaging.[9,23–26] The advantages of the grating couplers are a large fiber-alignment tolerance and the ability to conduct on-wafer optical testing without dicing. Alignment tolerance larger than ±2 μm at 1-dB excess optical loss was reported in measurements, and more than ±2.5 μm at 0.5-dB excess optical loss in numerical analysis.[27,28] Photonic-electronic packaging based on the surface coupling was implemented for a QSFP module for AOC application as presented in Fig. 8.13. An array of I/O fiber ribbon was directly contacted and glued to the surface of an array of grating couplers.[17]

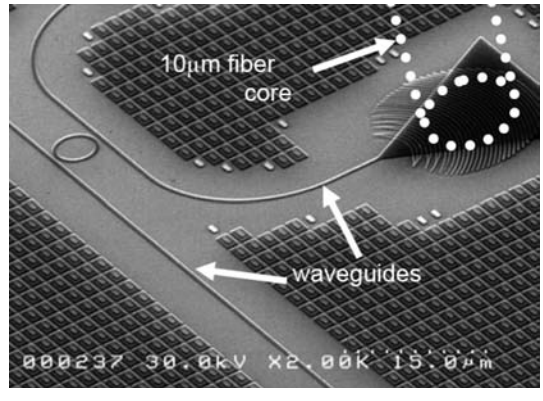

Figure 8.12 Grating coupler for direct-contact surface coupling.[11]

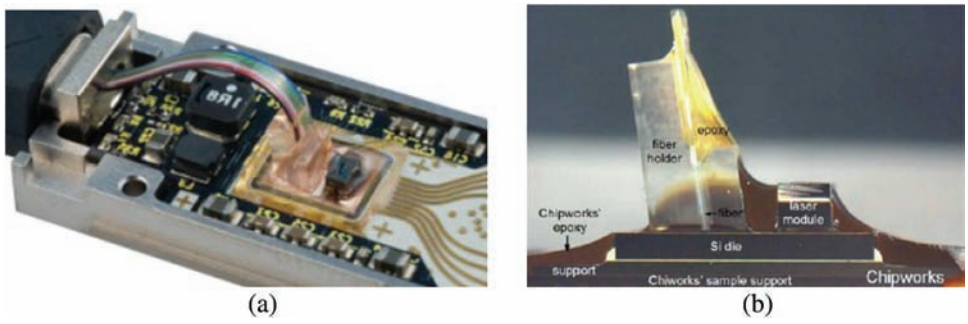

Figure 8.13 Photonic–electronic packaging of an integrated silicon-photonics optical transceiver chip in a QSFP module using direct contact surface coupling.[17]

The emission or incidence angles of the grating couplers are determined by the diffraction angles of gratings patterned in their slab optical waveguides because the grating couplers are essentially diffraction gratings.[23,24,29] This implies that the optical coupling efficiencies of the grating couplers depend strongly on the wavelengths of light emitted from or incident to the grating couplers. Therefore, butt-joint edge coupling using nano-taper optical waveguides is more suitable to optical coupling in photonic–electronic packaging of integrated optical modulators for optical transceivers with low profiles and compact form factors in broadband WDM transmission of high-capacity optical networks.

In high-capacity optical networks, the SMF, which transmits an optical mode that has a mode-field diameter of $\sim$10 μm, has been used extensively. For high-efficiency optical-fiber coupling, the optical mode field with a sub-micron diameter must be expanded up to 10 μm by using MFCs in the above methods. This is a challenging task for edge couplers in particular because the top silica layer of an MFC must be deposited in thickness more than several micrometers to expand the mode field closer to that in an SMF. Such a thickness is far beyond the allowable thickness of the silica layer deposited in the ordinary CMOS process and makes silicon-photonics fabrication processes cumbersome. Therefore, small-core single-mode fiber supporting a mode field with a diameter of $\sim$4 μm or smaller has often been used instead of an SMF for the edge coupling.[20] In this case, the top silica layer, which is a few microns thick and can be deposited on the basis of CMOS fabrication processes, allows high-efficiency coupling to the small-core fiber. To establish fiber coupling using small-core fiber as a practical method in photonic–electronic packaging on a silicon-photonics platform, a reduction in mode-mismatch loss in splicing the SMF and small-core fiber remains an issue. This issue has been resolved recently by applying a heat gradient in the splicing process to produce a profile of tapered, thermally expanded core along the light-propagation direction in small-core fiber, as illustrated in Fig. 8.14. A fiber-coupling loss of 1.5 dB or lower, including a splice loss <0.2 dB,

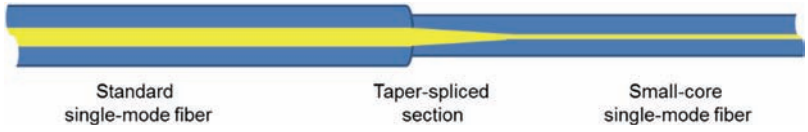

Figure 8.14 Schematic cross-section of tapered, thermally expanded core in small-core fiber spliced to an SMF.

has been realized in edge coupling with a nano-taper MFC.[30] Very high-efficiency edge coupling with a loss lower than 1 dB will be possible with the latest high-efficiency, suspended nano-taper MFC fabricated by high-resolution photolithography developed for the latest CMOS node.[31]

There is another aspect to optical coupling with respect to optical access in a PIC on a silicon-photonics platform. For complex layouts in on-chip photonic–electronic integration (illustrated in Fig. 8.15), vertical optical couplers allow 3D optical interconnections to access multiple PIC layers stacked vertically on each other.[32] The membrane LDs integrated by the die-bonding method can be optically coupled by vertical optical couplers. Two types of vertical optical-coupler waveguides have been designed, fabricated, and characterized for 3D optical access on a silicon-photonics platform.[32]

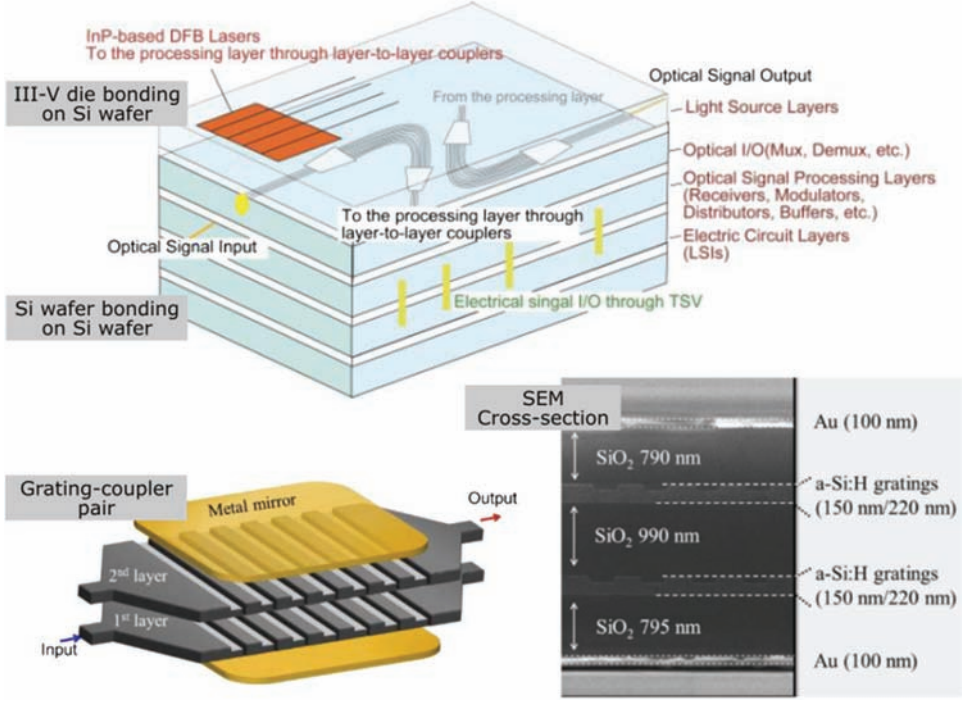

Figure 8.15 Illustration of a 3D PIC, and illustrated and SEM images of grating couplers for vertical optical interconnection on a silicon-photonics platform (image reprinted courtesy of N. Nishiyama, Tokyo Institute of Technology).

One of them is layer-to-layer grating-coupler pair with back-side metal mirrors in Fig. 8.15. A hydrogenated amorphous silicon layer of 220-nm thickness deposited by plasma-enhanced CVD, as well as a 220-nm-thick crystalline SOI layer, provides the core materials for the grating couplers. A grating coupler is 5 μm wide and ~13 μm long (640 nm × 20 periods). A vertical coupling efficiency up to 85% per grating coupler pair was obtained with gold mirrors in both sides opposite the emitting faces.[32]

The other type is an adiabatic waveguide coupler using a pair of nano-taper optical-waveguide MFCs, as shown in Fig. 8.16. The amorphous silicon layer and the SOI layer have also been used also for the nano-taper MFCs as the core materials. A vertical coupling efficiency as high as 87% was obtained with a pair of cascaded, double linear nano-taper MFCs 190 μm long. The nano-taper MFC pair can be used as a high-efficiency vertical optical interconnect without back-side metal layer deposition but in a larger footprint than that of the grating coupler pair.[32]

8.2 Integration of Optical Performance Monitoring

8.2.1 Technical background

Optical performance monitoring plays a crucial role in the fault management of optical data transmission.[33–36] The optical characteristics of the *ER* and *OMA* of the optical intensity modulators and the *Q*-factor of the optical phase modulators affect the performance of the optical networks in which the modulators are deployed via the BER and OSNR. With respect to silicon-based MZ optical modulators, the temperature dependence of the refractive

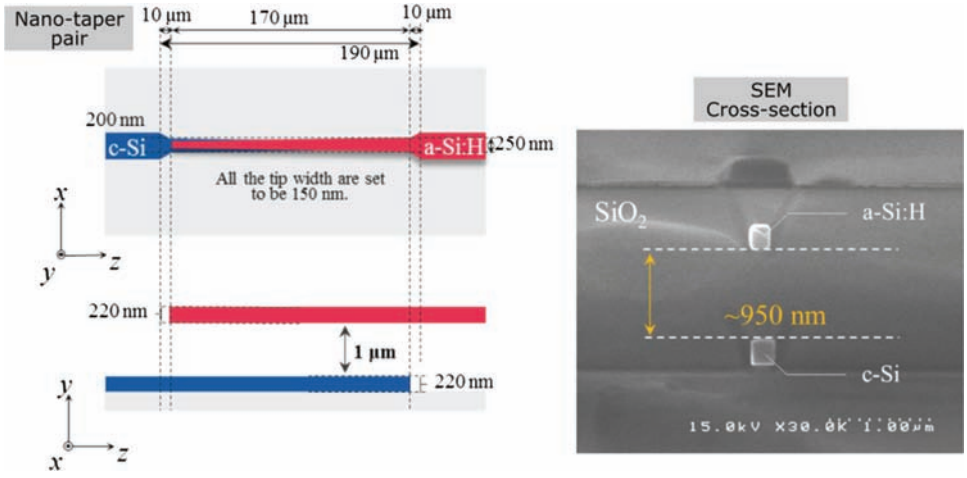

Figure 8.16 Nano-taper optical-waveguide MFCs for vertical optical interconnection on a silicon-photonics platform (image reprinted courtesy of N. Nishiyama, Tokyo Institute of Technology).

index of host materials such as crystalline silicon causes temperature dependence of the static phase errors and thus a temperature-dependent imbalance in the MZIs, whereby all of the optical characteristics above deteriorate due to drift in the ambient temperature. The temperature dependence of the refractive index also influences the deviation of the I–Q phase difference from 90 deg and causes a BER due to crosstalk between the I and Q components. All such impairments lead to faults in optical data transmission.

To recover error-free transmission, the TO phase shifters must be controlled adequately to generate phase offsets counter to the static phase errors and the deviation of the I–Q phase difference. For this purpose, it is necessary to monitor the phase states in MZIs in the operational optical modulators. A simple monitoring method applies small-amplitude pilot electrical signals, which are single-frequency trigonometric, saw-tooth, or square-wave signals superimposed on input electrical data, to the RF phase shifters in the MZIs to be controlled; after that, a portion of the output optical power is monitored by photodetection and then the phase states of the MZI with phase comparators are extracted with reference to the phase of the original pilot signals. Monitor PDs are thus integrated with the optical modulators for performance monitoring.

8.2.2 Conventional approach

In conventional approach to integrate monitor PDs with optical modulator, discrete PDs are copackaged with optical modulators.[37,38] In the off state of a single MZ optical intensity modulator consisting of straight optical waveguides and a Y-branch splitter/coupler, for example, the output light is not launched to the output optical waveguide but emitted out of the Y-branch coupler as a radiation mode (see Chapters 3 and 4). A fraction of the optical power of the radiation mode is incident to a monitor PD placed beside the Y-branch coupler, as illustrated in Fig. 8.17, and the phase of the MZI is detected with reference to the original phase of the pilot electrical signal.[37]

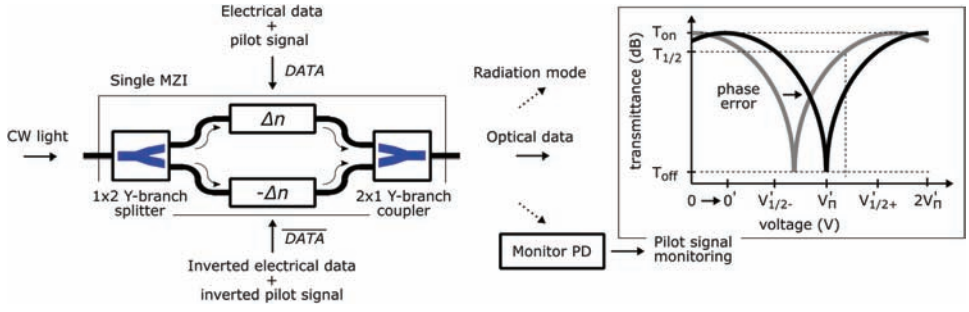

Figure 8.17 Optical-waveguide layout diagram of a single MZ optical modulator with a monitor PD.

8.2.3 Optical layout for integration

In integrated silicon-based MZ optical modulators, 1×2 MMIs are used for MZI splitters and couplers. In contrast to a Y-branch coupler, the output light in the OFF state is not coupled to the radiation mode but to the first higher-order mode of the output optical waveguide after the small-footprint 2×1 MMI coupler on a silicon-photonics platform. Propagation in the first higher-order mode in the output optical waveguide will be verified experimentally with the near-field mode profile of the output light in the OFF state in the following subsection. Performance-monitoring circuits for integrated silicon-based MZ optical modulators thus comprise monitor PDs and passive monitor optical waveguides that are coupled to the output optical waveguides to extract the first higher-order mode from the output optical waveguides. Selective optical coupling to the first higher-order mode in the OFF state with a monitor optical waveguide is schematically shown in Fig. 8.18.[39]

In the ON state, the output light is coupled to the fundamental mode $m = 0$ of the output channel optical waveguide due to constructive interference and is launched to the output optical fiber. In the OFF state, however, destructive interference leads to the generation of radiation-like output light, which is not coupled to the fundamental mode but to the first higher-order mode $m = 1$ because its mode-field profile overlaps efficiently with the field profile of the OFF-state light. The OFF-state light is therefore propagated as the first higher-order mode in the output channel optical waveguide. To suppress the first higher-order mode and support only the fundamental mode in the output optical waveguide, the width of the channel

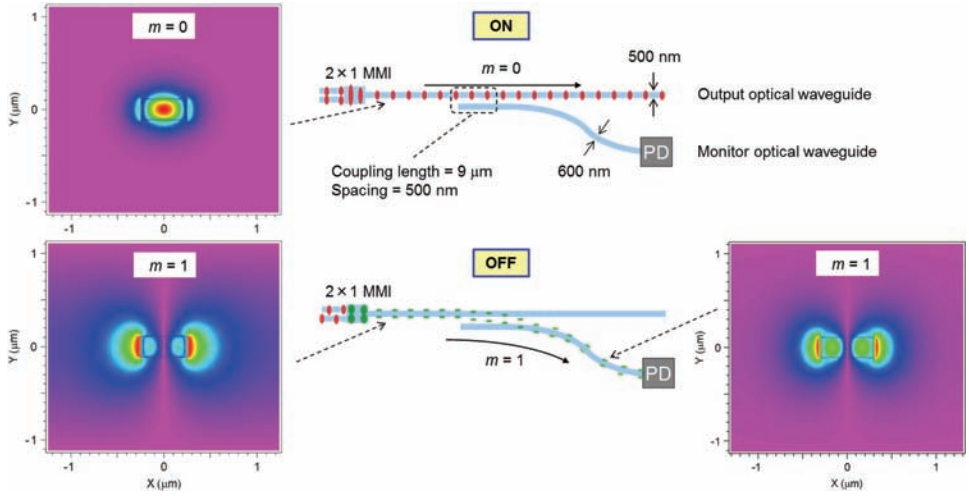

Figure 8.18 Selective extraction of the first higher-order mode in the OFF state with monitor optical waveguide.

waveguide is narrower than 450 nm. Optical loss due to the side-wall roughness is, however, higher with a waveguide width narrower than 450 nm, according to the width dependence of optical loss (see Chapter 6). A significant portion of the mode field of the first higher-order mode is distributed in the silica cladding region and efficiently coupled to the monitor channel optical waveguide placed in a side of the output channel optical waveguide. The both waveguides in the parallel layout form a directional coupler. The spacing between the output and monitor waveguides is 500 nm, which is too wide for the fundamental mode to transfer from the output waveguide to the monitor waveguide. The first higher-order mode is selectively extracted from the output channel optical waveguide. The width of the monitor waveguide is 600 nm, wider than the output-waveguide width, and thus the higher-order mode is more tightly confined as shown in Fig. 8.18 and propagated in the monitor waveguide stably. This scheme of the first higher-order mode transfer is regarded as adiabatic mode transfer, analogous to the adiabatic-mode conversion discussed in Chapter 4.[40]

One may argue that more straightforward circuit design of optical performance monitor is possible if 2×2 MMI is employed for the combiner, where the two output ports are allocated both to optical signal output and optical performance monitoring. Structural symmetry of a 1×2 MMI, however, allows a constant and stable optical power-splitting ratio between the optical signal power output and the optical performance monitoring against change in a wavelength channel over the wide range of temperature without electrical power consumption for active tuning of the power-splitting ratio. Thereby, an optical performance monitoring circuit using a 1×2 MMI is suitable for compact transceivers such as CFP series, for which electrical power consumption is critical.

Monitor PICs, each of which comprises a passive monitor channel optical waveguide and a monitor PD, as described above, can be monolithically integrated with MZ optical modulators on a silicon-photonics platform. The monitor PICs integrated with a PDM IQ optical modulator on a silicon-photonics platform is presented with an optical-waveguide layout diagram in Fig. 8.19.[41] Six monitor PICs are integrated beside the output optical waveguides of sub-MZ optical modulator units and I and Q quadrature optical modulators as white circles in the top-view microscope photograph. The locations where the monitor PICs are integrated are shown in the schematic layout of the optical waveguides that compose the modulator. The modulator chip is the same as presented in Fig. 3.12. The monitor PICs are embedded in the small footprint with germanium PDs.

Extensive research and development have been devoted to germanium PDs for many decades. Early efforts on discrete germanium PDs for high gain-bandwidth optical detection in long-wavelength optical-fiber communications

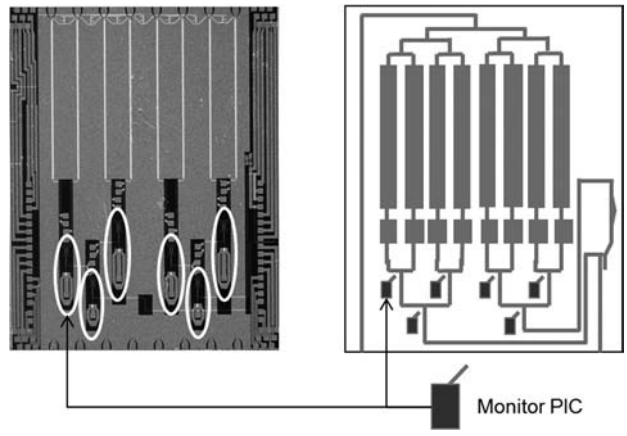

Figure 8.19 Monitor PICs integrated with a PDM IQ optical modulator on a silicon-photonics platform.

were reviewed.[42] Research and development efforts for germanium PDs on crystalline silicon wafer started in the 1980s, where germanium active layers grown on crystalline silicon contained dislocations and defects induced by strain due to a mismatch in the lattice constants between silicon and germanium.[43] Strained $Si_{1-x}Ge_x$ superlattices on crystalline silicon were also introduced to manage strain and attain high photodetection responsivity in the near-infrared spectral region.[44] Strained superlattices were used as buffer layers for strain relaxation, vertical incidence germanium PDs were studied, and high-speed photodetection was demonstrated.[45–48]

Strained germanium PDs on an SOI platform without buffer layers have now been studied and exploited to PICs on a silicon-photonic platform extensively because of its high compatibility with silicon-photonics optical waveguide systems designed and fabricated on SOI wafers.[49–51] Strained germanium PDs with PIN junctions allow high-responsivity photodetection in a long wavelength extending to the L band because of efficient photocarrier extraction in PIN junctions and a bandgap reduction under tensile strain.[49,51] Evanescently coupled optical-waveguide germanium PIN PDs are most suitable to applications such as monolithic silicon-photonics PICs.[52–57] High-speed PDs and integrated balanced PD units were developed on the basis of PD technology on silicon-photonics platforms.[58,59] Germanium avalanche photodiodes (APDs) were developed for silicon-based PDs with a high gain-bandwidth product in optical data transmission.[60–63] Extensive research and development on the germanium PDs are reviewed in the literature.[56,64,65] To enhance responsivity in the L band and further spectral extension to the mid-infrared region, a germanium–tin alloy and crystalline silicon doped with deep-level impurities such as zinc atoms have been applied.[66,67]

8.2.4 Photonic integrated performance-monitoring circuit

The operational principle of performance monitoring based on the selective extraction of the first higher-order mode has been proved experimentally with a PIC device specially designed for proof of the principle.[39] A passive monitor optical-waveguide circuit for the first higher-order mode extraction is shown in Fig. 8.20 with a near-field image of optical modes from the output and monitor optical waveguides. An asymmetric single MZI and a monitor optical waveguide coupled to an output optical waveguide comprise the passive optical-waveguide circuit as shown in the plan-view microscope photograph in the top. The monitor optical waveguide is coupled to the output optical waveguide with a coupling section as short as 9 μm, as depicted in the optical-mask layout drawing in the middle. The near-field image at the bottom was captured with broadband light from an ASE source in the C and L bands launched to the input optical waveguide of the asymmetric MZI. Some portions of the broadband light, which satisfy constructive interference in the asymmetric MZI, are propagated in the fundamental mode through the output optical waveguide, while the rest portions, which cause destructive interference in the asymmetric MZI are propagated in the first higher-order mode and transferred to the monitor optical waveguides with transmission characteristics in Fig. 8.21. The double-peak profile in the near-field image is characteristic of the first higher-order mode propagated in the monitor optical waveguide. Counter phases in the spectral fringes of the transmission spectra imply interference condition, namely constructive or destructive interference, which is reversed between the output lights from these waveguides, according to the principle described above.

Various types of strained germanium PDs have been reported, such as an evanescently coupled PD in waveguide configuration, normal-incidence metal–semiconductor–metal PD, and normal-incidence APD, as shown in Fig. 8.22.[57] An evanescently coupled germanium PD is most suitable to

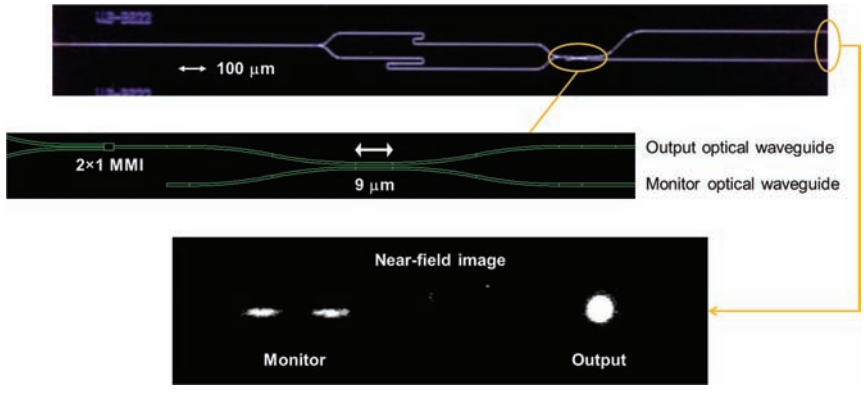

Figure 8.20 Silicon-based asymmetric MZI with a monitor optical waveguide and near-field image of the output optical power profiles.

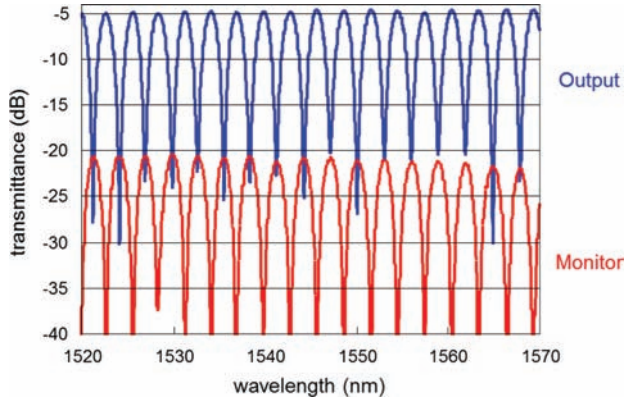

Figure 8.21 Transmission spectra in output and monitor optical waveguides.

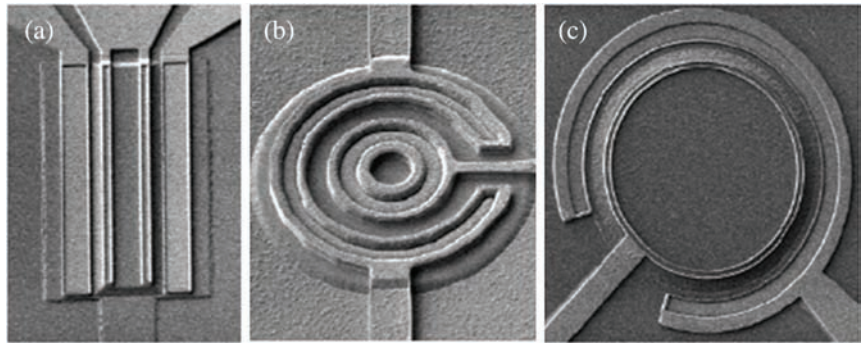

Figure 8.22 (a) Evanescent waveguide-type germanium PD, (b) normal-incidence metal–semiconductor–metal germanium PD, and (c) normal-incidence germanium APD.[57]

monitor PICs on a silicon-photonics platform. As illustrated in Fig. 8.23, the germanium photoconductive layer is grown on an SOI layer, both of which act as the core of the PIN-junction PD optical waveguide connected to a front-end PIC. Guided lightwave propagated through the PD optical waveguide is evanescently coupled to upper germanium layer and photoelectric conversion occurs along the propagation direction the PD waveguide.[56]

Photocurrent characteristics of evanescently coupled germanium PDs are presented in Fig. 8.23. The peak responsivity is about 0.6 A/W at a wavelength of 1540 nm for an isolated, evanescently coupled germanium PD connected with a single straight channel optical waveguide. The responsivity of the PD is higher than 0.2 A/W even at the longer wavelength edge of the L band because of the red shift of the electronic bandgap under tensile strain in crystalline germanium and the enhanced long-wavelength optical absorption in the evanescent PD as long as 60 μm. The photocurrent is more than three order higher than the dark current at a DC reverse bias of 5 V or lower with an optical power of 0 dBm (1 mW) launched to the single straight channel optical

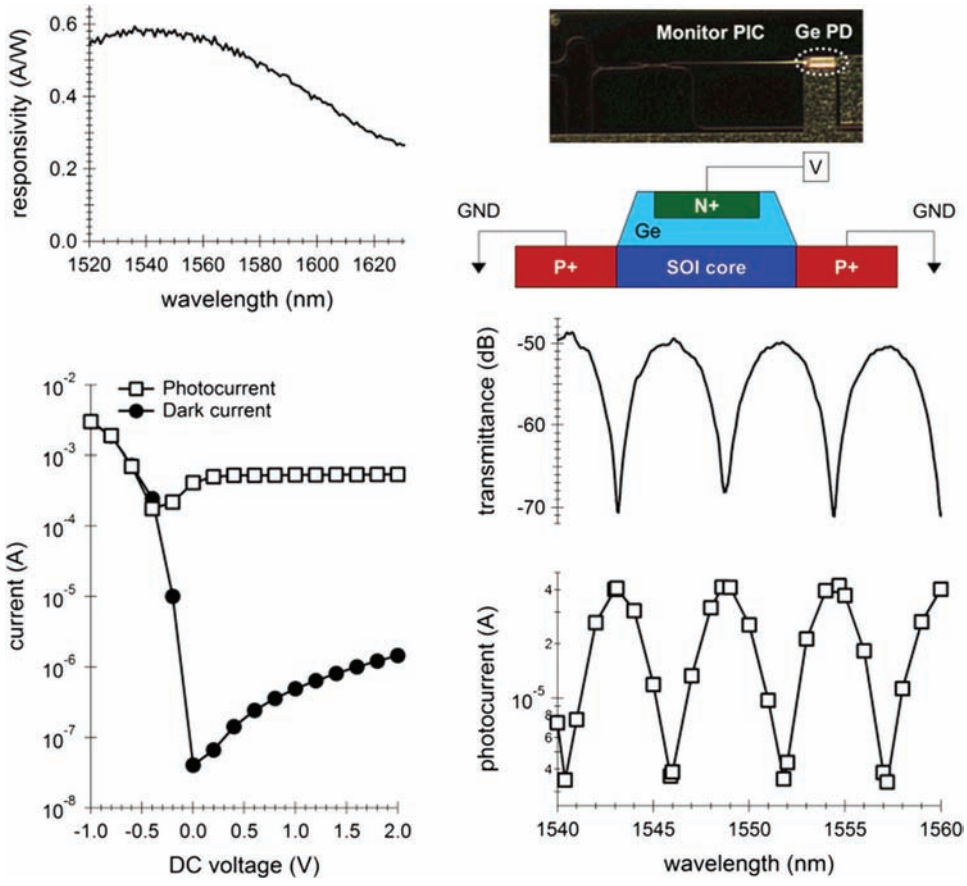

Figure 8.23 Responsivity spectrum, current-voltage characteristics, and spectral response of photocurrent in a test monitor PIC.

waveguide. The evanescently coupled germanium PIN-junction PD has been integrated with the passive optical-waveguide circuit of the test monitor PIC described above, and the operation of the monitor PIC is been verified with the spectral response of photocurrent in Fig. 8.23.[39] The maximum photocurrent is 4×10^{-5} A with 0-dBm optical power launched to the test PIC. The first higher-order mode propagated though the monitor optical waveguide in the OFF state is efficiently converted to photocurrent with an ON/OFF photocurrent contrast higher than 10 dB. Thereby, the monitor PIC with the evanescently coupled germanium PD is suitable to performance monitoring in small-footprint integrated optical modulators on silicon-photonics platforms.

8.2.5 All-silicon performance monitoring

Photocurrent is also generated in reverse-bias vertical PN-junction rib-waveguide phase shifters, as shown in Chapter 6, although the level of photocurrent in the

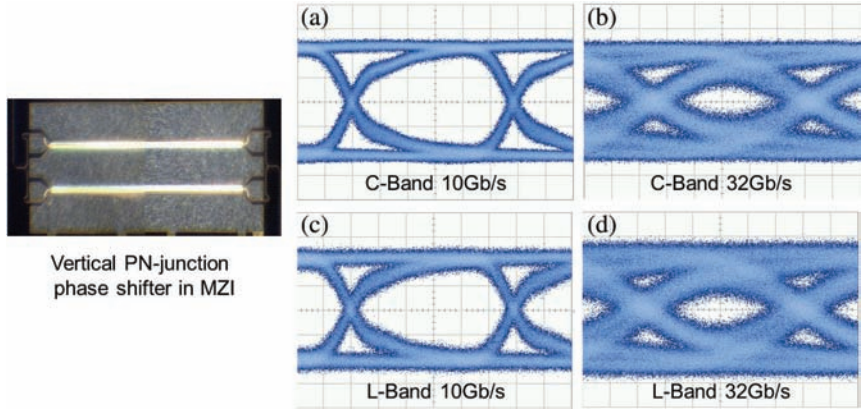

Figure 8.24 Eye diagrams of the photocurrent response of reverse-bias vertical PN-junction rib-waveguide phase shifters in a single MZI.

phase shifter is one order lower than in a germanium PD.[68] Therefore, the phase shifters in the MZI, as shown in Fig. 8.24, can be used as monitor PDs built in integrated MZ optical modulators. The phase shifters allow simultaneous monitoring of the optical power from input CW LDs for performance monitoring. Separate monitor PDs are required to sustain input optical power and accurately control emission wavelength.[69] The built-in monitor function in the phase shifters will open a way to advanced packaging of LDs with integrated optical modulators on a silicon-photonics platform with reduced photonic components such as discrete PDs. All-silicon performance monitoring is possible. In addition to performance monitoring, a high-speed response in the photocurrent detection is verified, which indicates the potential of vertical PN-junction phase shifters for the high-speed detection of transmitted optical data in 10-Gb/s and 32-Gb/s NRZ OOK in the C and L bands as eye diagrams (Figs. 8.24(a)–(d), which have been acquired in 10-km SMF transmission).

References

1. M. Hochberg and T. Baehr-Jones, "Towards fabless silicon photonics," *Nature Photon.* **4**(8), 492–494 (2010).
2. F. A. Kish, D. Welch, R. Nagarajan, J. L. Pleumeekers, V. Lal, M. Ziari, A. Nilsson, M. Kato, S. Murthy, P. Evans, S. W. Corzine, M. Mitchell, P. Samra, M. Missey, S. DeMars, R. P. Schneider, M. S. Reffle, T. Butrie, J. T. Rahn, M. Van Leeuwen, J. W. Stewart, D. J. H. Lambert, Muthiah R. C., H.-S. Tsai, J. S. Bostak, A. Dentai, K.-T. Wu, H. Sun, D. J. Pavinski, J. Zhang, J. Tang, J. McNicol, M. Kuntz, V. Dominic, B. D. Taylor, R. A. Salvatore, M. Fisher, A. Spannagel, E. Strzelecka, P. Studenkov, M. Raburn, W. Williams, D. Christini, K. J. Thomson, S. S. Agashe, R. Malendevich, G. Goldfarb, S. Melle, C. Joyner,

M. Kaufman, and S. G. Grubb, "Current status of large-scale InP photonic integrated circuits," *IEEE J. Sel. Top. Quantum Electron.* **17**(6), 1470–1489 (2011).
3. M. J. R. Heck, "Hybrid and heterogeneous photonic integrated circuits for high-performance applications," *Proc. SPIE* **9365**, 936503-1–936503-8 (2015).
4. K. Kikuchi, K. Tsuzuki, S. Kamei, S. Yamanaka, S. Asakawa, T. Itoh, Y. Nasu, K. Takeda, K. Honda, Y. Kawamura, M. Jizodo, M. Takahashi, M. Usui, H. Mawatari, and T. Saida, "Silicon-photonics-based coherent optical subassembly (COSA) for ultra-compact coherent transceiver," *IEEE Compound Semiconductor Integrated Circuit Symposium*, 1–3 (2017).
5. J. E. Bowers, T. Komljenovic, M. Davenport, J. Hulme, A. Y. Liu, C. T. Santis, A. Spott, S. Srinivasan, E. J. Stanton, and C. Zhang, "Recent advances in silicon photonic integrated circuits," *Proc. SPIE* **9774**, 977402-1–977402-18 (2016).
6. Y. Urino, T. Usuki, J. Fujikata, M. Ishizaka, K. Yamada, T. Horikawa, T. Nakamura, and Y. Arakawa, "High-density optical interconnects by using silicon photonics," *Proc. SPIE* **9010**, 901006-1–901006-9 (2014).
7. S. Meister, M. Grehn, H. Rhee, M. Vitali, C. Theiss, Se. Kupijai, A. Al-Saadi, D. Bronzi, S. Otte, M. Henniges, David Selicke, Muhammad Atif, E. Schwartz, S. Lischke, D. Stolarek, A. Mai, M. Kaynak, H. H. Richter, and L. Zimmermann, "Silicon photonics for 100 Gbit/s intra-data center optical interconnects," *Proc. SPIE* **9753**, 975308-1–975308-7 (2016).
8. L. C. Kimerling, D. Ahn, A. B. Apsel, M. Beals, D. Carothers, Y-K. Chen, T. Conway, D. M. Gill, M. Grove, C.-Y. Hong, M. Lipson, J. Liu, J. Michel, D. Pan, S. S. Patel, A. T. Pomerene, M. Rasras, D. K. Sparacin, K-Y. Tu, A. E. White, and C. W. Wong, *Proc. SPIE* **6125**, 612502-1–612502-10 (2006).
9. C. Gunn, A. Narasimha, B. Analui, Y. Liang, and T. J. Sleboda, "A 40Gbps CMOS photonics transceiver," *Proc. SPIE* **6477**, 64770N-1–64770N-8 (2007).
10. T. L. Koch, M. Liehr, D. Coolbaugh, J. E. Bowers, R. Alferness, M. Watts, and L. Kimerling, "The American Institute for Manufacturing Integrated Photonics: advancing the ecosystem," *Proc. SPIE* **9772**, 977202-1–977202-6 (2016).
11. G. Fish and A. Fang, "Heterogeneous integration: the More-Than-Moore path to silicon photonic microsystems," *Proc. SPIE* **9366**, 93660H-1–93660H-3 (2015).
12. Y. Suematsu and K. Iga, "Semiconductor lasers in photonics," *J. Lightwave Technol.* **26**(9), 1132–1144 (2008).
13. G. T. Reed and A. P. Knights, *Silicon Photonics: An Introduction*, John Wiley and Sons, Chichester, UK 223–250 (2004).

14. D. Inoue, J. Lee, T. Hiratani, Y. Atsuji, T. Amemiya, N. Nishiyama, and S. Arai, "Sub-milliampere threshold operation of butt-jointed built-in membrane DFB laser bonded on Si substrate," *Opt. Express* **23**(6), 7771–7778 (2015).
15. T. Hiratani, D. Inoue, T. Tomiyasu, Y. Atsuji, K. Fukuda, T. Amemiya, N. Nishiyama, and S. Arai, "Room-temperature continuous-wave operation of membrane distributed-reflector laser," *Appl. Phys. Express* **8**(11), 112701-1–112701-4 (2015).
16. T. Hiratani, D. Inoue, T. Tomiyasu, K. Fukuda, T. Amemiya, N. Nishiyama, and S. Arai, "R High-efficiency operation of membrane distributed-reflector lasers on silicon substrate," *IEEE J. Sel. Top. Quant. Electron.* **23**(6), 3700108-1–3700108-8 (2017).
17. P. De Dobbelaere, G. Armijo, J. Balardeta, B. Chase, Y. Chi, A. Dahl, Y. De Koninck, S. Denton, M. Eker, S. Fathpour, D. Foltz, F. Gholami, S. Gloeckner, K.Y. Hon, S. Hovey, S. Jackson, W. Li, Y. Liang, M. Mack, G. Masini, G. McGee, A. Mekis, S. Pang, M. Peterson, T. Pinguet, L. Planchon, K. Roberson, S. Sahni, J. Schramm, M. Sharp, C. Sohn, K. Stechschulte, P. Sun, G. Vastola, S. Wang, B. Weber, G. Wong, K. Yokoyama, S. Yu, and R. Zhou, "Silicon-photonics-based optical transceivers for high-speed interconnect applications," *Proc. SPIE* **9775**, 977503-1–977503-5 (2016).
18. H. Fukuda, T. Tsuchizawa, H. Nishi, R. Kou, T. Hiraki, K. Takeda, K. Wada, Y. Ishikawa, and K. Yamada, "Silicon, silica, and germanium photonic integration for electronic and photonic convergence," *Proc. SPIE* **8628**, 862806-1–862806-8 (2013).
19. K. Ogawa, H. Ishihara, K. Goi, Y. Mashiko, S. T. Lim, M. J. Sun, S. Seah, C. E. Png, T.-Y. Liow, X. Tu, G.-Q. Lo, and D.-L. Kwong, "Fundamental characteristics and high-speed applications of carrier-depletion silicon Mach-Zehnder modulators," *IEICE Electron. Express* **11**(24), 20142010 (2014).
20. T. Tsuchizawa, K. Yamada, H. Fukuda, T. Watanabe, J. Takahashi, M. Takahashi, T. Shoji, E. Tamechika, S. Itabashi, and H. Morita, "Microphotonics devices based on silicon microfabrication technology," *IEEE J. Sel. Top. Quantum Electron.* **11**(1), 232–240 (2005).
21. K. K. Lee, D. R. Lim, D. Pan, C. Hoepfner, W.-Y. Oh, K. Wada, L. C. Kimerling, K. P. Yap, and M. T. Doan, "Mode transformer for miniaturized optical circuits," *Opt. Lett.* **30**(5), 498–500 (2005).
22. Q. Fang, J. Song, X. Luo, M. Yu, G.-Q. Lo, and Y. Liu, "Mode-size converter with high coupling efficiency and broad bandwidth," *Opt. Express* **19**(22), 21588–21594 (2011).
23. A. Yariv and M. Namamura, "Periodic structures for integrated optics," *IEEE J. Quantum Electron.* **13**(4), 233–253 (1977).

24. T. Suhara and H. Nishihara, "Integrated optics components and devices using periodic structures," *IEEE J. Quantum Electron.* **22**(6), 845–867 (1986).
25. T. W. Ang, G. T. Reed, A. Vonsovici, A. G. R. Evans, P. R. Routley, and M. R. Josey, "Effects of grating heights on highly efficient unibond SOI waveguide grating couplers," *IEEE Photon. Technol. Lett.* **12**(1) 59–61 (2000).
26. D. Taillaert, W. Bogaerts, P. Bienstman, T.F. Krauss, P. Van Daele, I. Moerman, S. Verstuyft, K. De Mesel, and R. Baets, "An out-of-plane grating coupler for efficient butt-coupling between compact planar waveguides and single-mode fibers," *IEEE J. Quantum Electron.* **38**(7), 949–955 (2002).
27. D. Taillaert, F. Van Laere, M. Ayre, W. Bogaerts, D. Van Thourhout, P. Bienstman, and Roel Baets, "Grating couplers for coupling between optical fibers and nanophotonic waveguides," *Japanese J. Appl. Phys.* **45**(8A), 6071–6077 (2006).
28. C. Alonso-Ramos, A. Ortega-Moñux, I. Molina-Fernández, P. Cheben, L. Zavargo-Peche, and R. Halir, "Efficient fiber-to-chip grating coupler for micrometric SOI rib waveguides," *Opt. Express* **18**(14), 15189–15200 (2010).
29. M. Born and E. Wolf, *Principles of Optics*, 7th Ed., Cambridge University Press, Cambridge, New York, 446–476 (1999).
30. T. Oda, K. Hirakawa, K. Ichii, S. Yamamoto, and K. Aikawa, "Thermally expanded core fiber with a 4-μm mode field diameter suitable for low-loss coupling with silicon photonic devices," *Optical Fiber Communications Conference and Exhibition (OFC)*, Tu3K.5 (2017).
31. L. Jia, T.-Y. Liow, C. Li, X. Luo, X. Tu, Y. Huang, H. Zhou, M. Yu, and G.-Q. Lo, "High efficient suspended coupler based on IME's MPW platform with 193nm lithography," *Optical Fiber Communications Conference and Exhibition (OFC)*, Tu3K.1 (2017).
32. N. Nishiyama, J.H. Kang, Y. Kuno, K. Itoh, Y. Atsumi, T. Amemiya, and S. Arai, "Si-photonics-based layer-to-layer coupler toward 3D optical interconnection," *IEICE Trans. Electron.* **E101**(7), 501–508 (2018).
33. D. C. Kilper, R. Bach, D. J. Blumenthal, D. Einstein, T. Landolsi, L. Ostar, M. Preiss, and A. E. Willner, "Optical performsnce monitoring," *J. Lightwave Technol.* **22**(1), 294–304 (2004).
34. A. E. Willner, Z. Pan, and C. Yu, "Optical performance monitoring," in *Optical Fiber Telecommunications V B*, Eds. I. P. Kaminow, T. Li and A. E. Willner, Academic Press, New York, 233–292 (2008).
35. B. Kozicki, O. Takuya, and T. Hidehiko, "Optical performance monitoring of phase-modulated signals using asynchronous amplitude histogram analysis," *J. Lightwave Technol.* **26**(10), 1353–1361 (2008).
36. Z. Dong, F. N. Khan, Q. Si, K. Zhong, C. Lu, and A. P. T. Lau, "Optical performance monitoring: A review of current and future technologies," *J. Lightwave Technol.* **34**(2), 525–543 (2016).

37. N. Miyazaki, K. Ooizumi, T. Hara, M. Yamada, H. Nagata, and T. Sakane, "LiNbO3 optical intensity modulator packaged with monitor photodiode," *IEEE Photon. Technol. Lett.* **13**(5), 442–444 (2001).
38. L. N. Binh, *Wireless and Guided Wave Electromagnetics: Fundamentals and Applications*, CRC Press, Boca Ranton, 301–302 (2013).
39. H. Kusaka, A. Oka, K. Goi, K. Ogawa, T.-Y. Liow, X. Tu, G.-Q. Lo, and D.-L. Kwong, "Monolithic photonic integrated circuit for optical performance monitoring of silicon Mach-Zehnder modulator in C and L bands," *18th OptoElectronics and Communications Conference and International Conference on Photonics in Switching (OECC/PS)*, MM1-4 (2013).
40. Y. Shani, Ch. H. Henry, R. C. Kistler, R. F. Kazarinov, and K. J. Orlowsky, "Integrated optic adiabatic devices on silicon," *IEEE J. Quantum Electron.* **27**(3), 556–566 (1991).
41. K. Goi, H. Kusaka, A. Oka, K. Ogawa, T.-Y. Liow, X. Tu, G.-Q. Lo, and D.-L. Kwong, "128-Gb/s DP-QPSK using low-loss monolithic silicon IQ modulator integrated with partial-rib polarization rotator," *Optical Fiber Communications Conference and Exhibition (OFC)*, W1I.2 (2014).
42. T. Kaneda, "Silicon and germanium avalanche photodiodes," in *Semiconductors and Semimetals* 22 Part D, Ed. W. T. Tsang, 247–328 (1985).
43. S. Luryi, A. Kastalsky, and J. C. Bean, "New infrared detector on a silicon chip," *IEEE Trans. Electron Dev.* **31**(9), 1135–1139 (1984).
44. H. Temkin, T. P. Pearsall, J. C. Bean, R. A. Logan, and S. Luryi, "Ge_xSi_{1-x} strained-layer superlattice waveguide photodetectors operating near 1.3 μm," *Appl. Phys. Lett.* **48**(15), 963–965 (1986).
45. L. Colace, G. Masini, and G. Assanto, "Ge-on-Si approaches to the detection of near-infrared light," *IEEE J. Quantum Electron.* **35**(12), 1843–1852 (1999).
46. J. Oh, J. C. Campbell, S. G. Thomas, S. Bharatan, R. Thoma, C. Jasper, R. E. Jones, and T. E. Zirkle, "Interdigitated Ge p-i-n photodetectors fabricated on a Si substrate using graded SiGe buffer layers," *IEEE J. Quantum Electron.* **38**(9), 1238–1241 (2002).
47. O.I. Dosunmu, D.D. Cannon, M.K. Emsley, L.C. Kimerling, and M.S. Ünlü, "High-speed resonant cavity enhanced Ge photodetectors on reflecting Si substrates for 1550-nm operation," *IEEE Photon. Technol. Lett.* **17**(1), 175–177 (2005).
48. M. Jutzi, M. Berroth, G. Wohl, M. Oehme, and E. Kasper, "Ge-on-Si vertical incidence photodiodes with 39-GHz bandwidth," *IEEE Photon. Technol. Lett.* **17**(7), 1510–1512 (2005).
49. Y. Ishikawa, K. Wada, D. D. Cannon, J. Liu, H.-C. Luan, and L. C. Kimerling, "Strain-induced band gap shrinkage in Ge grown on Si substrate," *Appl. Phys. Lett.* **82**(11), 2044–2046 (2003).

50. G. Dehlinger, S. J. Koester, J. D. Schaub, J. O. Chu, Q. C. Ouyang, and A. Grill, "High-speed germanium-on-SOI lateral PIN photodiodes," *IEEE Photon. Technol. Lett.* **16**(11), 2547–2549 (2004).
51. J. Liu, D. D. Cannon, K. Wada, Y. Ishikawa, S. Jongthammanurak, D. T. Danielson, J. Michel, and L. C. Kimerling, "Tensile strained Ge p-i-n photodetectors on Si platform for C and L band telecommunications," *Appl. Phys. Lett.* **87**(1), 011110-1–011110-3 (2005).
52. L. C. Kimerling, D. Ahn, A. B. Apsel, M. Beals, D. Carothers, Y-K. Chen, T. Conway, D. M. Gill, M. Grove, C.-Y. Hong, M. Lipson, J. Liu, J. Michel, D. Pan, S. S. Patel, A. T. Pomerene, M. Rasras, D. K. Sparacin, K-Y. Tu, A. E. White, and C. W. Wong, *Proc. SPIE* **6125**, 612502-1–612502-10 (2006).
53. L. Colace, G. M. A. Altieri, and G. Assanto, "Waveguide photodetectors for the near-infrared in polycrystalline germanium on silicon," *IEEE Photon. Technol. Lett.* **18**(9), 1094–1096 (2006).
54. T. Yin, R. Cohen, M. M. Morse, G. Sarid, Y. Chetrit, D. Rubin, and Mario J. Paniccia, "31GHz Ge n-i-p waveguide photodetectors on Silicon-on-Insulator substrate," *Opt. Express* **15**(21), 13965–13971 (2007).
55. S. Park, T. Tsuchizawa, T. Watanabe, H. Shinojima, H. Nishi, K. Yamada, Y. Ishikawa, K. Wada, and S. Itabashi, "Monolithic integration and synchronous operation of germanium photodetectors and silicon variable optical attenuators," *Opt. Express* **18**(8), 8412–8421 (2010).
56. Y. Ishikawa and K. Wada, "Near-infrared Ge photodiodes for Si Photonics: Operation frequency and an approach for the future," *IEEE Photon. J.* **2**(3), 303–320 (2010).
57. T.-Y. Liow, Q. Fang, A. E.-J. Lim, L. Ding, Q. X. Zhang, J. Zhang, N. Duan, J. Song, F.-F. Ren, H. Cai, S. T. H. Silalahi, M. Yu, G.-Q. Lo, and D.-L. Kwong, "Silicon photonic integrated circuits: from devices to integration," *Proc. SPIE* **7942**, 79420E-1–79420E-10 (2011).
58. L. Chen and M. Lipson, "Ultra-low capacitance and high speed germanium photodetectors on silicon," *Opt. Express* **17**(10), 7901–7906 (2009).
59. M. S. Hai, Me. N. Sakib, and O. Liboiron-Ladouceur, "A 16 GHz silicon-based monolithic balanced photodetector with on-chip capacitors for 25 Gbaud front-end receivers," *Opt. Express* **21**(26), 32680–32689 (2013).
60. Y. Kang, H.-D. Liu, M. Morse, M. J. Paniccia, M. Zadka, S. Litski, G. Sarid, A. Pauchard, Y.-H. Kuo, H.-W. Chen, W. S. Zaoui, J. E. Bowers, A. Beling, D. C. McIntosh, X. Zheng, and J. C. Campbell, "Monolithic germanium/silicon avalanche photodiodes with 340 GHz gain-bandwidth product," *Nature Photon.* **3**, 59–63 (2009).

61. S. Assefa, F. Xia, and Y. A. Vlasov, "Reinventing germanium avalanche photodetector for nanophotonic on-chip optical interconnects," *Nature* **464**, 80–85 (2010).
62. N. Duan, T. Liow, A. Lim, L. Ding, and G. Q. Lo, "310 GHz gain-bandwidth product Ge/Si avalanche photodetector for 1550 nm light detection," *Opt. Express* **20**(10), 11031–11036 (2012).
63. K.-S. Jang, S. Kim, I. G. Kim, J. H. Oh, S. A. Kim, J. Joo, and G. Kim, "High-speed integrated Ge PD for receiver," *Proc. SPIE* **9753**, 97351C-1–97531C-6 (2016).
64. J. Michel, J. Liu, and L. C. Kimerling, "High-performance Ge-on-Si photodetectors," *Nature Photon*. **4**, 527–534 (2010).
65. K.-W. Ang, G.-Q. Lo, and D.-L. Kwong, "Germanium photodetector technologies for optical communication applications," in *Semiconductor Technologies*, Ed. J. Grym, InTech, Rijeka, Shanghai, 373–406 (2010); Available from: http://www.intechopen.com/books/semiconductor-technologies/germanium-photodetector-technologies-for-optical-communication-applications.
66. S. Su, B. Cheng, C. Xue, W. Wang, Q. Cao, H. Xue, W. Hu, G. Zhang, Y. Zuo, and Q. Wang, "GeSn p-i-n photodetector for all telecommunication bands detection," *Opt. Express* **19**(7), 6400–6405 (2011).
67. R. R. Grote, B. Souhan, N. Ophir, J. B. Driscoll, K. Bergman, H. Bahkru, W. M. J. Green, and R. M. Osgood, Jr, "Extrinsic photodiodes for integrated mid-infrared silicon photonics," *Optica* **1**(4), 264–267 (2014).
68. H. Zhu, K. Goi, and K. Ogawa, to be presented in OECC 2017.
69. H. Ishii, K. Kasaya, H. Oohashi, Y. Shibata, H. Yasaka, and K. Okamoto, "Widely wavelength-tunable DFB laser array integrated with funnel combiner," *IEEE J. Sel. Top. Quantum Electron.* **13**(5), 1089–1094 (2007).

Appendix

A.1 Bit Rates and Modulation Formats in High-Capacity Optical Networks

A.1.1 Bit rates

Transmission capacity is measured as the bit rate, as mentioned in Chapter 2.[1] Bit rate is the total number of bits contained in the symbols transmitted per second. The number of bits per symbol depends on the modulation format selected in the optical networks in which optical data are transmitted. Bit rate is measured in various units, such as 1 b/s, with a unit prefix (as listed in Table A.1) according to the transmission capacity of the optical network involved.

One byte contains eight bits. A Blu-Ray disc, for instance, accommodates digital content up to 50 GB in dual layers (25 GB per layer), and thus 400 Gbit in dual layers. All of the contents can be transmitted in 4 s in a 100-Gb/s optical transmission system and in 1 s in a 400-Gb/s optical transmission system.

A.1.2 Formats in intensity modulation

The most basic format in intensity modulation is binary modulation, called on–off keying (OOK) or amplitude-shift keying (ASK), in which each symbol contains one bit of information in IM-DD transmission systems.[2] The optical modulator in use has the highest power transmission T_{on} in the ON state "1," whereas it has the lowest power transmission T_{off} in the OFF state "0." Eye diagrams generated in two OOK formats are illustrated in Fig. A.1. One is non-return-to-zero (NRZ) format, and the other is return-to-zero (RZ) format, respectively. The former format is more extensively used than the latter because slower electronics can be used for electrical on–off signal generation and higher spectral efficiency can be achieved with the narrower modulation frequency bandwidth of the NRZ-OOK format. The latter format is employed if symbol interference in the time domain is an issue. The both formats yield schematically the same constellation diagram, which is a graphic representation of the modulated signals in a complex electric-field plane spanned with the real axis of the in-phase (I) component and the imaginary axis of the quadrature (Q) component, respectively.

Table A.1 Bit rates with unit prefixes.

1 megabit per second, 1 Mb/s = 10^6 b/s
1 gigabit per second, 1 Gb/s = 10^9 b/s
1 terabit per second, 1 Tb/s = 10^{12} b/s
1 petabit per second, 1 Pb/s = 10^{15} b/s
1 exabit per second, 1 Eb/s = 10^{18} b/s
1 zettabit per second, 1 Zb/s = 10^{21} b/s
1 yottabit per second, 1 Yb/s = 10^{24} b/s

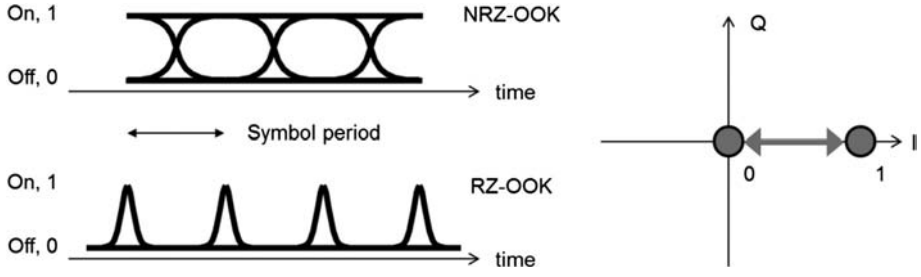

Figure A.1 Eye diagrams of NRZ-OOK and RZ-OOK, and a constellation diagram in both formats.

Multi-level intensity modulation formats, called pulse amplitude modulation (PAM*n*), have been employed to increase the number of bits per symbol, i.e., bit rate. Here, a numeric n stands for the number of modulated intensity levels, and $n = 2^{N_{\text{bit}}}$ with the number of bits N_{bit}. If the letter is 4, which represents the format of PAM4, one symbol contains four intensity levels, namely two bits ($N_{\text{bit}} = 2$). An eye diagram and a constellation diagram in PAM4 are shown in Fig. A.2. This format has been developed for high-capacity WDM datacom links such as 400-Gb/s ethernet.[3] The multi-level intensity modulation formats are more sensitive to noise than OOK because fractional intensity levels are assigned to the modulation bits.

A.1.3 Formats in phase modulation

Binary phase-shift keying is the most fundamental modulation format in phase-shift keying (PSK).[2] The schematic optical power and envelope field eye

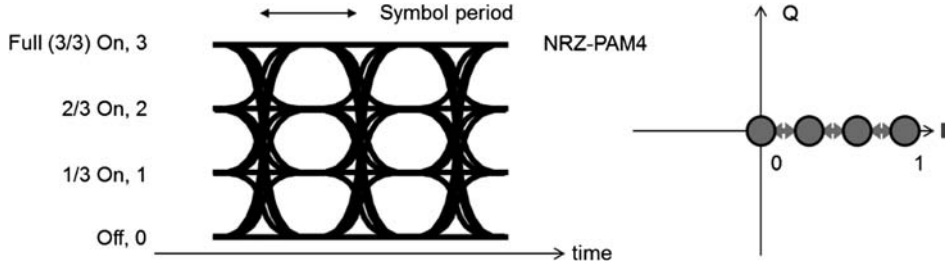

Figure A.2 Eye diagram and constellation diagram in PAM4.

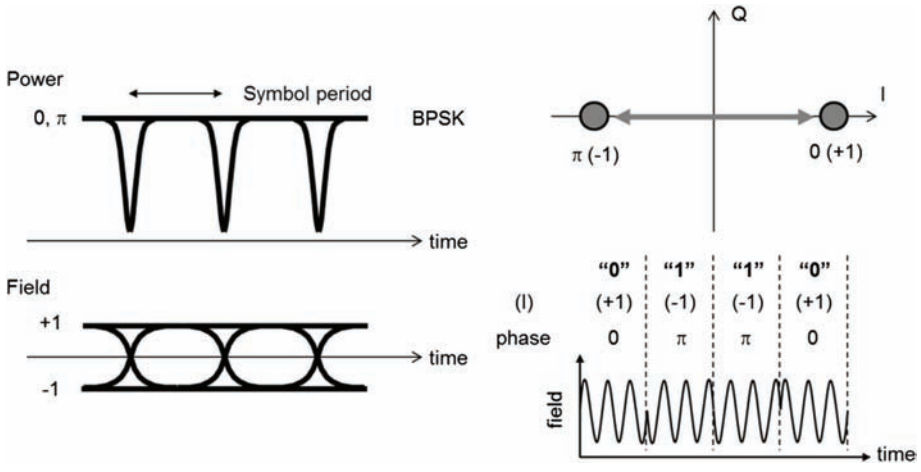

Figure A.3 Eye diagrams, constellation diagram, and time-domain waveform in BPSK.

diagrams are presented in Fig. A.3 with a schematic constellation diagram in BPSK. One symbol in this format contains one-bit data of 0 and π. Experimentally, the field diagram can be acquired in differential voltage outputs from a photoreceiver. Zero-chirp modulation using a push–pull MZ optical modulator is anticipated. An intensity dip observed in the power eye diagram in PSK is caused by a bit transition between 0 and π levels, characteristic of push–pull modulation. (See Chapter 3 for more details on the operational principles of push–pull optical modulators.) This format allows for an improvement in receiver sensitivity in comparison with OOK, whereby the SNR in signal detection is increased.[4]

Quadrature phase-shift keying (QPSK) is more suitable to high-capacity optical networks because one symbol contains two bits, one bit in the I component and another bit in the Q component.[3] Power and envelope field eye diagrams and a constellation diagram are shown schematically in Fig. A.4. Four states of carrier phase are separated by π/2 between adjacent phase states. Two levels are observed in an intensity dip according to two types of trajectory paths. One type of trajectory goes through the origin in transition between π/4- and 5π/4-phase states or between 3π/4- and 7π/4-phase states. The other type of trajectory between adjacent phase states does not go through the origin but provides a half-intensity dip. The I and Q components are orthogonal, and so these components can be represented mathematically with cosine and sine trigonometric functions, respectively. A push–pull quadrature optical modulator is used for optical signal generation in this format. In digital coherent communication, which is the most advanced communication system in optical transport networks, data in the QPSK format are multiplexed in two orthogonal linear polarization states. The format with PDM is called dual-polarization quadrature phase-shift keying (DP-QPSK), which is the most fundamental modulation format in PDM IQ schemes.[5,6]

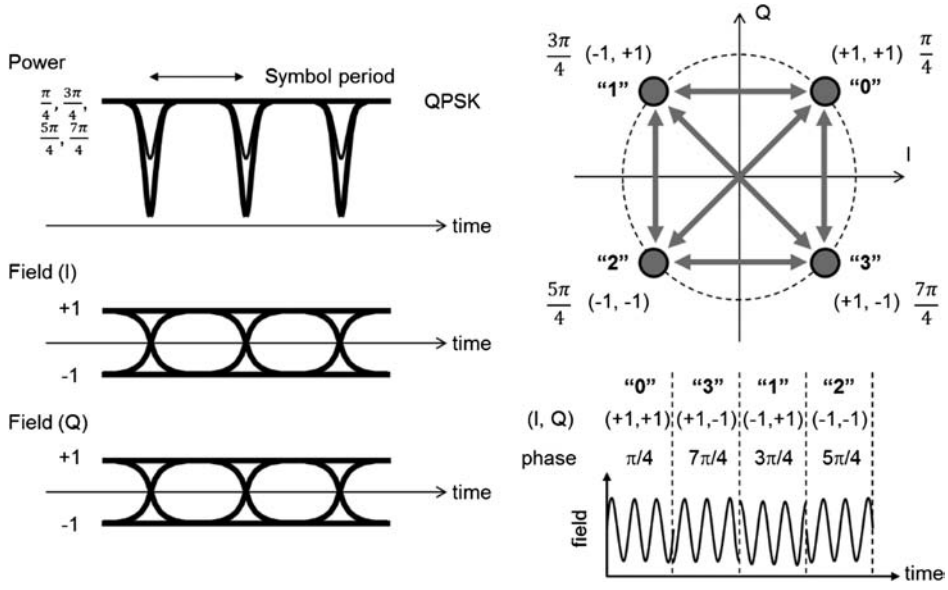

Figure A.4 Eye diagrams, constellation diagram, and time-domain waveform in QPSK.

Quadrature amplitude modulation (QAM) accommodates multi-level intensity modulation in conjunction with QPSK.[5] The number of signal levels in QAM is denoted as a numeric in front of QAM (nQAM). Similar to PAMn, $n = 2^{N_{\text{bit}}}$, whereby nQAM contains N_{bit} per symbol. Schematic envelope field eye diagrams and a constellation diagram in the case of four bits per symbol (e.g., 16QAM) are presented in Fig. A.5. The minimum number of bits is two,

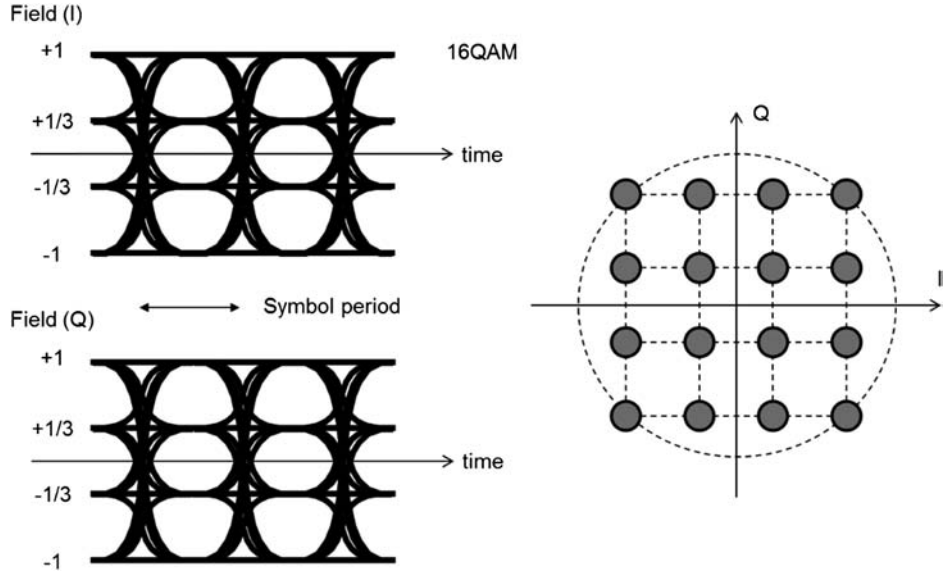

Figure A.5 Eye diagrams and constellation diagram in 16QAM.

which implies that 4QAM is equivalent to QPSK. This format is most suitable to increase transmission capacity with an increase in the bit multiplication of optical intensity. However, noise is more serious, and a higher SNR is required with an increased number of bits, similar to PAM*n*. Polarization multiplexing of the *n*QAM data is also exploited in digital coherent communication. Details on the transmission characteristics associated this type of modulation formats is described in Chapter 7.

A theoretical BER has been derived for *n*QAM including QPSK on the basis of Gray coding under additive white Gaussian noise.[7] The BER is plotted in Fig. A.6 as a function of the SNR from QPSK ($N_{\text{bit}} = 2$) to 256QAM ($N_{\text{bit}} = 8$). One can verify that a higher SNR per bit is required with increasing multiplicity to sustain a specified BER. Square QAM with even N_{bit} is more efficient than rectangular QAM with odd N_{bit} in terms of SNR. This difference is qualitatively explained on the basis of schematic constellation diagrams in 8QAM ($N_{\text{bit}} = 3$) and 16QAM ($N_{\text{bit}} = 4$). In the rectangular QAM, there are unused states as indicated with white circles, and the space is not filled sufficiently with signals.

A.1.4 Format in sub-carrier modulation

A discrete multi-tone (DMT) has been exploited for digital subscriber metal-cable lines and further developed for high-capacity WDM datacom links as 400-Gb/s ethernet. This format is classified as a sub-carrier modulation format based on IM-DD.[9] The modulation scheme is illustrated in Fig. A.7 according to Ref. 9. Signals in a DMT comprise the sub-carrier components, and the modulation format of each sub-carrier component is determined by the response of the transmission line at the center frequency of each component.

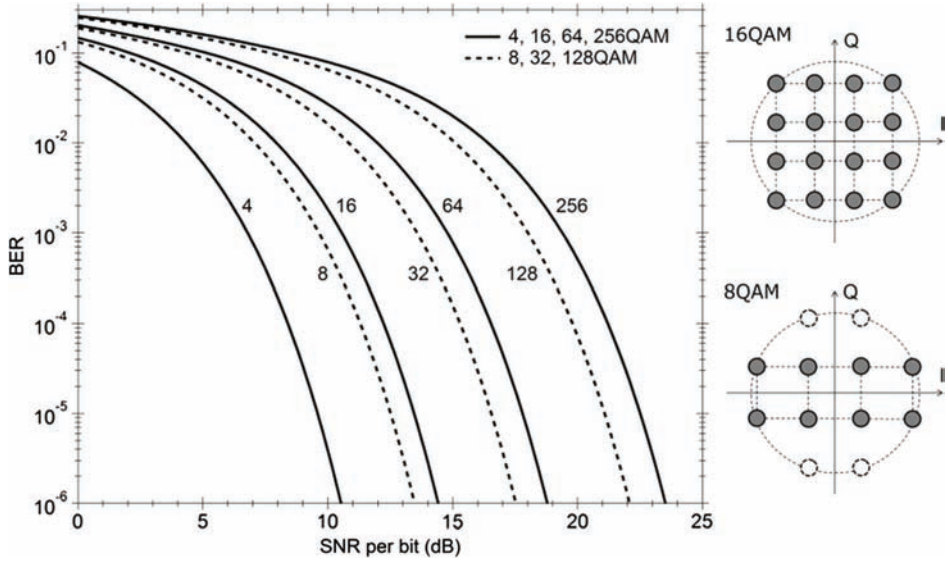

Figure A.6 Theoretical BER characteristics of *n*QAM.

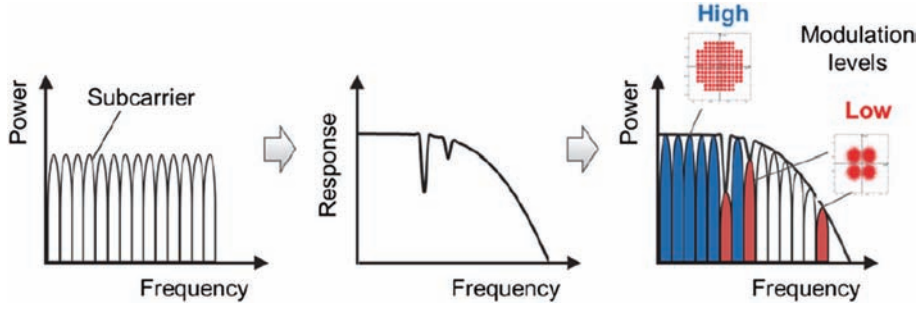

Figure A.7 Modulation schematic in DMT.[9]

Transmission capacity is increased by allocating a higher degree of multi-level modulation format to a sub-carrier component exhibiting a better response.

A.2 Kramers–Kronig Transformation

A.2.1 General principle

A mathematical formula based on the Kramers–Kronig transformation allows converting the optical absorption spectrum into the refraction spectrum and thus has been extensively used to characterize the dispersive characteristics of various optical materials and structures.[10,11] The dispersion relation has derived from the causality of the linear response of polarizability to an external field, and mathematically from Cauchy's theorem on the complex analytical function and also his principal value integral. The Kramers–Kronig formula has been obtained simply with two steps that comprise a Fourier transform of the causality step function and then a Fourier transform of the convolution integral in the linear response including the causality step function.[12] These steps lead to the well-known formulae written as[10–12]

$$\chi_R(\omega) = \frac{2}{\pi} P \int_0^\infty d\omega' \frac{\omega' \chi_I(\omega')}{\omega'^2 - \omega^2} \tag{A.1}$$

and

$$\chi_I(\omega) = -\frac{2\omega}{\pi} P \int_0^\infty d\omega' \frac{\chi_R(\omega')}{\omega'^2 - \omega^2} \tag{A.2}$$

for the real and imaginary parts of polarizability χ_R and χ_I. Refractive index $n_0 + \Delta n(\omega)$ and absorption coefficient $\alpha(\omega)$ are related with the polarizability terms through the relation

$$\chi_R(\omega) + i\chi_I(\omega) = \left\{ n_0 + \Delta n(\omega) + i\frac{ca(\omega)}{2\omega} \right\}^2. \tag{A.3}$$

Here, n_0 and $\Delta n(\omega)$ denote the background refractive index and refractive index term, respectively, related to the source of the optical response causing

the optical absorption. The refractive index term and optical absorption coefficient are analytic functions, thus producing the following formulae:[13]

$$\Delta n(\omega) = \frac{c}{\pi} P \int_0^{\infty} d\omega' \frac{\alpha(\omega')}{\omega'^2 - \omega^2} \tag{A.4}$$

and

$$\alpha(\omega) = -\frac{4\omega^2}{\pi c} P \int_0^{\infty} d\omega' \frac{\Delta n(\omega)}{\omega'^2 - \omega^2}. \tag{A.5}$$

A.2.2 Computational method

The refractive index term defined in Eq. (A.4) can be produced computationally by implementing a numerical algorithm of Cauchy's principal value integral.[14,15] The dispersive lineshape plotted in Fig. A.8 is a numerical result of the refractive index term obtained from the mathematical function of the Lorentzian peak for the optical absorption spectrum. The dispersive lineshape agrees well with the mathematical form of the refractive index term in the classical theory of a damped harmonic oscillator driven under an AC electric field. The computational method is applied to derive the numerical electrorefraction spectrum from the experimental optical absorption spectrum associated with electronic states in biased semiconductor quantum wells.

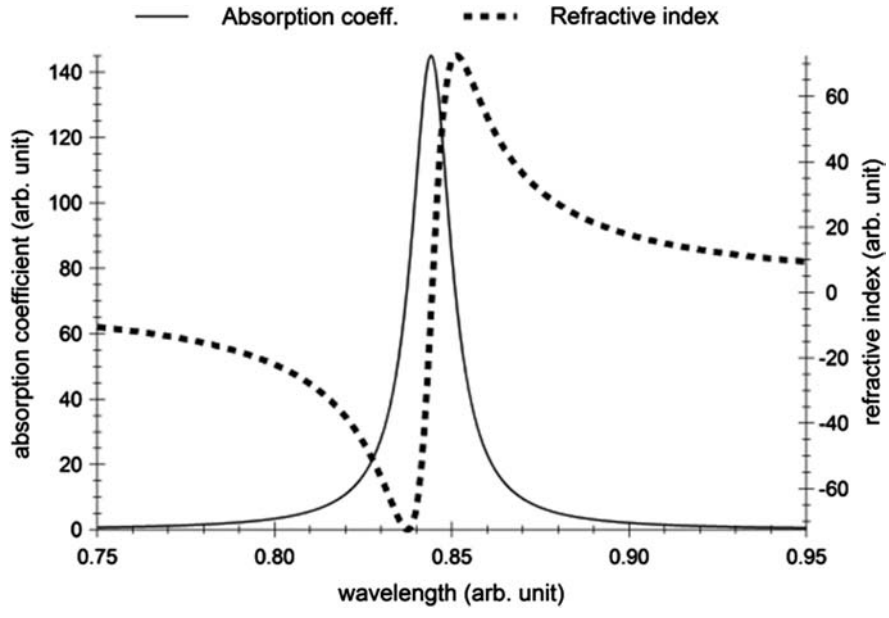

Figure A.8 Computational optical-absorption and refraction spectra for a Lorentzian absorption peak.

References

1. C. E. Shannon, "A mathematical theory of communication," *Bell System Tech. J.* **27**(3) 379–423 (1948).
2. P. J. Winzer and R.-J. Essiambre, "Advanced modulation formats for high-capacity optical transport networks," *J. Lightwave Technol.* **24**(12), 4711–4727 (2006).
3. W. I. Way, T. K. Chan, and A. Lebedev, "Short-haul transmission links based on 28- and 56-Gbaud PAM4 modulation," *Proc. SPIE* **9775**, 977505-1–977505-4 (2016).
4. K. Kikuchi, "Coherent transmission systems," *34th European Conference on Optical Communication (ECOC)*, Th.2.QA.1 (2008).
5. A. H. Gnauck, P. J. Winzer, S. Chandrasekhar, X. Liu, B. Zhu, and D. W. Peckham, "10 × 224-Gb/s WDM transmission of 28-Gbaud PDM 16-QAM on a 50-GHz grid transmission over 1,200 km of fiber," *Optical Fiber Communication Conference and Exposition and the National Fiber Optic Engineers Conference (OFC/NFOEC)*, PDPB8 (2010).
6. K. Kikuchi, "Fundamentals of coherent Optical fiber communications," *J. Lightwave Technol.* **34**(1), 157–179 (2016).
7. K. Cho and D. Yoon, "On the general BER expression of one- and two-dimensional amplitude modulations," *IEEE Trans. Commun.* **50**(7), 1074–1080 (2002).
8. W. J. Weber III, "Differential encoding for multiple amplitude and phase shift keying systems," *IEEE Trans. Commun.* **26**(3), 385–391 (1978).
9. M. Nishihara, T. Tanaka, T. Takahara, L. Li, Z. Tao, and J. C. Rasmussen, "Impact of modulator chirp in 100 Gbps class optical discrete multi-tone transmission system," *Proc. SPIE* **8646**, 86860N-1–86460N-11 (2013).
10. R. de L. Kronig, "On the theory of the dispersion of X-rays," *J. Opt. Soc. Am.* **12**(6), 547–557 (1926).
11. M. S. Dresselhaus, *Solid State Physics Part II Optical Prpoerties of Solids*, MIT course, 6.732 Solid State Physics, 58–65 (2001); http://web.mit.edu/course/6/6.732/www/6.732-pt2.pdf.
12. B. Y.-K. Hu, "Kramers-Kronig in two lines," *Am. J. Phys.* **57**(9), 821–821 (1989).
13. C. F. Bohren, "What did Kramers and Kronig do and how did they do it?," *Eur. J. Phys.* **31**(3), 573–577 (2010).
14. http://mathworld.wolfram.com/CauchyPrincipalValue.html
15. W. H. Press, S. A. Teukolsky, W. T. Vetterling, and B. P. Flannery, *Numerical Recipes, The Art of Scientific Computing*, 3rd Ed., Cambridge University Press, Cambridge, New York, 178–179 (2007).

Index

Kensuke Ogawa received Ph.D. in physics in 1987 from Osaka University, Japan. That same year, he joined the Central Research Laboratory, Hitachi Ltd., Japan, where he performed research on semiconductor photonic devices for optical computing. From May 1992 to September 1994, he was appointed as a Senior Researcher of the Hitachi Cambridge Laboratory, UK, in collaboration with the Microelectronics Research Centre, University of Cambridge, UK, to conduct ultrafast electro-optic studies on quantum semiconductor devices in time-resolved electro-optic sampling using ultrashort pulse lasers. In May 2002, he joined XNRI (Mitsui-founded nanotechnology institute), where he organized the research and development of photonic integrated circuits on silicon-photonics platforms in collaboration with the Institute of Microelectronics, Singapore. The properties and assets were transferred to Fujikura Ltd., Japan in July 2006. He accordingly moved to the Optics and Electronics Laboratory (reorganized thereafter as the Advanced Technology Laboratory) of the company as Chief Researcher to continue the research and development of photonic integrated circuits.

Since November 2017, Ogawa has been with the Department of Electrical and Electronic Engineering, Tokyo Institute of Technology, to perform research and education related to photonic integrated circuits. He has been a Specially Appointed Professor at the university since April 2018. His current research interests include photonic and magneto-optic integrated circuits on heterogeneous integration platforms for communication and sensing, ultrafast optical nonlinearity in photonic integrated circuits for optical signal processing and computing, and optical metrology based on laser interferometry for sensing.